

Technische Universität München  
Fakultät für Elektrotechnik und Informationstechnik  
Lehrstuhl für Hochfrequenztechnik

**Steerable Millimeter-Wave Gaussian Beam Shaping Phased  
Array Antenna for Doppler Reflectometry of Nuclear Fusion  
Plasma Turbulence in ASDEX Upgrade Tokamak**

Christian Koenen

Vollständiger Abdruck der von der Fakultät für Elektrotechnik und  
Informationstechnik der Technischen Universität München zur Erlangung des  
akademischen Grades eines

*– Doktor-Ingenieurs –*

genehmigten Dissertation.

Vorsitzender: Prof. Dr.-Ing. habil. Dr. h.c. Alexander W. Koch  
Prüfer der Dissertation: 1. Prof. Dr.-Ing. Thomas F. Eibert  
2. Prof. Dr. Ulrich Stroth

Die Dissertation wurde am 02.10.2019 bei der Technischen Universität München  
eingereicht und durch die Fakultät für Elektrotechnik und Informationstechnik am  
20.01.2020 angenommen.



## Zusammenfassung

Die vorliegende Arbeit entstand im Rahmen einer internationalen Kollaboration zwischen Kernfusions-Forschungseinrichtungen und Universitäten, die im „Helmholtz Virtual Institute: Plasma Dynamical Processes and Turbulence Studies using Advanced Microwave Diagnostics“ organisiert war. Das Ziel der Kollaboration bestand darin, das Verständnis über Transportmechanismen durch Plasmaturbulenzen zu erweitern sowie neue mikrowellenbasierte Diagnostikinstrumente für die Messung von Plasmaturbulenzen zu erforschen.

Turbulenzen in einem magnetisch eingeschlossenen Plasma werden durch radiale Gradienten der Plasmatemperatur und Plasmadichte verursacht. Sie sind für den Teilchen- und Wärmetransport aus dem Plasmakern nach außen zur Plasmawand verantwortlich und beschränken dadurch die Energieeinschlusszeit. Eine möglichst lange Energieeinschlusszeit ist für eine ökonomische und effiziente Realisierung eines Kernfusionsreaktors allerdings notwendig. Um diese zu erreichen, müssen die Prozesse und Bedingungen, welche zu einer Reduzierung der Plasmaturbulenzen führen, verstanden werden.

Zur Messung von Plasmaturbulenzen werden ein komplexer Versuchsaufbau sowie verlässliche diagnostische Instrumente benötigt, welche den rauen Umgebungsbedingungen in einem Fusionsexperiment standhalten müssen. Das Design und die Realisierung der Strahlformungseinheit eines solchen diagnostischen Instrumentes, welches mit elektromagnetischen Wellen im Millimeterwellenbereich arbeitet, ist Thema dieser Arbeit.

Plasmaturbulenzen können mittels Doppler Reflektometrie gemessen und untersucht werden. Das Frontend des in Betracht gezogenen Doppler Reflektometers zur Untersuchung von Plasmaturbulenzen soll einen definierten Gaußstrahl im Millimeterwellenbereich formen und schwenken. Aufgrund des begrenzten Installationsraumes innerhalb des Gefäßes und den Umgebungsbedingungen in der Nähe des Plasmas ist das einzige realisierbare Antennenkonzept eine phasengesteuerte Gruppenantenne die im Wesentlichen aus Metall gefertigt ist.

Diese Arbeit beinhaltet das Design und die Realisierung einer phasengesteuerten Gruppenantenne, welche einen definierten Gaußstrahl im *W*-band von 75 GHz bis 105 GHz formt und schwenkt. Der Gaußstrahl benötigt einen frequenzunabhängigen Amplitudenbelag und einen frequenzabhängigen Phasenbelag auf der Apertur. Alle individuellen Komponenten des Speisenetzwerkes, die zu der gewünschten Aperturbelebung führen, werden beschrieben. Prototypen der individuellen Komponenten werden

vorgestellt und diskutiert. Das Schwenken des Gaußstrahles wird durch aktiv gesteuerte Phasenschieber ermöglicht. Das abgestrahlte Feld der Gruppenantenne wird auf Basis des Spektrums ebener Wellen des Aperturfeldes berechnet. Der dadurch ermittelte Gaußstrahl für die berechnete Aperturebelegung wird mit Vollwellensimulationen der gesamten Antennengeometrie verglichen.

Die wesentlichen Beiträge dieser Arbeit umfassen eine breitbandige Koppelstruktur, einen Phasenschieber in WR10 Rechteckhohlleiter-Technologie, sowie die Gesamtarchitektur der phasengesteuerten Gruppenantenne.

Die Koppelstruktur stellt den Amplitudenbelag der Gruppenantenne ein, wobei die realisierten Prototypen einen nahezu frequenzunabhängigen Teilungsfaktor (Koppelfaktor) von 75 GHz bis 110 GHz sowie eine Anpassung besser  $-20$  dB aufweisen. Die Konstruktion der Koppelstruktur besteht aus zwei Teilen: einer Passung im WR10 Split-Block sowie einem Einstekteil. Das Einstekteil kann mittels Laserschneiden oder Drahterosion gefertigt werden. Mit den drahterodierte Einstekteilen wurden die Teilungsfaktoren  $(-14.6 \pm 0.5)$  dB,  $(-21.7 \pm 0.5)$  dB, und  $(-30.9 \pm 0.9)$  dB realisiert. Die gewünschten und realisierten Teilungsfaktoren haben hier eine Abweichung von  $0.1$  dB.

Der Phasenschieber nutzt einen Hybrid-Koppler, um die Reflektion von zwei Kurzschlusschiebern in eine Transmission mit variabler elektrischer Länge zu wandeln. Der Kurzschlusschieber richtet sich innerhalb des WR10 Hohlleiters selber aus, wodurch unerwünschte Kontakte mit den Hohlleiterwänden verhindert werden. Die Abweichung der reflektierten Phase von 10 zufällig gewählten Prototyp-Kurzschlusschiebern ist kleiner  $1^\circ$ . Der Hybrid-Koppler ist als Branch-Guide Koppler ausgelegt. Die Einfügedämpfung des Phasenschiebers beträgt  $0.2$  dB bis  $0.4$  dB und die Anpassung ist besser  $-25$  dB im Frequenzbereich von  $80$  GHz bis  $105$  GHz. Der theoretische und der realisierte Phasenversatz unterscheiden sich im Bereich  $8^\circ$  bis  $-6^\circ$  für Frequenzen von  $75$  GHz bis  $105$  GHz bei drei Kurzschlusschieberpositionen  $0.467$  mm,  $0.982$  mm, und  $1.507$  mm.

Die Gesamtarchitektur der phasengesteuerten Gruppenantenne ermöglicht die Installation im ASDEX Upgrade Tokamak. Die Gruppenantenne besteht aus 39 Reflektor-Einzelstrahlern, welche den Gaußstrahl formen. Die Einzelstrahler sind mit einem fünf-lagigen Split-Block Speisennetzwerk verbunden. Das Schwenken des Gaußstrahls wird durch zwei Piezo-Aktoren ermöglicht, wobei eine Frequenzabhängigkeit der Abstrahlrichtung unterdrückt wird. Der aus Vollwellensimulationen der gesamten Gruppenantenne ermittelte Gaußstrahl hat eine Strahltaille, die um 5% bis 10% kleiner ist als die gewünschte Strahltaille. Die Nebenkeulen sind bei Querabstrahlung unter  $-25$  dB. Der Eingangsreflektionsfaktor der Gruppenantenne ist unterhalb von  $-20$  dB, was für einen monostatischen Aufbau des Doppler Reflektometers vorteilhaft ist.

# Abstract

This thesis evolved as part of an international collaboration of nuclear fusion research centers and universities in the framework of the “Helmholtz Virtual Institute” on “Plasma Dynamical Processes and Turbulence Studies using Advanced Microwave Diagnostics”. The aims of this cooperation were to advance the understanding of turbulent transport in thermo-nuclear fusion experiments and to establish new microwave-based diagnostic instruments for plasma turbulence measurements.

Turbulence in a magnetically confined plasma is driven by radial gradients in plasma density and temperature. Turbulence is responsible for particle and heat transport from the plasma core to the plasma edge and, thereby, limiting the energy confinement time. Extending the energy confinement time, however, is important for an economical and efficient realization of nuclear fusion reactors. Towards the achievement of this goal, it is essential to understand the processes and conditions that lead to a suppressed turbulence level.

Measuring plasma turbulence is not a trivial task. It requires a sophisticated experimental setup and reliable diagnostic instruments that survive in the harsh environment inside the nuclear fusion experiment. The design and realization of the transceiver part of such a diagnostic instrument working with electromagnetic waves in the millimeter-wave regime is the scope of this thesis.

Plasma turbulence can be measured and investigated by Doppler reflectometry. The front-end of the considered Doppler reflectometer for plasma turbulence studies is intended to shape and steer a well defined Gaussian beam in the millimeter-wave region. Due to limited space at the installation location inside the vessel and the environmental conditions near the plasma, the only reasonable antenna concept is a phased array antenna built predominately from metal.

This thesis focuses on the design and realization of a phased array antenna that shapes and steers a well defined Gaussian beam in the *W*-band from 75 GHz to 105 GHz. The desired Gaussian beam requires a frequency invariant amplitude taper and a frequency dependent phase taper. All individual feed components that lead to the desired aperture field distribution are presented, prototyped, and discussed. Steering the beam is enabled by actively controlled reflection-type phase shifters. The computation of the radiated beam follows from evaluating the plane wave spectrum of the aperture field. The theoretically predicted Gaussian beam shape for the derived array taper is compared to full-wave simulations of the whole antenna geometry.

The major accomplishments of this work are a full-band coupling structure and a

phase shifter in WR10 rectangular hollow waveguide technology as well as the overall architecture of the phased array antenna.

The coupling structure controls the amplitude taper of the phased array antenna, where the realized prototype coupling structures have an almost frequency invariant power division ratio from 75 GHz to 110 GHz with a matching better than  $-20$  dB. The construction consists of two-pieces: a fixture in a WR10 split-block and an insert. The insert is either manufactured by laser-cutting or wire-erosion. With the wire-eroded inserts, the realized division ratios are  $(-14.6 \pm 0.5)$  dB,  $(-21.7 \pm 0.5)$  dB, and  $(-30.9 \pm 0.9)$  dB. Here, the desired and realized coupling factors differ by about 0.1 dB.

The reflection-type phase shifter employs a hybrid-junction that transforms the reflection of a sliding short into a transmission with variable electrical length. The sliding short is self-aligning within the WR10-waveguide to avoid any undesired wall contact. The reflection phase of 10 randomly selected prototype sliding shorts differs by less than  $1^\circ$ . The hybrid-junction is realized as a branch-guide coupler. The insertion loss of the phase-shifter is between 0.2 dB to 0.4 dB and the matching is better than  $-25$  dB in the frequency range from 80 GHz to 105 GHz. The theoretical and the realized phase shift differ by  $8^\circ$  and  $-6^\circ$  in the frequency range from 75 GHz to 105 GHz for the three sliding short positions 0.467 mm, 0.982 mm, and 1.507 mm.

The overall architecture of the phased array antenna enables its installation in the available space within the ASDEX Upgrade tokamak. The array is composed of 39 individual radiating reflector elements that shape the Gaussian beam. They are connected to a five layer split-block feed network. Steering of the Gaussian beam is possible by two Piezo actuators in a true time-delay fashion. The predicted Gaussian beam from full-wave simulations of the whole phased array antenna has a beam waist radius that is about 5% to 10% smaller than the desired beam waist radius. The side-lobe level is below  $-25$  dB for broadside radiation. The input reflection of the phased array antenna is below  $-20$  dB, which is important in a mono-static Doppler reflectometry arrangement.

# Contents

<b>1</b>	<b>Introduction</b>	<b>1</b>
1.1	Nuclear Fusion . . . . .	1
1.2	Plasma Turbulence Studies . . . . .	3
1.3	Scope of this Thesis . . . . .	4
1.4	Outline of this Thesis . . . . .	6
<b>2</b>	<b>Fundamental Concepts</b>	<b>7</b>
2.1	Electromagnetic Fields . . . . .	7
2.1.1	Maxwell's Equations . . . . .	7
2.1.2	Constitutive Relations . . . . .	8
2.1.3	Boundary Conditions . . . . .	10
2.2	Plane Waves and Plane Wave Spectrum Representation . . . . .	10
2.2.1	General Plane Wave Solution . . . . .	10
2.2.2	Plane Wave Spectrum Representation . . . . .	12
2.2.3	Propagation of the Plane Wave Spectrum . . . . .	13
2.3	Gaussian Beams . . . . .	14
2.3.1	Paraxial Wave Propagation . . . . .	15
2.3.2	Fundamental Gaussian Beam . . . . .	16
2.3.3	Limitations of the Paraxial Approximation . . . . .	20
2.3.4	Higher-Order Gaussian Beams and Bessel Beams . . . . .	22
2.4	Guided Waves . . . . .	24
2.4.1	Rectangular Hollow Waveguide . . . . .	26
2.4.2	Radial Parallel Plate Waveguide . . . . .	32
2.5	Electromagnetic Waves in Plasma . . . . .	36
2.5.1	Ordinary Mode (O-Mode) . . . . .	39
2.5.2	Extraordinary Mode (X-Mode) . . . . .	40
<b>3</b>	<b>Doppler Reflectometry with Phased Array Antennas</b>	<b>41</b>
3.1	Doppler Reflectometry of Plasma Turbulence . . . . .	41
3.1.1	Principle of Doppler Reflectometry . . . . .	41
3.1.2	Turbulence Wavenumber Spectrum . . . . .	43
3.1.3	Turbulence Velocity . . . . .	44
3.2	Phased Array Antennas . . . . .	45

3.3	Gaussian Beam Synthesis from a Phased Array Antenna . . . . .	49
3.3.1	Sampling of the Gaussian Beam Transverse Field . . . . .	50
3.3.2	Influence of the Edge Taper (Number of Elements) . . . . .	55
3.3.3	Influence of Aperture Amplitude and Phase Errors . . . . .	56
3.3.4	Steering of the Gaussian Beam . . . . .	58
3.3.5	Suitable Radiating Elements . . . . .	61
3.3.6	Consideration of Mutual Coupling . . . . .	62
3.3.7	Synthesis of a Full-Band Gaussian Beam . . . . .	64
<b>4</b>	<b>Individual Antenna Components</b>	<b>69</b>
4.1	Coupling Structure or Power Divider . . . . .	69
4.1.1	Fundamental Model . . . . .	70
4.1.2	Laser-Cut Insert . . . . .	73
4.1.3	Wire-Eroded Insert . . . . .	78
4.2	Variable Phase Shifter . . . . .	82
4.2.1	Fundamental Model . . . . .	83
4.2.2	Self-Aligning Sliding Short . . . . .	84
4.2.3	Hybrid-Junction (Branch-Guide Coupler) . . . . .	91
4.2.4	Prototype Reflection-Type Phase Shifter . . . . .	93
4.3	Invariable Phase Shifter . . . . .	96
4.3.1	Focusing of Wavelength-Dependent Gaussian Beams . . . . .	97
4.3.2	Constant-Phase Relative Phase Shift . . . . .	98
4.4	WR10 Waveguide Load . . . . .	103
4.4.1	Absorbing Materials/Dielectrics . . . . .	103
4.4.2	Fundamental Model . . . . .	104
4.4.3	Evaluation of a Prototype Load . . . . .	104
4.5	WR10 Split-Block Transitions . . . . .	104
4.5.1	Fundamental Model of a Forward-Aligned Transition . . . . .	105
4.5.2	Fundamental Model of a Backward-Aligned Transition . . . . .	106
4.5.3	Evaluation of a Prototype Multilayer WR10-Network . . . . .	107
4.6	Parallel Plate Radiating Array Element . . . . .	109
4.6.1	Fundamental Reflector Model . . . . .	111
4.6.2	<i>H</i> -plane Sectoral Horn Antenna . . . . .	113
4.6.3	Equivalent Representation of the Horn Field . . . . .	114
4.6.4	Computation of the Reflector Contour . . . . .	115
4.6.5	Evaluation of a Prototype Reflector . . . . .	119
<b>5</b>	<b>The Phased Array Antenna</b>	<b>123</b>
5.1	System Design . . . . .	123
5.1.1	Environment, Materials, and Installation Space . . . . .	123
5.1.2	Schematic of the Phased Array Antenna . . . . .	125

5.1.3	Desired Gaussian Beam and Steering Properties . . . . .	126
5.1.4	Synthesis of the Array Taper . . . . .	127
5.2	Design of the Phased Array Antenna . . . . .	128
5.2.1	Periodic Element in the Serial Feed Chain . . . . .	128
5.2.2	Central Element in the Serial Feed Chain . . . . .	131
5.2.3	Phase-Equalizing Waveguide Sections . . . . .	132
5.2.4	Focusing and Frequency-Invariant Phase Compensation . . . . .	135
5.2.5	Waveguide-Model of the Phased Array Antenna . . . . .	136
5.2.6	Synthesis of the Coupling Structures . . . . .	138
5.2.7	Control of the Variable Phase Shifters . . . . .	140
5.2.8	Model of the Phased Array Antenna . . . . .	141
5.3	Simulation Results . . . . .	143
5.3.1	Amplitude and Phase at the Array Aperture . . . . .	143
5.3.2	Radiated Beam in the Steering Plane . . . . .	145
5.3.3	Cross-Sectional Beam with Beam Steering . . . . .	149
<b>6</b>	<b>Conclusions</b>	<b>153</b>



## **Legend**

### **List of Abbreviations**

**TE** transverse electric

**TM** transverse magnetic

**PEC** pefectly electrically conducting

**AUG** ASDEX Upgrade tokamak

**TCV** Tokamak à Configuration Variable

## List of Symbols

$\alpha$	$\text{m}^{-1}$	attenuation constant
$\beta$	$\text{m}^{-1}$	propagation constant
$\beta_{10}$	$\text{m}^{-1}$	propagation constant of the $\text{TE}_{10}$ -mode
$\gamma$	$\text{m}^{-1}$	complex propagation constant
$\Delta\ell$	m	relative sliding-short movement
$\Delta\varphi$	rad	phase-offset between two neighboring elements
$\varepsilon$	$\text{AsV}^{-1}\text{m}^{-1}$	permittivity
$\varepsilon'$	$\text{AsV}^{-1}\text{m}^{-1}$	real part of the permittivity
$\varepsilon''$	$\text{AsV}^{-1}\text{m}^{-1}$	imaginary part of the permittivity
$\bar{\varepsilon}$	$\text{AsV}^{-1}\text{m}^{-1}$	dielectric tensor
$\varepsilon_0$	$\text{AsV}^{-1}\text{m}^{-1}$	vacuum permittivity $8.854 \dots \times 10^{-12} \text{ AsV}^{-1}\text{m}^{-1}$
$\varepsilon_i$	$\text{AsV}^{-1}\text{m}^{-1}$	components of the dielectric tensor ( $i = 1 \dots 3$ )
$\eta$	$\text{VA}^{-1}$	wave impedance
$\Theta_p$	rad	steering angle of the array antenna
$\Theta_s$	rad	scattering angle
$\Theta_t$	rad	tilt angle towards the plasma cut-off layer
$\kappa$	$\text{Sm}^{-1}$	electric conductivity
$\lambda$	m	wavelength
$\lambda_{c,mn}$	m	mode-dependent cut-off wavelength
$\lambda_{c,n}$	m	mode-dependent cut-off wavelength
$\lambda_d$	m	wavelength at the design frequency
$\lambda_D$	m	Debye length
$\lambda_g$	m	guided wavelength of the $\text{TE}_{10}$ -mode
$\Lambda_\perp$	m	turbulence length or size
$\mu$	$\text{VsA}^{-1}\text{m}^{-1}$	permeability
$\mu'$	$\text{VsA}^{-1}\text{m}^{-1}$	real part of the permeability
$\mu''$	$\text{VsA}^{-1}\text{m}^{-1}$	imaginary part of the permeability
$\mu_0$	$\text{VsA}^{-1}\text{m}^{-1}$	vacuum permeability $4\pi \times 10^{-7} \text{ VsA}^{-1}\text{m}^{-1}$
$v$	$\text{s}^{-1}$	mean collision frequency
$\xi$		normalized $z$ variable
$\xi_x$		normalized $z$ variable in the $xz$ -plane
$\xi_y$		normalized $z$ variable in the $yz$ -plane
$\rho, \phi$		polar coordinates
$\rho_e$	$\text{Asm}^{-3}$	electric charge density
$\rho_{e,s}$	$\text{Asm}^{-2}$	surface electric charge density
$\rho_{\text{eff}}$	m	effective radius of curvature
$\rho_h, \phi_h$		polar horn coordinate system
$\rho_{h,0}$	m	radial position of the horn source field

---

$\phi$	rad	Gouy phase shift
$\phi_x$	rad	Gouy phase shift in the $xz$ -plane
$\phi_y$	rad	Gouy phase shift in the $yz$ -plane
$\varphi$	rad	tilt angle between beam and horn antenna
$\varphi_f$	rad	total phase lag in the focusing section
$\varphi_{f,r}$	rad	relative phase lag between two channels
$\varphi_g$	rad	phase lag of the $TE_{10}$ -mode
$\varphi_n$	rad	phase of the element weight $a_n$
$\varphi_n$	rad	constant and arbitrary phase
$\varphi_x^a$	rad	phase distribution at array aperture
$\tilde{\varphi}_x^a$	rad	phase distribution at array aperture for $\tilde{w}_{0x}$
$\bar{\varphi}_x^a$	rad	phase distribution at array aperture for $\bar{z}'_x$
$\Phi$	rad	phase of the electric field tensor
$\chi_e$		electric susceptibility
$\chi_m$		magnetic susceptibility
$\omega$	$s^{-1}$	angular frequency
$\omega_c$	$s^{-1}$	electron cyclotron frequency
$\omega_D$	$s^{-1}$	Doppler shift
$\omega_L$	$s^{-1}$	left-hand cut-off frequency
$\omega_p$	$s^{-1}$	plasma frequency
$\omega_R$	$s^{-1}$	right-hand cut-off frequency
$\omega_{uh}$	$s^{-1}$	upper-hybrid resonance
$a$	m	rectangular hollow waveguide width
$a_f$	m	waveguide width in the focusing section
$a_{f1}, a_{f2}$	m	waveguide width in the focusing section
$a_m, b_m, c_m$		coefficients for cylindrical wave representation
$a_n$		complex weights of radiating elements
$A$	m	aperture width of the horn antenna
$A, B, C, D$		arbitrary constants
$b$	m	rectangular hollow waveguide height
$b_s$	m	height of the quarter-wave section
$\mathcal{B}$	$Vsm^{-2}$	instantaneous magnetic flux density
$B$	$Vsm^{-2}$	magnetic flux density
$B_0$	$Vsm^{-2}$	static magnetic flux that confines the plasma
$B_0$	$Vsm^{-2}$	magnitude of the static magnetic flux
$B_d$	$AV^{-1}$	susceptance in the equivalent circuit
$c_0$	$ms^{-1}$	vacuum speed of light
$c_{coup}$		coupling factor of coupling structure (corresp. $s_{31}$ )
$d$	m	distance between horn aperture and reflector
$d, d'$	m	reference plane shift in the equivalent circuit

---

$d_x$	m	spacing between individual array elements
$\mathcal{D}$	$\text{Asm}^{-2}$	instantaneous electric flux density
$D$	$\text{Asm}^{-2}$	electric flux density
$D_x, D_y, D_z$	m	maximum dimension of the phased array antenna
e	As	elementary charge
$\mathcal{E}$	$\text{Vm}^{-1}$	instantaneous electric field
$E$	$\text{Vm}^{-1}$	electric field
$\hat{E}$	$\text{Vm}^{-1}$	plan wave spectrum of the electric field
$E_c$	$\text{Vm}^{-1}$	coupled electric field
$\hat{E}_i$	$\text{Vm}^{-1}$	plan wave spectrum of $E_i$ ( $i = x, y, z$ )
$E_{imn}$	$\text{Vm}^{-1}$	mode-dependent $i$ -component of the electric field
$E_{mn}$	$\text{Vm}^{-1}$	mode-dependent phasor of the electric field
$E_{\text{pw}}$	$\text{Vm}^{-1}$	electric field of a plane wave
$\hat{E}_{\text{rect}}$	$\text{Vm}^{-1}$	plane wave spectrum of the rectangular function
$E_s$	$\text{Vm}^{-1}$	electric field of the source
$E'_s$	$\text{Vm}^{-1}$	equivalent electric field of the source
$E_t$	$\text{Vm}^{-1}$	transverse components of the electric field
$\hat{E}_t$	$\text{Vm}^{-1}$	transverse components of the plan wave spectrum
$E_x, E_y, E_z$	$\text{Vm}^{-1}$	$x$ -, $y$ -, $z$ -component of the electric field
$E_x^h$	$\text{Vm}^{-1}$	electric field of the horn antenna
$E_x^g$	$\text{Vm}^{-1}$	electric field of the Gaussian beam
$\bar{E}_x$	$\text{Vm}^{-1}$	synthesized or sampled relative field $\tilde{E}_x$
$\hat{\bar{E}}_x$	$\text{Vm}^{-1}$	plane wave spectrum of $\bar{E}_x$
$\tilde{E}_x$	$\text{Vm}^{-1}$	relative field $E_x$ of a Gaussian beam
$\hat{\tilde{E}}_x$	$\text{Vm}^{-1}$	plane wave spectrum of $\tilde{E}_x$
$\bar{E}_z$	$\text{Vm}^{-1}$	relative field $E_z$ of a Gaussian beam
$\hat{\bar{E}}_z$	$\text{Vm}^{-1}$	synthesized or sampled relative field $\tilde{E}_z$
$\hat{\tilde{E}}_z$	$\text{Vm}^{-1}$	plane wave spectrum of $\tilde{E}_z$
$f$	$\text{s}^{-1}$	frequency
$f, f_0$	$\text{Vm}^{-1}$	auxiliary electric field variables
$f_{c,mn}$	$\text{s}^{-1}$	mode-dependent cut-off frequency
$f_{c,n}$	$\text{s}^{-1}$	mode-dependent cut-off frequency
$f_{c,o}$	$\text{s}^{-1}$	cut-off frequency of the ordinary mode
$f_n(\Theta, \Phi)$	1	radiation pattern of an array element
$\mathcal{F}$	$\text{kgms}^{-2}$	instantaneous force
$F$	$\text{kgms}^{-2}$	force
$g, g_0$	$\text{Vm}^{-1}$	auxiliary electric field variables
$h$	m	spacing between parallel plates
$\mathcal{H}$	$\text{Am}^{-1}$	instantaneous magnetic field

---

$H$	$\text{Am}^{-1}$	magnetic field
$H_{imn}$	$\text{Am}^{-1}$	mode-dependent $i$ -component of the magnetic field
$H_m^{(1)}$		Hankel function of the first kind
$H_m^{(2)}$		Hankel function of the second kind
$H_{mn}$	$\text{Am}^{-1}$	mode-dependent phasor of the magnetic field
$H_n$		Hermite polynomials
$H_{\text{pw}}$	$\text{Am}^{-1}$	magnetic field of a plane wave
$H_t$	$\text{Am}^{-1}$	transverse components of the magnetic field
$H_x, H_y, H_z$	$\text{Am}^{-1}$	$x$ -, $y$ -, $z$ -component of the magnetic field
$\mathcal{J}$	$\text{Am}^{-2}$	instantaneous electric current density
$J$	$\text{Am}^{-2}$	electric current density
$J_i$	$\text{Am}^{-2}$	impressed electric current density
$J_m$		Bessel function of the first kind
$\mathcal{J}_p$	$\text{Am}^{-2}$	instantaneous plasma current density
$J_s$	$\text{Am}^{-1}$	surface electric current density
$J_{sh}$	$\text{Am}^{-1}$	horizontal surface electric current density
$J_{sv}$	$\text{Am}^{-1}$	vertical surface electric current density
$k$	$\text{m}^{-1}$	wavenumber
$k_0$	$\text{m}^{-1}$	vacuum wavenumber
$\mathbf{k}$	$\text{m}^{-1}$	wave vector
$k_B$	$\text{m}^2 \text{kgs}^{-2} \text{K}^{-1}$	Boltzman constant ( $1.381 \dots \times 10^{-23} \text{ m}^2 \text{kgs}^{-2} \text{K}^{-1}$ )
$k_r$	$\text{m}^{-1}$	turbulence wavenumber radial to $\mathbf{B}_0$
$k_\rho$	$\text{m}^{-1}$	wavenumber in radial direction
$k_t$	$\text{m}^{-1}$	wavenumber in transverse direction
$\mathbf{k}_t$	$\text{m}^{-1}$	transverse part of the wave vector
$k_x, k_y, k_z$	$\text{m}^{-1}$	wavenumbers in Cartesian coordinates
$k_z$	$\text{m}^{-1}$	wavenumber in propagation direction
$k_{zmn}$	$\text{m}$	mode-dependent wavenumber in propag. direction
$k_\perp$	$\text{m}^{-1}$	turbulence wavenumber perpendicular to $\mathbf{B}_0$
$k_\parallel$	$\text{m}^{-1}$	turbulence wavenumber parallel to $\mathbf{B}_0$
$\ell$	$\text{m}$	offset position of the sliding-short
$\ell_0$	$\text{m}$	initial sliding-short position
$\ell_1, \ell_2$	$\text{m}$	length of a waveguide section
$\ell_d$	$\text{m}$	desired length of the quarter-wave section
$\ell_f$	$\text{m}$	length of the focus section
$\ell_o$	$\text{m}$	additional length for the focus section
$\ell_p$	$\text{m}$	physical length of the quarter-wave section
$L$	$\text{m}$	length of the horn antenna
$L$	$\text{m}$	scale length of the plasma parameters
$L_{pm}$		Laguerre polynomials

---

$m$		Bragg scattering order
$m, n$		mode or polynomial indices
$ m $		amplitude taper of the array antenna
$\tilde{m}$		array taper of Gaussian beam for $\tilde{w}_{0x}$
$m_e$	kg	electron rest mass
$M_s$	$\text{Vm}^{-1}$	magnetic surface current density
$M'_s$	$\text{Vm}^{-1}$	equivalent magnetic surface current density
$n$		index of the radiating element
$n_e$	$\text{m}^{-3}$	electron density
$\nabla n_e$	$\text{m}^{-4}$	electron density gradient
$N$		number of elements
$p, q$		mode or polynomial indices
$p$		wavelength-multiplier of the beam waist radius
$P$	VA	power
$P_c$	VA	coupled power at coupling structure
$P_{\text{in}}$	VA	input power
$P_\ell$	VA	dissipated power of the $\text{TE}_{10}$ -mode
$P_{\text{rad}}$	VA	radiated power
$P_{\text{rem}}$	VA	remaining power at the end of the feed network
$q$	As	electric charge
$r, \Theta, \Phi$		spherical coordinates
$r$	m	coordinates in space
$r'_n$	m	position of the radiating element
$r_t$	m	coordinates transverse to the propagation direction
$R$	m	radius of curvature
$R_b$	m	incident beam radius of curvature
$R_c$	m	cut-off layer radius of curvature
$R_s$	$\text{VA}^{-1}$	surface resistivity
$R_x$	m	radius of curvature in the $xz$ -plane
$\tilde{R}_x^a$	m	radius of curvature at array aperture for $\tilde{w}_{0x}$
$\tilde{R}'_x^a$	m	radius of curvature at array aperture for $\tilde{z}'_x$
$R_y$	m	radius of curvature in the $yz$ -plane
$R_z$	m	surface roughness
$s_{ij}$	1	scattering parameter from port $j$ to port $i$
$t$	s	time
$t_{\text{comp}}$		transmission coefficient of a compensation line
$\tan \delta_e$		dielectric loss-tangent
$\tan \delta_m$		magnetic loss-tangent
$T_e$	K	electron temperature
$u$		auxiliary variable

---

$u_c$		proportionality constant
$u_n$		surface unit normal
$u_n$		propagation direction of a plane wave
$u_r$		unit vector between source and observation point
$v$	$\text{ms}^{-1}$	velocity
$v_e$	$\text{ms}^{-1}$	mean electron velocity
$v_f$	$\text{ms}^{-1}$	mean velocity of the fluctuating cut-off layer
$v_r$	$\text{ms}^{-1}$	velocity of the fluctuation radial to $B_0$
$v_p$	$\text{ms}^{-1}$	phase velocity
$v_\perp$	$\text{ms}^{-1}$	velocity of the fluctuation perpendicular to $B_0$
$v_{\parallel}$	$\text{ms}^{-1}$	velocity of the fluctuation parallel to $B_0$
$w$	m	beam radius along the propagation axis
$w_0$	m	beam waist radius
$w_{0x}$	m	beam waist radius in the $xz$ -plane
$\tilde{w}_{0x}$	m	wavelength-dependent beam waist radius
$\bar{w}_{0x}$	m	beam waist radius for $\tilde{z}'_x$
$w_{0x}^d$	m	beam waist radius at the design frequency
$w_{0y}$	m	beam waist radius in the $yz$ -plane
$w_{\text{opt}}$	m	optimum beam waist radius
$w_x$	m	beam radius in the $xz$ -plane
$w_x^a$	m	beam radius at the array aperture
$w_y$	m	beam radius in the $yz$ -plane
$x, y, z$		Cartesian coordinate system
$X$	$\text{VA}^{-1}$	reactance in the equivalent circuit
$y_c, z_c$	m	coordinates of a point on the reflector contour
$Y_m$	1	Bessel function of the second kind
$z$	m	position observation plane
$z', z'_x, z'_y$	m	abbreviation for the Gaussian beam $z$ -variation
$z_0$	m	position of the source plane
$z_{0x}$	m	focal plan position of the beam in the $xz$ -plane
$z_{0y}$	m	focal plan position of the beam in the $yz$ -plane
$z_r$	m	Rayleigh length
$z_{rx}$	m	Rayleigh length of the beam in the $xz$ -plane
$z_{ry}$	m	Rayleigh length of the beam in the $yz$ -plane
$z'_x^d$	m	focal distance from aperture at the design frequency
$\tilde{z}'_x$	m	focal distance from aperture for $\tilde{w}_{0x}$
$\tilde{z}'_x$	m	focal distance from aperture
$Z$	$\text{VA}^{-1}$	wave impedance
$Z_w$	$\text{VA}^{-1}$	characteristic impedance of the waveguide
$Z_s$	$\text{VA}^{-1}$	characteristic impedance of the quarter-wave section

## Notation

Symbol	Description
$j$	imaginary unit
$x$	scalar
$X$	vector
$u_x$	unit vectors of $x$
$\nabla$	nabla operator
$\nabla^2$	Laplace operator
$\nabla_t$	transverse nabla operator
$\nabla x$	gradient of $x$
$\nabla \cdot X$	divergence of $X$
$\nabla \times X$	curl of $X$
$\text{Re}\{x\}$	real component of $x$
$\text{Im}\{x\}$	imaginary component of $x$
$ x $	magnitude of $x$
$\arg(x)$	argument of $x$

# 1 Introduction

## 1.1 Nuclear Fusion

Nuclear fusion is the process in which light atomic nuclei are combined to form heavier elements. In this process, energy is released due to the larger nuclear binding energy of heavier elements (required to separate the elements again) that is released in their fusion. For a fusion to occur, the reaction partners require a kinetic energy that is large enough to overcome the repelling Coulomb force acting on the equally charged ions and, thus, eventually leading to an attraction by nuclear forces. In 1939, this process has been identified to be the energy source of the sun [Bet39]. Since then, considerable effort has been made to enable a controlled nuclear fusion on earth.

In the sun, energy is created in a rather slow reaction scheme with a weak interaction (low probability of a fusion) between the reaction partners [HG13]. On earth, nuclear fusion of Deuterium ( $^2\text{D}$ ) and Tritium ( $^3\text{T}$ ) as



is envisaged because it has the highest probability to overcome the Coulomb barrier at lower plasma temperatures and densities [Str11]. The total energy that is released in the reaction (1.1) is 17.6 MeV. It is released in the form of a larger kinetic energy of the fusion products (values in brackets), which is distributed inversely to the element mass. The temperatures required to overcome the Coulomb forces are on the order of  $10^8$  K. At these temperatures, the reaction partners are in the fully ionized plasma state [HG13]. Most nuclear fusion plasma experiments investigate Deuterium plasma without Tritium due to the radioactivity of Tritium (12 years half life). Even though Deuterium-Deuterium reaction schemes have a fusion cross section almost two orders of magnitude lower than that of Deuterium-Tritium, physics experiments of Deuterium-Deuterium plasma still allow valuable physics and engineering insights into confined plasma without the costs and infrastructure overhead due to the reactivity of Tritium [Str11].

To heat the fusion partners up to temperatures required for their fusion (approximately  $10^8$  K), they should not contact with any other matter that would absorb energy. In order to minimize lost energy due to radiation from heavier atoms, the plasma is kept in a vacuum. The reaction partners are magnetically confined inside this vessel, preventing them from touching the surrounding walls. The magnetic confinement is realized by a strong and static magnetic field  $\mathbf{B}$  on the order of several T, which causes

the Lorentz force  $\mathbf{F} = q(\mathbf{v} \times \mathbf{B})$  acting on accelerated electric charges  $q$  that move with velocity  $\mathbf{v}$ . The strong magnetic field causes the charges to gyrate around the magnetic field lines with their cyclotron frequency. The velocity vector parallel to the magnetic field line is not affected by the static magnetic field. Consequently, electric charges are not accelerated in this direction and, thus, are bound to the static magnetic field lines.

Most promising magnetic confinement devices are the tokamak and the stellarator [Str11]. Both devices form a torus geometry, with the static magnetic field being toroidal and twisted in poloidal direction. The magnetic field lines form closed surfaces, so-called flux surfaces. On these surfaces, temperature and density of both, electrons and ions, can be assumed constant. Thus, an equilibrium or force-balanced state exists between the plasma pressure and the external magnetic field [HG13]. The outermost closed flux surface is called separatrix. Magnetic field lines beyond the separatrix are in contact with the vessel walls which stops and absorbs the flux surface. At the intersection with the vessel wall, particles and, thus, energy leave the plasma and eventually are absorbed by the walls [HG13]. The tokamak realizes the toroidal magnetic field component by poloidal coils arranged in a torus geometry. The poloidal magnetic field is realized by an electric current that flows through the plasma along the toroidal axis. This plasma current itself is induced in the plasma, which requires an increasing external current in a coil. As the rise duration cannot extend to infinity, tokamak devices operate in a pulsed mode with a pulse duration on the order of a few seconds up to several minutes. The stellarator, on the other hand, generates both magnetic field components solely by means of poloidal coils. These coils are individually shaped such that they realize the desired magnetic field configuration. Continuous operation is possible when using super-conductive coils. However, these custom-made coils are more challenging to realize. For this thesis, only two tokamak devices will be discussed in more detail. These are the ASDEX Upgrade tokamak in Garching, Germany and the Tokamak à Configuration Variable in Lausanne, Switzerland.

To realize temperatures that are required for a thermo-nuclear fusion, the reactants may be heated by four mechanisms. Ohmic heating due to Ohmic losses of the plasma current, ion- and electron cyclotron heating where the charge carriers are accelerated by an electromagnetic field that is in-phase with their cyclotron frequency, neutral beam injection increasing the kinetic energy of particles by collisions with injected high-energetic particles, and heating by the released energy from fusion products. The first three heating methods are used for plasma formation and for continuous heating in experiments as the reaction rate of fusion of Deuterium at current plasma experiments is too small to produce enough energy. The released kinetic energy of the  ${}^3\text{He}$  isotope from Deuterium-Deuterium plasma can be converted directly and is considered as an advanced reaction for a continuous burning of the plasma in future fusion reactors [HG13].

In both confinement devices, the tokamak and the stellarator, the static magnetic field and the vacuum have to be within a finite volume. This leads to gradients in plasma

pressure and, thus, in electron and ion temperature and density. Due to the geometry of the flux surfaces, these gradients are directed radially outward of the plasma torus, i.e., from the plasma core to its edge [HG13]. There are three loss mechanisms that cool the plasma and reduce the confined energy: impurity radiation, the radiation of energy (e.g., cyclotron radiation), and the particle or heat transport perpendicular to the flux surfaces which leave the confined plasma. In the neoclassical theory, particle and heat transport perpendicular to the flux surfaces is driven by collisions of particles [HG13]. All three components make up the total energy and particle transport.

In experiments, however, the heat and particle transport exceeds the classical neoclassical prediction by two orders of magnitude [HG13]. Neither of the before-mentioned mechanisms could explain this effect. It is now widely accepted that this anomalous particle and energy transport in magnetically confined plasma is due to small-scale turbulence. These small-scale turbulences are microscopic random fluctuations in particle density, temperature, potential, and the magnetic field. They are driven by the radial gradients in electron and ion temperatures and densities [Con08]. Turbulences transport energy and particles (heat) from the plasma core to the plasma edge, where it is dissipated. By this means, small-scale turbulences are cooling the plasma [Con08].

For a self-sustained burning of the plasma, the plasma temperature has to be kept at a level that enables a fusion. This requires the released energy from the fusion reaction to be larger as compared to the energy lost due to diffusion and radiation. The energy confinement time (i.e., energy content per unit volume divided by the power loss density) is, therefore, a key parameter to be optimized for an economical realization of fusion reactors. A longer energy confinement time can be realized by a larger plasma volume, stronger magnetic fields (both increasing building costs of a fusion reactor) or through an operation in a plasma mode with improved confinement properties [Str11]. In 1982 a plasma mode with a transport barrier at the plasma edge has been observed in ASDEX Upgrade tokamak (AUG) [WBB+82]. In this mode, the turbulence level is reduced and the energy confinement is consequently improved. As the main loss mechanism in a plasma are small-scale turbulences, understanding the transport mechanisms and processes that lead to the formation of a transport barrier is essential.

## 1.2 Plasma Turbulence Studies

To improve the understanding and increase knowledge, theories always have to be compared with and validated by experiments. The parameters of interest in turbulence studies, however, are not easy to measure as they are time-dependent and small-scale quantities. They require sufficient spatial and temporal resolution. Direct contact with the plasma for measurement purposes must be avoided, as it directly influences the plasma. Microwave-based diagnostics enable a contact-less measurement of plasma

parameters. They are widely used for plasma control and investigation. Diagnostic concepts based on microwaves measure the influences on the propagation of an electromagnetic wave in a plasma.

If the frequency of the probing electromagnetic wave is not at a plasma cut-off frequency, it can penetrate through the plasma. The presence of electrons, however, influences the propagation constant of the wave. Interferometry utilizes this effect and measures plasma density profiles based on the phase difference between a wave propagating through the plasma and a wave propagating through vacuum. It delivers a line-integral information about the plasma density. Therefore, accessing local density and temperature effects are not possible with multiple lines of sight.

If the frequency of the probing electromagnetic wave is at a cut-off frequency of the plasma, it cannot propagate any further. In case the wave propagates parallel to the electron density gradient, it is reflected at the cut-off layer. Conventional reflectometry utilizes this effect and measures the delay time of a wave traveling towards the plasma cut-off layer and back, yielding information at the cut-off layer radial location such as fluctuations. However, this measurement is locally limited and is not able to filter different turbulence sizes. For an oblique incident angle of the electromagnetic wave towards the electron density gradient, the wave is gradually refracted and eventually scattered by Bragg scattering at the fluctuating cut-off layer. Doppler reflectometry utilizes this effect and, thus, enables a good spatial as well as temporal resolution of plasma turbulences.

To experimentally measure the plasma turbulence, a Gaussian beam can be radiated into the plasma with the focal plane overlapping with the plasma cut-off layer. If this is accomplished, the modulations of the plasma cut-off layer result in a Bragg back-scattered beam. This back-scattered beam contains the information about the turbulence intensity and relative velocity. The actual plasma configuration has a strong influence on the measured quantities. To correctly interpret the measured data, the true scattering location and the beam propagation path need to be known. To accomplish this, the avenue pursued at the “Helmholtz Virtual Institute” is to compare gyro-kinetic plasma simulations with experimental plasma discharges [SNC+15]. This is, synthetic diagnostic instruments are used in the simulation and the data is compared with the measured quantities of a real diagnostic instrument.

An experimental Doppler reflectometer consists of a data acquisition unit and a front-end. The data acquisition unit emits the probing signal and measures the returned spectrum. The front-end shapes and steers the desired probing beam.

### 1.3 Scope of this Thesis

This thesis focuses on the design and realization of a Gaussian beam shaping and steering front-end for Doppler reflectometry in the ASDEX Upgrade tokamak. The

desired operational frequencies are from 75 GHz to 105 GHz. For optimal performance of the Doppler reflectometer, the beam waist should only be a few wavelength large and coincide with the plasma cut-off layer. As the transversal beam shape spreads for larger distances from the focal plane, the antenna needs to be fairly close to the plasma in order to reduce the antenna aperture dimension.

However, the close proximity to the plasma requires that it is in-vessel and must, therefore, sustain the environmental conditions. In particular, the strongest environmental restrictions follow from the ultra-high vacuum, the neutron radiation, and the strong static magnetic field strength. Due to the ultra-high vacuum only non-out-gassing metals can be used, which sustain bake-out temperatures up to 160 °C. Neutron radiation further restricts the materials to those which are not activated by strong neutron radiation. Lastly, the static magnetic field rules out all materials that are magnetic. These materials would perturb the static magnetic field causing field errors.

In addition to the environmental issues, the in-vessel installation space as well as the vacuum interfaces (ports between ex-vessel and in-vessel) are limited in AUG. The space constrains require the antenna to be reasonably compact and fit into the provided installation space (maximum aperture size roughly 90 mm by 120 mm). The limited number and size of vacuum interfaces restrict the connecting waveguides in size. Preferably, the front-end is composed of a mono-static antenna since it halves the installation space as compared to a bi-static setup.

Apart from the environmental and space constrains, the front-end has to radiate a well defined Gaussian beam. This beam needs to be steered with reasonable speed and angular precision.

The requirements described above are best achieved with an all metal construction which has a minimal number of moving parts. The latter is to increase reliability and device life-time. Moreover, given the small installation space and the requirement to steer the beam, the only suitable antenna concept is a phased array antenna. In the framework of the “Helmholtz Virtual Institute”, two phased array antennas with different beam steering approaches are investigated: beam steering by waveguide dispersion with a frequency-dependent steering angle and beam steering by actively controlled phase shifters with a frequency-independent steering angle. The latter is the subject of this thesis.

Thus, the scope of this thesis is the design and realization of a Gaussian beam steering phased array antenna with actively controlled phase shifters and a frequency-independent steering angle. The thesis covers the array taper that is necessary to radiate the desired Gaussian beam, the individual elements of the feed network that generate this array taper, and finally the complete phased array antenna as a composition of the individual elements.

## 1.4 Outline of this Thesis

In Chapter 2, the fundamental concepts are discussed. Starting from Maxwell's equations and the plane wave solution, the field in a transverse plane is represented by a set of plane waves. From this plane wave spectrum follows the Gaussian beam description. Guided waves in a rectangular hollow waveguide as well as in a radial parallel plate waveguide are discussed. The electromagnetic wave propagation in a magnetized plasma wraps up this chapter.

The subsequent Chapter 3, covers the measurement principle of Doppler reflectometry and the design goals for the Gaussian beam on ASDEX Upgrade tokamak. Phased array antennas are briefly discussed as an antenna architecture to synthesize a certain aperture distribution with the ability to steer the radiated beam. The end of this chapter comprises the aperture field synthesis to radiate a certain Gaussian beam from a phased array antenna. The influences from the sampling element, their finite number, as well as amplitude and phase errors of the array taper are investigated. Suitable radiating elements and the consideration of their mutual coupling are discussed. The chapter ends with the derivation of an array taper for a Gaussian beam with a wavelength-dependent beam waist and an array taper for a Gaussian beam with a frequency-independent focal length.

In Chapter 4, the individual components of the feed-network for the phased array antenna are presented. Each component is described by a fundamental model. The functionality of the design is supported by simulations and measurements of prototypes. The following components are covered: a coupling structure or power divider that controls the aperture amplitude taper, a variable phase shifter for beam steering, an invariable phase shifter for the correct phase taper, a waveguide load to terminate the feed-network, a split-block transition to enable a multilayer network, and, finally, the radiating element as a parallel plate reflector.

In the last Chapter 5, the system design is presented which connects the previously presented components of the whole phased array antenna. Here, the phased array antenna is divided into four parts. These are the periodic and the central element in the serial feed chain, the phase-equalizing waveguide section, and the focusing section. The first two parts, the periodic and the central element in the serial feed chain, control the amplitude taper and contain the variable phase shifters. The third part, the phase-equalizing waveguide sections, cancel or omit any frequency steering of the radiated beam. Finally, the focusing section realizes the frequency-dependent phase taper. The dimensions of the individual components and how to obtain these dimensions is prescribed. A waveguide model as well as the manufacturing model of the phased array antenna are also presented. The chapter closes by showing benchmarking simulation results of the realized array taper and the radiated beam from the whole phased array antenna. The manufacturing of the phased array antenna is still ongoing. Measurement results will be published elsewhere.

## 2 Fundamental Concepts

### 2.1 Electromagnetic Fields

In the presence of an electromagnetic field, the Coulomb force and the Lorentz force according to [Jac99]

$$\mathcal{F} = q(\mathcal{E} + \mathbf{v} \times \mathcal{B}), \quad (2.1)$$

act on a charge  $q$ , where the time-varying electric field is denoted as  $\mathcal{E}(\mathbf{r}, t)$ , the motion of the charge as  $\mathbf{v}(\mathbf{r}, t)$  and the magnetic flux density as  $\mathcal{B}(\mathbf{r}, t)$ . An accelerated charge can in turn be the source of a time-varying electromagnetic field. These fields are not locally bound to the charge, but rather propagate in free-space with the speed of light  $c_0 = 1/\sqrt{\mu_0 \epsilon_0} = 2.997 \dots \times 10^8 \text{ ms}^{-1}$  away from the source. The free-space permeability is real valued and defined as  $\mu_0 = 4\pi \times 10^{-7} \text{ VsA}^{-1}\text{m}^{-1}$ , and the free-space permittivity follows from the vacuum speed of light as  $\epsilon_0 = 8.854 \dots \times 10^{-12} \text{ AsV}^{-1}\text{m}^{-1}$ .

#### 2.1.1 Maxwell's Equations

The propagation of time-varying electromagnetic fields and their interaction with macroscopic matter are comprehensively described by Maxwell's equations [Jac99]. Macroscopic means here that the interaction with charge carriers is averaged over a volume. Maxwell connected Faraday's law of induction, Ampère's circuital law, and Gauss' law (electric flux lines ending on a electric charge) by introducing the electric displacement current. Together with the observation that magnetic flux lines are closed contours (no magnetic monopole charge has been found, yet [Jac99; Poz11]), they form the basis of classical electrodynamics. In differential form and in the SI system of units, the Maxwell's equations are [Har01; Jac99]

$$\nabla \times \mathcal{E} = -\frac{\partial \mathcal{B}}{\partial t}, \quad (2.2)$$

$$\nabla \times \mathcal{H} = \frac{\partial \mathcal{D}}{\partial t} + \mathcal{J}, \quad (2.3)$$

$$\nabla \cdot \mathcal{D} = \rho_e, \quad (2.4)$$

$$\nabla \cdot \mathcal{B} = 0. \quad (2.5)$$

The electric field and the magnetic field are denoted as  $\mathcal{E}(\mathbf{r}, t)$  and  $\mathcal{H}(\mathbf{r}, t)$ , respectively. The electric current density is  $\mathcal{J}(\mathbf{r}, t)$  with the corresponding electric charge density

$\rho_e(\mathbf{r}, t)$ . The electric flux density is denoted as  $\mathcal{D}(\mathbf{r}, t)$  and the magnetic flux density is denoted as  $\mathcal{B}(\mathbf{r}, t)$ . All field quantities are functions of an observation point in Cartesian coordinates  $\mathbf{r} = xu_x + yu_y + zu_z$  and time  $t$ .

Taking the divergence of (2.3) with  $\nabla \cdot \nabla \times \mathbf{H} = 0$  and inserting (2.4) yields the continuity equation in differential form (i.e., conservation of charge) [Poz11]

$$\nabla \cdot \mathcal{J} = -\frac{\partial \rho_e}{\partial t}. \quad (2.6)$$

Whenever an electric current density flows out of a volume, the number of electric charges in this volume changes accordingly. Thus, the number of charges is conserved.

When considering only time-harmonic fields with angular frequency  $\omega$  and a time dependency  $\cos(\omega t)$  in a time-invariant medium or space, the time-varying field  $\mathcal{F}(\mathbf{r}, t)$  (script letter) can be represented by the complex-valued phasor  $F(\mathbf{r}, \omega)$  (roman letter) and the relation [Poz11]

$$\mathcal{F} = \operatorname{Re} \left\{ F e^{j\omega t} \right\} = \operatorname{Re} \left\{ |F| e^{j\Phi} e^{j\omega t} \right\}. \quad (2.7)$$

The phasor  $F$  represents the magnitude and phase as  $F = |F|e^{j\Phi}$  of any vector component of the field  $\mathcal{F} = |F| \cos(\omega t + \Phi)$ . The time derivative of the time-harmonic field is

$$\frac{\partial F}{\partial t} = \operatorname{Re} \left\{ j\omega F e^{j\omega t} \right\}. \quad (2.8)$$

Consequently, the time-harmonic Maxwell's equations are [Har01; Jin15]

$$\nabla \times E = -j\omega B, \quad (2.9)$$

$$\nabla \times H = j\omega D + J, \quad (2.10)$$

$$\nabla \cdot D = \rho_e, \quad (2.11)$$

$$\nabla \cdot B = 0. \quad (2.12)$$

If not explicitly stated, throughout this thesis, the time dependency  $e^{j\omega t}$  is assumed and suppressed. The instantaneous field can be obtained with the relation (2.7).

### 2.1.2 Constitutive Relations

The influence of the medium on the fields is linked to Maxwell's equations by the so-called constitutive relations. For many electromagnetic problems, a couple of assumptions can be made regarding the medium. In particular, the medium can be assumed homogeneous, isotropic, non-dispersive, and linear (linear dependency between field and flux). As a consequence, it can be specified by scalar material constants. These are the permittivity  $\epsilon$ , the permeability  $\mu$ , and the electric conductivity  $\kappa$ . The

material constants  $\epsilon$ ,  $\mu$ , and  $\kappa$  are a macroscopic representation of the interaction of electromagnetic fields with the charge carriers in a certain material or medium [Kit68]. They link the electric and magnetic fields with their flux or current densities according to [Har01]

$$\mathbf{D} = \epsilon_0 \mathbf{E} + \epsilon_0 \chi_e \mathbf{E} = \epsilon \mathbf{E}, \quad (2.13)$$

$$\mathbf{B} = \mu_0 \mathbf{H} + \mu_0 \chi_m \mathbf{H} = \mu \mathbf{H}, \quad (2.14)$$

$$\mathbf{J} = \kappa \mathbf{E} + \mathbf{J}_i. \quad (2.15)$$

The permittivity  $\epsilon$  of a medium is due to the electric polarization of atoms or molecules aligning with an external electric field (bound electrons in a medium). It depends on the complex electric susceptibility  $\chi_e$  leading to an additional electric flux density in the medium of  $\epsilon_0 \chi_e \mathbf{E}$ . The permeability  $\mu$  is affected similarly by the magnetization of the medium (alignment of atoms/molecules and their magnetic dipole moment with an external magnetic field). It depends on the complex magnetic susceptibility  $\chi_m$  leading to an additional magnetic flux density in the medium of  $\mu_0 \chi_m \mathbf{H}$ . The electric current density  $\mathbf{J}$  is composed of a conducting current density, which is dependent on the conductivity  $\kappa$  of a medium and the applied electric field, and an impressed electric current density  $\mathbf{J}_i$ , which is regarded as a source of electromagnetic fields.

From (2.10), the conduction current of (2.15) (of a dielectric material) may be included in the permittivity of the material to form a single material parameter as [Poz11]

$$\epsilon = \epsilon' - j\epsilon'' = \epsilon_0 (1 + \chi_e) - j\frac{\kappa}{\omega} = \epsilon_0 \epsilon_r (1 - j \tan \delta_e), \quad (2.16)$$

where  $\epsilon_r = \epsilon'/\epsilon_0$  is the real-valued relative dielectric constant and the complex part is modeled by the dielectric loss-tangent

$$\tan \delta_e = \frac{\omega \epsilon'' + \kappa}{\omega \epsilon'}. \quad (2.17)$$

In a similar manner, the permeability may be represented as [Poz11]

$$\mu = \mu' - j\mu'' = \mu_0 \mu_r (1 - j \tan \delta_m), \quad (2.18)$$

with the real-valued relative permeability  $\mu_r = \mu'/\mu_0$  and the magnetic loss-tangent

$$\tan \delta_m = \frac{\mu''}{\mu'}. \quad (2.19)$$

For non-homogeneous materials, the material parameters depend on the spatial position. For non-isotropic materials such as crystals, the material parameters depend on the orientation of the field and would be tensors. For non-linear materials, field and flux have no linear dependence and the permittivity and permeability can be represented by a Taylor series.

### 2.1.3 Boundary Conditions

At discontinuities of a medium, boundary conditions are valid that link the fields from medium 1 to that of medium 2. These boundary conditions can be derived from Maxwell's equations in integral form. Considering only electric charge and current densities, the boundary conditions at the interface between two media are [Jin15; Poz11]

$$\mathbf{u}_n \times (\mathbf{H}_2 - \mathbf{H}_1) = \mathbf{J}_s, \quad (2.20)$$

$$\mathbf{u}_n \times (\mathbf{E}_2 - \mathbf{E}_1) = 0, \quad (2.21)$$

$$\mathbf{u}_n \cdot (\mathbf{B}_2 - \mathbf{B}_1) = 0, \quad (2.22)$$

$$\mathbf{u}_n \cdot (\mathbf{D}_2 - \mathbf{D}_1) = \rho_{e,s}, \quad (2.23)$$

where the subscripts 1 and 2 indicate the field and flux in the respective medium at the boundary. The impressed electric surface current density at the discontinuity is  $\mathbf{J}_s$  with the impressed surface charge density  $\rho_{e,s}$ . The unit vector  $\mathbf{u}_n$  is the surface normal pointing from medium 1 to medium 2.

If no sources are present or supported by the medium, as is the case for a lossless dielectric where no surface charges or currents are supported on the boundary, the right-hand side of the above equations vanishes. As a consequence, the tangential components of the fields and the normal components of the fluxes have to be continuous over the interface [Jin15; Poz11].

## 2.2 Plane Waves and Plane Wave Spectrum Representation

### 2.2.1 General Plane Wave Solution

The propagation of a time-harmonic field in a source-free, isotropic, homogeneous, time-invariant, and linear space can be described by Maxwell's curl equations (2.9) and (2.10). Together with the constitutive relations from (2.13) and (2.14), these are [Poz11]

$$\nabla \times \mathbf{E} = -j\omega\mu\mathbf{H}, \quad (2.24)$$

$$\nabla \times \mathbf{H} = j\omega\epsilon\mathbf{E}. \quad (2.25)$$

Taking the curl of (2.24),

$$\nabla \times (\nabla \times \mathbf{E}) = -j\omega\mu(\nabla \times \mathbf{H}) \quad (2.26)$$

follows. With  $\nabla \times (\nabla \times \mathbf{X}) = \nabla(\nabla \cdot \mathbf{X}) - \nabla^2 \mathbf{X}$  and the fact that  $\nabla \cdot \mathbf{E} = 0$  in the source-free case, inserting (2.26) into (2.25) leads to the homogeneous vector Helmholtz equation of the electric field [Poz11]

$$\nabla^2 \mathbf{E} + \omega^2 \mu\epsilon \mathbf{E} = \nabla^2 \mathbf{E} + k^2 \mathbf{E} = 0, \quad (2.27)$$

with the wavenumber  $k$  defined as  $k = 2\pi/\lambda = \omega\sqrt{\mu\epsilon}$ . By taking the curl of (2.25) and advancing in similar steps, a vector Helmholtz equation of the magnetic field can be derived. It equals (2.27), just that  $E$  is replaced by  $H$  [Poz11].

The vector Helmholtz equation can be solved by the method of separation of variables, where the partial differential equation of (2.27) reduces to the solution of three ordinary differential equations [Poz11]. The Laplace operator  $\nabla^2$  applies on every vector component of  $E$ , such that a vector solution is found by the superposition of solutions to the scalar Helmholtz equation for each vector component  $E_i$ , with  $i = x, y, z$ . Together they must additionally fulfill the divergence condition  $\nabla \cdot E = 0$  (and  $\nabla \cdot H = 0$ ), to yield only source-free solutions. From the separation of variables and their individual separation constants  $k_x$ ,  $k_y$ , and  $k_z$  fulfilling the dispersion relation [Poz11]

$$k^2 = k_x^2 + k_y^2 + k_z^2, \quad (2.28)$$

a scalar solution to the Helmholtz equation can be found as [Poz11]

$$E_{\text{pw},i}(\mathbf{r}) = \hat{E}_i(\mathbf{k}) e^{-jk \cdot \mathbf{r}}, \quad (2.29)$$

with the complex and constant (amplitude) coefficient  $\hat{E}_i$ , and the wave vector

$$\mathbf{k} = k_x \mathbf{u}_x + k_y \mathbf{u}_y + k_z \mathbf{u}_z = k \mathbf{u}_n, \quad (2.30)$$

with the propagation direction  $\mathbf{u}_n$ . A vector solution to the Helmholtz equation (2.27) is composed of individual scalar solutions to (2.27) as [Ker76]

$$E_{\text{pw}}(\mathbf{r}) = \hat{\mathbf{E}}(\mathbf{k}) e^{-jk \cdot \mathbf{r}}. \quad (2.31)$$

The complex vector  $\hat{\mathbf{E}}$  is constant and independent of the observation point  $\mathbf{r}$ . It describes the amplitude and phase of a single plane wave with the wave vector  $\mathbf{k}$ . For (2.31) to be a solution to (2.27) and, thus, the source-free Maxwell equations, also the divergence criteria  $\nabla \cdot E = 0$  (and  $\nabla \cdot H = 0$ ) have to hold. From the identity  $\nabla \cdot (aX) = X \cdot \nabla a + a \nabla \cdot X$ , it follows [Poz11]

$$\hat{\mathbf{E}} \cdot \nabla e^{-jk \cdot \mathbf{r}} + e^{-jk \cdot \mathbf{r}} \nabla \cdot \hat{\mathbf{E}} = \hat{\mathbf{E}} \cdot \nabla e^{-jk \cdot \mathbf{r}} = -jk \cdot \hat{\mathbf{E}} e^{-jk \cdot \mathbf{r}} = 0. \quad (2.32)$$

For (2.32) to be true for every observation point  $\mathbf{r}$ , the divergence condition

$$\mathbf{k} \cdot \hat{\mathbf{E}} = 0 \quad (2.33)$$

must hold. In other words, the complex amplitude  $\hat{\mathbf{E}}$  is perpendicular to the propagation vector  $\mathbf{k}$  (only transverse components). Its magnetic field follows from (2.24) as [Poz11]

$$\mathbf{H}_{\text{pw}} = \frac{j}{\omega\mu} \nabla \times (\hat{\mathbf{E}} e^{-jk \cdot \mathbf{r}}), \quad (2.34)$$

and with  $\nabla \times (aX) = (\nabla a) \times X + a \nabla \times X$  this yields [Poz11]

$$H_{\text{pw}} = \frac{-j}{\omega\mu} \hat{E} \times (-jk e^{-jk \cdot r}) \quad (2.35)$$

$$= \frac{k}{\omega\mu} \mathbf{u}_n \times \hat{E} e^{-jk \cdot r} \quad (2.36)$$

$$= \frac{1}{\eta} \mathbf{u}_n \times \hat{E} e^{-jk \cdot r}. \quad (2.37)$$

From (2.31) and (2.37), the ratio between electric and magnetic field is given by the wave impedance  $\eta = \sqrt{\mu/\epsilon}$ . The magnetic field is in-phase and perpendicular to the electric field. The amplitudes of the fields are constant in the transverse plane and the lines of constant amplitude are parallel to the lines of constant phase. This wave is referred to as uniform plane wave [Ker76], where it is assumed that  $k$ ,  $k_x$ ,  $k_y$ , and  $k_z$  are all real quantities.

### 2.2.2 Plane Wave Spectrum Representation

The propagation vector  $\mathbf{k}$  of the general plane wave might be divided into its transverse part  $\mathbf{k}_t$  and the component in  $z$ -direction  $k_z$ . In this case, the dispersion relation  $\mathbf{k} \cdot \mathbf{k} = k^2 = \omega^2 \mu \epsilon$  yields

$$k_z = \sqrt{k^2 - \mathbf{k}_t \cdot \mathbf{k}_t}, \quad (2.38)$$

where the transverse wavenumber is  $\mathbf{k}_t = k_x \mathbf{u}_x + k_y \mathbf{u}_y$  in the rectangular coordinate system. The individual wavenumbers are positive real valued. For  $k^2 > \mathbf{k}_t \cdot \mathbf{k}_t$ , the wavenumber  $k_z$  is chosen positive real corresponding to a wave propagation in positive  $z$ -direction. For  $k^2 < \mathbf{k}_t \cdot \mathbf{k}_t$ , the wavenumber  $k_z$  is chosen negative imaginary corresponding to an attenuation of the wave in positive  $z$ -direction [Ker76].

A plane wave propagating in positive  $z$ -direction with a source at  $z \rightarrow -\infty$  in the form of (2.31) can be described in a plane perpendicular to the propagation direction with  $z = \text{const.}$  as

$$E_{\text{pw}}(\mathbf{r}_t, z) = \hat{E}_{\text{pw}}(\mathbf{k}_t) e^{-jk_z z} e^{-jk_t \cdot \mathbf{r}_t}. \quad (2.39)$$

The plane wave coefficient  $\hat{E}_{\text{pw}}(\mathbf{k}_t)$  is the complex amplitude of the plane wave and the exponential term  $e^{-jk_z z}$  models the propagation in  $z$ -direction (dependent on  $k_z$ ). With the dispersion relation (2.38), the plane wave coefficient is only dependent on the transverse wavenumber  $\mathbf{k}_t$ .

A plane wave (2.39) evaluated at a plane  $z_0$  propagates in  $z$ -direction (with  $z > z_0$ ) according to the propagator [Sie86]

$$e^{-jk_z(z-z_0)}, \quad (2.40)$$

such that

$$E_{\text{pw}}(\mathbf{r}_t, z) = E_{\text{pw}}(\mathbf{r}_t, z_0) e^{-jk_z(z-z_0)}. \quad (2.41)$$

Now, similar to the derivation in [Sie86], equation (2.39) serves as basis to expand the electric field in the plane  $z = \text{const.}$  as an infinite set of plane waves according to

$$E(\mathbf{r}_t, z) = \iint_{-\infty}^{\infty} \hat{E}(\mathbf{k}_t) e^{-jk_z z} e^{-jk_t \cdot \mathbf{r}_t} d\mathbf{k}_t. \quad (2.42)$$

The former plane wave coefficient is now a continuous function  $\hat{E}(\mathbf{k}_t)$  representing all transverse wavenumbers. It is therefore specified as a spectrum (the plane wave spectrum) [Ker76; Orf16]. As  $E$  and  $\hat{E}$  are vectors, the integral relation holds for each vector component independently. The inverse transform to the plane wave spectrum representation (2.42) is [Sie86]

$$\hat{E}(\mathbf{k}_t) = \frac{1}{4\pi^2} \iint_{-\infty}^{\infty} E(\mathbf{r}_t, z) e^{+jk_z z} e^{+jk_t \cdot \mathbf{r}_t} d\mathbf{r}_t. \quad (2.43)$$

The plane wave spectrum is composed of an infinite set of plane waves that are each a solution of the Helmholtz equation. However, for the plane wave spectrum to be a solution of Maxwell's equation, the electric field also has to satisfy the divergence condition from (2.32) as  $\mathbf{k} \cdot \hat{E} = 0$ . If the transverse electric field components  $\hat{E}_t$  or in particular  $\hat{E}_x(\mathbf{k}_t)$  and  $\hat{E}_y(\mathbf{k}_t)$  are chosen arbitrarily, the remaining electric and magnetic field components follow accordingly. To fulfill the divergence criterion for any arbitrary transverse field, a correction term of the vector electric field in form of the  $z$ -component is necessary [Orf16]

$$\hat{E}_z(\mathbf{k}_t) = -\frac{\mathbf{k}_t \cdot \hat{E}_t}{k_z} = -\frac{k_x \hat{E}_x(\mathbf{k}_t) + k_y \hat{E}_y(\mathbf{k}_t)}{k_z}. \quad (2.44)$$

In the following, the plane wave spectrum representation of the electric field is employed to derive possible field solutions of propagating (and collimated) beams.

### 2.2.3 Propagation of the Plane Wave Spectrum

As a consequence of (2.41), the concept of the plane wave spectrum allows the propagation of the field from a source plane  $z_0$  with transverse coordinates  $\mathbf{r}'_t$  to an observation plane  $z$  with transverse coordinates  $\mathbf{r}_t$  for  $z > z_0$ . In this case, the plane wave spectrum in the source plane is given by (2.43) as

$$\hat{E}(\mathbf{k}_t) = \frac{1}{4\pi^2} \iint_{-\infty}^{\infty} E(\mathbf{r}'_t, z_0) e^{+jk_z z_0} e^{+jk_t \cdot \mathbf{r}'_t} d\mathbf{r}'_t. \quad (2.45)$$

Inserting this expression in (2.42) to obtain the field in the observation plane, yields

$$\begin{aligned} E(\mathbf{r}_t, z) &= \iint_{-\infty}^{\infty} \hat{E}(\mathbf{k}_t) e^{-jk_z z} e^{-j\mathbf{k}_t \cdot \mathbf{r}_t} d\mathbf{k}_t \\ &= \frac{1}{4\pi^2} \iint_{-\infty}^{\infty} E(\mathbf{r}'_t, z_0) \iint_{-\infty}^{\infty} e^{-jk_t \cdot (\mathbf{r}_t - \mathbf{r}'_t)} e^{-jk_z(z - z_0)} d\mathbf{k}_t d\mathbf{r}'_t. \end{aligned} \quad (2.46)$$

In conclusion from (2.46), the propagation of a field from one perpendicular plane to another is a convolution of the source field with a filter function. Plane waves with  $\text{Im}\{\mathbf{k}_z\} < 0$  do not propagate in  $z$ -direction and, thus, are evanescent.

When defining only the transverse components of the source field denoted as  $E_t$ , the plane wave spectrum follows from (2.45) as

$$\hat{E}_t(\mathbf{k}_t) = \frac{1}{4\pi^2} \iint_{-\infty}^{\infty} E_t(\mathbf{r}'_t, z_0) e^{+jk_z z_0} e^{+jk_t \cdot \mathbf{r}'_t} d\mathbf{r}'_t \quad (2.47)$$

and the inverse transform to obtain the transverse field components in the observation plane is

$$E_t(\mathbf{r}_t, z) = \iint_{-\infty}^{\infty} \hat{E}_t(\mathbf{k}_t) e^{-jk_z(z - z_0)} e^{-j\mathbf{k}_t \cdot \mathbf{r}_t} d\mathbf{k}_t. \quad (2.48)$$

The previous two integral pairs propagate the transverse field from a source plane  $z_0$  to the transverse field in an observation plane  $z$ . To fulfill the divergence criterion and yield a valid solution to Maxwell's equations, as stated in the previous section, the  $z$ -component of the electric field in the observation plane has to follow [Orf16]

$$E_z(\mathbf{r}_t, z) = \iint_{-\infty}^{\infty} -\frac{\mathbf{k}_t \cdot \hat{E}_t(\mathbf{k}_t)}{k_z} e^{-jk_z(z - z_0)} e^{-j\mathbf{k}_t \cdot \mathbf{r}_t} d\mathbf{k}_t. \quad (2.49)$$

The electric field component  $E_z$  scales with the ratio of the transverse wavenumber  $\mathbf{k}_t$  to the wavenumber in propagation direction  $k_z$ . For  $k_z \gg |\mathbf{k}_t|$ , the  $E_z$  component is much smaller compared to the transverse field components  $E_t$ .

## 2.3 Gaussian Beams

Gaussian beams are one type of collimated beams. Those beams can be investigated by the paraxial wave equation [Gol98] or by means of Fourier optics, which represents

the electric field as a plane wave spectrum [Sie86]. In this thesis, the second avenue is pursued. This is, the electric field in a source plane is related to the electric field in an observation plane. The connection between both fields are the two Fourier transforms (2.46).

In the first step, a fundamental Gaussian beam with different beam waist radii and focal plane position in the  $xz$ - and  $yz$ -planes is derived. This beam represents the foundation for the design of the phased array antenna in this thesis. For a sketch of the derived Gaussian beam, see Fig. 2.1. In the subsequent sections, limitations of the Gaussian beam propagation, higher-order Gaussian beam modes, and Bessel beams (another collimated beam) are briefly described.

### 2.3.1 Paraxial Wave Propagation

Paraxial wave propagation describes the propagation of an electromagnetic wave (or beam) along an axis of propagation under certain assumptions. The field is collimated around this propagation axis. Due to the exponential decay with  $k_x$  and  $k_y$ , most contributions in the corresponding plane wave spectrum come from transverse wavenumbers  $|k_t|$  that are close to zero (small compared to the wavenumber  $k$ ). Thus, the Fresnel or paraxial approximation [MB93; Sch62] to (2.38) can be introduced according to

$$k_z = k\sqrt{1 - (\mathbf{k}_t \cdot \mathbf{k}_t) / k^2} \approx k - (\mathbf{k}_t \cdot \mathbf{k}_t) / (2k) + \dots \quad (2.50)$$

as a binomial series expansion with neglect of the higher-order terms. This simplifies the analytical evaluation of the integral pairs in (2.46). The smaller the transverse cross-section of the beam, the broader is its plane wave spectrum due to the Fourier transform relation. Consequently, there are certain limits to the paraxial approximation in (2.50), which are discussed in Section 2.3.3.

Collimated or focused beams have the property that their transverse field distribution varies slowly as compared to its variation in propagation direction. As the propagation of a field from one plane to another is described by two Fourier integrals (2.45) and (2.46), a suitable transverse field distribution has to be isomorphic. Thus, the transverse field distribution is replicated along the propagation axis [Sie86]. Functions that fulfill these conditions are for example the Gaussian and the Bessel function. Further variation in the transverse direction might be introduced in the rectangular coordinate system by Hermite polynomials, and in the polar coordinate system by Laguerre polynomials [CP71; MB93].

Fundamental Gaussian beams are beams with the lowest beam divergence, which means they remain collimated over the longest propagation distance [Gol98]. They have a real-valued electric field distribution in the focal plane which is of Gaussian shape and, thus, decay exponentially for larger distances from the propagation axis. The lack of an imaginary part implies that the field in this region has an equi-phase plane.

### 2.3.2 Fundamental Gaussian Beam

For the derivation of the Gaussian beam propagating in positive  $z$ -direction, an  $x$ -polarized electric field is assumed in the transverse plane of the rectangular coordinate system. Other polarizations might be found by evaluating the  $x$ - and  $y$ -polarized field separately and superimposing the results subsequently [FT61; MB93]. However, for this thesis only the linearly polarized case is of interest. As the collimated beam might have different shapes in  $x$ - and  $y$ -direction, its plane wave spectrum may be defined as the product of two functions according to

$$\hat{E}_x(k_x, k_y) = \hat{f}(k_x)\hat{g}(k_y), \quad (2.51)$$

where  $f$  and  $g$  are independently defined in the spatial space at positions  $z_{0x}$  and  $z_{0y}$ , respectively. Both functions have a Gaussian shape according to

$$f(x, z_{0x}) = f_0 e^{-x^2/w_{0x}^2}, \quad (2.52)$$

$$g(y, z_{0y}) = g_0 e^{-y^2/w_{0y}^2}, \quad (2.53)$$

where  $f_0$  and  $g_0$  are constants scaling the amplitude of the electric field. The scalars  $w_{0x}$  and  $w_{0y}$  define the shape of the Gaussian distribution in the transverse plane and are referred to as the beam waist radii. They specify the 1/e-electric field amplitude radius in the focal plane [Gol98]. The choice of different variables for each transverse coordinate allows different beam shapes along both axis. The plane wave coefficients of  $f$  and  $g$  are obtained by evaluating (2.47) leading to

$$\hat{E}_x(k_x, k_y) = \frac{f_0 g_0}{4\pi^2} e^{jk_z(z_{0x}+z_{0y})} \iint_{-\infty}^{\infty} e^{-x^2/w_{0x}^2 + jk_x x} e^{-y^2/w_{0y}^2 + jk_y y} dx dy. \quad (2.54)$$

Evaluating (2.54) with the paraxial approximation of  $k_z$  from (2.50) in rectangular coordinates

$$k_z = k - (k_x^2 + k_y^2)/(2k), \quad (2.55)$$

eventually leads to the plane wave spectrum of the Gaussian beam  $\hat{E}_x(k_x, k_y)$  as

$$\hat{E}_x(k_x, k_y) = f_0 g_0 \frac{w_{0x} w_{0y}}{4\pi} e^{jk(z_{0x}+z_{0y})} e^{-k_x^2(w_{0x}^2/4 + jz_{0x}/2k) - k_y^2(w_{0y}^2/4 + jz_{0y}/2k)}. \quad (2.56)$$

The propagation of this plane wave spectrum in  $z$ -direction is again governed by the propagator (2.40) with the paraxial approximation of  $k_z$ . Introducing the abbreviations

$$z' = z - z_{0x} - z_{0y}, \quad (2.57)$$

$$z'_x = z - z_{0x}, \quad (2.58)$$

$$z'_y = z - z_{0y}, \quad (2.59)$$

the plane wave spectrum of the Gaussian beam at  $z$  is

$$\hat{E}_x(k_x, k_y, z) = f_0 g_0 \frac{w_{0x} w_{0y}}{4\pi} e^{-jkz'} e^{-k_x^2 (w_{0x}^2/4 - jz'_x/2k) - k_y^2 (w_{0y}^2/4 - jz'_y/2k)}. \quad (2.60)$$

The electric field follows from the inverse transform (2.42) according to

$$E_x(k_x, k_y, z) = f_0 g_0 \frac{w_{0x} w_{0y}}{4\pi} e^{-jkz'} \int_{-\infty}^{\infty} e^{-k_x^2 (w_{0x}^2/4 - jz'_x/2k) - k_x x} dk_x \\ \int_{-\infty}^{\infty} e^{-k_y^2 (w_{0y}^2/4 - jz'_y/2k) - k_y y} dk_y. \quad (2.61)$$

Evaluating the integrals yields

$$E_x(k_x, k_y, z) = \frac{f_0 g_0 w_{0x} w_{0y} e^{-jkz'}}{w_{0x} \sqrt{1 - j\xi_x} w_{0y} \sqrt{1 - j\xi_y}} e^{-x^2 (1 + j\xi_x) / (w_{0x}^2 (1 + \xi_x^2))} \\ e^{-y^2 (1 + j\xi_y) / (w_{0y}^2 (1 + \xi_y^2))}, \quad (2.62)$$

with the normalized variables

$$\xi_x = z'_x / z_{rx}, \quad (2.63)$$

$$\xi_y = z'_y / z_{ry}, \quad (2.64)$$

and the Rayleigh length in  $x$ - and  $y$ -direction [Gol98]

$$z_{rx} = w_{0x}^2 k / 2, \quad (2.65)$$

$$z_{ry} = w_{0y}^2 k / 2. \quad (2.66)$$

Using the relation  $\frac{1}{(1 - j\xi_i)^{0.5}} = \frac{(1 + j\xi_i)^{0.5}}{(1 + \xi_i^2)^{0.5}} = \frac{e^{j\arctan(\xi_i)/2}}{(1 + \xi_i^2)^{0.25}}$  with the Gaussian beam phase shift  $\phi_x$  and  $\phi_y$  (Gouy phase shift) defined as [Gol98]

$$\phi_x = \arctan(\xi_x), \quad (2.67)$$

$$\phi_y = \arctan(\xi_y), \quad (2.68)$$

and the beam radius  $w_x$  and  $w_y$  along the propagation axis as [Gol98]

$$w_x = w_{0x} \sqrt{1 + \xi_x^2}, \quad (2.69)$$

$$w_y = w_{0y} \sqrt{1 + \xi_y^2}, \quad (2.70)$$

the dependency of  $E_x$  in (2.62) can be reformulated towards

$$E_x(k_x, k_y, z) = f_0 g_0 \frac{\sqrt{w_{0x} w_{0y}}}{\sqrt{w_x w_y}} e^{-x^2/w_x^2 - y^2/w_y^2} e^{-j(kz' + x^2 \xi_x / w_x^2 + y^2 \xi_y / w_y^2 - \phi_x/2 - \phi_y/2)}. \quad (2.71)$$

The complex exponential term can be reformulated by investigating the stationary phase

$$kz' + x^2 \xi_x / w_x^2 + y^2 \xi_y / w_y^2 - \phi_x/2 - \phi_y/2 \approx kz' + x^2 \xi_x / w_x^2 + y^2 \xi_y / w_y^2 = \text{const}. \quad (2.72)$$

Here, the Gouy phase shifts are neglected as their variation in  $z$  is small compared to the other variables. Solving for  $z$  in the  $xz$ -plane (i.e., for  $y = 0$ ) yields a parabola as

$$z = -\frac{\xi_x x^2}{w_x^2 k} + z_{0x} + z_{0y}. \quad (2.73)$$

The osculating circle radius of the parabola follows from  $r(x) = |(1 + f'(x))^{3/2} / f''(x)|$  with the derivatives  $f' = -2\xi_x x / (kw_x^2)$  and  $f'' = -2\xi_x / (kw_x^2)$ . On the  $z$ -axis, for  $x = 0$ , this yields the definition of the radius of curvature  $R_x$  as [Gol98]

$$R_x = r(0) = z_{rx} (\xi_x + 1/\xi_x). \quad (2.74)$$

The radius of curvature in the  $yz$ -plane,  $R_y$ , is defined analogously as

$$R_y = z_{ry} (\xi_y + 1/\xi_y). \quad (2.75)$$

Combining the scalar constants  $f_0$  and  $g_0$  to  $E_{0x} = f_0 g_0$  and reformulating the complex exponent in (2.71) with  $R_x$  and  $R_y$  yields

$$E_x(x, y, z) = E_{0x} \frac{\sqrt{w_{0x} w_{0y}}}{\sqrt{w_x w_y}} e^{-\frac{x^2}{w_x^2} - \frac{y^2}{w_y^2} - jkz' - j\frac{x^2 z_{rx}}{w_{0x}^2 R_x} - j\frac{y^2 z_{ry}}{w_{0y}^2 R_y} + j\frac{\phi_x}{2} + j\frac{\phi_y}{2}}. \quad (2.76)$$

This is a Gaussian beam with independent beam parameters (i.e., beam waist radius and focal plane position) in the transverse coordinates  $x$  and  $y$ , see Fig. 2.1. The variation of the electrical field in  $x$ -direction is not dependent on the variation in  $y$ -direction and, vice versa. Consequently, both principal planes can be shaped individually.

To verify the previous derivation, the analytical beam from (2.76) is compared to the propagation of its transverse field by means of the plane wave spectrum (2.46). The beam configuration is  $z_{0x} = 200$  mm,  $w_{0x} = 7\lambda$ ,  $z_{0y} = 300$  mm, and  $w_{0y} = 5\lambda$  at  $f = 90$  GHz. The source plane for the plane wave spectrum is  $z = 0$  mm. The integrals

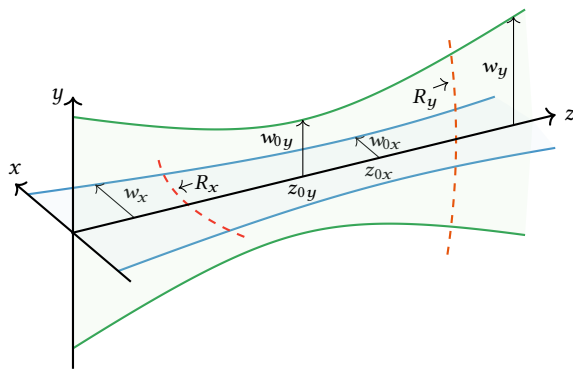


**Fig. 2.1:** Fundamental Gaussian beam mode with different and independent focal plane positions and beam waist radii in the  $x$ - and  $y$ -planes.

in (2.46) are evaluated numerically by the trapezoidal rule. For the result, see Fig. 2.2. The analytically derived Gaussian beam equals exactly the reference evaluation of the plane wave spectrum.

As a conclusion, the derived Gaussian beam (2.76) enables individually shaping the beam contour in both transversal directions, where the array taper of the phased array antenna may shape the beam in the  $xz$ -plane, while the radiating element shapes the beam in the  $yz$ -plane, see Fig. 2.1.

For comparison with a Gaussian beam that has a radially defined beam waist at  $z = 0$ ,

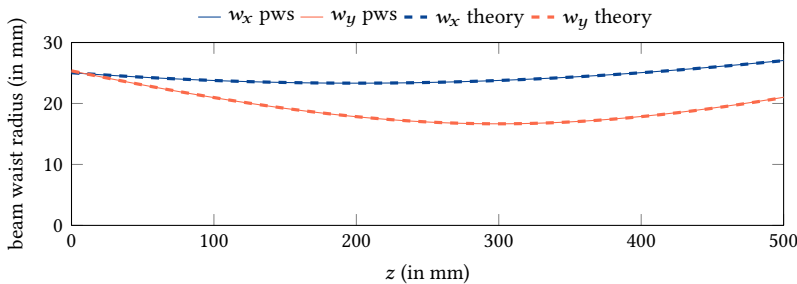


**Fig. 2.2:** Comparison of theoretical fundamental Gaussian beam mode to the plane wave spectrum representation. The beam has different and independent focal plane positions as well as beam waist radii in the  $xz$ - and  $yz$ -planes.

the beam waist radii are set to  $w_{0x} = w_{0y} = w_0$  and the offset positions to  $z_{0x} = z_{0y} = 0$ . This yields an equal Rayleigh length  $z_{rx} = z_{ry} = z_r$  and an equal normalized variable  $\xi_x = \xi_y = \xi$ . From this follows that all other parameters are equal in  $x$ - and  $y$ -direction, i.e.,  $\phi_x = \phi_y = \phi$ ,  $R_x = R_y = R$ , and  $w_x = w_y = w$ . Inserting this into (2.76) with  $\rho = \sqrt{x^2 + y^2}$  yields

$$E_x(\rho, z) = E_{0x} \frac{w_0}{w} e^{-\rho^2/w^2} e^{-j(kz + \frac{\rho^2 z_r}{w^2 R} - \phi)}, \quad (2.77)$$

which exactly equals the fundamental Gaussian beam with radial transverse dependency as found in [Gol98].

### 2.3.3 Limitations of the Paraxial Approximation

The paraxial approximation (2.50) simplifies the expression of the wavenumber in propagation direction of the plane wave spectrum (2.38) and enables the notation of the Gaussian beam. However, this approximation can only be made for  $|\mathbf{k}_t| \ll k$ . Hence, only beams with an appropriately large beam waist and, thus, a plane wave spectrum that permits the approximation (spectrum is narrow enough such that  $|\mathbf{k}_t| \ll k$ ) are correctly prescribed and modeled. In [MB93] and [Gol98], the paraxial approximation (2.50) is said to be valid when the beam waist is larger than the wavelength, i.e.,  $w_0 > \lambda$ . The error due to the paraxial approximation is investigated in the following paragraphs for the beam waist radii  $w_{0x} = 7\lambda$  and  $w_{0y} = 0.7\lambda$ . The beam waist radius  $w_{0x} = 7\lambda$  equals that of the desired beam for the Doppler reflectometry in ASDEX Upgrade tokamak to be realized with the phased array antenna.

Most Gaussian beam representations consider only the transverse field components. Small beam waist radii, however, require field components in propagation direction. These field components can be derived from the transverse electric field components by means of the divergence condition, where the transverse field components are chosen and the field components in propagation direction follow subsequently. To fulfill the divergence criterion (2.33), the  $\hat{E}_z$ - and consequently the  $E_z$ -component of the electric field is chosen according to (2.49). Considering the plane wave spectrum of the Gaussian beam in (2.60), which only has an  $x$ -component and no  $y$ -component, the electric field in  $z$ -direction follows from (2.49) with (2.60) as

$$E_z(x, y, z) = - \iint_{-\infty}^{\infty} \frac{k_x \hat{E}_x(k_x, k_y, z)}{k_z} e^{-jk_x x} e^{-jk_y y} dk_x dk_y \quad (2.78)$$

$$= -2k \iint_{-\infty}^{\infty} \frac{k_x \hat{E}_x(k_x, k_y, z)}{2k^2 - k_x^2 - k_y^2} e^{-jk_x x} e^{-jk_y y} dk_x dk_y. \quad (2.79)$$

To evaluate the impact of the divergence condition, the plane wave spectrum of the Gaussian beam (2.76) from (2.60) is evaluated at the focal plane by the inverse transform (2.42). The  $E_z(x, y, z)$ -component required to fulfill the divergence condition follows from (2.79). As previously stated, two different beams with beam waist radii along the  $x$ -axis of  $w_{0x} = 7\lambda$  and  $w_{0x} = 0.7\lambda$  are investigated. The integrals in (2.79) are not evaluated analytically here. In order to answer the question if it is appropriate to neglect the  $E_z$ -component, the integrals in (2.79) are evaluated numerically. See the left plot in Fig. 2.3 for the results. The electric field is normalized to the maximum value of  $E_x$  (i.e., value at  $x = 0$ ). The  $x$ -axis is normalized with the beam waist radius to allow a direct comparison between both beams. The  $E_x$ -components of the beams with  $w_{0x} = 7\lambda$  and  $w_{0x} = 0.7\lambda$  overlay almost exactly. The  $E_z$ -component of the beam with  $w_{0x} = 7\lambda$  is below  $-35$  dB. The  $E_z$ -component is roughly  $30$  dB smaller than the  $E_x$  component and can, thus, be considered small enough to be neglected. For the beam waist radius  $w_{0x} = 0.7\lambda$  the  $E_z$  component is considerably larger and increases up to about  $-15$  dB. In addition, for transverse positions  $x > w_{0x}$ , the difference between the  $E_x$ - and the  $E_z$ -component is only about  $5$  dB. This difference is definitely too small to be neglected. In conclusion, the  $E_z$ -component for Gaussian beams with beam waist radii larger  $w_{0x} = 7\lambda$  is small and, thus, negligible (violating the divergence criterion). For beam waist radii smaller than a wavelength, the  $E_z$ -component approaches the strength of the transverse field components and has to be considered.

To investigate the degree to which the paraxial approximation of  $k_z$  in (2.50) is appropriate, the propagation of a transverse beam field with the exact wavenumber  $k_z$  (by means of the plane wave spectrum) is compared to the field obtained by propagation with the paraxial approximation of  $k_z$ . The investigated beams are again of Gaussian shape with beam waist radii  $w_{0x} = 7\lambda$  and  $w_{0x} = 0.7\lambda$ . The plane wave spectrum of their transverse electric field is propagated along the  $z$ -axis over a distance of  $10z_{rx}$ ; ten times the Rayleigh length which is in the far-field of the beam [Gol98]. The large propagation distance is chosen, since the error introduced by approximating  $k_z$  becomes larger for larger propagation distances. The numerical results are visualized in the right plot of Fig. 2.3. The abscissa is the angle in the  $xz$ -plane between the evaluated point and the  $z$ -axis. For the beam waist radius  $w_{0x} = 7\lambda$ , the computed fields overlay almost exactly. The error between both curves is below  $-60$  dB. Thus, using the paraxial approximation is valid. On the other hand, for the beam waist radius of  $0.7\lambda$ , there are considerable differences. On and near to the  $z$ -axis, the error is still small and can be neglected. However, for angles above about  $20^\circ$ , the difference gets visible and the error is about  $20$  dB. In conclusion, for large beam waist radii or for small angles near to the propagation axis, the paraxial approximation of  $k_z$  is valid.

In summary, for beam waist radii larger than a wavelength, the paraxial approximation and considering only transverse field components yields good enough solutions. These are approximations and, thus, do not fulfill Maxwell's equations exactly. The smaller the beam waist, the larger is the deviation. For beam waist radii  $w_{0x} \rightarrow \infty$ , the

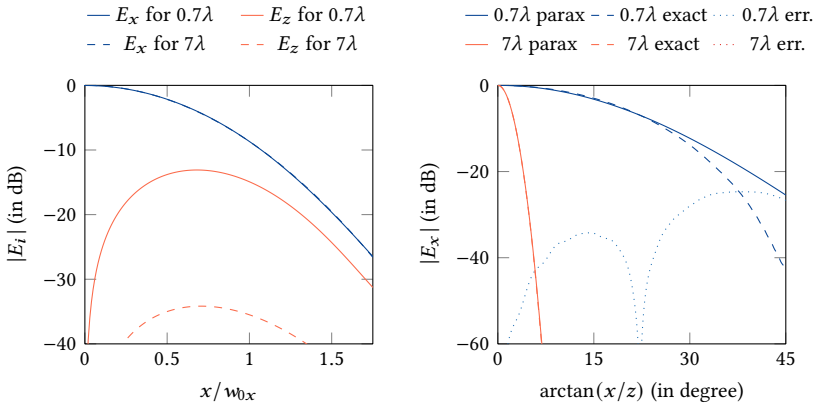


**Fig. 2.3:** Left: Comparison of the normalized  $|E_x|$ - and  $|E_z|$ -component of a Gaussian beam at the focal plane as a function of the beam waist radius evaluated for the beam waist radii  $0.7\lambda$  and  $7\lambda$ . Right: Comparison of the field propagation for the exact  $k_z$  and its paraxial approximation. The field is evaluated in a distance of  $10z_r$  from the source plane. Plotted are the two fields and the error between them for the beam waist radii  $0.7\lambda$  and  $7\lambda$ .

transverse field distribution tends to that of a plane wave, which is a valid solution to Maxwell's equations.

### 2.3.4 Higher-Order Gaussian Beams and Bessel Beams

Higher-order Gaussian beams are obtained by introducing a further modulation in transverse direction. This variation is realized by multiplying the fundamental Gaussian beam with polynomials that are also isomorphic. There are different polynomials in the cylindrical and in the rectangular coordinate system. In the cylindrical coordinate system, Laguerre polynomials describe the higher-order variation. In rectangular coordinates, Hermite polynomials describe the higher-order variation. These lead to the so-called Gauss-Laguerre and Gauss-Hermite beams [Gol98; MB93]. Similar to the derivation of the fundamental mode Gaussian beam an  $x$ -polarized electric field is assumed in the transverse plane of the rectangular coordinate system and other polarizations might be found by superposition of a  $y$ -polarized field [FT61; MB93].

For the cylindrical case, the Laguerre polynomials in series representation are

$$L_{pm}(u) = \sum_{l=0}^{l=p} \frac{(p+m)! (-u)!}{(m+l)! (p-l)! l!}. \quad (2.80)$$

The resulting Gauss-Laguerre beams are [Gol98]

$$\begin{aligned} E_{x,pm}(\rho, \varphi, z) = & \left( \frac{2p!}{\pi(p+m)!} \right)^{0.5} \frac{1}{w(z)} \left( \frac{\sqrt{2\rho}}{w(z)} \right)^m L_{pm} \left( \frac{2\rho^2}{w^2(z)} \right) E_{0x} \\ & \exp \left( \frac{-\rho^2}{w^2(z)} - jkz - \frac{j\pi\rho^2}{\lambda R(z)} - j(2p+m+1)\Phi(z) \right) \\ & \exp(jm\varphi). \end{aligned} \quad (2.81)$$

The index  $m$  describes the variation in  $\varphi$  direction and the index  $p$  describes the dependency in radial direction. The individual modes are orthogonal, as [Gol98]

$$\iint \rho E_{x,pm}(r, \varphi, z) E_{x,qn}^*(r, \varphi, z) dr d\varphi = \delta_{pm} \delta_{qn}, \quad (2.82)$$

and, thus, may be used to expand the transverse field, for example that of a cylindrical feed horn, in terms of Gauss-Laguerre modes.

For the rectangular case, the Hermite polynomials are obtained from the expression

$$H_n(u) = (-1)^n e^{u^2} \frac{d^n}{du^n} \left( e^{-u^2} \right), \quad (2.83)$$

with  $n = 1, 2, 3, \dots$ . The higher-order Gaussian beams in rectangular coordinates are [Gol98; MB93]

$$\begin{aligned} E_{x,mn}(x, y, z) = & \left( \frac{1}{\pi w_x w_y 2^{m+n+1} m! n!} \right)^{0.5} H_m \left( \frac{\sqrt{2}x}{w_x} \right) H_n \left( \frac{\sqrt{2}y}{w_y} \right) E_{0x} \\ & \exp \left( -\frac{x^2}{w_x^2} - \frac{y^2}{w_y^2} - jkz - j \frac{x^2 z_{rx}}{w_{0x}^2 R_x} - j \frac{y^2 z_{ry}}{w_{0y}^2 R_y} \right) \\ & \exp \left( j \frac{(2m+1)}{2} \Phi_x + j \frac{(2n+1)}{2} \Phi_y \right). \end{aligned} \quad (2.84)$$

The index  $m$  defines the variation in  $x$ -direction, and the index  $n$  defines the variation in  $y$ -direction. In fact, the indices  $m$  and  $n$  are the number of zero-crossings of the electric field on the respective axis. The modes are called Gauss-Hermite modes. They also form an orthogonal set, as [Gol98]

$$\iint E_{x,mn}(x, y, z) E_{x,pq}(x, y, z)^* dx dy = \delta_{mn} \delta_{pq}. \quad (2.85)$$

Both, the fundamental Gaussian beam and its higher-order solutions spread transversely when propagating away from the beam waist. However, there is a non-diverging solution to the Helmholtz equation that was first discovered by Durnin [Dur87; DME87]. The transverse field has a variation in radial direction and no variation in  $\varphi$  direction. The variation in transverse direction is that of a Bessel function  $J_0(\alpha\rho)$ , with  $0 < \alpha < k$ , as [Dur87]

$$E_x(\rho, z) = E_{0x} J_0(\alpha\rho) \exp(-jkz). \quad (2.86)$$

The transverse field does not vary with  $z$  and, thus, the beam is non-diverging. As the radial variation is that of a Bessel function, the beam is called Bessel beam. However, to realize an ideal Bessel beam, an infinite aperture and, hence, infinite energy is required. Employing only a finite aperture is possible. Then, the Bessel beam with beam radius  $r$  has a constant or non-spreading transverse field distribution over a distance depending on the aperture width as  $z_{\max} = \pi r^2/\lambda$  [Dur87].

## 2.4 Guided Waves

Apart from the propagation of electromagnetic waves in free-space, they can be guided by materials of various forms in so-called waveguides. For the subsequent analysis, the waveguide cross-section is assumed constant along the  $z$ -direction. The field distribution in the transverse plane has to fulfill the boundary conditions required by the cross-sectional shape and material of the waveguide. For the analysis of wave propagation, the fields are assumed to be of the form [Jin15]

$$\mathbf{E} = [\mathbf{E}_t(x, y) + \mathbf{u}_z E_z(x, y)] e^{\pm jk_z z}, \quad (2.87)$$

$$\mathbf{H} = [\mathbf{H}_t(x, y) + \mathbf{u}_z H_z(x, y)] e^{\pm jk_z z}. \quad (2.88)$$

The fields may have a variation in the transverse coordinates ( $x$  and  $y$ ), while the variation in  $z$ -direction is governed by the propagator  $e^{\pm jk_z z}$ . The “-”-sign indicates a wave traveling in positive  $z$ -direction and the “+”-sign a wave traveling in negative  $z$ -direction. In the following, only a wave propagating in positive  $z$ -direction is considered. Substituting (2.87) and (2.88) into the source-free Maxwell's equations (2.24) and (2.25) one obtains a relation between the fields in  $z$ -direction  $E_z$  and  $H_z$  and the transverse fields  $\mathbf{E}_t$  and  $\mathbf{H}_t$  as [Jin15]

$$\mathbf{u}_z \times \nabla_t E_z + jk_z \mathbf{u}_z \times \mathbf{E}_t = j\omega \mu \mathbf{H}_t, \quad (2.89)$$

$$\nabla_t \times \mathbf{E}_t = -j\omega \mu \mathbf{u}_z H_z, \quad (2.90)$$

and

$$\mathbf{u}_z \times \nabla_t H_z + jk_z \mathbf{u}_z \times \mathbf{H}_t = -j\omega \varepsilon \mathbf{E}_t, \quad (2.91)$$

$$\nabla_t \times \mathbf{H}_t = -j\omega \mu \mathbf{u}_z E_z. \quad (2.92)$$

By taking the cross-product with  $\mathbf{u}_z$ , it is possible to eliminate  $\mathbf{u}_z \times \mathbf{H}_t$  and  $\mathbf{u}_z \times \mathbf{E}_t$ , which finally yields [Jin15]

$$\mathbf{E}_t = (\mathrm{j}\omega\mu \mathbf{u}_z \times \nabla_t H_z - \mathrm{j}k_z \nabla_t E_z) / (k^2 - k_t^2), \quad (2.93)$$

$$\mathbf{H}_t = (-\mathrm{j}\omega\epsilon \mathbf{u}_z \times \nabla_t E_z - \mathrm{j}k_z \nabla_t H_z) / (k^2 - k_t^2). \quad (2.94)$$

By substituting (2.93) and (2.94) into (2.90) and (2.92), respectively, gives the relations [Jin15]

$$\nabla_t \times [(\omega\epsilon \mathbf{u}_z \times \nabla_t E_z + k_z \nabla_t H_z) / k_t^2] = -\omega\epsilon \mathbf{u}_z E_z, \quad (2.95)$$

$$\nabla_t \times [(\omega\mu \mathbf{u}_z \times \nabla_t H_z + k_z \nabla_t E_z) / k_t^2] = -\omega\mu \mathbf{u}_z H_z, \quad (2.96)$$

where the transverse wavenumber is defined via

$$k_t^2 = k^2 - k_z^2. \quad (2.97)$$

The previous equations hold also for inhomogeneously filled waveguides. For homogeneously filled waveguides, with scalar material constants  $\epsilon$  and  $\mu$ , the equations for  $E_z$  and  $H_z$  in the transverse plane simplify to [Jin15]

$$\nabla_t^2 E_z + k_t^2 E_z = 0, \quad (2.98)$$

$$\nabla_t^2 H_z + k_t^2 H_z = 0, \quad (2.99)$$

with the transverse Laplacian operator  $\nabla_t^2 = \nabla_t \cdot \nabla_t$ . In case of a homogeneously filled waveguide, the fields  $E_z$  and  $H_z$  are not coupled through the medium  $\epsilon$  or  $\mu$ . Also the boundary conditions on a conductor yield no coupling. Consequently,  $E_z$  and  $H_z$  can exist independently and lead to different wave solutions. Solutions to (2.98) and (2.99) can thus be found by setting one of both field components to zero. This is,  $E_z = 0$  and  $H_z \neq 0$  leads to a field solution that has solely transverse electric field components and is called transverse electric (TE). Similarly, finding a solution with  $E_z \neq 0$  and  $H_z = 0$  yields a magnetic field only in transverse direction that is consequently called transverse magnetic (TM).

In the following, empty metallic waveguides are considered. For the derivation of the fields, the conductivity is assumed perfectly electrically conducting (PEC). Field solutions are found by imposing appropriate boundary conditions on  $E_z$  and  $H_z$ . As the waveguide has no variation in  $z$ -direction, the electric field  $E_z$  on the boundary is always tangential and has to vanish for PEC. Thus, for TM-modes the boundary condition

$$E_z = 0 \quad (2.100)$$

holds on the inner conduction surface of the waveguide. The magnetic field on a perfectly electrically conducting surface satisfies  $\mathbf{u}_n \cdot \mathbf{H} = 0$ . With (2.94) and  $\mathbf{u}_n \cdot (\mathbf{u}_z \times \nabla_t E_z) = (\mathbf{u}_n \times \mathbf{u}_z) \cdot \nabla_t E_z$  with  $E_z = 0$  yields according to [Jin15]

$$\mathbf{u}_n \cdot \mathbf{H} = \mathbf{u}_n \cdot \mathbf{H}_t = \frac{1}{k_t^2} [-j\omega\epsilon \mathbf{u}_n \cdot (\mathbf{u}_z \times \nabla_t E_z) - jk_z \mathbf{u}_n \cdot \nabla_t H_z] = 0, \quad (2.101)$$

and consequently on the boundary

$$\frac{\partial H_z}{\partial n} = 0, \quad (2.102)$$

where  $n$  is the coordinate aligned with the surface normal.

#### 2.4.1 Rectangular Hollow Waveguide

A rectangularly-shaped PEC-boundary in transverse directions without an inner conductor forms the rectangular hollow waveguide as depicted in Fig. 2.4. The rectangular cross-section spans from  $(x, y) = (0, 0)$  to  $(a, b)$ , where  $a$  represents the waveguide width and  $b$  the waveguide height. The cross-section is considered uniform in  $z$ -direction. The field solutions in the transverse plane are obtained by imposing the PEC boundary conditions for  $H_z$  and  $E_z$  for the TE- and TM-modes, respectively.

A general solution to the Helmholtz equation (2.98) in Cartesian coordinates with wave propagation in positive  $z$ -direction is obtained by separating the variables in the transverse plane. In case of the rectangular hollow waveguide sketched in Fig. 2.4, where the domain is bounded in the transverse plane, a general solution to (2.98) or (2.99) can have the form [Jin15]

$$[A \cos(k_x x) + B \sin(k_x x)] [C \cos(k_y y) + D \sin(k_y y)] e^{-jk_z z}, \quad (2.103)$$

with the separation condition or dispersion relation

$$k_x^2 + k_y^2 + k_z^2 = k^2. \quad (2.104)$$

The variables  $A$ ,  $B$ ,  $C$ , and  $D$  are arbitrary constants. The sin-functions fulfill the condition that the (electric) field vanishes on the boundary (for  $k_x x = 0, \pi, \dots$  or  $k_y y = 0, \pi, \dots$ ), and the cos-functions fulfill the condition that the component of the (magnetic) field normal to the boundary vanishes on the boundary (for  $k_x x = 0, \pi, \dots$  or  $k_y y = 0, \pi, \dots$ ). The constants  $A$ ,  $B$ ,  $C$ , and  $D$  are problem specific and are defined such that  $E_z$  or  $H_z$  fulfill the boundary condition. The transverse wavenumbers  $k_x$  and  $k_y$  define different modes of operation.

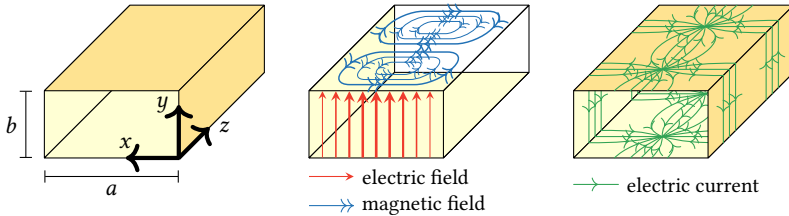


**Fig. 2.4:** Left: Geometrical configuration of a rectangular hollow waveguide; Middle: Sketch of the electric and magnetic field lines of the  $\text{TE}_{10}$ -mode; Right: Sketch of the electric wall currents of the  $\text{TE}_{10}$ -mode.

### TE-modes

TE-modes are constructed from  $H_z$  and fulfill the boundary condition (2.102) on the waveguide walls. From the geometry of Fig. 2.4, this yields for the rectangular hollow waveguide

$$\frac{\partial H_z}{\partial x} \Big|_{x=0,a} = 0, \quad \frac{\partial H_z}{\partial y} \Big|_{y=0,b} = 0. \quad (2.105)$$

These boundary conditions define the constants of the general solution to (2.103). They yield  $B = 0$ ,  $D = 0$  and  $\cos(k_x a) = 0$  as well as  $\cos(k_y b) = 0$ . From the last two equations, the separation constants  $k_x$  and  $k_y$  can be determined as

$$k_x = \frac{m\pi}{a} \quad m = 0, 1, 2, \dots \quad k_y = \frac{n\pi}{b} \quad n = 0, 1, 2, \dots, \quad (2.106)$$

while  $m$  and  $n$  are not allowed to be zero simultaneously. Combining the remaining constants  $A$  and  $C$  to a mode-dependent constant  $H_{mn}$  yields

$$H_{zmn} = H_{mn} \cos(k_x x) \cos(k_y y) e^{-jk_{zmn} z}, \quad (2.107)$$

where the wavenumber in propagation direction is also dependent on the mode indices  $m$  and  $n$  as

$$k_{zmn} = \sqrt{k^2 - k_x^2 - k_y^2} = \sqrt{k^2 - \left(\frac{m\pi}{a}\right)^2 - \left(\frac{n\pi}{b}\right)^2}. \quad (2.108)$$

These waveguide modes are denoted as  $\text{TE}_{mn}$ , where the subscripts  $m$  and  $n$  refer to the indices of the corresponding wavenumbers  $k_x$  and  $k_y$ . The remaining field components

follow from the  $H_{zmn}$  in (2.107) together with (2.93) and (2.94) as [Jin15]

$$E_x = -j \frac{\omega \mu}{k_t^2} \frac{\partial H_z}{\partial y}, \quad E_y = j \frac{\omega \mu}{k_t^2} \frac{\partial H_z}{\partial x}, \quad (2.109)$$

$$H_x = -j \frac{k_z}{k_t^2} \frac{\partial H_z}{\partial x}, \quad H_y = -j \frac{k_z}{k_t^2} \frac{\partial H_z}{\partial y}, \quad (2.110)$$

with the transverse wavenumber  $k_t^2 = k_x^2 + k_y^2$ .

### TM-modes

TM-modes are constructed similarly from  $E_z$  and fulfill the boundary condition (2.100) on the waveguide walls. From the geometry of Fig. 2.4, this yields in the rectangular hollow waveguide

$$E_z|_{x=0,a} = 0, \quad E_z|_{y=0,b} = 0. \quad (2.111)$$

These boundary conditions again define the constants of the general solution to (2.103). They yield  $A = 0$ ,  $C = 0$ ,  $\sin(k_x a) = 0$  and,  $\sin(k_y b) = 0$ . The wavenumbers  $k_x$  and  $k_y$  are defined as those for the TE <sub>$mn$</sub> -modes in (2.106). However, for the case of TM-modes the mode-indices  $m$  and  $n$  must not be zero, i.e.,  $m, n \neq 0$ , as this would lead to a vanishing field. Combining the remaining constants ( $B$  and  $D$ ) to  $E_{mn}$ , the TM rectangular waveguide modes are defined by

$$E_{zmn} = E_{mn} \sin(k_x x) \sin(k_y y) e^{-jk_{zmn} z}. \quad (2.112)$$

Similarly, these waveguide modes are denoted as TM <sub>$mn$</sub> , where the subscripts  $m$  and  $n$  refer to the indices of the corresponding wavenumbers  $k_x$  and  $k_y$ . The remaining field components follow from  $E_{zmn}$  in (2.112) together with (2.93) and (2.94) as [Jin15]

$$H_x = j \frac{\omega \epsilon}{k_t^2} \frac{\partial E_z}{\partial y}, \quad H_y = -j \frac{\omega \epsilon}{k_t^2} \frac{\partial E_z}{\partial x}, \quad (2.113)$$

$$E_x = -j \frac{k_z}{k_t^2} \frac{\partial E_z}{\partial x}, \quad E_y = -j \frac{k_z}{k_t^2} \frac{\partial E_z}{\partial y}, \quad (2.114)$$

with the transverse wavenumber  $k_t^2 = k_x^2 + k_y^2$ .

The total field in a rectangular waveguide can be a superposition of TE <sub>$mn$</sub> - and TM <sub>$mn$</sub> -modes from (2.107) and (2.112). However, at a certain frequency not every mode can propagate. Indeed, having a look at (2.108), the wavenumber in propagation direction can be real or imaginary – dependent on the choice of  $m$  and  $n$ . The transition from either of both regimes to the other follows from

$$k^2 - \left(\frac{m\pi}{a}\right)^2 - \left(\frac{n\pi}{b}\right)^2 = 0, \quad (2.115)$$

which leads to the definition of the cut-off wavelength

$$\lambda_{c,mn} = \frac{2\pi}{\sqrt{\left(\frac{m\pi}{a}\right)^2 + \left(\frac{n\pi}{b}\right)^2}}. \quad (2.116)$$

For wavelengths larger than  $\lambda_{c,mn}$  or frequencies smaller than  $f_{c,mn} = 2\pi/\lambda_{c,mn}$ , the wavenumber is imaginary (chosen negative imaginary for an attenuation in propagation direction) and, thus, represents an evanescent wave. For wavelength smaller than  $\lambda_{c,mn}$  or frequencies larger than  $f_{c,mn} = 2\pi/\lambda_{c,mn}$ , the wavenumber in propagation direction is real and, thus, represents a propagating wave.

### TE<sub>10</sub>-mode – Fields, Currents, and Power

For a waveguide cross-section with  $a > b$ , the mode with the lowest cut-off frequency is the TE<sub>10</sub>-mode, as it minimizes the denominator in (2.116). The next higher mode depends on the ratio between  $a$  and  $b$ . To maximize the frequency range in which a single mode operation is guaranteed, this is, the TE<sub>10</sub>-mode is the only propagating mode, the ratio is chosen as  $a/b = 2$ , and the TE<sub>10</sub>-mode is called the fundamental mode. In the following, the subscript ( $mn = 10$ ) is assumed for all variables and not further shown. Further, the variable  $a$  is also denoted as the waveguide width and the variable  $b$  is also denoted as the waveguide height. From (2.108) follows the wavenumber in propagation direction as

$$k_z = \sqrt{k^2 - (\pi/a)^2}, \quad (2.117)$$

and consequently the guided wavelength in propagation direction is

$$\lambda_g = \frac{\lambda_0}{\sqrt{1 - \lambda_0^2/(4a^2)}}, \quad (2.118)$$

where  $\lambda_0$  is the free-space wavelength. The electromagnetic fields of the TE<sub>10</sub>-mode follow from (2.107), which yields

$$H_z = H_{10} \cos(\pi x/a) e^{-jk_z z}. \quad (2.119)$$

The remaining field components are obtained from (2.109) and (2.110) as

$$E_x = 0, \quad E_y = -jH_{10} \frac{\omega\mu a}{\pi} \sin(\pi x/a) e^{-jk_z z}, \quad (2.120)$$

$$H_y = 0, \quad H_x = jH_{10} \frac{k_z a}{\pi} \sin(\pi x/a) e^{-jk_z z}. \quad (2.121)$$

The electric field has only an  $E_y$ -component which has a half-sine amplitude distribution in  $x$ -direction. The magnetic field has an  $H_x$ - and an  $H_z$ -component. Both fields are depicted in the centered sketch of Fig. 2.4.

The power transferred in propagation direction follows from the  $z$ -component of the Poynting vector, according to [Poz11], as

$$\begin{aligned} P &= \frac{1}{2} \int_{x=0}^a \int_{y=0}^b \operatorname{Re} \{(\mathbf{E} \times \mathbf{H}^*) \cdot \mathbf{u}_z\} dy dx \\ &= \frac{\omega \mu a^3 b}{4\pi^2} |H_{10}|^2 \operatorname{Re} \{k_z\}. \end{aligned} \quad (2.122)$$

There is only power transfer in propagation direction, if  $k_z$  has a real part and is thus not purely evanescent.

The surface currents on the waveguide walls follow from the magnetic field and the boundary condition (2.20). On the top- and bottom walls, this yields

$$\begin{aligned} J_{sh} &= \mp \mathbf{u}_y \times (\mathbf{u}_x H_{x10} + \mathbf{u}_z H_{z10}) \\ &= \mp \mathbf{u}_x H_{z10} \pm \mathbf{u}_z H_{x10} \\ &= \left( (\mp \mathbf{u}_x) \cos(\pi x/a) + (\pm \mathbf{u}_z) \frac{ak_{z10}}{\pi} \sin(\pi x/a) \right) H_{10} e^{-jk_{z10}z}, \end{aligned} \quad (2.123)$$

and similarly on the left and right sidewall

$$\begin{aligned} J_{sv} &= \mp \mathbf{u}_x \times (\mathbf{u}_x H_{x10} + \mathbf{u}_z H_{z10}) \\ &= \pm \mathbf{u}_y H_{z10}|_{x=0,a} \\ &= -\mathbf{u}_y H_{10} e^{-jk_{z10}z}. \end{aligned} \quad (2.124)$$

For  $x = a/2$ , the  $x$ -component of the electric surface current on the top and bottom walls vanishes, leaving only an electric current in propagation direction. This is beneficial when realizing such a rectangular hollow waveguide, as the waveguide walls can be cut in  $z$ -direction at  $x = a/2$  without interrupting a surface current. On the sidewalls, there is a  $y$ -directed surface current. The electric surface currents are sketched on the right side of Fig. 2.4. The conductor losses can be specified by assuming the electromagnetic fields to be distributed as in the PEC boundary case, leading to the surface currents (2.123) and (2.124) (perturbation method). With a finite conductivity, the electric surface currents would modify the electromagnetic fields (leading to an  $E_z$  component). However, this modification is assumed small for good conductors. The

power dissipated in the conductor follows according to [Poz11] as

$$\begin{aligned} P_\ell &= R_s \int_{y=0}^b |J_{sv}|^2 dy + R_s \int_{x=0}^a |J_{sh}|^2 dx \\ &= R_s |H_{10}|^2 \left( b + \frac{a}{2} + \frac{k_z^2 a^3}{2\pi^2} \right). \end{aligned} \quad (2.125)$$

The TE<sub>10</sub>-wave impedance follows, according to [Poz11], from

$$Z = \frac{-E_y}{H_x} = \frac{\omega\mu}{k_z} = \frac{\omega\mu}{\sqrt{k^2 - (\pi/a)^2}}, \quad (2.126)$$

and, thus, is dependent on the geometry ( $a$ ) and the frequency. Note, that the wave impedance is different for every mode, as it follows from the mode-dependent transverse field components.

### TE<sub>10</sub>-mode – Propagation and Attenuation

The propagation constant of the TE<sub>10</sub>-mode is specified by  $k_z$  in (2.117). From the ratio between dissipated (2.125) and transferred power (2.122), also an attenuation constant per unit length can be derived. This constant is [Poz11]

$$\alpha = \frac{P_\ell}{2P} = \frac{R_s}{a^3 b k_z k \eta} (2b\pi^2 + a^3 k^2) \text{ Np.} \quad (2.127)$$

Attenuation and propagation constants might be combined to a single complex propagation constant as

$$\gamma = \alpha + jk_z, \quad (2.128)$$

with the modified dependency of the field components in  $z$ -direction

$$H_z = H_{10} \cos(\pi x/a) e^{-\gamma z}. \quad (2.129)$$

The phase velocity of the TE<sub>10</sub>-mode is specified by

$$v_p = \frac{\omega}{k_z} = \frac{c_0}{\sqrt{1 - \left(\frac{\lambda_0}{2a}\right)^2}}, \quad (2.130)$$

which is always larger than the phase velocity in free-space for propagating modes. The phase velocity of the TE<sub>10</sub>-mode is only dependent on the waveguide width  $a$  and on the frequency. It is not dependent on the waveguide height  $b$ . For a fixed waveguide width and increasing frequency, the denominator in (2.130) tends to unity and, thus, the phase velocity approaches that of free-space.

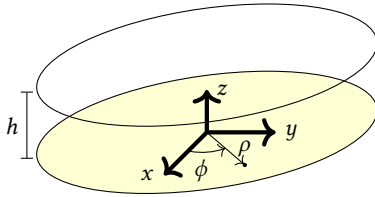


**Fig. 2.5:** Geometrical configuration of the radial parallel plate waveguide consisting of two parallel PEC-plates in a distance of  $h$ . The upper plate is sketched translucently and indicated by the solid circle.

#### 2.4.2 Radial Parallel Plate Waveguide

The radial parallel plate waveguide consists of two infinitely extended and parallel PEC plates. The bottom plate is located in the  $xy$ -plane at  $z = 0$  and the top plate is located in the  $xy$ -plane at  $z = h$ , where  $h$  is the spacing between both plates. A sketch of the geometry is given in Fig. 2.5. In the following, only waves that exist in-between both plates are considered.

To find wave solutions in the cylindrical coordinate system, as sketched in Fig. 2.5, the Laplace operator in the Helmholtz equation has to be represented in the cylindrical coordinate system. It basically follows from  $\nabla^2 \mathbf{A} = \nabla(\nabla \cdot \mathbf{A}) - \nabla \times \nabla \times \mathbf{A}$ , which leads to scalar and coupled partial differential equations for the  $E_\rho$  and  $E_\phi$  components [Bal12]. The field components in  $\rho$ - and  $\phi$ -direction are coupled as the components of the coordinate system are position dependent. Only the  $E_z$ - and the  $H_z$ -components lead to uncoupled scalar Helmholtz equations [Bal12]. Solutions to these equations are called cylindrical wave functions and are separated in  $TE^z$ - and  $TM^z$ -solutions. They can be found by the method of separation of variables and subsequently solving for the separated functions [Bal12; Jin15]. They fulfill the dispersion relation in cylindrical coordinates as [Bal12]

$$k_\rho^2 + k_z^2 = k^2. \quad (2.131)$$

Field solutions in  $z$ - and  $\phi$ -direction can have an exponential or a trigonometric dependency as [Bal12]

$$Ae^{-jk_z z} + Be^{+jk_z z}, \quad (2.132)$$

$$A \cos(k_z z) + B \sin(k_z z), \quad (2.133)$$

$$Ce^{-jm\phi} + De^{+jm\phi}, \quad (2.134)$$

$$C \cos(m\phi) + D \sin(m\phi). \quad (2.135)$$

Those with the exponential dependency represent traveling waves and those solutions with the trigonometric functions represent standing waves. Solutions in radial direction

$\rho$  are Bessel or Hankel functions [Bal12], where  $J_m$  and  $Y_m$  are the Bessel functions of the first and second kind, respectively. The Bessel functions, are linearly independent. Both yield real values for real arguments and, thus, represent standing waves in radial direction. The Bessel function of the first kind tends to a finite value and the Bessel function of the second kind tends to a (negative) infinite value for  $k_\rho \rho \rightarrow 0$  [Jin15]. A proper combination of  $J_m$  and  $Y_m$  leads to two other linearly independent solutions in radial direction – the Hankel functions of the first and second kind,  $H_m^{(1)}(k_\rho \rho)$  and  $H_m^{(2)}(k_\rho \rho)$ , respectively. According to [Jin15], they are defined as

$$H_m^{(1)}(k_\rho \rho) = J_m(k_\rho \rho) + j Y_m(k_\rho \rho), \quad (2.136)$$

$$H_m^{(2)}(k_\rho \rho) = J_m(k_\rho \rho) - j Y_m(k_\rho \rho). \quad (2.137)$$

With the large-argument expression of  $J_m(k_\rho \rho)$  and  $Y_m(k_\rho \rho)$  for  $k_\rho \rho \gg 1$ , an approximation of the Hankel functions for large arguments is [Jin15]

$$H_m^{(1)}(k_\rho \rho) \approx \sqrt{\frac{2}{\pi k_\rho \rho}} e^{+j(k_\rho \rho - m\pi/2 - \pi/4)} \quad \text{for } k_\rho \rho \gg 1, \quad (2.138)$$

$$H_m^{(2)}(k_\rho \rho) \approx \sqrt{\frac{2}{\pi k_\rho \rho}} e^{-j(k_\rho \rho - m\pi/2 - \pi/4)} \quad \text{for } k_\rho \rho \gg 1. \quad (2.139)$$

Thus, the Hankel function of the first kind  $H_m^{(1)}(k_\rho \rho)$  represents a wave traveling in negative radial direction (positive sign in the exponent and the time dependency  $e^{j\omega t}$ ) and the Hankel function of the second kind  $H_m^{(2)}(k_\rho \rho)$  represents a wave traveling in positive radial direction (negative sign in the exponent). In summary, the Bessel functions are more suitable in case the problem is bounded in radial direction. The Hankel functions are the more suitable choice in case the problem is unbounded in radial direction allowing waves to propagate.

The previous considerations yield a general solution in cylindrical coordinates for the  $z$ -components of the field. The radial parallel plate waveguide in Fig. 2.5 is unbounded in radial direction and has two infinitely-extended PEC walls at  $z = 0$  and at  $z = h$ . The first condition implies that the field propagates in radial direction and, thus, the Hankel functions give the correct radial dependency. Moreover, if only interested in waves propagating away from the origin, the Hankel functions of the second kind  $H_m^{(2)}(k_\rho \rho)$  are appropriate. The problem is bounded in  $z$ -direction, which can be modeled by the trigonometric functions (2.133). The field has to be periodic in  $\phi$ -direction. This is fulfilled by the trigonometric functions in (2.135), provided the index  $m$  for the angular dependency is an integer. In summary, a wave-function for waves propagating away

from the origin in the radial parallel plate waveguide Fig. 2.5 is of the form

$$H_m^{(2)}(k_\rho \rho) \begin{Bmatrix} \cos(m\phi) \\ \sin(m\phi) \end{Bmatrix} [A \cos(k_z z) + B \sin(k_z z)], \quad (2.140)$$

where both  $\cos(m\phi)$  and  $\sin(m\phi)$  are possible (for  $m = 0$  only the  $\cos(m\phi)$ ). The index  $m$  is an integer. The boundary conditions define the constants  $A$  and  $B$ . The  $\text{TM}^z$ - and  $\text{TE}^z$ -solutions are derived in the following subsections.

### TE<sup>z</sup>-Modes

Transverse electric modes are constructed from  $H_z$ , which has to fulfill the boundary condition (2.102) on PEC. For the radial parallel plate waveguide this is

$$\left. \frac{\partial H_z}{\partial z} \right|_{z=0,h} = 0. \quad (2.141)$$

Assuming a solution of  $H_z$  in form of (2.140) yields the  $z$ -derivative

$$\frac{\partial H_z}{\partial z} = k_z H_m^{(2)}(k_\rho \rho) \begin{Bmatrix} \cos(m\phi) \\ \sin(m\phi) \end{Bmatrix} [-A \sin(k_z z) + B \cos(k_z z)]. \quad (2.142)$$

To fulfill the boundary condition, the wavenumber is specified by

$$k_z = \frac{n\pi}{h} \quad n = 1, 2, \dots, \quad (2.143)$$

and the constant  $A$  has to vanish. The possible field solutions / modes are consequently given by

$$H_z^{mn}(\rho, \phi, z) = a_{mn} H_m^{(2)}(k_\rho \rho) \begin{Bmatrix} \cos(m\phi) \\ \sin(m\phi) \end{Bmatrix} \sin\left(\frac{n\pi}{h} z\right). \quad (2.144)$$

The remaining field components can be obtained, according to [Jin15], from

$$E_\rho = -\frac{j\omega\mu}{k_\rho^2} \frac{1}{\rho} \frac{\partial H_z}{\partial \phi}, \quad (2.145)$$

$$E_\phi = \frac{j\omega\mu}{k_\rho^2} \frac{\partial H_z}{\partial \rho}, \quad (2.146)$$

$$H_\rho = -\frac{jk_z}{k_\rho^2} \frac{\partial^2 H_z}{\partial z \partial \rho}, \quad (2.147)$$

$$H_\phi = -\frac{jk_z}{k_\rho^2} \frac{\partial^2 H_z}{\partial z \partial \phi}. \quad (2.148)$$

### TM<sup>z</sup>-Modes

Transverse magnetic modes, with respect to the  $z$ -direction, are constructed from  $E_z$ . The tangential electric field components have to vanish on PEC. Consequently, the boundary conditions for the radial parallel plate waveguide are

$$E_\rho|_{z=0,h} = 0, \quad E_\phi|_{z=0,h} = 0. \quad (2.149)$$

The electric field components in radial and axial direction follow according to [Jin15] from

$$E_\rho = -\frac{jk_z}{k_\rho^2} \frac{\partial^2 E_z}{\partial z \partial \rho}, \quad (2.150)$$

$$E_\phi = -\frac{jk_z}{k_\rho^2} \frac{1}{\rho} \frac{\partial^2 E_z}{\partial z \partial \phi}. \quad (2.151)$$

Assuming an  $E_z^{mn}$ -dependency in form of the (2.140), it follows

$$E_\rho^{mn} = -k_z a_{mn} \frac{dH_m^{(2)}(k_\rho \rho)}{d\rho} \begin{Bmatrix} \cos(m\phi) \\ \sin(m\phi) \end{Bmatrix} [-A \sin(k_z z) + B \cos(k_z z)], \quad (2.152)$$

$$E_\phi^{mn} = -mk_z a_{mn} H_m^{(2)}(k_\rho \rho) \begin{Bmatrix} -\sin(m\phi) \\ \cos(m\phi) \end{Bmatrix} [-A \sin(k_z z) + B \cos(k_z z)], \quad (2.153)$$

where the partial derivatives in  $\rho$ - and  $\phi$ -direction do not change the dependency in  $z$ -direction. Moreover,  $E_\rho$  and  $E_\phi$  have the same  $z$ -dependency. To enforce the boundary conditions (2.149) the constant  $B$  has to vanish and  $k_z$  is equal to that of the TE-modes in (2.143). The possible modes are consequently given by

$$E_z^{mn}(\rho, \phi, z) = a_{mn} H_m^{(2)}(k_\rho \rho) \begin{Bmatrix} \cos(m\phi) \\ \sin(m\phi) \end{Bmatrix} \cos\left(\frac{n\pi}{h} z\right), \quad (2.154)$$

while the index  $n$  is now  $n = 0, 1, 2, \dots$ . In contrast to the TE-solution, the index  $n = 0$  leads to a non-vanishing field. The remaining magnetic field components follow from [Jin15]

$$H_\rho = \frac{j\omega \epsilon}{k_\rho^2} \frac{\partial E_z}{\partial \phi}, \quad H_\phi = -\frac{j\omega \epsilon}{k_\rho^2} \frac{\partial E_z}{\partial \rho}. \quad (2.155)$$

From the dispersion relation (2.131) follows the wavenumber in radial (or propagation) direction as

$$k_\rho = \sqrt{k^2 - k_z^2} = \sqrt{k^2 - (n\pi/h)^2}. \quad (2.156)$$

As we are interested only in propagating waves,  $k_\rho$  has to be positive real. Consequently,  $k^2 > (n\pi/h)^2$ . From this follows the cut-off wavelength as

$$\lambda_{c,n} = \frac{2h}{n}, \quad (2.157)$$

and the cut-off frequency as

$$f_{c,n} = \frac{n}{2h\sqrt{\epsilon\mu}}. \quad (2.158)$$

Modes with index  $n = 0$  have no cut-off frequency. For heights of the radial parallel plate waveguide of half a wavelength, this is  $h < \lambda/2$ , the next higher-order mode has a cut-off frequency of  $f_{c,n} > f$ . Consequently, only the mode with index  $n = 0$  is propagating and it is a TM-mode as the field of the TE-mode would vanish.

### **TM<sub>m0</sub><sup>z</sup>-Mode**

The TM<sub>m0</sub><sup>z</sup> has no cut-off frequency and the wavenumber in radial direction is  $k_\rho = k$ . The field components are

$$E_z^{m0} = a_{m0} H_m^{(2)}(k\rho) \begin{Bmatrix} \cos(m\phi) \\ \sin(m\phi) \end{Bmatrix}, \quad (2.159)$$

$$H_\rho^{m0} = \frac{j\omega\epsilon}{k_\rho^2} m a_{m0} H_m^{(2)}(k\rho) \begin{Bmatrix} -\sin(m\phi) \\ \cos(m\phi) \end{Bmatrix}, \quad (2.160)$$

$$H_\phi^{m0} = -\frac{j\omega\epsilon}{k_\rho^2} a_{m0} \frac{dH_m^{(2)}(k\rho)}{d\rho} \begin{Bmatrix} \cos(m\phi) \\ \sin(m\phi) \end{Bmatrix}, \quad (2.161)$$

the remaining vector field components vanish. The field is uniform in  $z$ -direction.

## **2.5 Electromagnetic Waves in Plasma**

When matter is a plasma, it is in an fully ionized state. To achieve this state, it has to be heated to or above the ionization energy of the atoms — allowing electrons to separate from ions. Viewed from the outside, the plasma can be seen as a neutral gas consisting of three elements: electrons, ions, and neutral atoms (the background). The electrons and ions in a plasma interact with electromagnetic fields and, as a consequence, electromagnetic fields influence or are influenced by the properties of the plasma (e.g., electron density, temperature, etc.). The Debye length [HG13]

$$\lambda_D = \sqrt{\frac{\epsilon_0 k_B T_e}{q_e^2 n_e}} \quad (2.162)$$

is an indicator if the macroscopic treatment of the charge distributions is valid or if their discrete nature has to be considered [HG13]. The former is the case if  $\lambda \gg \lambda_D$ . The Debye length depends on the electron density  $n_e$  and temperature  $T_e$ . For nuclear fusion plasmas, the Debye length is about  $\lambda_D \approx 10^{-5}$  m [HG13].

As a consequence of the previous considerations, the interaction of millimeter-waves with the plasma can be treated from a macroscopic point of view. There is no need to consider the discrete nature of the charge distribution. Thus, the electromagnetic fields in a plasma (with  $\lambda \gg \lambda_D$ ) are governed by Maxwell's Equations (2.2) to (2.5). The plasma is modeled by the charge density [HG13]

$$\rho_e(\mathbf{r}, t) = -en_e, \quad (2.163)$$

with the electron density  $n_e(\mathbf{r}, t)$ , and the elementary charge  $e$ . The electric current density follows from the mean electron velocity  $\mathbf{v}_e(\mathbf{r}, t)$  as [HG13]

$$\mathcal{J}_p(\mathbf{r}, t) = \rho_e \mathbf{v}_e = -en_e \mathbf{v}_e. \quad (2.164)$$

The contributions of ions can be neglected for high frequencies due to their larger mass [HG13]. The electron motion in a static magnetic field (required for plasma confinement) follows Newton's motion equation and the Coulomb and Lorentz force acting on the electron as [WC74; ZB90]

$$\frac{\partial \mathbf{v}_e}{\partial t} = -\frac{e}{m_e} (\mathcal{E} + \mathbf{v}_e \times \mathbf{B}_0) - \mathbf{v}_e \nu, \quad (2.165)$$

with the electron mass  $m_e$  and the mean collision frequency  $\nu$ . The total electric current of the plasma is in part due to the electric displacement and the electric current due to the electron motion as [ZB90]

$$\frac{\partial \mathcal{D}}{\partial t} = \epsilon_0 \frac{\partial \mathcal{E}}{\partial t} + \mathcal{J}_p. \quad (2.166)$$

In the following, only time-harmonic fields are considered. The electron density  $n_e(x)$  varies only in  $x$ -direction and the static magnetic field  $\mathbf{B}_0 = B_0 \mathbf{u}_z$  is aligned in  $z$ -direction. Further, the mean collision frequency  $\nu$  is assumed to be very small and, thus, can be neglected. From (2.165) and (2.166) follows the dielectric tensor  $\bar{\epsilon}$  of the plasma according to [ZB90] as

$$\bar{\epsilon} = \begin{pmatrix} \epsilon_1 & +j\epsilon_2 & 0 \\ -j\epsilon_2 & \epsilon_1 & 0 \\ 0 & 0 & \epsilon_3 \end{pmatrix}, \quad (2.167)$$

with

$$\varepsilon_1 = \varepsilon_0 \left[ 1 + \frac{\left( \frac{\omega_p}{\omega} \right)^2}{\left( \frac{\omega_c}{\omega} \right)^2 - 1} \right], \quad \varepsilon_2 = \varepsilon_0 \frac{\frac{\omega_c}{\omega} \left( \frac{\omega_p}{\omega} \right)^2}{\left( \frac{\omega_c}{\omega} \right)^2 - 1}, \quad \varepsilon_3 = \varepsilon_0 \left[ 1 - \left( \frac{\omega_p}{\omega} \right)^2 \right], \quad (2.168)$$

the plasma frequency

$$\omega_p = e \sqrt{\frac{n_e}{\varepsilon_0 m_e}}, \quad (2.169)$$

and the electron cyclotron frequency

$$\omega_c = \frac{B_0 e}{m_e}. \quad (2.170)$$

The electric current density (2.164) is embedded in Maxwell's equation (2.10) by means of the dielectric tensor (2.167). From (2.25) and (2.26), with  $\mu = \mu_0$  follows the curl-curl-equation in plasma as

$$\nabla \times (\nabla \times E) - \omega^2 \mu_0 \bar{\epsilon} E = 0. \quad (2.171)$$

Assuming a plane wave of the form  $E = e^{-jk\cdot r}$ , the curl-curl-equation yields each component of the electric field as [ZB90]

$$\begin{pmatrix} k_y^2 + k_z^2 - \omega^2 \mu_0 \varepsilon_1 & -k_x k_y - j\omega^2 \mu_0 \varepsilon_2 & -k_x k_z \\ -k_x k_y + j\omega^2 \mu_0 \varepsilon_2 & k_z^2 + k_x^2 - \omega^2 \mu_0 \varepsilon_1 & -k_y k_z \\ -k_x k_z & -k_y k_z & k_x^2 + k_y^2 - \omega^2 \mu_0 \varepsilon_3 \end{pmatrix} \begin{pmatrix} E_x \\ E_y \\ E_z \end{pmatrix} = 0. \quad (2.172)$$

If the wave propagates in a plane perpendicular to the static magnetic field  $\mathbf{k} \perp \mathbf{B}_0$  with  $k_z = 0$ , (2.172) simplifies to

$$\begin{pmatrix} k_y^2 + -\omega^2 \mu_0 \varepsilon_1 & -k_x k_y - j\omega^2 \mu_0 \varepsilon_2 & 0 \\ -k_x k_y + j\omega^2 \mu_0 \varepsilon_2 & k_x^2 - \omega^2 \mu_0 \varepsilon_1 & 0 \\ 0 & 0 & k_x^2 + k_y^2 - \omega^2 \mu_0 \varepsilon_3 \end{pmatrix} \begin{pmatrix} E_x \\ E_y \\ E_z \end{pmatrix} = 0. \quad (2.173)$$

In a similar way, the curl-curl-equation simplifies for a plane wave propagation parallel to the static magnetic field  $\mathbf{k} \parallel \mathbf{B}_0$  with  $k_x = k_y = 0$ .

The plasma configuration of the previous derivation is uniform, as neither the electron density  $n$  nor the magnetic field  $\mathbf{B}_0$  vary in space. In a laboratory frame, however, the spatial variation of the plasma or the scale length  $L$  of the plasma parameters has to be large compared to the wavelength such that the previous considerations still lead to meaningful results [HG13]. At millimeter-wave frequencies, the scale length or spatial variation of the laboratory plasma is larger compared to the wavelength [HG13].

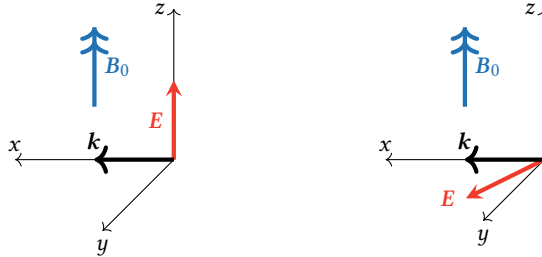


**Fig. 2.6:** Electromagnetic wave propagation (in  $x$ -direction) perpendicular to that static magnetic field  $B_0$ . Left: O-mode propagation with the electric field *parallel* to the static magnetic field. Right: X-mode propagation with the electric field *perpendicular* to the static magnetic field.

In the following, only two modes of wave propagation in magnetized plasma are considered, where the wave propagates in the plane perpendicular to the magnetic field  $\mathbf{k} \perp \mathbf{B}_0$  with the simplified wave equation (2.173). Wave propagation parallel to the magnetic field is not important for the topic of this thesis.

For the wave propagation perpendicular to the static magnetic field  $B_0$ , two cases need to be distinguished. Either, the electric field polarization is parallel to the static magnetic field (i.e.,  $E_x = E_y = 0$ ) or the electric field polarization is perpendicular to  $B_0$  (i.e.,  $E_z = 0$ ), see Fig. 2.6. The former case is denoted as the ordinary mode (O-mode), the latter case is denoted as the extraordinary mode (X-mode). Both modes are described in the following sections.

### 2.5.1 Ordinary Mode (O-Mode)

In the ordinary mode (O-mode), the wave enters the plasma in the plane  $\mathbf{k} \perp \mathbf{B}_0$  with the electric field being  $z$ -polarized, see Fig. 2.6. This is,  $E \parallel \mathbf{B}_0$  with  $E_x = E_y = 0$ . For a straight propagation along the  $x$ -axis, the dispersion relation follows from (2.173) as [WC74]

$$k_x^2 = \omega^2 \mu_0 \epsilon_0 \left( 1 - \left( \frac{\omega_p}{\omega} \right)^2 \right) = k_0^2 \left( 1 - \left( \frac{\omega_p}{\omega} \right)^2 \right). \quad (2.174)$$

If the wavenumber in propagation direction  $k_x$  is zero, a cut-off occurs. For normal incidence in O-mode, the cut-off frequency occurs for  $\omega = \omega_p$  and follows from (2.169) as

$$f_{c,o} = \frac{e}{2\pi} \sqrt{\frac{n_e}{\epsilon_0 m_e}}. \quad (2.175)$$

The cut-off frequency increases for denser plasmas. If the plasma density is increasing along the  $x$ -axis, higher frequencies can probe deeper into the plasma. Note that the static magnetic field  $B_0$  has no influence on the wave propagation in O-mode.

### 2.5.2 Extraordinary Mode (X-Mode)

In the extraordinary mode (X-mode), the wave enters the plasma in the plane  $\mathbf{k} \perp \mathbf{B}_0$  with the electric field being  $xy$ -polarized, see Fig. 2.6. This is,  $E \perp \mathbf{B}_0$  with  $E_z = 0$ . Wave propagation is governed by the first two components of (2.173). Wave propagation is assumed in the  $x$ -direction. Consequently, the wave has transverse as well as longitudinal components. For normal incidence into the plasma, the dispersion relation is [HG13]

$$k_x^2 = k_0^2 \frac{(\omega^2 - \omega_L^2)(\omega^2 - \omega_R^2)}{\omega^2 (\omega^2 - \omega_{uh}^2)}, \quad (2.176)$$

with the left-hand and right-hand cut-off frequencies [HG13]

$$\omega_L = 0.5 \left( -\omega_c + \sqrt{\omega_c^2 + 4\omega_p^2} \right) \leq \omega_p, \quad (2.177)$$

$$\omega_R = 0.5 \left( \omega_c + \sqrt{\omega_c^2 + 4\omega_p^2} \right) \geq \omega_p, \quad (2.178)$$

and the upper-hybrid resonance at [HG13]

$$\omega_{uh}^2 = \omega_p^2 + \omega_c^2. \quad (2.179)$$

The right-hand cut-off occurs at frequencies above or equal to the plasma frequency. Thus, the cut-off in X-mode occurs at lower densities as compared to the O-mode.

## 3 Doppler Reflectometry with Phased Array Antennas

Doppler reflectometry enables the measurement of plasma turbulences, see Section 1.2, with a high spatial and temporal resolution. The measurement setup consists of a front-end that radiates and steers a well defined Gaussian beam, a heterodyne Doppler reflectometer as source and for data acquisition [Trö08], and hollow waveguides that connect the reflectometer with the front-end. The hollow waveguides also include low-reflectivity vacuum windows that suppress reflections at the waveguide interface into the vessel [KHS+18].

In the following section, the principle of Doppler reflectometry for the measurement of nuclear fusion plasma turbulence is described. As the topic of this thesis is a phased array antenna that shapes and steers the desired Gaussian beam, the concept of phased array antennas is introduced subsequently. The last section of this chapter describes the procedure to obtain the aperture field distribution that leads to the desired (Gaussian) beam. The influence of aperture size as well as of amplitude and phase errors on the Gaussian beam is evaluated.

### 3.1 Doppler Reflectometry of Plasma Turbulence

#### 3.1.1 Principle of Doppler Reflectometry

To measure plasma turbulences, a microwave beam is launched into the plasma (in either X-mode or O-mode polarization, see Section 2.5) at a tilt angle  $\Theta_t$  with respect to the cut-off layer normal or the plasma density gradient  $\nabla n_e$  [CPHt10]. The beam propagates into the plasma and gets refracted due to the increasing plasma density. Thus, the wavenumber in direction of the plasma density gradient is decreasing, see Fig. 3.1. If no turbulence is present, the beam is reflected at the cut-off layer, while the position of the cut-off layer is dependent on the polarization mode of the beam, see Section 2.5.

Plasma turbulences result in a perturbation of the plasma density and, thus, a fluctuation of the cut-off layer. These density fluctuations can be modeled by the superposition of small sinusoidal corrugations of the cut-off layer, see Fig. 3.1. The physical length of a perturbation is denoted as  $\Lambda_\perp$  with the turbulence wavenumber  $k_\perp = 2\pi/\Lambda_\perp$ . By superposition, the whole density fluctuations can be represented by a turbulence wavenumber spectrum.

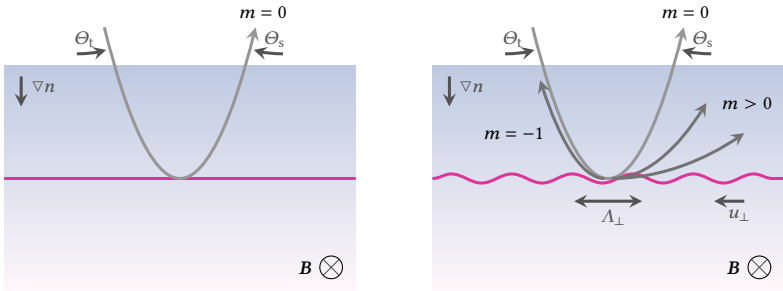


**Fig. 3.1:** Sketch of the beam alignment and reflection/scattering of the beam at the turbulent cut-off layer. Left: Cut-off layer without turbulences. The incident beam gets refracted in the plasma and eventually reflected; Right: Turbulent cut-off layer. The incident beam is additionally Bragg scattered.

If turbulences are present and the cut-off layer is corrugated, the beam gets scattered according to the Bragg diffraction equation [CSK+04]

$$mk_\perp = k_0 (\sin \Theta_t - \sin \Theta_s), \quad (3.1)$$

with the scattered angle  $\Theta_s$  and the Bragg scattering order  $m$ . In the monostatic arrangement, where the beam is transmitted and received by the same antenna, the  $m = -1$  order Bragg scattered beam is selected and received by the antenna. In this case, the Bragg condition is [CSK+04]

$$k_\perp = 2k_0 \sin \Theta_t. \quad (3.2)$$

The waves with positive scattering orders  $m \geq 0$  propagate away from the antenna, see Fig. 3.1. For small tilt angles  $\Theta_t$ , however, an additional scattering order  $m$  (especially the strong zeroth order/direct reflection) might be picked up by the monostatic antenna setup, if the beam is not well collimated or has strong side-lobes [CSK+04; HH04].

Within the plasma, the effective wavelength of the probing beam and the effective tilt angle are different from the ideal values in vacuum due to the modified permittivity. In theory, both effects cancel each other in the first order and keep the probed turbulence wavenumber  $k_\perp$  unchanged [HHB+01]. In practice, however, each discharge scenario with the corresponding plasma density profile that is obtained experimentally, is simulated using a beam tracing code (e.g., TORBEAM [PPP01]). From these simulations, the actual measurement location and probed turbulence wavenumber  $k_\perp$  is obtained [CPHt10; HHT+04; LCG+17]. The backscattered power is assumed proportional to the turbulence level at the probed turbulence wavenumber  $k_\perp$ , which is valid for small turbulence amplitudes [CPHt10; LCG+17]. To get an actual measure of

the scattering efficiency for varying tilt angles, full-wave simulations are necessary that also consider the scattering contributions along the beam path [HHT+04; LCG+17].

### 3.1.2 Turbulence Wavenumber Spectrum

The tilted arrangement of the beam towards the cut-off layer normal in the plasma enables the selection of a certain turbulence length  $\Lambda_{\perp}$ , where the antenna arrangement (transmitted and received beam) is sensitive to a certain turbulence wavenumber  $k_{\perp}$ , only. This wavenumber filter is dependent on the tilt angle of the beam according to the Bragg condition (3.2). Sweeping the tilt angle at a fixed frequency leads to a scattering process at equal plasma densities with a roughly constant radial location in the plasma torus. Hence, it enables the measurement of the turbulence wavenumber spectrum  $S(k_{\perp})$  at a given radial position. If, in addition to the tilt angle, also the frequency of the radiated beam is swept/stepped, the turbulence wavenumber spectrum is measured for different radial positions in the plasma. Thus, Doppler reflectometry enables the measurement of turbulence spectra for a turbulence wavenumber range limited by the maximum steering angle  $\Theta_t$  of the beam and at radial positions given by the probing frequency and plasma density.

The localization of the scattering process is possible due to the strong intensity of the incident field at the cut-off layer, which amplifies the scattering process [HHT+04]. The spectral resolution  $\Delta k_{\perp}$  of the wavenumber spectrum is a measure of how well the individual turbulence wavenumbers are separated in the turbulence wavenumber spectrum. The scattering integrals, two subsequent Fourier transforms evaluating the overlapping shape and field intensity of incident and scattered beams, can be evaluated analytically for, e.g., the fundamental mode Gaussian beam [HM78]. The fundamental Gaussian beam, in addition, leads to a minimum product of beam half-width in the spatial and in the wavenumber domain. Hence, it is optimal for simultaneously good localization of the scattering process and high spectral resolution [HM78].

In the ideal case, where a wave with a plane phase-front is scattered from a straight and corrugated cut-off layer, the spectral resolution increases with the illuminated spot-size at the expense of spatial localization capabilities. In terms of a Gaussian beam with the focal plane coinciding with the cut-off layer, the spectral resolution depends on the beam waist radius  $w$  according to [HHB+01; HM78]

$$\Delta k_{\perp} = \sqrt{2} \frac{2}{w}. \quad (3.3)$$

Note that this relation is only valid for small tilt angles  $\Theta_t$ , where the effect of the projection of the beam-spot onto the cut-off layer can be neglected [HHB+01]. For a curved cut-off layer, as it is the case for the confined nuclear fusion plasma, the spectral resolution is coarser compared to a straight cut-off layer. The curved cut-off layer can

be considered by an effective radius of curvature [LNIM01]

$$\rho_{\text{eff}} = \frac{R_c R_b}{R_c + R_b}, \quad (3.4)$$

with the radius of curvature  $R_c$  of the the cut-off layer and the radius of curvature  $R_b$  of the incident beam (no plane phase-front). If the beam waist of the Gaussian beam is coinciding with the cut-off layer, the beam radius of curvature is  $R_b \rightarrow \infty$  and the effective radius of curvature reduces to the plasma cut-off radius of curvature  $\rho_{\text{eff}} \rightarrow R_c$ . The spectral resolution of the curved cut-off layer and phase front follows from [HHB+01; LNIM01]

$$\Delta k_{\perp} = \sqrt{2} \frac{2}{w} \sqrt{1 + \left( \frac{w^2 k_0}{\rho_{\text{eff}}} \right)^2}. \quad (3.5)$$

The optimum beam size can be obtained by setting the derivative of (3.5) to zero, yielding [Hap10]

$$w_{\text{opt}} = \sqrt{\frac{\rho_{\text{eff}}}{k_0}}. \quad (3.6)$$

As already stated, the actual scattering volume and position of a certain beam can be obtained by beam tracing simulations [CPHt10; HHT+04; LCG+17]. In the framework of the Helmholtz Virtual Institute on “Plasma Dynamical Processes and Turbulence Studies using Advanced Microwave Diagnostics”, the optimum beam size was communicated by Garrard Conway and Tim Happel to be

$$w_{\text{opt}} = 7\lambda_0 \quad (3.7)$$

for the dedicated position and view of the phased array antenna in ASDEX Upgrade tokamak. The focal plane may lie in a range from 200 mm to 400 mm apart from the antenna aperture. The dedicated beam shape is a fundamental mode Gaussian beam as a matter of practicality. The polarization of the antenna is in X-mode with the electric field being perpendicular to the static magnetic field. The steering plane is also perpendicular to the magnetic field in order to maximize the sensitivity towards the perpendicular turbulence wavenumber (minimize contribution of the parallel-to- $B$  components) [CPHt10].

### 3.1.3 Turbulence Velocity

If the fluctuating cut-off layer moves with a mean velocity  $v_f$ , the scattered beam is Doppler-shifted. The induced Doppler shift follows from the mean velocity of the density fluctuation as [CPHt10]

$$\omega_D = 2\pi f_D = v_f \cdot \mathbf{k} = v_{\perp} k_{\perp} + v_{\parallel} k_{\parallel} + v_r k_r, \quad (3.8)$$

where the actual movement is decomposed into a radial component  $v_r$ , a component parallel to the static magnetic field  $v_{\parallel}$  and a component perpendicular to the static magnetic field  $v_{\perp}$  with the corresponding components of the probed turbulence wavenumber  $k_r$ ,  $k_{\parallel}$ , and  $k_{\perp}$ . The parallel turbulence wavenumber is considered much smaller than its perpendicular counterpart, such that  $k_{\parallel} \ll k_{\perp}$ . In addition, the radial turbulence movement is centered around the cut-off layer with a balanced inward and outward movement, where the radial component broadens the turbulence spectrum but does not contribute to the Doppler shift [CPHt10]. Consequently, the Doppler shift of the backscatter beam is

$$\omega_D \approx v_{\perp} k_{\perp}. \quad (3.9)$$

The movement of the turbulence is in part due to gyro-centered motion of the electrons relative to the antenna  $v_{E \times B}$  and the phase velocity of the turbulence  $v_p$  in this stream [CPHt10]

$$v_{\perp} = v_{E \times B} + v_p. \quad (3.10)$$

If the phase velocity is small compared to the mean electron velocity, i.e.,  $v_p \ll v_{E \times B}$ , the Doppler shift reveals the  $E_r \times B$ -velocity. From  $v_{E \times B}$  and the knowledge of the magnetic field  $B$ , the radial electric field  $E_r$  can be estimated [CPHt10; Hap10; LCG+17]. Fluctuations in  $E_r$  appear as a fluctuating Doppler shift and, thus, allow the measurement of  $E_r$  flow oscillations such as geodesic acoustic modes and zonal flows [CPHt10].

## 3.2 Phased Array Antennas

Antennas transform the fields of guided waves into fields that propagate in free-space. The radiated field distribution can be shaped by the source distribution on the antenna. The larger the antenna is, the better the radiated field can be focused towards a certain angular direction, whereas small antennas do commonly radiate in a broad angular range. By combining several small antennas in an array, however, their overall radiation pattern can synthesize that of a large antenna. This is, by sampling a continuous source distribution, array antennas can approximate arbitrary aperture field distributions. Here, the array elements are excited by a relative amplitude and phase. Dependent on the complex weights  $a_n$ , the position of the radiating elements  $\mathbf{r}'_n$ , and their individual radiation patterns  $f_n(\Theta, \Phi)$ , the radiated fields superpose and form an overall array radiation characteristic. Here,  $\mathbf{r}$  is the observation point, and  $n \in \mathbb{R}$  denotes the element number in the array. By an appropriate phasing of the individual elements, the radiated beam can be focused and steered [Bal05; Mai05].

In the following, a linear array with the array elements placed on the  $x$ -axis of the rectangular coordinate system is considered. The spacing between the individual

elements is  $d_x$ . With the element index  $n$ , the element position is given by

$$\mathbf{r}'_n = n d_x \mathbf{u}_x, \quad (3.11)$$

where the element with index  $n = 0$  is the phase reference for all other elements. The elements are fed simultaneously (coherent waves) with a phasor represented by the complex element factor  $a_n = |a_n| e^{j\varphi_n}$ . The electric field at an observation point  $\mathbf{r}$  follows from the weighted superposition of the radiated electric field of the individual array elements  $f_n(\Theta, \Phi)$  in the direction towards the observation point according to [Mai05]

$$\mathbf{E}(\mathbf{r}) = \sum_n f_n(\Theta, \Phi) a_n \frac{e^{-jk|\mathbf{r}-\mathbf{r}'_n|}}{|\mathbf{r}-\mathbf{r}'_n|}. \quad (3.12)$$

The numerator  $e^{-jk|\mathbf{r}-\mathbf{r}'_n|}$  represents the phase variation and the denominator  $|\mathbf{r}-\mathbf{r}'_n|$  the amplitude variation from the source to the observation point. The previous expression is valid only in the far-field of the individual array elements.

If the radiation pattern  $f_n$  of the individual elements is obtained in the array environment, it is called embedded element pattern. In contrast to the isolated element pattern (radiation element placed in a free-space environment), the embedded element pattern includes electromagnetic effects concerning the array radiation [Mai05]. This is, the embedded element pattern includes mutual coupling effects between the array elements. Mutual coupling is the effect that radiated fields of a single element in an array are received and eventually re-radiated by neighboring array elements. This influences the overall radiation characteristic of the individual elements and requires the radiation patterns of the array elements to be obtained in the array environment.

If the distance between the individual elements is small compared to the distance of the array to the observation point  $d_x \ll |\mathbf{r} - \mathbf{r}'_n|$  (i.e., the array is small compared to the distance to the observation point), the scalar array factor can be simplified. This is, the distance from each element to the observation point  $r_n$  can be approximated by [Mai05]

$$r_n = |\mathbf{r} - \mathbf{r}'_n| \approx r_0 - \mathbf{r}'_n \cdot \mathbf{u}_r, \quad (3.13)$$

with the distance  $r_0$  from the array origin to the observation point and the unit vector  $\mathbf{u}_r = (\mathbf{r} - \mathbf{r}'_0) / |\mathbf{r} - \mathbf{r}'_0|$  pointing into the direction of the observation point from the array origin. With  $\mathbf{r}'_n \cdot \mathbf{u}_r \ll r_0$ , the amplitude dependence on the element position can be approximated by  $r \approx r_0$  and, consequently, the radiated field from the array antenna follows as [Mai05]

$$\mathbf{E}(\mathbf{r}) = \frac{e^{-jkr_0}}{r_0} \sum_n f_n(\Theta, \Phi) a_n e^{jkr'_n \cdot \mathbf{u}_r}. \quad (3.14)$$

If the element patterns of all array elements are equal, the array radiation pattern may be reformulated to [Mai05]

$$E(\mathbf{r}) = \frac{e^{-jk\mathbf{r}_0}}{r_0} f(\Theta, \Phi) \sum_n a_n e^{jk\mathbf{r}'_n \cdot \mathbf{u}_r} = \frac{e^{-jk\mathbf{r}_0}}{r_0} f(\Theta, \Phi) F(\mathbf{u}_r). \quad (3.15)$$

with the scalar array factor  $F(\mathbf{u}_r) = \sum_n a_n e^{jk\mathbf{r}'_n \cdot \mathbf{u}_r}$ . For a larger number of elements, the array factor commonly dominates the element pattern. Similarly, if the element pattern is relatively broad (element radiates equally in all directions), the overall radiation characteristic is predominantly determined by the array factor.

Steering of the radiated field to a desired direction is possible by choosing the complex element weights  $a_n$  such that the phase terms  $e^{j\varphi_n}$  of the weights cancel those of the geometrical phase variation  $e^{jk\mathbf{r}'_n \cdot \mathbf{u}_r}$  in the scalar array factor  $F(\mathbf{u}_r)$ . This maximizes the scalar array factor in the desired direction [Mai05]. If the vector  $\mathbf{u}_r$  (in the  $xz$ -plane) is specified by an angle  $\Theta$  between the  $z$ -axis and the vector toward the observation point  $\mathbf{u}_r$ , the scalar array factor can be denoted as

$$F(\Theta) = \sum_n a_n e^{jknd_x \cos(90^\circ - \Theta)} = \sum_n a_n e^{jknd_x \sin \Theta}. \quad (3.16)$$

For steering the beam towards  $\Theta_p$ , the phase of each element weight  $a_n$  has to be

$$\varphi_n = -knd_x \sin \Theta_p \quad (3.17)$$

in order to cancel those of the geometrical configuration/phase variation in (3.16). In turn, the steering direction can be deduced from the phase between two adjacent array elements  $\Delta\varphi = \varphi_n - \varphi_{n+1}$  as

$$\Theta_p = \arcsin\left(\frac{\Delta\varphi}{kd_x}\right). \quad (3.18)$$

Consequently, if the phase-offset  $\Delta\varphi$  between each element is equal, the beam is steered towards the respective direction. The phase-offset can be controlled by a phase shifter allowing the beam to be steered/scanned while the array geometry does not change.

Denoting the argument of (3.18) as  $u = \frac{\Delta\varphi}{kd_x}$ , the wavenumber  $k_z$  in  $z$ -direction (i.e., away from the array) follows from the dispersion relation and the steering angle as

$$k_z = k \cos \Theta_p = k \cos (\arcsin u) = k \sqrt{1 - \sin^2 (\arcsin (u))} = k \sqrt{1 - u^2}. \quad (3.19)$$

Only arguments  $u$  in the range from  $-1$  to  $1$  lead to a real-valued  $k_z$  and, thus, wave propagation away from the array. Hence,  $|u| \leq 1$  specifies the visible region of the array configuration. As a consequence, the progressive phase may be in the range

$$-kd_x \leq \Delta\varphi \leq kd_x. \quad (3.20)$$

For  $d_x \leq \lambda/2$ , this leads to  $|\Delta\varphi| \leq \pi$ , which is unique. In contrast, an element spacing of  $d_x > \lambda/2$  leads to  $|\Delta\varphi| > \pi$  and, thus, a repetition of the array factor. Depending on the steering angle, other maxima apart from the desired main beam occur within the visible region of the array factor. These other maxima are called grating-lobes as they are dependent on the spacing of the array elements (i.e., the geometrical configuration of the array). To ensure that no grating-lobe is within the visible range for a given maximum steering angle  $\Theta_{p,\max}$ , the element spacing has to be small enough to fulfill the condition [Kar05; Mai07]

$$d_x \leq \frac{\lambda}{1 + |\sin \Theta_{p,\max}|}. \quad (3.21)$$

If the full angular range needs to be covered, the element spacing has to be  $d_x \leq \lambda/2$ .

Due to the finite width of an array antenna and due to the fact that it samples a continuous aperture distribution, errors toward the desired aperture field occur. These errors lead to so-called side-lobes next to the main-beam. However, the intensity of the side-lobes can be optimized by the array taper – similar to window functions in the Fourier transform. There are numerous procedures to shape and synthesize the radiated field. These methods try to optimize the far-field beam-width, the side-lobe-level, and/or the aperture efficiency of the array antenna. In principle, these procedures optimize/synthesize the far-field radiation of the array antenna [Mai05; Mai07]. None of these synthesis procedures may be applied to shape a desired beam in the near vicinity of the array antenna. Nevertheless, shaping a desired beam can be accomplished by sampling its transverse field distribution at the position of the array elements. In this work, Section 3.3 covers the synthesis/shaping of a defined Gaussian beam by sampling its transverse field.

The array taper of an array antenna is realized by a feed network that provides each individual (radiating) array element with the required complex weight  $a_n$ . There are two prevailing types of feed networks: the parallel feed network and the serial feed network. A parallel feed divides the input wave into several branches, whereas a serial feed taps-off the required amplitude from a main-line and directs it towards the individual radiating elements.

The type of feed network that is suitable for a problem depends on the circumstances and goals. If efficiency of the phased array antenna is the main goal, a parallel feed outperforms the serial feed. In this case, each element has its dedicated phase shifter and the connecting waveguide can be relatively short. In contrast, with a serial feed network the progressive phase to steer the beam can be realized with a single actuator (equal phase offset in-between two adjacent elements). The reduced complexity for the phase control in a series feed network comes at the expense of a reduced efficiency, as the wave travels from the input trough all phase shifters to arrive at the last element. As a consequence, the losses scale with the number of phase shifters or radiating elements. These issues are even more pronounced for phased array antennas with a large number

of elements and when the phase shifter and the connecting waveguides are the main contributors of loss. In this case, one can either optimize for efficiency and take a parallel feed network or minimize the number of actuators and decide for a series feed network.

The phase control of the array antenna can either be active or passive. An actively steered phased array antenna is controlled by actuators that control the phase of each element. Passive phased array antennas can steer the beam by sweeping the frequency due to varying waveguide lengths towards the radiating elements.

For this thesis, focus is on an actively steered phased array antenna supporting a frequency-invariant steering angle. The number of actuators should be minimal due to the harsh environment inside the vessel. Thus, a serial feed design is envisaged.

### 3.3 Gaussian Beam Synthesis from a Phased Array Antenna

With the plane-wave spectrum representation from Section 2.2, any source-free electromagnetic field can be described by the transverse components of either the electric or the magnetic field in a plane. The expansion of the transverse field in plane waves allows the propagation of this field. With the paraxial approximation, this propagation mechanism led to the Gaussian beam (2.76). This Gaussian beam supports independent beam parameters in both transverse directions and it might be realized by separately shaping the beam in each transverse direction. In this section, the realization of a well-defined one-dimensional Gaussian beam by sampling its transverse field on a line is investigated.

To unify the Gaussian beam definition for the following considerations, a Gaussian beam with beam waist  $w_{0x} = 7\lambda$  at a focal distance  $z_{0x} = 300$  mm and for the frequency  $f = 90$  GHz is used for all computations. This allows comparison between the results and, further, this beam configuration is similar to that of the phased array antenna for the ASDEX Upgrade tokamak described in Chapter 5.

In the following, the transverse electric field of the desired beam is synthesized by an array of open-ended rectangular hollow waveguides. For the computation of the synthesized field, the  $E$ -plane cut of the open-ended rectangular hollow waveguide is modeled by a rectangular window. The influence of the rectangular window, the number of radiating elements, the possibility of beam-steering as well as amplitude and phase errors on the plane wave spectrum and the radiated beam are investigated. The realization of such a discretized field distribution and the procedure to consider mutual coupling between the source elements is presented. Finally, the required amplitude and phase distribution to radiate a Gaussian beam over a full waveguide band (in particular the  $W$ -band) is described.

### 3.3.1 Sampling of the Gaussian Beam Transverse Field

Consider a linearly polarized ( $u_x$ -polarized) Gaussian beam with only an electric field component  $E_x$ . The electric field in the  $xz$ -plane is described by (2.76) as

$$E_x(x, 0, z) = E_{0x} \frac{\sqrt{w_{0x} w_{0y}}}{\sqrt{w_x w_y}} e^{-\frac{x^2}{w_x^2} - j k z' - j \frac{x^2 z_{rx}}{w_{0x}^2 R_x} + j \frac{\phi_x}{2} + j \frac{\phi_y}{2}}, \quad (3.22)$$

for  $y = 0$ , and in the  $yz$ -plane for  $x = 0$  the electric field is

$$E_x(0, y, z) = E_{0x} \frac{\sqrt{w_{0x} w_{0y}}}{\sqrt{w_x w_y}} e^{-\frac{y^2}{w_y^2} - j k z' - j \frac{y^2 z_{ry}}{w_{0y}^2 R_y} + j \frac{\phi_x}{2} + j \frac{\phi_y}{2}}. \quad (3.23)$$

The terms in the exponent of both equations that are independent of  $x$  or  $y$ , respectively, realize a phase shift of the complete beam field. The absolute phase of the radiated field, however, is not important for the synthesis of the Gaussian beam. The terms preceding the exponential scale the magnitude of the field and are also independent of  $x$  or  $y$ , respectively. These terms are only necessary to keep the energy content of the beam along the propagation axis constant. For the synthesis of a Gaussian beam in a transverse plane, however, also these normalizing terms can be neglected. Consequently, the relative transverse field  $\tilde{E}_x$  of a Gaussian beam on a line  $y = 0$  and  $z = \text{const.}$  can be represented by

$$\tilde{E}_x(x, 0, z) = e^{-\frac{x^2}{w_x^2} - j \frac{x^2 z_{rx}}{w_{0x}^2 R_x}}, \quad (3.24)$$

and on a line  $x = 0$  and  $z = \text{const.}$  it is

$$\tilde{E}_x(0, y, z) = e^{-\frac{y^2}{w_y^2} - j \frac{y^2 z_{ry}}{w_{0y}^2 R_y}}. \quad (3.25)$$

The real-valued term in the exponent of both previous equations represents the amplitude distribution and the imaginary part represents the phase distribution on the  $x$ - and  $y$ -axis, respectively. Note, that these representations are indicated by the tilde.

In a similar fashion, by neglecting the absolute phase and the amplitude normalizing terms of the two-dimensional Gaussian beam (transverse plane) (2.76), the relative electric field of this Gaussian beam in a plane  $z = \text{const.}$  follows as

$$\tilde{E}_x(x, y) = e^{-\frac{x^2}{w_x^2} - j \frac{x^2 z_{rx}}{w_{0x}^2 R_x} - \frac{y^2}{w_y^2} - j \frac{y^2 z_{ry}}{w_{0y}^2 R_y}} = \tilde{E}_x(x, 0, z) \tilde{E}_x(0, y, z). \quad (3.26)$$

As a consequence, the transverse electric field  $E_x$  of the Gaussian beam may be separated in  $x$  and  $y$ . Thus, the Gaussian beam (2.76) can be decomposed in separate field

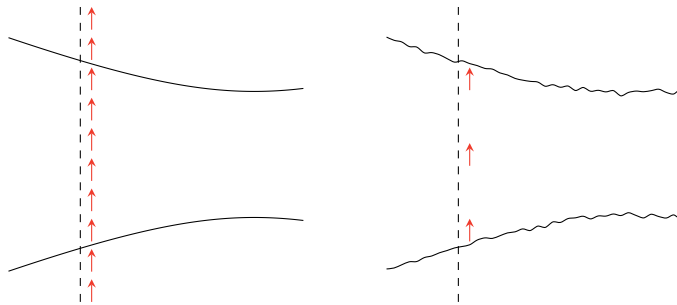


**Fig. 3.2:** Left: Gaussian beam from a continuous transverse field distribution. Right: Gaussian beam from a sampled and truncated transverse field distribution.

distributions for both principal axis in the transverse plane. These field distributions are mutually independent and, thus, they can be synthesized individually.

In the following, synthesizing the field on one principle axis by individual radiating elements is investigated. Due to similarity, the other principle axis would follow equally. However, in this work the beam shape in only one principle plane (in particular the  $xz$ -plane) is synthesized by the taper of the phased array antenna, whereas the beam shape in the orthogonal plane (in particular the  $yz$ -plane) is synthesized by the radiating element itself (a reflector).

The relative electric field distribution on the  $x$ -axis  $\tilde{E}_x(x, 0, z)$  from (3.24) is a continuous function. To realize such a field distribution, it might as well be sampled and truncated. This allows the aperture distribution to be arbitrarily synthesized from a finite aperture and, in addition, enables the steering of the beam by appropriate phasing of the individual samples, see the discussion about phased array antennas in Section 3.2. The continuous as well as the sampled transverse field distribution are sketched in Fig. 3.2. The continuous distribution might be considered as the ideal one, while the sampled field distribution is an approximation which incorporates discretization and truncation errors.

The transverse field (3.24) of the Gaussian beam is sampled by  $N$  rectangular sampling elements assembling a comb, where  $N$  is an odd integer (even is also possible, but odd results in a zero-centered sampling element). The width of the rectangular sampling element is specified by  $h$  and the spacing between the individual sampling points is defined by  $d_x$ , with the condition  $d_x > h$ . The Gaussian beam field from (3.24) is sampled at the center of the rectangular sampling element and this value is utilized over the appropriate width and position. In summary, the sampled electric field is described

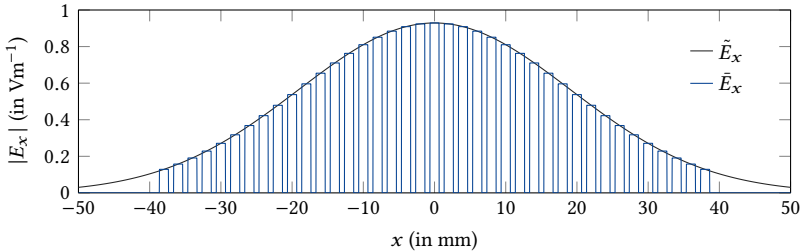


**Fig. 3.3:** Transverse electric field amplitude at  $z = 0$  mm for the theoretical and sampled Gaussian beam with beam waist  $w_{0x} = 7\lambda$  at  $z_{0x} = 300$  mm for  $f = 90$  GHz. The sampling element has a width  $h = 1.27$  mm and the spacing is  $d_x = 2$  mm.

by

$$\bar{E}_x = \sum_{n=-(N-1)/2}^{(N-1)/2} \tilde{E}_x(x - nd_x, 0, z) \operatorname{rect}((x - nd_x)/h). \quad (3.27)$$

The continuous as well as the sampled Gaussian beam with beam waist  $w_{0x} = 7\lambda$  at  $z_{0x} = 300$  mm for  $f = 90$  GHz are plotted in Fig. 3.3. The element spacing is  $d_x = 2$  mm and the width of the rectangular sampling element is  $h = 1.27$  mm (equal to the height of the WR10-rectangular hollow waveguide). Due to the sampling and truncation, the area (or line-length, when considering the electric field on an axis) that is used for radiation does not equal that of the ideal Gaussian beam. Hence, when directly comparing both beams, the energy contained in the sampled beam is smaller than the energy in the continuous beam. This basically says that a sampled field distribution uses the available area less efficiently.

The influence of the sampling process on the radiated beam is investigated by means of its plane wave spectrum, see Section 2.2.2. Due to the sampling, the plane wave spectrum will be periodic and the sampling element introduces a deviation in the spectrum from the ideal one. As the sampling process is a multiplication in spatial domain (3.27), the rectangular sampling element results in a convolution with a sinc-function in the spectral domain. The width of the sinc function is dependent on the width of the rectangular sampling element: the smaller the width, the broader the sinc and, consequently, the smaller the influence on the plane wave spectrum. The plane wave spectrum of the continuous and of the sampled Gaussian beam with beam waist radius  $w_{0x} = 7\lambda$  at a focal distance  $z_{0x} = 300$  mm for  $f = 90$  GHz is shown in Fig. 3.4. The field is assumed uniform in  $y$ -direction (i.e.,  $k_y = 0$ ). The rectangular sampling element has a width  $h = 1.27$  mm and the spacing between the individual samples is  $d_x = 2$  mm.

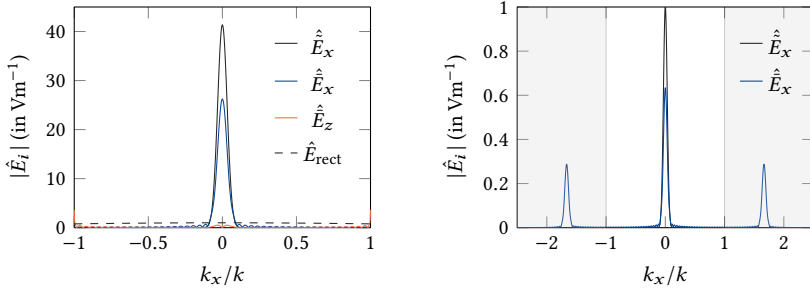


**Fig. 3.4:** Plane wave spectrum of the continuous and the sampled Gaussian beam with beam waist  $w_{0x} = 7\lambda$  at  $z_{0x} = 300$  mm for  $f = 90$  GHz. The sampling element has a width  $h = 1.27$  mm and the spacing is  $d_x = 2$  mm. Left: Propagating wavenumber range ( $|k_x| < k$ ). Right: Extended wavenumber range ( $|k_x| < 2.5k$ ).

The left plot of Fig. 3.4 is restricted to the propagating wavenumbers  $|k_x| < k$ . The continuous field distribution  $\hat{E}_x$  leads to a plane wave spectrum with a vanishing  $z$ -component of the electric field. Moreover, the spectrum of the continuous field distribution has a peak around  $k_x/k = 0$ , which can be interpreted as the beam propagating along the  $z$ -direction with a certain spread ( $|k_x|/k \neq 0$  components).

The spectrum of the sampled field distribution has an  $\hat{E}_x$  as well as an  $\hat{E}_z$ , while the  $z$ -component is considerably smaller. The peak of  $\hat{E}_x$  is also around  $k_x/k = 0$  and the shape follows that of  $\hat{E}_x$ . Due to the sampling, the peak of the sampled field distribution is smaller in amplitude as compared to the continuous field distribution. Further, the sampled and truncated plane wave spectrum has small ripples. The sampling process (3.27) can be considered as a sum of complex weighted Fourier transforms of the rectangular sampling element. The sampling element itself leads to a sinc-function in the spectral domain. As the width  $h$  of the rectangular function is relatively small, the first-null width of the sinc-function is rather large, see  $\hat{E}_{\text{rect}}$  in Fig. 3.4. The superposition of the complex weighted sinc-function spectra leads to the interference pattern or ripples observable in  $\hat{E}_x$ , see Fig. 3.4.

The periodicity of the sampling elements leads to aliasing effects in the plane wave spectrum, similar to the grating lobes of a phased array antenna as discussed in Section 3.2. This can be seen in the right plot of Fig. 3.4. The two grating lobes appear in the invisible or non-propagating wavenumber range. The invisible range is highlighted with a gray background color. The periodicity is dependent on the wavelength and on the spacing between the sampling elements. The grating lobes are no problem for broadside radiation. However, if the main beam is steered it may happen that a grating lobe moves into the visible or propagating wavenumber range and, thus, disturbs the

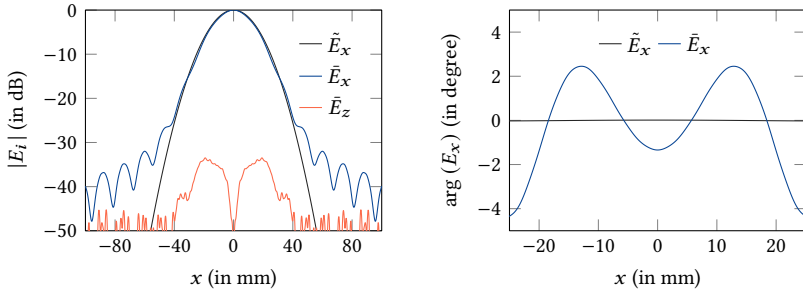


**Fig. 3.5:** Evaluated electric field of continuous and sampled source field from Fig. 3.3 in the focal plane  $z = 300$  mm. Left: normalized amplitude. Right: phase within beam waist  $|x| \leq 23$  mm.

radiation characteristic.

With the inverse transforms (2.48) and (2.49) of the plane wave spectrum, the electric field can be evaluated on an arbitrary plane in propagation direction of the beam. The focal plane in a distance of  $z = 300$  mm is used as the observation plane. The electric fields in the focal plane of the continuous and sampled field distribution follow from (2.48) and (2.49). For the results, see Fig. 3.5. The normalized amplitude of the field is shown in the left plot and the relative phase within the beam waist is shown in the right plot. The sampled and continuous amplitudes agree well for amplitude levels above roughly  $-25$  dB. For lower amplitudes, the relative error increases. This is basically due to the truncation and sampling of the continuous field distribution, i.e., due to the ripples in the plane wave spectrum of the sampled field. The ratio between the synthesized beam waist and the desired beam waist is around 0.95. The slightly smaller beam waist is due to the sampling elements. To compensate for this effect, the array taper should be designed for a slightly larger beam waist (e.g., multiplied by a factor of 1.05 for this particular example). The  $z$ -component of the electric field of the sampled Gaussian beam is below  $-33$  dB. The phase of the desired Gaussian beam in the focal plane is uniform. The continuous source field yields the expected result, while the sampled source field leads to a small phase variation within the beam waist radius ( $w_{0x} = 23$  mm) of roughly  $2^\circ$  and  $-4^\circ$ , see Fig. 3.5.

Overall, the sampled aperture distribution can replicate the continuous distribution. The beam waist radius is almost equal and the phase variation in the beam waist is acceptable. Ripples occur and a  $z$ -component is present in case of a sampled transverse field.

### 3.3.2 Influence of the Edge Taper (Number of Elements)

The ratio between the amplitude of the outermost element (minimal amplitude) and the amplitude of the central element (maximum amplitude) is the edge taper. When the sampling element and spacing are defined, the edge taper is only dependent on the number of elements. The number of elements and, consequently, the edge taper, have an influence on the synthesized and radiated (Gaussian) beam. The quality of the radiated beam and its dependence on the edge taper are investigated in this section.

The Gaussian beam is again synthesized for a beam waist  $w_{0x} = 7\lambda$  at  $z_{0x} = 300$  mm and  $f = 90$  GHz. The sampling element has a width of  $h = 1.27$  mm and the individual elements are spaced by  $d_x = 2$  mm. The computation of the radiated field follows the three steps described in Section 3.3.1, which are in brief:

1. Sample the continuous transverse field (rectangular sampling elements).
2. Compute the plane wave spectrum of the sampled field.
3. Evaluate the plane wave spectrum in the focal plane.

These three steps are sequentially performed for element numbers  $N = 11, \dots, 49$ . Fewer elements do not replicate the desired beam at all, while more elements do not improve the results significantly.

To measure the agreement of the synthesized and the desired Gaussian beam, three measures are defined. The first measure is the *beam waist ratio*: the ratio between the synthesized beam waist radius to the desired beam waist radius. The second measure is the *phase deviation*: the maximum absolute variation of the phase within the beam waist from the constant or ideal phase. The last measure is the level of the *first side-lobe*. In addition, the relative total energy within the beam and the edge taper are given. The relative total energy is the percentage of energy in the beam with respect to sampling the whole transverse field. The results are shown in Fig. 3.6. The beam waist ratio and the phase deviation are in the left plot, whereas the first side-lobe, the energy content, and the edge taper (reduced by 13 dB, roughly corresponding to the level of the first side-lobe of a rectangular sampling element) are in the right plot.

The beam waist of the synthesized beam is too large for only a few radiating elements ( $N < 17$ ). It is smaller than the desired beam waist for element numbers between  $N = 17, \dots, 29$  and tends to the desired beam waist for more elements. Similarly, increasing the number of elements decreases the phase deviation within the beam waist. The phase deviation is not smaller than  $10^\circ$  for less than 29 elements.

In summary, the Gaussian beam is synthesized correctly for more than 29 elements or an corresponding edge taper of roughly  $-10$  dB. The level of the first side-lobe decreases for more radiating elements. Moreover, the side-lobe-level approximately follows the edge taper that has been decreased by 13 dB (roughly the level of the first side-lobe of the rectangular sampling element).

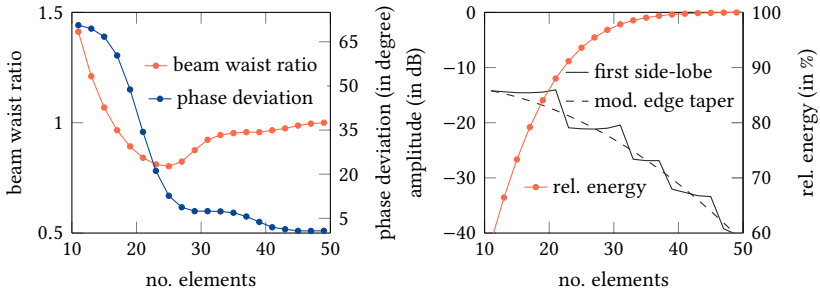


**Fig. 3.6:** Left: Dependency of the beam waist ratio and the phase deviation on the number of radiating elements. Right: Level of the first side lobe and relative energy content within the beam. Edge taper reduced by 13 dB for comparison.

### 3.3.3 Influence of Aperture Amplitude and Phase Errors

The amplitude and phase of the sampled elements is prone to errors in reality. These are either random and caused by manufacturing tolerances or systematic and a better realization is simply not possible. In this section, the random aperture errors are investigated.

The desired amplitudes follow from the sampling process (3.27). For the analysis,  $N = 39$  elements sample the Gaussian beam which has a beam waist radius  $w_{0x} = 7\lambda$  in a focal plane distance  $z_{0x} = 300$  mm. The amplitude and phase of each element is modified by a random error. The erroneous synthesized field is evaluated in the focal plane. The influence of these random errors on the beam waist ratio, the phase deviation within the beam waist and on the side-lobe level are shown in Fig. 3.7. In total, three different cases are investigated in the following: only amplitude errors, only phase errors, and simultaneous amplitude and phase errors.

In the first scenario, the amplitude of each element is varied by a random uniformly distributed relative error in-between error bounds according to the abscissa of Fig. 3.7. The phase is not erroneous. Each element has a different amplitude error. In Fig. 3.7, 39 different erroneous aperture amplitudes are evaluated for each error bound. The mean and maximum beam waist ratio, phase deviation within the beam waist as well as the mean and maximum side-lobe levels are shown. The mean beam waist ratio is not affected by the amplitude errors. However, there are outliers that have lead to a larger beam waist ratio. The phase deviation within the beam waist worsens for larger error bounds. Relative amplitude errors of  $\pm 1$  dB keep the phase deviation below  $\pm 5^\circ$ . The side-lobe level increases for larger amplitude errors. The maximum side-lobe level is still below  $-20$  dB for amplitude errors of  $\pm 1$  dB.

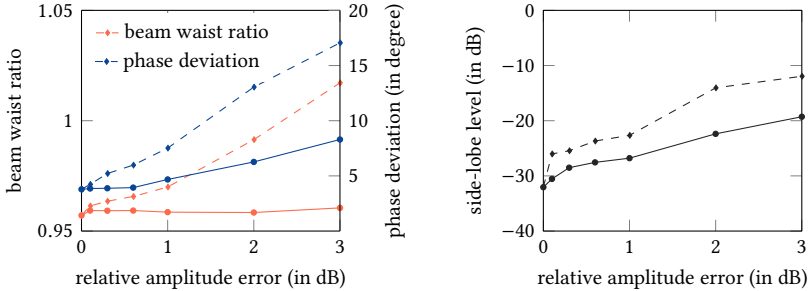


**Fig. 3.7:** Influence of relative aperture amplitude errors on the radiated beam. For each error bound ( $\pm$  the value on the abscissa) 39 random configurations are evaluated. The maximum of all configurations is represented by the dashed lines while the solid lines represent the mean value over all configurations.

Similarly in the second scenario, the influence of aperture phase errors is investigated. The phase of each element is varied by uniformly distributed random values with magnitude up to the bound according to the abscissa of Fig. 3.8, while the amplitude is not erroneous. In Fig. 3.8, 39 different configurations for each error bound are evaluated.

As with the amplitude errors, the mean beam waist ratio seems to be constant. However, the phase deviation within the beam waist worsens simultaneously indicating a poorer agreement with the ideal beam. The side-lobe level increases for larger error bounds. Overall, for phase errors with magnitude smaller than  $10^\circ$ , the side-lobe level

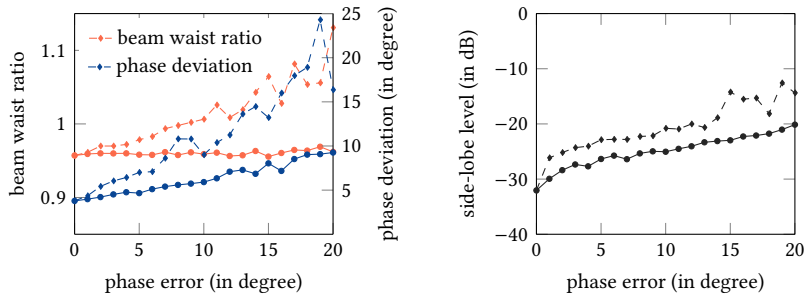


**Fig. 3.8:** Influence of aperture phase errors on the radiated beam. For each phase error magnitude bound according to the abscissa 39 random configurations were evaluated. The maximum of all configurations is represented by the dashed lines while the solid lines represent the mean value over all configurations.

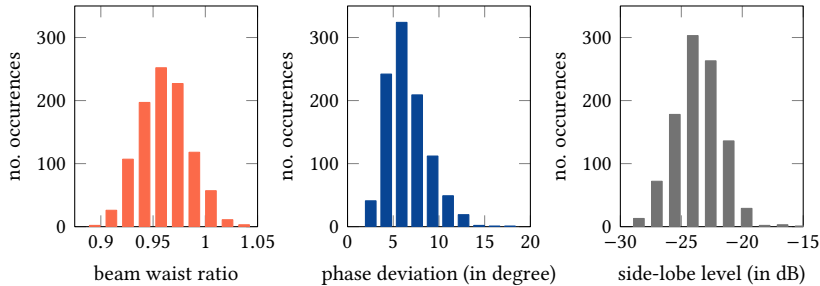


**Fig. 3.9:** Histogram of the beam waist ratio, the phase deviation, and the side-lobe level for 1000 randomly distorted aperture distributions. Amplitude error of each array element in the range of  $\pm 1$  dB and phase error of each array element in the range of  $\pm 10^\circ$ .

is still below  $-20$  dB and the phase deviation within the beam waist is acceptable.

The third scenario yields a statistical evaluation of simultaneous amplitude and phase errors at each element, see Fig. 3.9, where 1000 scenarios were evaluated. The amplitude and phase at each element is randomly (uniform distribution) varied in bounds of  $\pm 1$  dB and  $\pm 10^\circ$  of the desired amplitude and phase value. The radiated beam is evaluated in the focal plane. The beam waist ratio, the phase deviation within the beam waist, and the side-lobe level are the measures that describe the beam quality. The beam waist ratio varies slightly (about  $\pm 0.05$ ) around 0.95. The phase deviation is centered around  $6^\circ$  and most of the 1000 scenarios result in a phase deviation smaller than  $10^\circ$ . Similarly, the side-lobe level for most scenarios is below  $-20$  dB, while the histogram is centered around  $-24$  dB.

As a conclusion, a phased array antenna with  $N = 39$  radiating elements and amplitude as well as phases errors below  $\pm 1$  dB and  $\pm 10^\circ$ , respectively, is expected to yield a side-lobe level below  $-20$  dB. The beam waist is expected to vary by about 5% and the phase error within the beam waist is expected to be smaller than  $10^\circ$ .

### 3.3.4 Steering of the Gaussian Beam

Steering the Gaussian beam towards a desired direction is realized similar to steering the beam of a phased array antenna – by adding a progressive phase according to (3.17) to the elements. This is, in order to steer the sampled (one-dimensional) Gaussian beam (3.27) towards the  $\Theta_p$  direction (angle between broadside and steering direction), a phase shift  $\varphi_n$  according to (3.17) is added to each element  $n = [-(N-1)/2, (N-1)/2]$ . The elements are spaced with a regular distance  $d_x$ . The steering of the Gaussian beam is again investigated by means of the plane wave spectrum.

By multiplying the sampled Gaussian beam field distribution with the steering

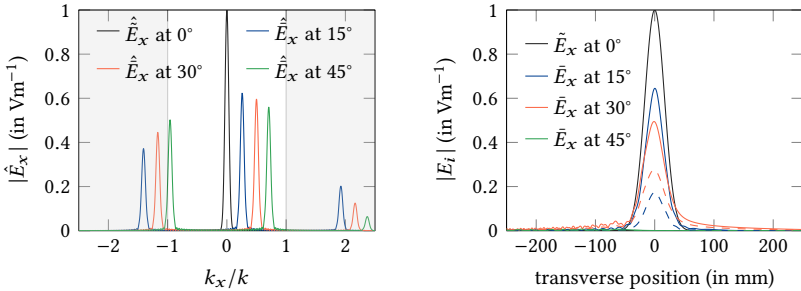


**Fig. 3.10:** Left: Plane wave spectrum of the sampled Gaussian beam steered to 15°, 30°, and 45° with the spectrum of the continuous distribution as reference. Right: The  $E_x$ - and  $E_z$ -component evaluated in the transverse plane in focal distance.

weights according to (3.17), the sampled and steered field is given by

$$\tilde{E}_x = \sum_{n=-(N-1)/2}^{(N-1)/2} \tilde{E}_x(x - nd_x, 0, z) \operatorname{rect}((x - nd_x)/h) e^{-jknd_x \sin \Theta_p}. \quad (3.28)$$

The plane wave spectrum and its propagation are evaluated according to (2.47), (2.48) and (2.49). The steering directions  $\Theta_p = 15^\circ$ ,  $30^\circ$ , and  $45^\circ$  are investigated. In the left plot of Fig. 3.10, the plane wave spectrum of the continuous aperture field distribution and that of the sampled and steered aperture field distribution are shown. The spectrum moves to larger relative wavenumbers  $k_x/k$  for larger steering angles. Moreover, the amplitude of the main lobe reduces, which is mostly caused by the single element pattern, i.e., by the sinc-function of the rectangular window.

When the main-lobe is steered in the plane wave spectrum, also its periodic repetitions are shifted. These so-called grating lobes were initially in the non-propagating part of the spectrum, see Fig. 3.4. For larger steering angles they move towards the propagating wavenumber range, see Fig. 3.10. When steering towards  $45^\circ$ , the first grating lobe is within the propagating part of the plane wave spectrum. This also follows from the maximum steering angle given by (3.21). For  $f = 90$  GHz and an element spacing of  $d_x = 2$  mm, the first grating lobe occurs at  $\Theta_{p,\max} = 41.8^\circ$ . For  $f = 75$  GHz and  $f = 105$  GHz, the maximum steering angles are  $\Theta_{p,\max} = 90^\circ$  and  $\Theta_{p,\max} = 25.4^\circ$ , respectively.

The inverse transforms (2.48) and (2.49) are employed to evaluate the electric field in a plane transverse to the steered propagation direction. The distance of this plane to the aperture origin corresponds to the focal distance  $z_{0x}$ . For the evaluated electric fields  $|E_x|$  and  $|E_z|$ , see the right plot of Fig. 3.10. The electric field of the  $45^\circ$ -steered

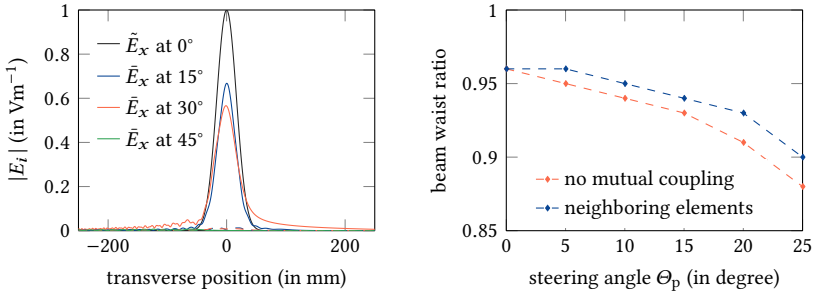


**Fig. 3.11:** Left: Transverse electric field of the steered Gaussian beam. The field is evaluated on a line transverse to the steered propagation direction. Right: Beam waist ratio of the steered beam without and with mutual coupling. Mutual coupling from a full-wave simulation of one active radiating element and two passive radiating elements on each side, see Section 3.3.6.

beam vanishes in the evaluation plane due to the grating lobe within the propagating wavenumber range. The other steering angles have a non-negligible  $z$ -component, which increases for larger steering angles. The increase of the  $z$ -component is accompanied by a reduction of the  $x$ -component. This, however, is to be expected. The propagation and the transverse direction of the radiated beam are no longer in  $z$ - and  $x$ -direction, respectively. When rotating the  $E_x$ - and  $E_z$ -components onto the corresponding vector components in the steered transverse plane, the electric field component in propagation direction almost vanishes, see left plot in Fig. 3.11. Thus, the radiated Gaussian beam has an electric field component transverse to the propagation direction. The phase in the steered transverse plane equals roughly that of Fig. 3.5. The phase deviations from the ideal focal plane are in the range of  $\pm 5^\circ$ . Besides, the focal plane is slightly shifted towards the antenna.

From the considerations on phased array antennas in Section 3.2, it follows that the radiation characteristic of the whole array is influenced by the array taper and the radiation characteristic of the single elements. The single element is represented by the rectangular window in (3.28). It has a relatively broad radiation characteristics and the number of array elements is rather large. Hence, the radiation characteristic of the whole array is dominated by the aperture taper. However, for larger steering angles the amplitude of the radiated beam decreases. The envelope is represented by the single element pattern, which follows from the multiplication of the element pattern with the array taper, see (3.15). Apart from the amplitude drop, the single element pattern also influences the beam waist. This influence is evaluated with the plane wave spectrum for the standard Gaussian beam with beam waist  $w_{0x} = 7\lambda$  at  $z_{0x} = 300$  mm for  $f = 90$  GHz. The sampling element has a width  $h = 1.27$  mm and the spacing is

$d_x = 2$  mm. For the ratio of the realized beam waist to the desired beam waist (i.e., the beam waist ratio) and its dependence on the steering angle, see the right plot in Fig. 3.11. At broadside radiation, the beam waist ratio is at about 0.95. For increasing steering angles, it decreases to 0.88. In summary, the sampling element reduces the beam waist and the realized beam waist is also dependent on the steering angle. To compensate the single element pattern, the array taper should be designed for a slightly larger beam waist (e.g., multiplied by a factor of 1.05 for this particular example).

### 3.3.5 Suitable Radiating Elements

The possibility of synthesizing and steering a Gaussian beam by a synthesized transverse field distribution has been shown in the previous sections. In the model, the synthesized field is composed of rectangular sampling elements with the electric field being aligned with the polarization of the Gaussian beam. To realize such a synthesized transverse field distribution, a radiating element is required. The radiating elements are considered to be the source of the Gaussian beam. They have to transform the guided wave field into that of the synthesized transverse field distribution in order to approximate the desired Gaussian beam.

For the electric field to be aligned with the sampling direction (as is the case for the phased array antenna designed in this thesis), the  $\text{TE}_{10}$ -mode in an rectangular hollow waveguide, see Section 2.4.1, or the  $\text{TM}_{m0}^z$ -mode in the radial parallel plate waveguide, see Section 2.4.2 are suitable. Here, either the small sidewall of the rectangular waveguide or the  $z$ -axis of the radial parallel plate waveguide is aligned with the sampling direction. With this orientation, both waveguides support only modes that have an electric field aligned with the sampling direction.

As already stated, the electric field is guided in a waveguide with conducting walls. In Fig. 3.12 a), the electric field in the aperture of an appropriate waveguide is shown. Shown is a cut along the sampling direction. The electric field at the aperture might be guided in a rectangular hollow waveguide or a radial parallel plate waveguide. To investigate the radiation into the right half-space, the fields can be represented by an equivalent magnetic surface current  $M_s = -\mathbf{n} \times \mathbf{E}_s$ , with the unit normal  $\mathbf{n}$  pointing into the right half-space [Bal05]. The resulting current is shown in Fig. 3.12 b). The waveguide in the left half-space must be filled with PEC, since electric surface currents shall be neglected. In a next step, the left half-space is replaced by vacuum. With the image principle, the magnetic surface currents in the right half-space are now  $M'_s = -2\mathbf{n} \times \mathbf{E}_s$ . The magnetic current  $M'_s$  yield the correct field solution only in the right half-space. For the sampling of the transverse field, however, this is exactly the electric field distribution that was modeled by the rectangular sampling element in (3.27) and as illustrated in Fig. 3.12 d). When comparing Fig. 3.12 d) with the sampled field distribution in Fig. 3.2 it can be seen that the sampled transverse field distribution is similar to the radiation from the aperture. Further, when using several of these

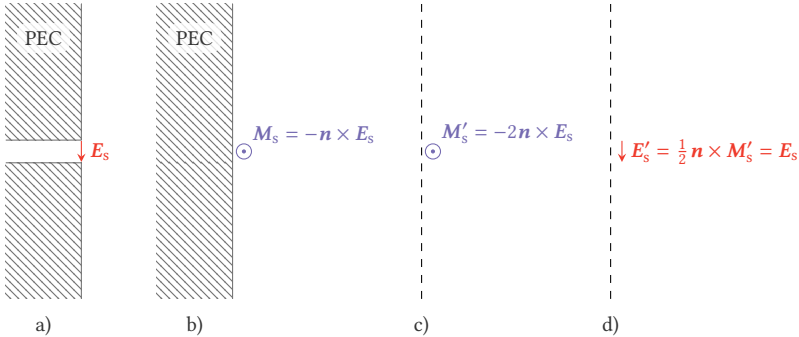


**Fig. 3.12:** Radiation of an electric field from an aperture using the equivalence principle and image theory. The aperture field in a) may be a guided TE<sub>10</sub>-mode in a rectangular hollow waveguide or TM<sub>m0</sub><sup>z</sup>-modes in the radial parallel plate waveguide.

apertures displaced by the sampling distance, the whole sampled field distribution can be replicated.

In summary, the previous considerations show the similarity between the radiation from an aperture antenna and the sampled field distribution. The bottom-line is: It is possible to realize the desired sampling pattern to approximate the Gaussian beam by placing several apertures side-by-side modeling the sampling process. Clearly, when using several apertures, the mutual coupling between the individual elements can in general not be neglected. The mutual coupling is investigated in the following section.

### 3.3.6 Consideration of Mutual Coupling

The fundamental model to compute the radiated field from the aperture in the previous sections is based on the assumption that the radiating element (i.e., the electric field in the aperture) is placed in an infinite PEC plane. This assumption, however, does not represent realistic scenarios. The influence of the neighboring elements is not considered in this simplified model. In fact, every active element in an array induces secondary radiation in the neighboring elements. This influencing mechanism is called mutual coupling [Mai05].

Consequently, a more realistic model of the array antenna (in contrast to the model in Fig. 3.12) has several apertures placed side-by-side in the PEC half-space or array aperture representing the individual radiating elements, see Fig. 3.13 a). The active element has a source field  $E_s$  in its aperture, whereas the neighboring apertures support an electric field in the aperture but are not active. Due to mutual coupling, however, there exists a coupled electric field denoted as  $E_c$ , which is due to the source field  $E_s$ .

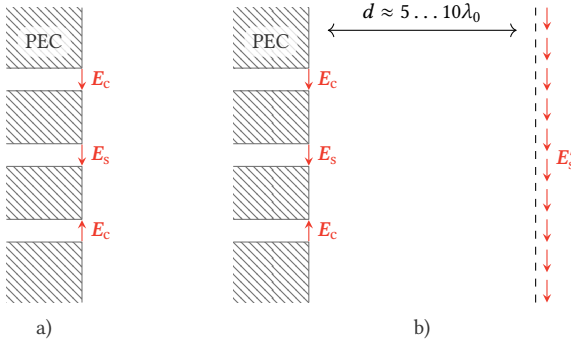


**Fig. 3.13:** Radiation model that considers mutual coupling of the individual elements. The active element leads to electric fields in neighboring elements a). The effect on the radiation characteristic follows from evaluating the radiated field on a plane in a distance  $d$  away from the aperture b).

The amplitude and phase of the coupled electric fields  $E_c$  are, in general, a function of the frequency, the spacing between the elements, and of the geometric shape of the radiating elements. To consider mutual coupling effects, a full-wave simulation of the embedded element in the array environment is required. The induced field on the neighboring radiating elements can then be described by a mutual impedance or coupling matrix [Mai05].

In this thesis, another avenue is pursued to evaluate the impact of mutual coupling on the radiated beam. The single element is simulated in the array environment and the radiated field is evaluated on a plane in a distance of about  $5 \dots 10\lambda_0$  from the array aperture, see Fig. 3.13 b). Thereby, the electric field on the evaluation plane represents an equivalent source field  $E'_s$  that includes all effects originating from the geometry of the radiating elements. To obtain the overall radiation characteristic of the array antenna, each element is simulated and the individual equivalent source fields  $E'_s$  are weighted by the element weights and finally superimposed. Similar to the previous sections, the plane wave spectrum is employed to compute the radiated field at an arbitrary observation point in propagation direction away from the equivalent plane with the source field being the superposition of all individual equivalent source fields.

The simulation of each element in the complete array geometry can be very time-consuming due to the large size of the array and a fine resolution of the individual elements. To reduce simulation time, it may be assumed that the mutual coupling acts stronger on direct neighbors of a radiating element and weaker on elements farther away. This is, the coupled field is stronger in the direct neighbor as it is in an element at the other end of the array. As a consequence, the effect of mutual coupling may

be approximated by including only direct neighbors in the full-wave simulation. This reduces the overall simulation time and still incorporates the mutual coupling effect due to direct neighbors. Moreover, a single simulation can be reused for all configurations that have an equal geometry (same simulation model). Here, only the equivalent source field  $E'_s$  has to be geometrically shifted according to the element position in the array. Thus, only the inner geometry of the array (elements leading to the same reduced geometry) and, in addition, the outermost elements incorporating the edge of the array have to be modeled and simulated.

The geometry of the phased array antenna for ASDEX Upgrade tokamak is introduced in the following chapters, the influence of mutual coupling is briefly outlined here. The coupling (in terms of S-parameters) from the radiating element to the neighboring elements is on the order of  $-17$  dB for the direct neighbor,  $-23$  dB and  $-26$  dB for the next two neighbors, respectively. The input reflection coefficient of a single element is about  $-14$  dB. Thus, the mutual coupling effect acts weaker on elements that are far away from the active element and, in addition, the overall effect is at relatively low amplitude levels. This is also underpinned by comparing the beam waist ratio of the sampled Gaussian beam (no mutual coupling) and that of the field obtained by simulating the whole array geometry (with mutual coupling). For broadside radiation at  $90$  GHz (only one frequency due to long simulation time), the beam waist radius is  $w_{0x} = 22.49$  mm with a corresponding beam waist ratio of  $0.964$  (desired beam waist radius  $w_{0x} = 23.33$  mm). Without mutual coupling, the beam waist radius is  $22.37$  mm with a beam waist ratio of  $0.959$ . If the mutual coupling of the two neighboring elements (two on each side) is considered, the realized beam waist is  $w_{0x} = 22.45$  mm with a beam waist ratio of  $0.962$ . Thus, for the phased array antenna in this thesis the mutual coupling is at a low level and its influence on the radiated beam is relatively small. The radiation characteristic of the single element has a stronger effect. Moreover, the mutual coupling can be computed by considering the mutual coupling of two neighboring elements. This saves simulation time and leads to equal results as compared to simulating the whole aperture.

For the dependency of the beam waist on the steering angle under the consideration of mutual coupling, see Fig. 3.11. For this plot, the radiation pattern of an active radiating element with four passive radiating elements (two on each side) was evaluated for different steering angles. The beam waist ratio is slightly larger than without mutual coupling. The trend for increasing steering angles, however, is similar.

### 3.3.7 Synthesis of a Full-Band Gaussian Beam

In the previous subsections, the focus was on the general radiation of a Gaussian beam from a phased array antenna. The Gaussian beam was synthesized for a fixed frequency by sampling its transverse field distribution at the array aperture. In the following, the Gaussian beam is synthesized to have a certain characteristic in the whole

waveguide band. This full-band synthesis is categorized in two cases. The synthesis of a Gaussian beam with a wavelength-dependent beam-waist, and the synthesis of a Gaussian beam with a wavelength-independent focal plane position. The Gaussian beam with a wavelength-dependent beam waist is dedicated for Doppler reflectometry in AUG, whereas the Gaussian beam with a wavelength-independent focal plane is suitable for Doppler reflectometry in Tokamak à Configuration Variable (TCV). As in the previous sections, the Gaussian beam transverse field is sampled only in one principle plane, the  $xz$ -plane according to (3.24) (sampled along the  $x$ -direction). The orthogonal plane ( $yz$ -plane, along the  $y$ -direction) would follow equally, see (3.25), but may also be synthesized by a continuous source distribution.

Nevertheless, both synthesis procedures have one thing in common: The amplitude distribution at the array aperture is frequency-invariant, because it is easier to be realized in a series feed structure as compared to modeling a certain frequency-dependent amplitude distribution. As a consequence, the Gaussian beam radius  $w_x^a$  at the array aperture is frequency-invariant. From (2.69), the beam radius at the array aperture and at the design wavelength  $\lambda_d$  follows from

$$w_x^a = w_{0x}^d \sqrt{1 + \left( \frac{\lambda_d z'_x}{\pi (w_{0x}^d)^2} \right)^2}, \quad (3.29)$$

with the focal distance  $z'_x$  and beam waist radius  $w_{0x}^d$  at the design wavelength. With the beam radius at the array aperture  $w_x^a$  and (3.24) follows the amplitude taper  $|m|$  of the array antenna as a function of the element position  $x$  as

$$|m| = e^{-(x/w_x^a)^2}. \quad (3.30)$$

The phase distribution at the array aperture  $e^{j\varphi_x^a}$  follows from the imaginary part of (3.24) as

$$e^{j\varphi_x^a} = e^{-j \frac{x^2 z_{rx}}{w_{0x}^2 R_x}}. \quad (3.31)$$

With the Rayleigh length  $z_{rx}$  (2.65), the phase distribution can be denoted as

$$\varphi_x^a = -\frac{\pi x^2}{\lambda R_x}. \quad (3.32)$$

Together, (3.30) and (3.32) reassemble the desired Gaussian beam, see Section 3.3.1. The other factors in (2.76) are either for the normalization of the Gaussian beam or do not dependent on the transverse direction. They merely introduce a phase offset to the total field. In the following two paragraphs, the array taper of the two different

frequency-dependencies (or independencies) is presented. For the phased array antenna in AUG, a fundamental-mode Gaussian beam with wavelength-dependent beam waist is synthesized. This is, the beam waist radius is controlled and the focal distance adjusts accordingly. For the phased array antenna in TCV, a fundamental-mode Gaussian beam with a focal plane distance that is constant over frequency is synthesized. This is, the focal distance is controlled and the beam waist radius adjusts accordingly.

### Radiation of a fundamental-mode Gaussian beam with a linear wavelength-dependent beam waist (for AUG)

The (linear) wavelength-dependent Gaussian beam waist radius is denoted as  $\tilde{w}_{0x} = p\lambda$ , with the positive real number  $p$  (for physically realistic beams  $p > 1$ ). As a consequence of the frequency-dependent beam waist radius and the frequency-invariant amplitude distribution  $w_x^a$  at the array aperture (3.29), the focal distance has to be frequency dependent. Using (2.69) with the fixed  $w_x^a$  and the wavelength-dependent beam waist  $\tilde{w}_{0x}$ , the frequency-dependent focal distance of the Gaussian beam follows as

$$\tilde{z}'_x = \pm \frac{\pi \tilde{w}_{0x}}{\lambda} \sqrt{(w_x^a)^2 - \tilde{w}_{0x}^2}, \quad (3.33)$$

while the negative sign represents the configuration in which the field propagates towards the beam waist and the positive sign represents the configuration where the field propagates away from the beam waist. For the phased array antenna, only the negative sign is of interest, as it yields the phase taper that radiates a converging field.

With (2.74) and (3.33), the frequency-dependent radius of curvature at the array aperture follow as

$$\tilde{R}_x^a = -\frac{\pi \tilde{w}_{0x} (w_x^a)^2}{\lambda \sqrt{(w_x^a)^2 - \tilde{w}_{0x}^2}}, \quad (3.34)$$

and, inserting  $\tilde{R}_x^a$  into (3.32) yields the required wavelength-dependent phase taper

$$\tilde{\varphi}_x^a = \frac{x^2 \sqrt{1 - \tilde{w}_{0x}^2 / (w_x^a)^2}}{\tilde{w}_{0x} w_x^a}. \quad (3.35)$$

The array taper for radiating a fundamental-mode Gaussian beam with a linear wavelength-dependent beam waist radius is  $\tilde{m} = |m| e^{j\tilde{\varphi}_x^a}$ , and, thus

$$\tilde{m} = e^{-x^2 / (w_x^a)^2 + jx^2 / (\tilde{w}_{0x} w_x^a)} \sqrt{1 - \tilde{w}_{0x}^2 / (w_x^a)^2}. \quad (3.36)$$

For verification, this array taper is sampled and propagated with the plane wave spectrum, similar to the procedure described in Section 3.3.1. The design wavelength is

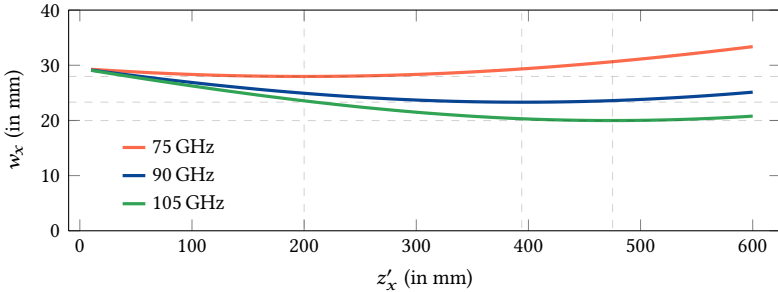


**Fig. 3.14:** The amplitude distribution at the array aperture is frequency-independent. The phase taper synthesizes the desired frequency-dependent beam waist radius  $w_{0x} = 7\lambda$ . The dashed lines indicate the beam waist at the evaluated frequencies.

$\lambda_d = 4$  mm (corresponding to  $f = 75$  GHz). The desired focal distance is  $z'_x^d = 200$  mm and the frequency-dependent beam waist radius is  $\tilde{w}_{0x} = 7\lambda$ . The beam waist at the array aperture follows from (3.29), and the array taper follows from (3.36). In Fig. 3.14, the result of the plane wave propagation is plotted. The beam radius at the aperture is constant. The beam waist radius scales with the frequency and the focal plane moves away for higher frequencies.

### Radiation of a fundamental-mode Gaussian beam with a frequency-independent focal plane distance (for TCV)

Although a phased array antenna for Tokamak à Configuration Variable is not topic of this thesis, a suitable aperture taper is discussed here. With the information from Stefano Coda, a Gaussian beam for Doppler reflectometry in TCV has to have a frequency-independent focal plane distance  $\bar{z}'_x = \text{const.}$ , while the beam waist  $\tilde{w}_{0x}$  may vary in certain bounds. A specific realization in V-band (50 GHz to 75 GHz) requires a beam waist that may vary in the range 10 mm to 15 mm in a focal plane distance from the aperture of 150 mm.

Similar to the previous considerations, the amplitude taper and, thus, the beam waist at the aperture  $w_x^a$  is constant and given by (3.29). With the desired focal distance  $\bar{z}'_x$  and solving (2.69) for the beam waist radius yields

$$\tilde{w}_{0x}^2 = \left( (w_x^a)^2 \pm \sqrt{(w_x^a)^4 - 4(\lambda \bar{z}'_x / \pi)^2} \right) / 2. \quad (3.37)$$

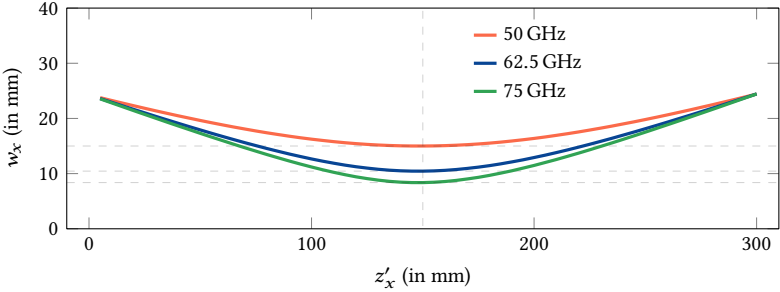


**Fig. 3.15:** The amplitude distribution at the array aperture is frequency-independent. The phase taper synthesizes the desired frequency-independent focal plane  $\bar{z}'_x = 150$  mm. The dashed lines indicate the beam waist at the evaluated frequencies.

Inserting this into (2.74) eventually leads to the radius of curvature at the array aperture

$$\bar{R}_x^a = \frac{\pi^2 (w_x^a)^4}{2\lambda^2 \bar{z}'_x} \left( 1 \pm \sqrt{1 - (2\lambda \bar{z}'_x)^2 / (\pi^2 (w_x^a)^4)} \right). \quad (3.38)$$

With the radius of curvature and (3.32), the required phase taper at the array aperture is

$$\bar{\varphi}_x^a = \frac{2x^2 \lambda \bar{z}'_x}{\pi (w_x^a)^4 \left( 1 \pm \sqrt{1 - (2\lambda \bar{z}'_x)^2 / (\pi^2 (w_x^a)^4)} \right)}. \quad (3.39)$$

The array taper is again composed of the amplitude taper (3.30) and the phase variation  $e^{j\bar{\varphi}_x^a}$ . Due to the lengthy expression of the phase taper, it is not given explicitly. For the TCV beam configuration ( $w_{0x} = 10$  mm ... 15 mm and  $\bar{z}'_x = 150$  mm), the phase taper with the minus sign yields a solution. The array taper is sampled and propagated by means of the plane wave spectrum as in Section 3.3.1. The design wavelength is  $\lambda_d = 6$  mm (corresponding to  $f = 50$  GHz). The Gaussian beam is synthesized for a focal plane distance of  $\bar{z}'_x = 150$  mm and the beam waist radius  $w_{0x}^d = 15$  mm. The frequency-dependency follows from the phase taper. The realized beams for the frequencies 50 GHz, 62.5 GHz, and 75 GHz are plotted in Fig. 3.15. The synthesized beam waist radius scales from 15 mm to 8.5 mm for increasing frequencies. The focal plane distance is constant.

## 4 Individual Antenna Components

The considered phased array antennas are composed of several waveguide feed components that realize the required aperture field distribution. The realization of these components depends on the waveguide technology (e.g., microstrip line or rectangular hollow waveguide) that is employed. The scope of this thesis is on millimeter-wave phased array antennas for nuclear fusion experiments. Due to the harsh environment inside the vessel of the experiment, hollow waveguides are the means of choice. In the following, rectangular hollow waveguide components for millimeter-wave phased array antennas are designed and analyzed by means of full-wave simulations and prototype measurements. The individual components are:

- a coupling structure, to tap-off a defined amount of power from a trunk line
- a variable phase shifter to steer the beam
- an invariable phase shifter, to realize the desired aperture phase taper
- a waveguide load, to absorb the remaining energy at the end of the serial feed
- a vertical transition, to realize a multilayer split-block network
- a radiating element in form of a parallel-plate reflector

The individual components have been designed in view of realizing a serial feed network, but they are not limited to this application.

### 4.1 Coupling Structure or Power Divider

A basic building block of the phased array antennas are power dividers that distribute the incoming wave from the input port to the radiating elements. In a parallel feed configuration, power dividers require a division ratio in the range of  $-3\text{ dB}$  to  $-6\text{ dB}$ . In a serial feed configuration, only a small portion of the power in the trunk line is tapped-off to the radiating elements. The required division ratio is in the range of  $-10\text{ dB}$  to  $-25\text{ dB}$ . In any case, the division ratio should be constant within the operational frequency range to realize the desired amplitude taper throughout this range.

The strong coupling values covering the full rectangular hollow waveguide band for a parallel feed configuration can be realized by a branch-guide coupler [Lev73; You62].

Smaller coupling values, as they are required by a serial feed configuration, lead to smaller slot heights of the individual branches and eventually to values that cannot be realized. The limit is the smallest groove that can be realized. To overcome this dilemma, coupling holes or slots in the waveguide walls are frequently used to tap-off the power [Ste48; Wat46]. At millimeter-wave frequencies, however, these structures are also difficult to realize. Moreover, even if one is able to acquire the required accuracy, these holes or slots exhibit a relatively strong frequency dependency [RWK+13].

To overcome the manufacturing difficulties of the aforementioned approaches and to realize a constant coupling factor over the full waveguide band, a new coupling structure has been developed. Electrically, it is built from a rectangular hollow waveguide *E*-plane (series) T-junction and a quarter-wave transformer section. The waveguide height of the quarter-wave section controls the coupling factor. Almost frequency independent coupling values between  $-25$  dB and  $-10$  dB covering the entire *W*-band ( $75$  GHz– $110$  GHz) can be realized [KSE+15a; KSE+17]. Mechanically, the proposed structure is composed of two parts: the rectangular hollow waveguide network in split-block technology and a separate and exchangeable insert that forms the quarter-wave section. Consequently, it is possible to adjust the coupling factor by modifying the insert without the need to manufacture the whole split-block again.

In the following, the fundamental model of the coupling structure is presented. Prototype coupling structures with inserts that are realized by two different manufacturing technologies (laser-cutting and wire-erosion) are described and evaluated subsequently.

#### 4.1.1 Fundamental Model

The fundamental model of the proposed coupling structure is sketched in Fig. 4.1 as a cut through the *E*-plane of the rectangular hollow waveguide network. The proposed structure is a rectangular hollow waveguide *E*-plane (series) T-junction where the vertical part of the “T” (the stub-guide) assembles a quarter-wave transformer section. The waveguide width  $a$  is constant throughout the structure (no variation in *H*-plane direction). The waveguide height of the quarter-wave section  $b_s$  controls the coupling factor. It is smaller than the height  $b$  of the remaining rectangular hollow waveguide structure, i.e.,  $b_s < b$ . The  $a$  and  $b$  correspond to those of the standard rectangular hollow waveguide ( $2.54$  mm ×  $1.27$  mm for WR10, respectively).

An equivalent circuit of the proposed coupling structure is derived in [KSE+15a] and sketched in Fig. 4.2. The equivalent circuit employs the characteristic impedance of the waveguide [MDP48; Riz88] and is based on the equivalent circuits given in the Waveguide Handbook for the T-junction [Mar51, pp. 337] and for the discontinuity change of the waveguide height [Mar51, pp. 307]. The equivalent circuit is correct only for  $b_s < b$  and it is more accurate, the smaller  $b_s$  is [AAP+87; KSE+15a; Mar51]. The characteristic impedance of a rectangular hollow waveguide with height  $b$  is denoted as  $Z_w$  and the characteristic impedance of a rectangular hollow waveguide with height

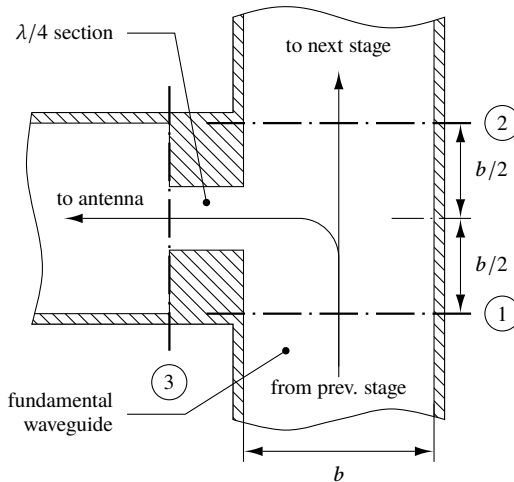
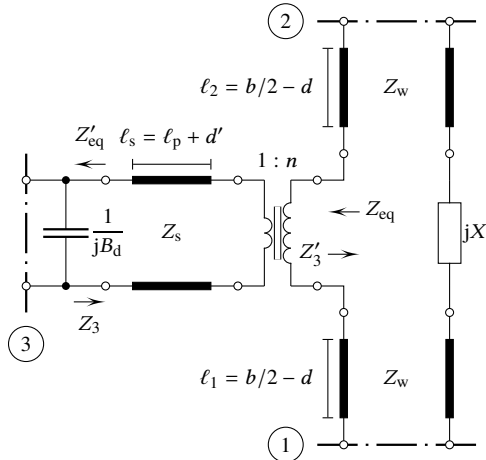


Fig. 4.1: Fundamental model of the coupling structure [KSE+15a].

$b_s$  is denoted as  $Z_s$ . The three ports in the equivalent circuit all have a characteristic impedance of  $Z_w$ .

The discontinuity change of the waveguide height at port 3 leads to a parasitic parallel capacitance (with a susceptance  $B_d$ ). The desired length of the quarter-wave section is  $\ell_s = \lambda_g/4$  at the design frequency, with the guided wavelength  $\lambda_g$ . In electrical terms it is composed of a physical length  $\ell_p$  and a length  $d'$  accounting for the reference plane shift within the T-junction from its characteristic terminals [Mar51, p. 120, p. 338]. An ideal transformer with a transfer ratio  $n$  connects the quarter-wave section in series to the waveguide between port 1 and 2. In the center of the T-junction is a series inductance (with a reactance  $X$ ). To shift the reference plane of the ports 1 and 2 to those indicated in Fig. 4.1 (virtual intersection of the stub-guide walls with the main-guide), two waveguides with length  $\ell_1 = \ell_2 = b/2 - d$  and characteristic impedance  $Z_w$  are in-between. The lengths  $d$  and  $d'$  as well as the susceptance  $B_d$  and the reactance  $X$  originate from the individual equivalent circuit models that are specified in the Waveguide Handbook [Mar51].

A comparison of the scattering parameters between the equivalent circuit model from Fig. 4.2 and a full-wave simulation of the whole coupling structure in CST Microwave Studio® (2015.02) is given in Fig. 4.3. The scattering parameters of the equivalent model are derived in [KSE+15a]. The width  $b_s$  is varied in order to achieve different coupling values while the length  $\ell_p = 0.8$  mm is kept constant. The equivalent circuit model and the full-wave simulation agree well. As expected, for larger slot heights the error



**Fig. 4.2:** Equivalent circuit model of the coupling structure [KSE+15a].

between simulation model and equivalent circuit model increases as  $b_s$  tends to  $b$ .

Besides the verification of the equivalent circuit model, there are two important results to be stated: A constant coupling factor with low reflection and insertion-loss can be realized. However, there is a resonance shift in the  $s_{11}$ . The first result is the proof of principle and the basis for further investigations. The second result indicates that the length  $\ell_p$  has to be adjusted according to the waveguide height  $b_s$  in order

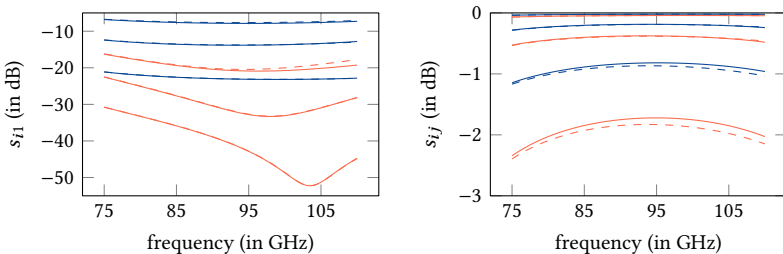


**Fig. 4.3:** Comparison between full-wave simulation (solid lines) and equivalent circuit model (dashed lines) for slot heights 90  $\mu\text{m}$ , 280  $\mu\text{m}$ , and 635  $\mu\text{m}$ . Left:  $|s_{11}|$  (red) and  $|s_{31}|$  (blue), bottom to top as 90  $\mu\text{m}$  to 635  $\mu\text{m}$ . Right:  $|s_{33}|$  (red) bottom to top as 90  $\mu\text{m}$  to 635  $\mu\text{m}$  and  $|s_{21}|$  (blue) top to bottom as 90  $\mu\text{m}$  to 635  $\mu\text{m}$ .

to achieve optimal performance. This is, to keep the electrical length  $\ell_s$  constant for varying heights  $b_s$ , the physical length of the stub-guide has to follow

$$\ell_p = \ell_s - d'. \quad (4.1)$$

The length  $d'$  is dependent on the slot height and is specified in the Waveguide Handbook [Mar51].

To realize the proposed structure, the relatively small height of the stub-guide  $b_s$  is the most challenging part. When fabricating it in one piece with the split-block network, the smallest slot height is limited by the smallest available milling tool. In the workshop of the Technical University of Munich, Chair of High-Frequency Engineering, the minimal diameter of a milling tool with milling depth  $> 1.27$  mm (for WR10 split-block network) has a diameter of  $200\text{ }\mu\text{m}$ . For the phased array antenna, however, smaller coupling values and, thus, slot heights are required to realize the desired amplitude taper. Thus, the coupling structure cannot be manufactured solely by milling. Consequently, the quarter-wave transformer section is realized by a separate piece, a so-called insert that is placed in the split-block network to model the quarter-wave section of the coupling structure.

In the following, two different manufacturing methods (laser-cutting and wire-erosion) to realize the insert are presented. The first method, laser-cutting the insert, is part of the first prototype coupling structure. It enables the realization of coupling slot heights in the range of  $90\text{ }\mu\text{m}$ . The second method, wire-eroding the insert, is an advancement over the laser-cut insert. While the former is attractive in terms of manufacturing costs, the latter has a better accuracy and repeatability. Besides, the wire-eroded prototype enables the optimization of the slot length  $\ell_p$  according to the slot height  $b_s$ . Both prototypes employ WR10 split-block technology for the underlying rectangular hollow waveguide network.

### 4.1.2 Laser-Cut Insert

This section describes the prototype of the coupling structure with a laser-cut insert. The insert is cut from a stainless-steel sheet (material number 1.4310) by means of a laser. The laser has a certain diameter in its focal region, which defines the smallest possible slot height  $b_s$ . The diameter of the laser at LaserJob GmbH in Fürstenfeldbruck was  $40\text{ }\mu\text{m}$ . The raw stainless-steel sheet has a certain thickness corresponding to the slot length  $\ell_p$ . The laser-cut insert is placed in a fitting groove in the split-block network to complete the coupling structure. This fitting groove requires the waveguide network to be modified slightly.

For the model of the laser-cut coupling structure, see Fig. 4.4. The blue geometries are vacuum, the dark-gray geometry is the laser-cut insert. The waveguide of the main-guide (from port 1 to port 2) is bent, providing an alignment for the insert towards the main-guide. The radius (measured from the arc-center to the middle of

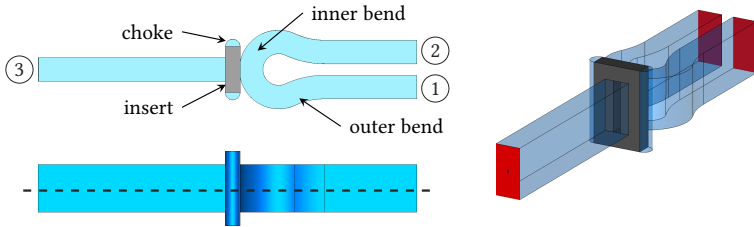


**Fig. 4.4:** Model of the laser-cut coupling structure. Trunk line is from port 1 to port 2; port 3 is the coupled port. The laser-cut insert is placed in a fitting groove and models the coupling slot (i.e., the quarter-wave section).

the waveguide) of the inner bend is  $r_{\text{inner}} = 1.536 \text{ mm}$  and the radius of the outer bend is  $r_{\text{outer}} = 4.909 \text{ mm}$ . Their angular extent is  $\varphi_{\text{inner}} = 229.5^\circ$  and  $\varphi_{\text{outer}} = 24.75^\circ$ , respectively. These dimensions are chosen such that two coupling structures can be placed side-by-side with a spacing of 4 mm. The depth of the groove for the insert is 2.00 mm (maximum milling depth of the 0.8 mm mill) in contrast to 1.27 mm of the rectangular hollow waveguide in each side of the split block (see the cutting plane in the lower-left plot in Fig. 4.4). The width of the groove for the insert equals the thickness of the stainless-steel sheet. The insert is clutched in the groove by the upper and lower part of the split block.

To suppress any cross-talk of the wave traveling around the insert, the length of the groove-section starting at the intersection with the broad waveguide wall (in the E-plane cut of Fig. 4.4, upper left plot) is chosen as a quarter-wavelength of the guided wave. The impedance change between a fictive 10  $\mu\text{m}$  misfit (between groove and insert) and the 0.4 mm radius at the end of the groove is enough to approximate and open at this point. Measurements and simulations show that there is no impact by this coupling mechanism or it is too weak to have any influence.

The model of the laser-cut insert is depicted in Fig. 4.5. The thickness of the insert models the physical length of the coupling slot  $\ell_p$  ("slot length"). The length of the cut (lower left in Fig. 4.5) equals the waveguide width (2.54 mm for the WR10). The width of the cut ("slot height") equals the waveguide height of the quarter-wave section  $b_s$ .

For the prototype, the thickness of the stainless-steel insert is  $\ell_p = 0.8 \text{ mm}$ . This represents a compromise between performance and ease to manufacture the different inserts. However, it does not realize the optimum performance for all slot heights as the slot length would have to be adjusted in order to mitigate the effect of the slot height on the electrical length of the slot from (4.1).

Laser-cutting at LaserJob GmbH in Fürstenfeldbruck enabled contour accuracies on the order of  $\pm 5 \mu\text{m}$  and a smallest possible slot height of 40  $\mu\text{m}$  due to the minimum laser diameter. This supersedes any attempt to mill the coupling structure in a WR10 split-

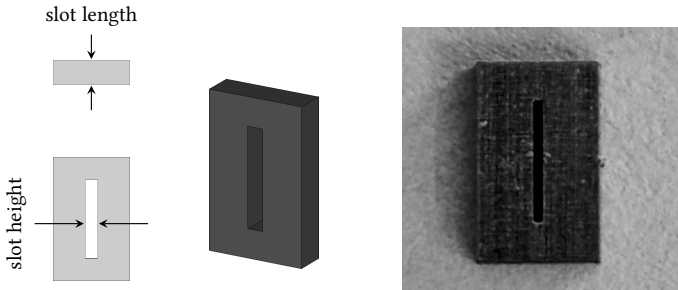


**Fig. 4.5:** Insert for the laser-cut coupling structure. Left: Model of the laser-cut insert. Right: Prototype of the laser-cut insert from stainless-steel (1.4310).

block. Nevertheless, cutting the insert from a stainless-steel sheet by means of a laser also reveals drawbacks. The laser has a certain opening angle which leads to slightly trapezoidal slots and, thus, a strong discrepancy between desired and manufactured slot heights. In addition, the surface within the slot is very rough and spans may seal a part of the laser-cut slot. These two points basically require that every insert is inspected and function-tested after fabrication.

The prototype of the split-block network is manufactured from brass (CW614N), see Fig. 4.6. The slot within the insert models the quarter-wave section with a specific height. As the insert does not stick to the split-block network, it can be replaced. Thus, the coupling factor of the network can be adjusted at any time without the need to mill the whole split block again.

The field distribution at the slot in the main-guide is different from that of the ideal model due to the additional bends that provide the alignment for the insert, see Fig. 4.4. As a consequence, the coupling and reflection coefficients are different from that of the ideal model and the equivalent circuit in Fig. 4.3. The ideal model could be realized by milling, where no end stop is required. However, the general trend (smaller slot height corresponds to a weaker coupling) and the dependency of the electrical length of the quarter-wave section on the slot height is still valid.

The dimensions of the slot height  $b_s$  of the laser-cut insert in the proposed split-block network were obtained by full-wave simulations in CST Microwave Studio<sup>®</sup> (version 2015.2). In the simulation model, a perfect connection between the insert and the split-block is assumed and the height of the waveguide throughout the quarter-wave section is constant (in contrast to the trapezoidal shape when laser-cutting). The slot length of the prototype is  $\ell_p = 0.8$  mm.

Measurements of a prototype coupling structure with six different inserts were carried out with an HP8510 C vector network analyzer with millimeter-wave extension



**Fig. 4.6:** Image of the prototype WR10 coupling structure split-block manufactured from brass (CW614N). Laser-cut insert is placed in the fitting groove. The long waveguide sections are required for connection of the WR10-waveguide flanges.

(effective directivity after calibration by means of time gating: at least 47.5 dB). The six different slot heights  $b_s$  are listed in Tab. 4.1. Here, the desired and the realized slot heights are listed. The manufactured slot heights were measured by means of a microscope, counting the pixels and equating it to the number of pixels of a known length. The mean simulated and measured coupling coefficients are also listed in Tab. 4.1.

The strong coupling values ( $-9.7$  dB to  $-16.3$  dB) can be realized with a discrepancy of  $0.3$  dB to  $0.6$  dB from the desired value, see Tab. 4.1. The variation from the mean coupling value is equal in simulation and measurement. Smaller coupling values cannot be realized with good reliability. The difference between desired and realized coupling value is larger than  $1$  dB. Moreover, the slot heights in the range from  $40$   $\mu\text{m}$  to  $70$   $\mu\text{m}$  are approximately all the same (not listed in the table).

For the frequency behavior of the simulation and the measured laser-cut prototype, see Fig. 4.7. The  $s_{11}$  has two minima due to the bent structure at about  $87$  GHz and  $97$  GHz. For large slot heights, the impact of the T-junction prevails the reflection coefficient. Hence, the limiting factor for large coupling values is the maximum acceptable reflection. The small ripples in the S-parameters are likely due to flange inaccuracies. The differences between simulation and measurement are in part due to the trapezoidal slots from the laser opening angle and in part due to higher losses of the manufactured rectangular hollow waveguide [KSE+15a].

In summary, the realized coupling values with the laser-cut inserts are nearly constant over the whole  $W$ -band for all configurations. The maximum deviation from the mean is  $\pm 0.9$  dB. The weakest coupling factor is  $-24.2$  dB with a maximum deviation of  $\pm 0.7$  dB from the mean. The strongest coupling is  $-9.7$  dB with a maximum deviation of  $\pm 0.9$  dB from the mean.

**Table 4.1:** Simulation and measurement results of the laser-cut coupling structure for six inserts with slot length  $\ell_p = 0.8$  mm and different slot heights  $b_s$ .

desired slot height (in $\mu\text{m}$ )	manufactured slot height (in $\mu\text{m}$ )	$ s_{31} $ simulated (in dB)	$ s_{31} $ measured (in dB)
400	$416 \pm 16$	$-9.7 \pm 0.9$	$-9.4 \pm 0.9$
280	$304 \pm 24$	$-12.4 \pm 0.9$	$-12.0 \pm 0.9$
170	$196 \pm 28$	$-16.3 \pm 0.8$	$-16.9 \pm 0.9$
120	$114 \pm 32$	$-19.3 \pm 0.7$	$-22.7 \pm 0.6$
90	$88 \pm 40$	$-21.6 \pm 0.6$	$-22.5 \pm 0.6$
60	$76 \pm 20$	$-25.0 \pm 0.5$	$-24.2 \pm 0.7$

While laser-cutting is relatively inexpensive compared to milling of the split-block network, it has three inevitable drawbacks. The realized slots are undesirably tapered due to widening of the laser beam beyond the focal point. This induces deviations between the predicted and the actually achieved coupling factors, see Tab. 4.1. Furthermore, there is a minimum amount of material that gets dissipated. This sets the limit of the lowest possible coupling factor which can be achieved by this manufacturing technology. The last drawback is concerned with the length of the slot  $\ell_p$ . In the laser-cut case it is fixed and equals the thickness of the metal sheet and the fitting groove in the split-block. This renders it impossible to optimize the slot lengths for different slot heights. However, it is sometimes necessary to implement very small coupling factors for the outermost elements of a series-fed array antenna and also to adjust the slot length according to the slot height to achieve the best performance.

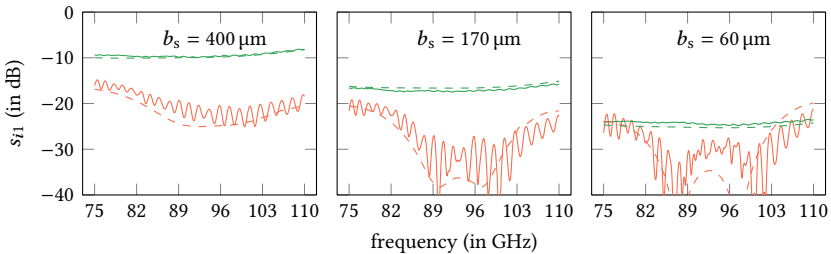


**Fig. 4.7:** Simulation (dashed line) and measurement (solid line) results of the laser-cut coupling structure for three different slot heights. The reflection  $s_{11}$  is red, the coupling  $s_{31}$  is green.

### 4.1.3 Wire-Eroded Insert

A coupling structure with an insert manufactured by wire-erosion is presented in this section. It is an improved version of the laser-cut insert, as it fulfills highest demands on accuracy and repeatability of the manufactured workpiece. Moreover, the wire-eroded insert provides more freedom to modify the coupling slot. This is, the length  $\ell_p$  and height  $b_s$  of the quarter-wave transformer section can be tuned individually. There is no lower bound for the slot height. The expense for the wire-eroded insert is a longer manufacturing time (each insert is manufactured individually) and, thus, additional costs [KSE+17].

Wire-erosion is a manufacturing technique based on spark erosion. Due to an electric potential difference between a wire (the tool, cathode) and the workpiece (anode), sparks emit when the distance between tool and workpiece is small enough. These sparks erode the material of the workpiece only in the near vicinity of the wire. By moving the wire into the workpiece, contours can be eroded. As this process is contact-less, the forces that act on the workpiece and the tool are relatively small, allowing high accuracies of the eroded contour (on the order of  $\pm 2 \mu\text{m}$  in the workshop of the Max Planck Institute for Plasma Physics in Garching). The smallest viable radius is  $100 \mu\text{m}$  and is mainly determined by the wire-diameter. The surface roughness of the wire-eroded faces has been measured and is on the order  $R_z = 2.1 \mu\text{m}$  (average distance between the highest peak and the lowest valley). For comparison, the expected surface roughness of a WR10 split-block waveguide from a precision mill is on the order of  $R_z = 1.6 \mu\text{m}$ . Hence, the surface roughness of the wire-eroded faces would lead to slightly higher Ohmic losses. However, the difference between the nominal conductivity of brass/Albromet W-200 (material of the split-block) and stainless steel (material of the insert) blurs this effect and, thus, the realized wire-eroded surface roughness is perfectly adequate.

For the model of the wire-eroded coupling structure, see Fig. 4.8, where the waveguides are colored blue and the stainless-steel insert is colored dark-gray. The main-guide (between port 1 and 2) is realized similar to a hairpin and, thus, requires less space in contrast to the three-bent design of the laser-cut coupling structure in Fig. 4.4. The wire-eroded insert has an “L”-shaped fit to provide correct positioning of the insert in the cutting plane. The part of the insert that reaches into the waveguide, represents the quarter-wave transformer section, see Fig. 4.4. Towards port 3, the rectangular hollow waveguide is slightly bent to align the center of the waveguide at port 3 with the center-line between port 1 and 2. This gives the possibility to rotate the whole coupling structure around this line (compare dashed line in Fig. 4.4 upper-left sketch) and, thus, to exchange port 1 with port 2 while port 3 is still at the same location.

As can be seen in Fig. 4.8, the height of the insert equals the width of the WR10-waveguide. To provide a good electrical contact between the split block and the insert, both parts have to be manufactured accurately. No choke-like structure is possible at the short walls of the WR10-waveguide without annihilating the flexibility to modify

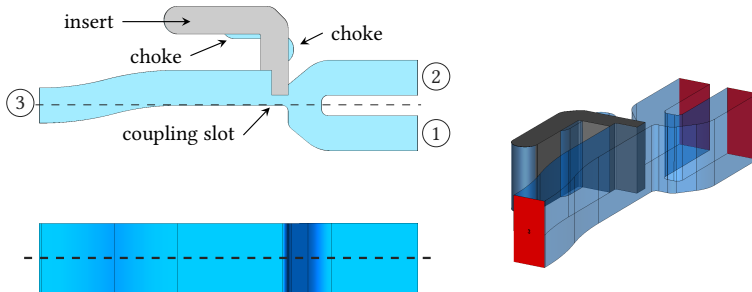


**Fig. 4.8:** Model of the wire-eroded coupling structure. The trunk line is from port 1 to port 2; port 3 is the coupled port. The wire-eroded insert is placed in a L-shaped fitting groove and realizes the coupling slot (i.e., the quarter-wave section).

the length and width of the quarter-wave section individually. If the insert is too small, an electric field will leak towards port 3 and alter the coupling factor. If the insert is too large, the two split blocks will have a poor contact and lead to a bad electrical performance. However, from experiments it is better to have a slightly larger insert, which is pressed into the split blocks, than a too short insert leaving slits for the field to couple. The tolerance range of the insert is chosen accordingly.

Only the straight sections of the L-shaped groove are dedicated for alignment of the insert and the radii are dimensioned such that they do not contact with the insert, see Fig. 4.8. To compensate the effect of manufacturing tolerances within the cutting plane (i.e., between the insert and the fitting groove) on the electrical performance, two choke structures are employed. These chokes realize a short and transform it through a quarter-wave line (approximately) to the location of the misfit between insert and groove, see Fig. 4.8 upper-left plot.

The insert itself is derived from a two-dimensional contour, which is required for fabrication by wire-erosion, see Fig. 4.9. The nose-piece of the insert reaches into the WR10-waveguide of the coupling structure and, thus, shapes the quarter-wave section. The geometric parameters that influence the length and height of the quarter-wave section are indicated in Fig. 4.9. They can be specified independently allowing the length of the quarter-wave section to be optimized for a certain slot-height.<sup>1</sup>

The start and end point of the wire-erosion path is placed inside the left choke on the long edge of the “L”, see Fig. 4.8, as a residual nose remains at this point and may lead to a misalignment or degraded coupling behavior if placed at another position.

A prototype of the insert is shown in Fig. 4.9. It was manufactured from a stainless-

<sup>1</sup>As a side-note: it is also possible to add a second quarter-wave transformer section to improve the electrical properties of the coupling structure.

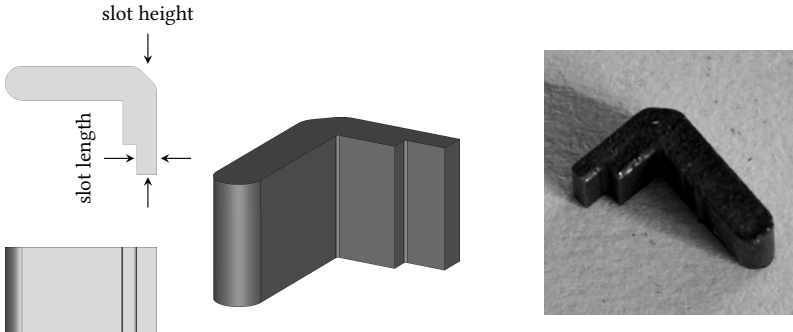


**Fig. 4.9:** Wire-eroded insert for the improved coupling structure. Left: Model. Right: Prototype.

steel (material number 1.4301) sheet that has been abraded to a thickness of 2.54 mm, first. For the evaluation of the wire-eroded coupling structure, three different inserts and the split-block network were manufactured. The split-block was milled in brass (material number CW614N), see Fig. 4.10. In one of the split blocks, an insert is placed in the fit. In order to lock the insert, the opposing part of the split block is mounted after the insert has been placed in its fit.

The realized slot lengths and slot heights are listed in Tab. 4.2. Each combination was numerically optimized by full-wave simulations using CST Microwave Studio® (version 2016.4). The goal was a flat coupling factor in the frequency range from 75 GHz–105 GHz. For each insert, the simulated  $s_{31}$ , the measured  $s_{31}$  right after fabrication,

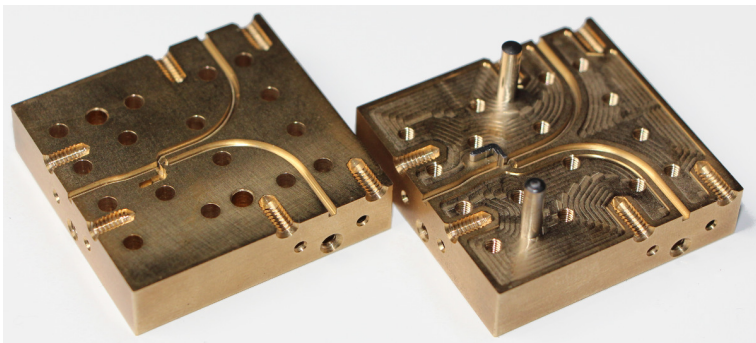


**Fig. 4.10:** Prototype WR10 coupling structure with a wire-eroded insert [KSE+17].

**Table 4.2:** Manufactured wire-eroded inserts with corresponding simulated and measured coupling factors (mean value and maximum deviations).

slot height (in $\mu\text{m}$ )	slot length (in $\mu\text{m}$ )	$ s_{31} $ simulated (in dB)	$ s_{31} $ measured after fabrication (in dB)	$ s_{31} $ measured after reworking (in dB)
200	635	$-14.5^{+0.5}_{-0.2}$	$-14.8^{+0.4}_{-0.3}$	$-14.6^{+0.7}_{-0.3}$
80	763	$-21.8^{+0.6}_{-0.2}$	$-22.5^{+0.6}_{-0.3}$	$-21.7^{+0.6}_{-0.3}$
25	865	$-31.5^{+0.5}_{-0.2}$	$-35.5^{+1.0}_{-1.3}$	$-30.9^{+0.9}_{-0.9}$

and the measured  $s_{31}$  after reworking of the insert are listed with their mean value and maximum and minimum deviation from that mean. The measurements were performed with a HP 8510C vector network analyzer with millimeter wave extensions. The calibration check showed a maximum reflection of  $s_{11} \leq -36$  dB for a standard waveguide section.

In Tab. 4.2, the realized coupling factors span the range from  $-31$  dB to  $-14$  dB. The insert with the largest slot height ( $b_s = 200 \mu\text{m}$ ) deviates by 0.3 dB from the desired coupling value. The  $80 \mu\text{m}$  slot height deviates by 0.7 dB and the  $25 \mu\text{m}$  slot height by 4.0 dB. The reason for this trend are the manufacturing tolerances. These are on the order of 40% for the smallest slot height and, thus, have a strong impact on the realized coupling factor. The smaller the desired slot height, the larger the relative impact of the manufacturing tolerance and, thus, the larger the difference between desired and manufactured coupling value.

The realized mean coupling factor is always below the expected coupling factor from the simulated model. The difference increased for smaller slot heights. Modeling this in a full-wave simulation showed that the discrepancy is due to a smaller realized slot height in the range of  $10 \mu\text{m}$ . The insertion loss from port 1 to port 2 is around 0.5 dB with the  $\sim 50$  mm waveguide from the measurement flange to the coupling structure as main contributor. The insertion loss of the coupling structure alone is about 0.2 dB for the  $200 \mu\text{m}$ -insert. It is basically driven by the tap-off towards port 3.

The frequency characteristic of the wire-eroded coupling structure is plotted in Fig. 4.11. For the  $200 \mu\text{m}$  and the  $80 \mu\text{m}$  slot, the trend of the measured S-parameter agrees very well with the simulated values. As already stated, the  $25 \mu\text{m}$  slot has the largest deviations from the expected behavior. The ripples in the measured  $s_{11}$  are due to flange inaccuracies.

The small differences between expected and realized coupling behavior can be corrected as the design of the insert allows to rework and tune it after fabrication and measurement. For this, the nose piece of the insert, see Fig. 4.9, is abraded with abrasive

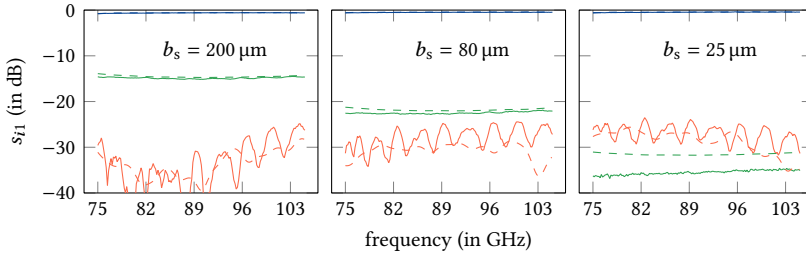


**Fig. 4.11:** Simulated (dashed lines) and measured (solid lines) S-parameters of the wire-eroded coupling structure. The  $s_{11}$  is red, the  $s_{31}$  is green, and the  $s_{21}$  is blue.

paper (a 400 grit was used in for this work). With two careful iterations of sanding and subsequent measurement, the error between desired and manufactured coupling factor was corrected (0.1 dB for the two largest slot heights), see Tab. 4.2. Tuning the insert for the smallest slot height is more challenging as even small modifications have a strong impact. After reworking, the difference between desired and achieved coupling value is 0.6 dB. This difference is considerably smaller as compared to the performance right after fabrication of the insert. Besides the outstanding manufacturing accuracy and good surface quality, it is possible to rework and tune the wire-eroded insert to the desired behavior after fabrication and to test it without the need to mill the whole split-block again.

The coupling structure based on a wire-eroded insert yields the desired behavior also in a prototype and is reliable in terms of manufacturing outcome. By design, the quarter-wave section of the coupling structure can be configured in both, their length and height. The realized coupling factors agree well with the desired values. Fine-tuning is possible without the need to manufacture the whole split-block another time.

## 4.2 Variable Phase Shifter

A phase shifter is a waveguide element that realizes a variable electrical length in-between two ports. The electrical length is either controlled in discretized states or in a continuous manner, while the controlling mechanism might be electrical or mechanical.

Phase shifters can be categorized into three prevailing technologies: Switched-line, loaded-line, and reflection-type phase shifters. Switched-line phase shifters are based on waveguides with different lengths. A switch changes the waveguide section that is connected to the external ports, thus, modifying the electrical length in-between them. Conventional switching elements are PIN diodes, field-effect transistors or

microelectromechanical systems (MEMS) [Gar72; GSB11; RTH02]. Loaded-line phase shifters modify the propagation constant in order to change the electrical length. This can be realized by periodic loading of the transmission line with shunt varactor diodes or MEMS, by variably modifying the permeability with a ferrite or the permittivity with liquid crystals [BR98; FKR+13; PZ02]. Reflection-type phase shifters transform a variable reflective load into a variable transmission coefficient by means of circulators or hybrid junctions. Variable reflective loads might be switched transmission lines, varactor diodes or sliding shorts [KPY+02; LCCS07; LC57; PZ02].

Considering the environmental conditions inside the vessel of a nuclear fusion experiment, see Section 1.3, the technological choice is clear. Switched-line and loaded-line phase shifters are built from materials that are not suitable for this environment. This is, they are either stressed by the strong radiation, are magnetic, or are not temperature and vacuum compatible. Reflection-type phase shifters, on the other hand, can be built predominantly from metal and, thus, can sustain the environmental conditions inside the vessel of a nuclear fusion experiment.

In the following, the fundamental model of a reflection-type phase shifter in rectangular hollow waveguide technology is introduced. Realizations of the individual components and the evaluation of prototypes are presented subsequently.

### 4.2.1 Fundamental Model

For a schematic of the reflection-type phase shifter, see Fig. 4.12. The basic building blocks are a quadrature hybrid (hybrid-junction) and two synchronously-moved sliding shorts that are located in a variable distance  $\ell$  from the hybrid-junction. The function of the hybrid-junction may be considered as interchanging the reflection coefficient of the sliding short with the transmission coefficients of the whole two-port.

A wave that enters the phase shifter at port 1 is split equally in power, see Fig. 4.12. The wave that travels through the hybrid-junction to the upper port at the right experiences a phase shift of  $90^\circ$  with respect to the wave traveling straight through the hybrid-junction (lower branch). The individual waves travel towards their dedicated sliding short in a distance of  $\ell$  from the hybrid-junction. There they get (totally) reflected and, thus, travel back towards the hybrid-junction where the individual waves split up again. The wave entering at the upper-right port has a  $90^\circ$  phase shift already. It is split into two parts (in terms of power) that are directed towards port 1 and 2. Towards port 1 there is an additional (fictitious) relative phase shift due to crossing the hybrid-junction again. Thus, the phase of the individual waves with respect to the reference phase is  $180^\circ$  for port 1 and  $90^\circ$  for port 2. The other wave coming from the second sliding short and entering the hybrid-junction at the lower-right port behaves equally. The wave is split equally in terms of power. The part that crosses the hybrid-junction gets a relative phase shift of  $90^\circ$  with respect to the other half. At port 1, the wave of the lower sliding short has a relative phase of  $0^\circ$  degree and the wave from the upper sliding

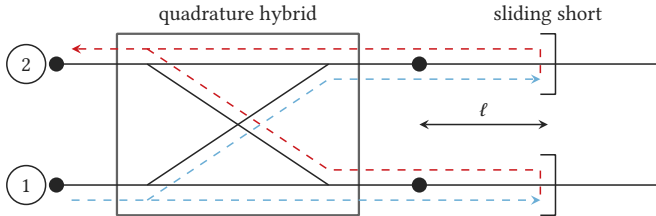


**Fig. 4.12:** Schematic drawing of a reflection-type phase shifter with a quadrature hybrid and two synchronously-moved sliding shorts.

short has a relative phase of  $180^\circ$ . They interfere destructively – in the ideal case no power is reflected at port 1. At port 2, the wave from the upper sliding short has a relative phase of  $90^\circ$  and the wave from the lower sliding short has a relative phase of  $90^\circ$ . They interfere constructively and, thus, the power entering the phase shifter at port 1 is delivered to port 2.

The previous paragraph described the core functionality of the reflection type phase shifter on the basis of ideal components. Possible inaccuracies have not been taken into account. The phase-shift can be realized by moving both sliding shorts simultaneously. If the initial state is  $\ell_0$  and the sliding shorts are moved by a  $\Delta\ell$ , the relative phase shift between both states is

$$\Delta \arg(s_{21}) = -\beta(2(\ell_0 + \Delta\ell) - 2\ell_0) = -2\beta\Delta\ell, \quad (4.2)$$

with the propagation constant  $\beta$  of the waveguide.

Due to the harsh environment, the reflection-type phase shifter is realized in a rectangular hollow waveguide manufactured in split-block technology. The hybrid-junction is a branch-guide coupler, which can cover the required frequency range [Lev73; Ree58]. The variable reflective load is a sliding short which enables a synchronous control of several phase shifters arranged in a row, where all sliding shorts share the same reference plane. The sliding short represents a filter structure in the rectangular hollow waveguide that has no contact to the side-walls.

In the following two sections, the design and prototypes of the sliding-short and the branch-guide coupler are discussed. The design of the whole phase shifter based on these individual elements is presented subsequently.

### 4.2.2 Self-Aligning Sliding Short

A sliding short can be realized by a contacting or a non-contacting plunger. The electrical performance of the contacting sliding short depends strongly on the quality and position of the physical ground short. At millimeter-wave frequencies, the ground

short may vary unpredictably due to surface roughness and frictional wear [BR82; Ker88] and result in random variation of the complex reflection coefficient. Furthermore, power leakage and radiation may occur [Ker88] in case of a non-ideal contact. A non-contacting sliding short (i.e. plunger) can be realized from metal only [BR82; Ker88; NK92; SB13] or with an additional dielectric as insulator [BR82; MWK95; WKM95]. A variable reflective load based solely on a dielectric [MPR01] changes the phase velocity of the guided wave over a variable length. However, dielectrics have to be avoided for in-vessel use in a nuclear fusion experiment due to unacceptable outgassing.

Metal-only sliding shorts or plungers often employ a quasi-periodic choke structure with alternating low- and high-impedance sections [BR82; Ker88; MWK95; SB13; WKM95]. These lead to a transmission stop-band of the supported wave and, thus, to an almost perfect reflection (except for Ohmic losses). An external mounting frame or an insulating dielectric can be used to position the plunger on the central axis of the rectangular hollow waveguide. Alternatively, a fitting groove may be used to direct the plunger [Ker88; MWK95; SB13; WKM95]. In any case, the coincidence of the plunger axis and the central axis of the rectangular hollow waveguide enable best performance. It is insignificant whether the choke structure has a rectangular or a circular cross-section [Ker88].

### Fundamental model of the proposed sliding short

The proposed design uses a cylindrical plunger inside the rectangular hollow waveguide. The plunger is composed of three sections: a non-contacting choke section, a guiding section, and a mechanical stop (see Fig. 4.13). The non-contacting choke “supports” an evanescent coaxial mode and, thus, provides the electrical short. The guiding section enables mechanical guidance and stabilization by a fitting hole. It prevents the non-contacting section from undesired and disruptive waveguide wall contact. The mechanical stop provides a means to control several sliding shorts that all share the same reference plane.

The non-contacting choke is designed according to the traditional  $\lambda/4$ -design, as this is superior to a low-pass filter technique within a single waveguide band [BR82]. The individual impedance sections have a length of 0.8 mm (about  $\lambda/4$  at 92.5 GHz). The low-impedance section has a diameter of 1.15 mm. The high-impedance section has a diameter of 0.6 mm. The electrical performance improves for larger impedance discontinuities [BR82]. The chosen values are basically determined by mechanical considerations while achieving an acceptable electrical performance. This is, the largest possible diameter that does not contact with the waveguide walls represents the low-impedance section. The high-impedance section is chosen as large as possible in order to achieve an acceptable electrical performance (a smaller diameter yields better performance). In total, the non-contacting choke section of the plunger consists of 3 alternating low-impedance and high-impedance sections. The maximum leakage is

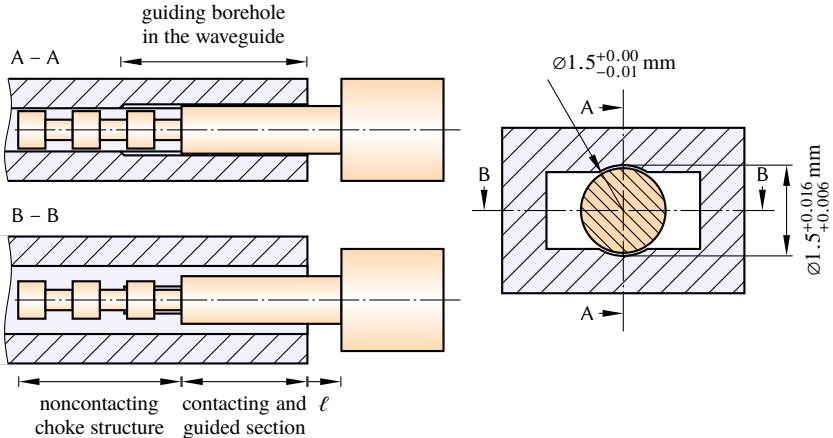


**Fig. 4.13:** Left: Axial cut of the sliding short in the rectangular hollow waveguide with a non-contacting and a guiding section [KSEC17]. Right: Cross-sectional few of the sliding short in the rectangular hollow waveguide [KSEC17].

below  $-40$  dB over the whole W-band [KSEC17]. Fewer sections imply higher leakage and vice versa. As more sections imply a larger space consumption (contacting section of the plunger has to be elongated, too), a deteriorated mechanical stability, and higher manufacturing cost, this leakage is considered sufficiently low.

The contacting section of the plunger guides the sliding short in a fitting hole along the center axis of the rectangular hollow waveguide. The diameter of the fitting hole is 1.5 mm with an ISO 286 tolerance grade on hole F7, see Fig. 4.13. The length of the guiding section of the plunger is 4.5 mm with a diameter of 1.5 mm with ISO 286 tolerance grade on shaft h7. Thus, the minimum and maximum shaft between plunger and fitting hole is 6  $\mu\text{m}$  and 26  $\mu\text{m}$ , respectively. The length of the guiding section guarantees that no wall contact will occur at the non-contacting section for a displacement of  $\ell = 1.5$  mm and the worst tolerance conditions. The only wall contact will be within the guiding section, where the field has already been attenuated due to the choke. Consequently, this contact has no effect on the electrical properties of the sliding short.

The proposed plunger is circularly symmetric and, thus, can be manufactured on a lathe. This provides sharp edges between low- and high-impedance sections. Furthermore, the lengths of the individual sections and the position of the reference plane can be manufactured with machine accuracy ( $\pm 5 \mu\text{m}$  at the workshop of the Technical University of Munich, Chair of High-Frequency Engineering).

## Investigation of plunger misalignment

Misalignment of the plunger within the rectangular hollow waveguide is possible in two different ways: the central axis of the plunger may have a translational offset relative to the central axis of the waveguide or both central axes may be tilted relative to each other. Reasons for the misalignment are mechanical tolerances in design and manufacturing. The impact of both misalignment scenarios (offset and tilt) from the ideal centered position is analyzed in the following – also considering the conditions where the misaligned plunger gets rotated around the waveguide central axis. For a visualization of these misalignment scenarios, see [KSEC17].

Both misalignment scenarios are empirically investigated by a parameter study in CST Microwave Studio® (version 2015.6). For the offset positions  $\ell$  from 0 mm to 1.5 mm, the maximum possible misalignment such that the plunger intersects with the waveguide walls is modeled (intersecting by 5  $\mu\text{m}$ ). In this misaligned position, the plunger gets rotated around the central axis of the rectangular hollow waveguide in angular steps of 1°. The S-parameter relative error of the last adaptive meshing cycle for each parameter set (offset position and angular rotation) was smaller than 0.01. The results are plotted in Figs. 4.14 and 4.15, respectively. At each offset position  $\ell$ , the maximum and minimum reflection and transmission (leakage) that occur over the whole frequency range (from 75 GHz–110 GHz) and all rotation positions (1° step width), are plotted. This is, each data point is either the maximum or the minimum reflection/transmission that occurs over the complete waveguide band and all rotations of the misaligned plunger around the central axis of the waveguide. The leakage  $|s_{21}|$  considers the total field of the first five modes as symmetry and homogeneity are destroyed due to the misalignment and higher order modes can exist [Ker88].

The results of the displacement scenario are depicted in Fig. 4.14. The maximum leakage occurs for the outermost offset position ( $\ell = 1.5 \text{ mm}$ ). It is always below  $|s_{21}| < -35 \text{ dB}$ . The reflectivity  $|s_{11}|$  decreases for increasing offset positions, which can be attributed to larger Ohmic losses due to a slightly longer transmission line to the plunger. The waveguide walls were modeled with a finite conductivity of  $15.9 \times 10^6 \text{ Sm}^{-1}$ . The reflected phase  $\arg(s_{11})$  varies over all rotation steps by  $\pm 0.04^\circ$  at 75 GHz and  $\pm 0.1^\circ$  at 110 GHz. Hence, this variation can be neglected.

The results of the tilting scenario are depicted in Fig. 4.15. The maximum leakage occurs again for the outermost offset position ( $\ell = 1.5 \text{ mm}$ ). It is always below  $|s_{21}| < -28 \text{ dB}$ . The reflected amplitude  $|s_{11}|$  decreases for increasing offset positions  $\ell$ , which can again be attributed to larger Ohmic losses. The reflected phase  $\arg(s_{11})$  varies over all rotation steps by  $\pm 0.6^\circ$  at 75 GHz and  $\pm 1.3^\circ$  at 110 GHz. The influence of the tilting on the reflected phase is stronger as compared to the displacement. However, the error is still relatively small.

From the previous investigations of the influence of the mechanical tolerances on the sliding short performance, three conclusions can be drawn. First, the reflection

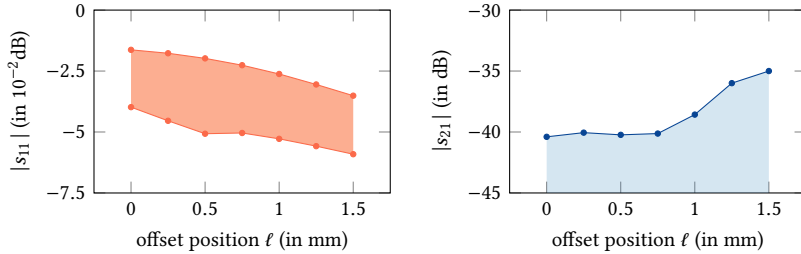


**Fig. 4.14:** Simulation of plunger displacement from the central axis of the rectangular waveguide. Plunger displaced such that it intersects with the waveguide wall. Minimum and maximum values are taken from all rotation steps and within the frequency range from 75 GHz–110 GHz.

amplitude decreases for increasing offset positions. This is due to increasing Ohmic losses, there is no influence from misalignment. Secondly, there is an influence of the misalignment on the reflected phase. This effect is, however, small and can be neglected. Lastly, the leakage is largest for the outermost offset positions. For all scenarios, it is still at a very low level (smaller than  $-28$  dB).

### Sliding-short prototype

To verify if the proposed sliding short can be realized and achieve the expected performance, a prototype of the sliding short plunger with the corresponding WR10 split-block waveguide and washers (with thickness 0.5 mm, 1.0 mm, and 1.5 mm) for a defined reference position were manufactured, see Fig. 4.16. The plunger was manufactured on

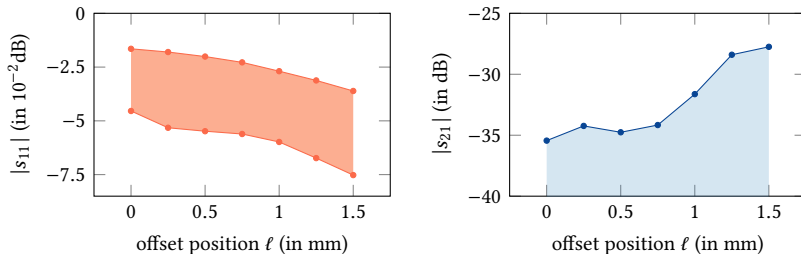


**Fig. 4.15:** Simulation of plunger tilting from the central axis of the rectangular waveguide. Plunger tilted such that it intersects with the waveguide wall. Minimum and maximum values are taken from all rotation steps and within the frequency range from 75 GHz–110 GHz.



**Fig. 4.16:** Left: Image of the sliding-short prototype with WR10 split-block waveguide, plunger, and washers [KSEC17]. Right: Split-block half with gliding sliding short.

a lathe from nickel silver. The expected machine accuracy is about  $\pm 10 \mu\text{m}$ . The guiding hole for the plunger was drilled into the split-block (brass with a nominal conductivity of  $15.9 \times 10^6 \text{ Sm}^{-1}$ ) before the waveguide was milled. The accuracy for milling is on the order of  $\pm 10 \mu\text{m}$  on the used machine at the workshop of the Technical University of Munich, Chair of High-Frequency Engineering. The three washers are placed between the stop-end of the plunger (reference plane) and the waveguide flange-face of the split-block. Thus, the position of the sliding short within the rectangular waveguide can be controlled and determined. The realized thickness of the individual washers was measured with a micrometer gauge (measurement uncertainty  $\pm 5 \mu\text{m}$ ). The measured values are listed in Tab. 4.3.

The S-parameters were measured with an HP 8510C vector network analyzer and millimeter-wave extensions (calibration with thru-reflect-line standards). During an S-parameter measurement, a rubber band established a certain contact pressure of the plunger and the washer on the flange face. The reflectivities from measurement and simulation are both plotted in Fig. 4.17. The measured reflectivity changes for the offset positions from 0 mm to 1.5 mm (washer thicknesses), where the maximum and minimum values over all offset positions are displayed in Fig. 4.17 left. The measured  $|s_{11}|$  is slightly smaller than that from the simulation with the nominal conductivity of brass. Besides, the reflection from the calibration kit short (covering the flange-face instead of inserting the sliding short) is lower as compared to that of the sliding short. The reason is the longer waveguide to the actual short position (50 mm as compared to 40.2 mm for the zero-offset sliding short).

From the reference measurement of the calibration-kit short, the realized conductivity of the waveguide (degraded due to surface roughness) was obtained and can be specified as  $10.5 \times 10^6 \text{ Sm}^{-1}$ . A simulation with the realized conductivity agrees well with the

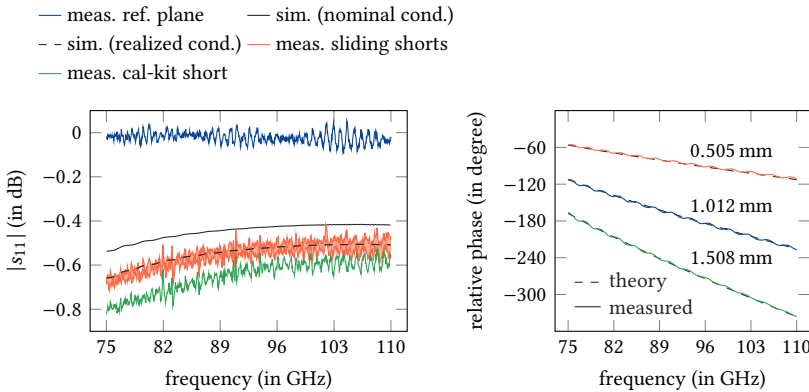


**Fig. 4.17:** Measurement and simulation of the proposed sliding short prototype. Left: Minimum and maximum reflection magnitude for offset positions between 0 mm and 1.5 mm. Right: Relative phase between two offset positions; measured and theoretical values.

measured reflectivity, see Fig. 4.17. A correction of the reference plane shift (40.2 mm waveguide attenuation) yields a reflectivity larger than  $-0.1$  dB. Also the ripples in the  $|s_{11}|$  blur the realized reflectivity, the mean reflectivity is about  $-0.02$  dB – which is expected from the simulations in Section 4.2.2. The ripples are due to flange inaccuracies.

The relative phase differences between the zero-offset and offset positions 0.5 mm, 1.0 mm, and 1.5 mm from the flange face are depicted in the right plot of Fig. 4.17. For comparison, the theoretically expected phases  $\Delta \arg(s_{11})$  for the corresponding offset positions from  $\Delta \arg(s_{11}) = -2\beta_{10}\Delta\ell$  (with  $\beta_{10}$  as the phase constant of a TE<sub>10</sub>-wave in a WR10-waveguide and the relative offset  $\Delta\ell$ ) are evaluated. Apart from small ripples, the measured and theoretically expected phases agree very well.

From the measured phase difference, the corresponding offset position can be retrieved. For this, the phase relation has to be reformulated to  $\Delta\ell = \Delta \arg(s_{11}) / (2\beta_{10})$ . The retrieved offsets are listed in Tab. 4.3 together with the physically measured offsets (from a micrometer gauge with  $\pm 5$   $\mu$ m uncertainty). The maximum difference between retrieved and physical offset is 6  $\mu$ m and, thus, smaller than the manufacturing accuracy.

To analyze the repeated accuracy of the sliding short manufacturing process, 10 out of 89 sliding shorts were measured. The deviation from the mean reflection and the deviation from the mean phase of all sliding shorts are evaluated, see Fig. 4.18. The deviation of the reflected amplitude is below  $-50$  dB and, thus, negligible. The phase deviation is smaller than  $\pm 1^\circ$ , which is slightly smaller than the expected  $\pm 1.3^\circ$  from the influence of plunger tilting in Section 4.2.2.

In summary, the performance of the proposed sliding short agrees well in simulation

**Table 4.3:** Comparison between theoretical and measured offset positions.

Mechanically measured	Retrieved from reflected phase
0.505 mm	0.499 mm
1.012 mm	1.014 mm
1.508 mm	1.505 mm

and measurement. The evaluation of 10 sliding shorts shows a good repeatability.

#### 4.2.3 Hybrid-Junction (Branch-Guide Coupler)

As each sub-component of the phase-shifter (or the array antenna) has to function in the desired frequency range, also the hybrid-junction has to have an operational frequency range from 75 GHz to 105 GHz. In literature, there are several types of hybrid-junctions for rectangular hollow waveguides. For example, the short-slot hybrid [Rib52] or the branch-guide coupler [Lev73; You62]. The latter, however, can achieve more than an octave bandwidth on a relatively small area [Lev73; You62]. In addition, manufacturing this component in a milled *E*-plane split-block network is possible. No other hybrid-junction has comparable features and, thus, the quadrature hybrid is realized as a branch-guide coupler.

A branch-guide coupler has two parallel waveguides with each end being a port.

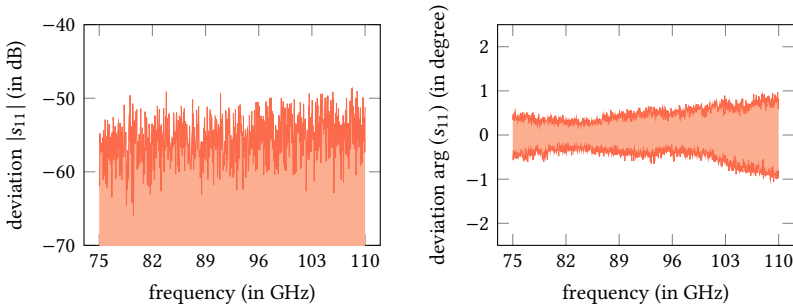


**Fig. 4.18:** Measurement of 10 randomly selected (out of 89) sliding shorts. Left: Maximum and minimum deviation of the reflection magnitude from the mean magnitude of all sliding-shorts. Right: Maximum and minimum deviation of the reflection phase from the mean phase of all sliding-shorts.

Both waveguides are interconnected by several branches. These branches have a length and spacing of roughly a quarter-wavelength of the guided wave, while, due to junction effects [Mar51], the real length and spacing of the branches need to be slightly shorter. The coupling factor is defined by the height of the branches and the bandwidth by the number of branches. Larger branch heights increase the coupling and, vice versa [Lev73; Ree58; You62]. More branches increase the bandwidth and, vice versa [You62]. Increasing the number of branches, however, requires to reduce the height of all branches in order to keep the coupling factor constant.

There are two possibilities to optimize the performance of the branch-guide coupler. One possibility is to vary the branch height (and, thus, the branch impedance) throughout the coupler [LC57; Ree58] to reduce reflection and maximize directivity. The other possibility additionally varies the waveguide height of the two parallel waveguides (main guides) [Lev73; You62] and, thus, allows to shape and optimize the pass-band performance of the hybrid-junction for a certain characteristic (e.g., Butterworth or Chebyshev) [Lev73]. Clearly, the latter type provides more possibilities and its performance is in general better than varying only the branch heights. However, the manufacturing is more difficult and the coupler requires more space [You62]. Besides, the branch-guide coupler design that varies the main-guide impedance yields no realizable geometry for a coupling strength of  $-3$  dB due to too small branch heights or vanishing metal walls in-between the individual branches [KSEC17; Lev73]. Consequently, the reflection-type phase shifter is based on a branch-guide coupler that keeps the main-guide height constant and varies only the branch heights. In particular, it is based on the design by Reed [Ree58] that has different heights of the outermost two branches (left and right branch in Fig. 4.19) and the inner ones.

The smallest millable slot at the workshop of the Technical University of Munich, Chair of High-Frequency Engineering is  $200\text{ }\mu\text{m}$  for a cutting depth of  $1.27\text{ mm}$  ( $W$ -band waveguide in split-block technology). The initial design values of the branch-guide coupler are deduced from the formulas in [Ree58] for a seven slot design. This corresponds to the maximum number of branches for the minimum slot height of  $200\text{ }\mu\text{m}$ . The formulas yield a branch height of  $192\text{ }\mu\text{m}$  for the two outermost branches and  $362\text{ }\mu\text{m}$  for the five inner ones. The spacing and the length of the individual branches should be, by design, a quarter-wavelength of the guided wavelength  $\lambda_g/4 = 1.100\text{ mm}$ . Considering the junction effects [Mar51, p.338] the slot length is on the order of  $0.8\text{ mm}$  [KSEC17]. The final values were obtained by full-wave simulation and optimization with CST Microwave Studio<sup>®</sup> (version 2015.6). These are  $200\text{ }\mu\text{m}$  branch height for the outermost branches (left and right branch, compare Fig. 4.19) and  $340\text{ }\mu\text{m}$  branch height for the inner five branches. The branch length of all branches is  $0.81\text{ mm}$  and the spacing in-between the individual branches is  $1.07\text{ mm}$ .

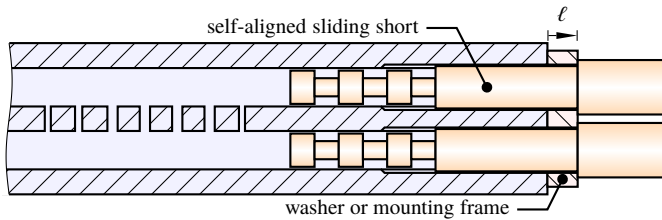


Fig. 4.19: Model of the reflection-type phase shifter [KSEC17].

#### 4.2.4 Prototype Reflection-Type Phase Shifter

The reflection-type phase shifter consists of the previously described branch-guide coupler and the non-contacting sliding short. The branch-guide coupler is milled in Albromet-W 200 (ALBROMET GmbH, 82538 Geretsried, Germany), which is a copper-nickel alloy and suitable for in-vessel use in the ASDEX Upgrade tokamak in Garching, Germany. The sliding short is manufactured on a lath from stainless steel (material number 1.4301). The sliding short plunger requires a fitting hole on the central axis of the rectangular hollow waveguide, which is also milled for this prototype with a 1.5 mm radial mill. A model of the reflection-type phase shifter is depicted in Fig. 4.19. The left two ports of the branch-guide coupler are the input and output port of the phase shifter. The right two ports are connected to two individual but synchronously moved sliding shorts. The plungers are guided in the fitting hole within the waveguide and a washer enables the equal positioning. The end-stop reference plane of all sliding shorts has a smaller diameter as compared to the prototype plunger. The reason is the small distance between both sliding shorts, see Fig. 4.19. For an image of the manufactured prototype see Fig. 4.20.

Measurements of the prototype phase shifter were carried out with an HP 8510C vector network analyzer and millimeter-wave extension modules. After the calibration with thru-reflection-line (TRL) standards the refection of a standard thru-section of the calibration kit showed a reflection below  $-40$  dB. To analyze different phase-states (i.e., plunger positions), four washers with measured thickness (micrometer gauge with  $\pm 5 \mu\text{m}$  uncertainty) 0.526 mm, 0.993 mm, 1.508 mm, and 2.034 mm were placed subsequently in-between the split block and the reference plane of the sliding shorts. A rubber band establishes sufficient contact pressure and equivalent alignment for all phase states, see Fig. 4.20 right. Simulations were carried out in CST Microwave Studio<sup>®</sup> (version 2016.4).

The insertion loss of the phase shifter is plotted in Fig. 4.20, while two different reference planes are considered. One reference plane is at the flange faces of the split block and another reference plane is 0.1 mm apart from the phase shifter ports. The

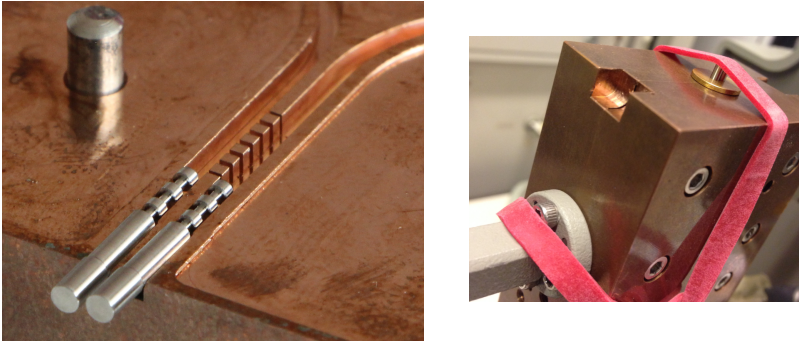


**Fig. 4.20:** Left: Image of the phase shifter prototype [KSEC17]. Split-block milled in Albromet-W 200 and sliding-short from stainless steel. Right: Measurement setup, sliding-shorts and washer fastened with a rubber band.

measured insertion loss is visualized as bound of the maximum and minimum values that occurred for the different washers (except the 2 mm washer as it is out of the sliding short specification). With the reference plane at the split-block flanges, an insertion loss of around 0.6 dB to 0.8 dB from 80 GHz to 105 GHz is achieved. With the shifted reference plane (removed Ohmic losses of the 68 mm waveguide in-between branch-guide coupler and flange face), the transmission improves to roughly  $-0.2$  dB and  $-0.4$  dB in the same frequency range.

Measured and simulated values with the nominal conductivity of Albromet-W 200 ( $22 \times 10^6 \text{ Sm}^{-1}$ ) do not agree, as the conductivity is degraded by the surface roughness. From a 50 mm reference waveguide section, the realized conductivity could be specified as  $12.3 \times 10^6 \text{ Sm}^{-1}$ . Simulations with this conductivity and both reference plane positions agree very well.

For the reflection of the phase shifter, see the lower-left plot of Fig. 4.21. In the frequency range from 80 GHz to 105 GHz reflection is below  $-25$  dB. For the frequencies from 75 GHz to 80 GHz, the performance of the phase shifter does not fulfill the requirements as the reflection and insertion loss increase to an unacceptable level. Most likely, this is due to slightly larger manufactured branch heights as compared to the specification. In the simulation this lead to the observed behavior of the insertion loss.

Three relative offsets can be realized with the four washers (relative to the 0.526 mm washer), which are 0.467 mm, 0.982 mm, and 1.507 mm. The corresponding measured phase and the theoretically expected phase are plotted in Fig. 4.21. The measured phase agrees with the theoretical phase within a range of  $+8^\circ$  to  $-6^\circ$  for all frequencies and offset positions. The only exception is the 1.5 mm relative offset at 75 GHz, where the measured and theoretical phase deviate by  $20^\circ$ . However, for this relative offset the

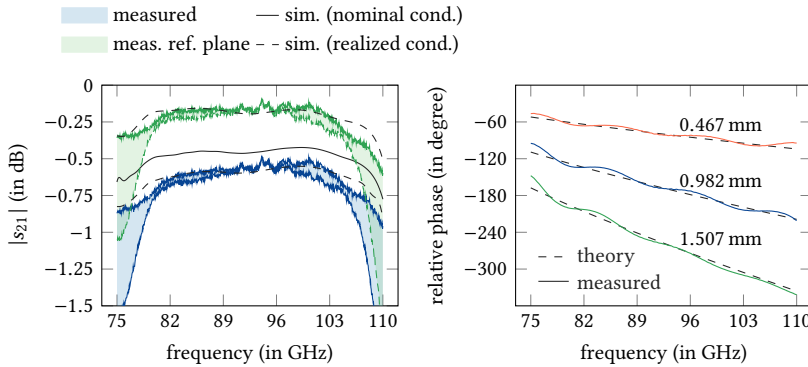


**Fig. 4.21:** Measurement and simulation of the proposed phase shifter prototype. Left: Maximum and minimum measured transmission for offset positions between 0.5 mm and 1.5 mm with a reference plane at the measurement flanges and a corrected reference plane 1 mm apart from the branch-guide coupler. Simulation data for both reference planes and nominal as well as realized conductivity. Right: Relative phase between two phase-states; measured and theoretical values.

2 mm washer has to be used which operates the sliding short outside its design limits.

Similar to the evaluation of the plunger, an equivalent length that the plunger has moved can be retrieved from the phase measurement. The results are listed in Tab. 4.4 together with the mechanical washer thicknesses. For this table, the measurement uncertainty is  $\pm 10 \mu\text{m}$  as two washer thicknesses are subtracted for the relative offset. The retrieved offset and the mechanically measured offset agree within  $\pm 10 \mu\text{m}$ . A better agreement cannot be expected due to the measurement uncertainty and manufacturing tolerances.

To evaluate the repeatability (at least in parts) when several phase shifters are realized, 20 out of 89 plungers were measured. The hybrid-junction was equal for all plunger

**Table 4.4:** Comparison between theoretical and measured offset position (retrieved from relative phase measurement) of the prototype phase shifter.

Mechanically measured	Retrieved from relative phase
0.467 mm	0.457 mm
0.982 mm	0.972 mm
1.507 mm	1.516 mm

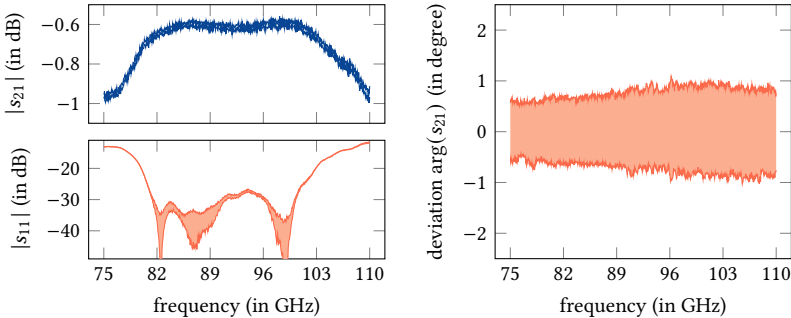


**Fig. 4.22:** Measurement of 20 randomly selected (out of 89) sliding shorts, i.e., 10 sliding short combinations, in the prototype phase shifter. Upper left: Maximum and minimum transmission magnitude. Lower left: Maximum and minimum reflection magnitude. Right: Maximum and minimum transmission phase difference.

configurations, no plunger was used twice. The transmission and reflection between maximum and minimum values from all measurements are plotted in the left part of Fig. 4.22. There is almost no difference in the insertion loss and the reflection is always below  $-25$  dB from 80 GHz to 105 GHz. The difference of the transmission phase is smaller than  $\pm 1^\circ$  for all 20 measurements, see right part of Fig. 4.22. Thus, this error is within the bound of the phase error deduced from the investigations of the plunger misalignment in Section 4.2.2.

For the phased-array antenna, the washer is replaced by a mounting frame that is driven by a piezo actuator, see Fig. 4.19. In total, 38 sliding shorts share the same mounting frame. The individual plungers are aligned within the rectangular hollow waveguide by the fitting hole. The mounting frame and their reference plane aligns them on the same axial position within the rectangular waveguide and, thus, controls the phase shift. The investigation of the prototypes shows a good repeated performance, meaning that the component performs as intended. The influence of manufacturing tolerances on the hybrid junction has not been investigated on the component level.

### 4.3 Invariable Phase Shifter

In contrast to the variable phase shifter, where a sliding short is employed to change the electrical length, the invariable phase shifter realizes a certain and immutable phase delay. This component is required in the phased array antenna to realize the aperture phase taper and to compensate the fixed  $90^\circ$  phase shift of the hybrid junction within the variable phase shifter. As metal is the material of choice and dielectrics have to be

avoided, the invariable phase shifter is solely built from rectangular hollow waveguides. To realize the desired phase shift, the dispersion characteristic of the fundamental mode is modified and synthesized in order to realize the required phase-frequency behavior. In the following paragraphs, two applications of the invariable phase shifter – one for realizing the Gaussian beam phase taper and one in a constant-phase waveguide section – are presented.

### 4.3.1 Focusing of Wavelength-Dependent Gaussian Beams

The phase taper for radiating a Gaussian beam with wavelength-dependent beam waist is dependent on the frequency. This dependency follows from sampling the Gaussian beam transverse field as a function of the element position  $x$ , see Section 3.3. The frequency-dependent phase of each element (3.35) for an arbitrary wavelength-dependent beam waist  $\tilde{w}_0 = p\lambda_0$  is

$$\tilde{\varphi}_a = \frac{x^2 \sqrt{1 - p^2 \lambda_0^2 / w_a^2}}{pw_a \lambda_0} \quad (4.3)$$

with the real-valued factor  $p$  specifying the size of the beam waist in terms of free-space wavelength  $\lambda_0$  and the beam waist  $w_a$  of the Gaussian beam at the aperture of the array antenna. The phase lag  $\varphi_g$  of the TE<sub>10</sub>-mode in a rectangular hollow waveguide section with waveguide width  $a_f$  and length  $\ell$  is given by (2.118) as

$$\varphi_g = -2\pi\ell/\lambda_g = -\frac{2\pi\ell \sqrt{1 - \lambda_0^2/(4a_f^2)}}{\lambda_0}, \quad (4.4)$$

where the minus sign is due to the time-dependency  $e^{j\omega t}$ . Comparing (4.3) and (4.4) their similarity reveals that the required phase taper (4.3) can be realized by a rectangular waveguide section with a specific width  $a_f$ . To force similarity of both equations (4.3) and (4.4), the terms outside the square root and those inside the square root have to be equal. To match the term outside the square-root, the condition  $-2\pi\ell = x^2/(pw_a)$  has to be fulfilled. This yields the length of the rectangular hollow waveguide section as

$$\ell = \frac{-x^2}{2\pi pw_a}. \quad (4.5)$$

To match the term inside the square-root, the equality  $p^2/w_a^2 = 1/(4a_f^2)$  has to hold. This yields the width of the rectangular hollow waveguide section as

$$a_f = \frac{w_a}{2p}. \quad (4.6)$$

The length of the individual waveguide sections is negative (4.5) and gets more negative for larger offsets from the beam axis, i.e., larger values of  $x$ . To realize a negative length, the central element has to be longer than the required negative length of the outermost element. This can be realized by an additional length  $\ell_0$  that leads to a long waveguide section for small values of  $|x|$  and to a vanishing waveguide length at the outermost elements. The resulting length for the focusing section thus is  $\ell_f = \ell_0 + \ell$ .

Reasonable values of  $a_f$  are those that support only the TE<sub>10</sub>-mode in the rectangular hollow waveguide. Hence, the upper limit for  $a_f$  is given by the cut-off width of the next higher mode. A lower bound is given by the cut-off width of the TE10-mode. If accepting somewhat higher losses the  $a_f$  might tend closely to the cut-off width of the lowest operational frequency.

The overall focusing section requires a taper from the standard WR10-waveguide width  $a$  to the focus-section width  $a_f$ . This can be realized by a smooth transition. The longer this transition, the better the matching and the lower the reflections.

The input and output ports of the focusing section should be at a fixed position, such that it does not influence the routing of other waveguide components and the position of the radiating elements. If designing the focus section as a straight waveguide, this is not possible. The solution is a trombone-like waveguide routing with a 180° bend in-between both ports, see Fig. 4.23. The trombone can also compensate for any other waveguide-length difference in-between the individual antenna channels.

In summary and by comparing with Fig. 4.23, five individual elements built up the focusing section: a first taper from the WR10 waveguide with  $a$  to  $a_f$ ; a first focusing waveguide with half of the total focusing length; a 180°  $H$ -plane bend; a second focusing waveguide with the remaining half of the total focusing length; a second taper from  $a_f$  to the WR10-waveguide width  $a$ . By design, the input and output ports do not move when varying the focusing waveguide length or the standard WR10-waveguide length.

Also there is a theoretical accordance between the required phase taper (4.3) and the phase lag of a rectangular hollow waveguide (4.4), the model is simulated in CST Microwave Studio® (version 2017.5), see Fig. 4.24. The insertion loss of the focusing structure with an  $a_f = 2.1$  mm and lengths  $\ell_f$  of 2 mm and 4 mm is around 0.25 dB. The reflection is below -15 dB for the frequency range from 75 GHz to 105 GHz. Both values are worst for the frequencies from 75 GHz to 78 GHz. In the frequency range above approximately 78 GHz the reflection is below -25 dB, see Fig. 4.24. The poor performance at lower frequencies is due to the closeness to the cut-off frequency of the  $a_f$  section which is at about 71.5 GHz. The maximum phase error between desired and simulated phase is below 1°.

### 4.3.2 Constant-Phase Relative Phase Shift

A constant-phase relative phase shift is necessary to compensate a frequency-invariant phase lag within the serial feed chain of the phased array antenna. Employing two

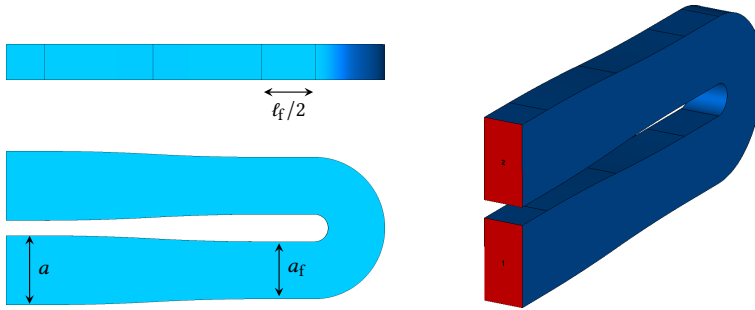


**Fig. 4.23:** Model of the focusing structure for realizing the frequency-dependent phase taper. The waveguide width  $a$  is reduced to the width of the focusing section  $a_f$  and the phase adjustment is realized by a trombone-like waveguide arrangement such that the input- and output ports do not move for varying focusing length  $\ell_f$ .

rectangular hollow waveguide sections with different width and variable length opens the possibility of a linear combination of their different dispersion characteristics. A constant phase shift between the individual channels can, thus, be synthesized by proper combination of the individual dispersion characteristics in each channel. This is, the overall phase lag is a linear combination of the dispersion characteristic of two individual rectangular hollow waveguides weighted by the individual waveguide length. This principle is employed to realize a relative and frequency-invariable phase shift between the individual radiating elements of  $-63^\circ$ ,  $-90^\circ$ ,  $-180^\circ$ , and  $-270^\circ$ .

For simplicity, the width of the first rectangular hollow waveguide is  $a_{f1} = 2.54$  mm

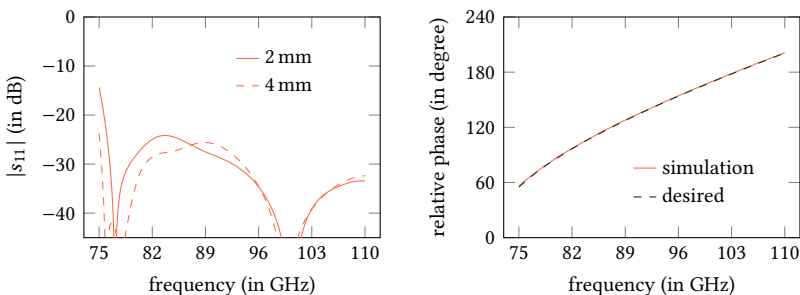


**Fig. 4.24:** Left: Simulated reflection of the proposed focusing section model. Right: Desired and achieved (in simulation) phase-frequency dependence for focusing length  $\ell = -2$  mm.

(the width of the WR10) with the corresponding length  $\ell_1$ . The width of the second waveguide is  $a_{f2} = 3.5$  mm, to guarantee that no higher-order mode is propagating, while the length is denoted as  $\ell_2$ . The larger the width of the second section, the larger is the difference of the dispersion characteristic of both waveguide section (2.130). A larger width of  $a_{f2}$  would consequently lead to shorter lengths  $\ell_1$  and  $\ell_2$  but opens up the possibility for higher-order modes and, thus, mode-conversion. The final width  $a_{f2} = 3.5$  mm was obtained by choosing a compromise for the overall length and the possibility of higher-order modes.

The synthesis process for the length of the individual waveguide sections is as follows. The total phase lag  $\varphi_f(f)$  of a channel with two different waveguide widths  $a_{f1}$  and  $a_{f2}$  is

$$\varphi_f(f) = -\frac{2\pi}{\lambda_{f1}(f)}\ell_{f1} - \frac{2\pi}{\lambda_{f2}(f)}\ell_{f2} = -k_{f1}\ell_{f1} - k_{f2}\ell_{f2}, \quad (4.7)$$

with the guided wavelengths  $\lambda_{f1}$  and  $\lambda_{f2}$  according to (2.118). The relative phase shift  $\varphi_{f,r}$  between two individual channels may be written as

$$\varphi_{f,r} = \varphi_f(f)' - \varphi_f(f)'' , \quad (4.8)$$

with the absolute phases  $\varphi_f(f)'$  and  $\varphi_f(f)''$  of each channels. The waveguide dispersion of the individual waveguides from (2.117),  $k_{f1}$  and  $k_{f2}$ , has a direct link on how long these waveguides will be.

The corresponding waveguide length for the waveguide widths  $a_{f1} = 2.54$  mm and  $a_{f2} = 3.5$  mm is obtained by a nonnegative linear least-squares minimization. For this purpose, the (4.7) and (4.8) are represented in matrix notation in the form of  $\mathbf{Ax} = \mathbf{b}$ . For a relative phase shift between two channels, where each channel is composed of a waveguide with width  $a_{f1}$  and a waveguide with width  $a_{f2}$ , the matrix may have the form

$$\mathbf{A} = \begin{bmatrix} k_{f1} & k_{f2} & -k_{f1} & -k_{f2} & 0 & 0 \\ k_{f1} & k_{f2} & 0 & 0 & -k_{f1} & -k_{f2} \end{bmatrix}. \quad (4.9)$$

The wavenumbers  $\mathbf{k}_{f1}$  correspond to the waveguide with width  $a_{f1}$  and the wavenumbers  $\mathbf{k}_{f2}$  correspond to the waveguide with width  $a_{f2}$ . The wavenumbers are vectors representing the dispersion characteristic of the waveguide section within the desired frequency range. Each row in (4.9) represents a different channel with a relative phase shift. The first two columns of (4.9) are common to all channels and represent the reference channel from (4.8) with a relative phase of  $0^\circ$ . The vector  $\mathbf{b}$  contains the desired relative phase shifts to this reference channel (corresponding to the row in (4.9)) as

$$\mathbf{b} = \begin{bmatrix} \varphi_{f,r1} \\ \varphi_{f,r2} \end{bmatrix}. \quad (4.10)$$

**Table 4.5:** Waveguide lengths for a relative and frequency-independent phase shift between two channels due to the linear combination of two rectangular hollow waveguides with width  $a_{f1} = 2.54$  mm and  $a_{f2} = 3.5$  mm in each channel. The  $0^\circ$  relative phase represents the configuration of the reference channel.

Relative phase to reference channel $0^\circ$	Length of waveguide 1 ( $\ell_{f1}$ )	Length of waveguide 2 ( $\ell_{f2}$ )
$0^\circ$	8.810 mm	0.000 mm
$-270^\circ$	0.000 mm	10.373 mm
$-180^\circ$	2.937 mm	6.916 mm
$-90^\circ$	5.874 mm	3.458 mm
$-63^\circ$	6.755 mm	2.420 mm

Each relative phase shift  $\varphi_{f,ri}$  (vector entry in  $\mathbf{b}$ ) is a vector with equal entries and the same length as the corresponding wavenumber  $k_{fi}$ . The required waveguide lengths are obtained by minimizing

$$\min_{\mathbf{x}} \|\mathbf{Ax} - \mathbf{b}\|, \text{ where } \mathbf{x} \geq 0. \quad (4.11)$$

The entries in  $\mathbf{x}$  contain the required lengths of the two waveguides in each channel. From the definition of  $\mathbf{A}$  in (4.9), the first two entries yield the waveguide lengths for the reference channel, i.e., the  $0^\circ$  phase shift. The third and fourth entry are the lengths of the waveguide sections yielding a relative phase of  $\varphi_{f,r1}$  to the reference channel. The fifth and sixth entry of  $\mathbf{x}$  are the lengths of the waveguide sections yielding a relative phase of  $\varphi_{f,r2}$  to the reference channel. To realize more relative phase shifts, the matrix  $\mathbf{A}$  can be extended. The individual dispersion characteristics do not perfectly complement each other (i.e., no orthogonal base) and, thus, deviations from the desired relative phase occur.

In brief, the dispersion characteristic of two rectangular hollow waveguides with non-equal width are employed to realize a relative phase shift between the individual channels/radiating elements of the phased array antenna. By linear-combination of the dispersion characteristics of both waveguides with an appropriate length, a frequency-invariant phase shift can be synthesized. The results of such an optimization is tabulated in Tab. 4.5 for the waveguide widths  $a_{f1} = 2.54$  mm and  $a_{f2} = 3.50$  mm. The length of the individual waveguides correspond to relative phase shifts of  $0^\circ$ ,  $-270^\circ$ ,  $-180^\circ$ ,  $-90^\circ$ , and  $-63^\circ$ .

To realize these constant-phase waveguide structure, tapers are required for a smooth transition from  $a_{f1}$  to  $a_{f2}$ . As the taper is equal for each channel, it has no influence on the relative phase between the individual channels. A simulation model of the

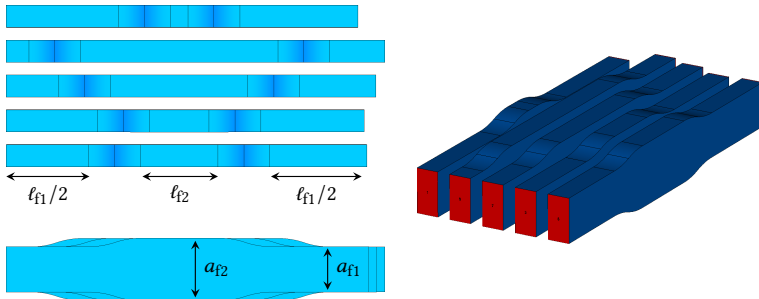


**Fig. 4.25:** Model of the constant phase or frequency-independent phase shifter. A combination of two dispersion characteristics realize a frequency-independent relative phase between two channels. The uppermost (left upper sketch) is the reference phase  $0^\circ$ . From top to bottom follow the relative phase shifts  $-270^\circ$ ,  $-180^\circ$ ,  $-63^\circ$ , and  $-90^\circ$ .

five channels from Tab. 4.5 is depicted in Fig. 4.25. The simulation was carried out in CST Microwave Studio<sup>®</sup> (version 2017.5). The conductivity of the waveguide walls is modeled with  $12.3 \times 10^6 \text{ Sm}^{-1}$ . In the frequency range from 75 GHz to 105 GHz, the reflection is below  $-25 \text{ dB}$  and the insertion loss around  $0.1 \text{ dB}$  for all channels. The transmission phase and the deviation from the desired phase shift are plotted in Fig. 4.26. The realized phase shifts are almost constant and oscillate slightly around the desired absolute phase shift. The maximum deviation occurs for the largest relative phase shift  $-270^\circ$  and is  $5^\circ$  and  $-7^\circ$ .

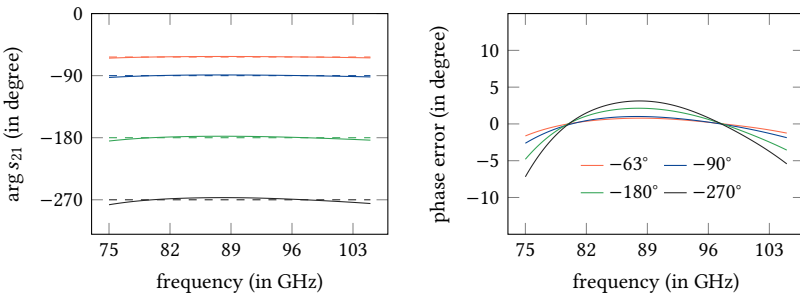


**Fig. 4.26:** Left: Simulated relative phase with reference lines at  $-63^\circ$ ,  $-90^\circ$ ,  $-180^\circ$ , and  $-270^\circ$ . Right: Deviation of the relative phase from the desired phase.

## 4.4 WR10 Waveguide Load

A waveguide load (or absorber) is required to dissipate non-radiated energy at the end of a serial feed network or in individual components to terminate a certain port which would otherwise disturb the system behavior. Dissipation of electromagnetic energy can in general be realized by Ohmic, dielectric, or magnetic losses. Ohmic losses can be realized by using a low-conductivity metal on the waveguide walls. These absorbers are very long (about 100 wavelength) in order to achieve acceptable low reflection levels. To realize dielectric or magnetic loss in a waveguide, the waveguide-filling has to have lossy properties (i.e., a non-vanishing loss tangent). Carbonyl iron or silicon carbide are commonly used for this purpose. The information given in the next two paragraphs is from a personal communication with H.-U. Nickel (Spinner GmbH) in February, 2016.

### 4.4.1 Absorbing Materials/Dielectrics

Carbonyl iron is available in form of powder or a coating. It is cheaper and easier to process as compared to silicon carbide. The powder is molded together with epoxy into the desired form (the mixing ratio is crucial), while the coating is used as aerospace painting for a reduced radar reflectivity. Carbonyl iron has a relative permittivity of about  $\epsilon_r = 9.5$  and a relative permeability  $\mu_r > 1$ . Both values decrease for increasing frequency. Carbonyl iron has a non-vanishing dielectric and magnetic loss tangent. The dielectric losses are constant over frequency with a dielectric loss tangent of about  $\tan \delta_e = 0.09$ . The magnetic loss increases with frequency and is here just specified as  $\tan \delta_m > 0$ . The material is magnetic and, thus, not suitable for in-vessel use in a nuclear fusion experiment.

Silicon carbide, on the other hand, is a ceramic that is sintered into the desired form. Once hardened, it can only be processed by diamond tools, which is the reason for the higher price. The relative permittivity is in the range  $\epsilon_r = 10 - 12$ , while the relative permeability is  $\mu_r = 1$ . It only possesses dielectric losses (i.e.,  $\tan \delta_m = 0$ ) with a dielectric loss tangent in the range of  $\tan \delta_e = 0.12 - 0.15$ . Silicon carbide is ultra-high vacuum compatible (measured leakage rate below  $8 \times 10^{-10}$  mbarLs<sup>-1</sup> which is the volume times differential pressure divided by the measurement time; the measured leakage rate is very low and would allow an installation in a ultra-high vacuum chamber) and the melting point is above 1500 °C.

By reason of the large space consumption of Ohmic loads and the inapplicability of carbonyl iron inside a fusion experiment, the waveguide load employed in this thesis is based on silicon carbide. More precisely, it is based on a non-porous caked silicon carbide as it is used in bearings. In particular, the silicon carbide Ekasic® F from ESK Ceramics GmbH & Co. KG (now 3M), 87405 Kempten, Germany, is used.

#### 4.4.2 Fundamental Model

To achieve a low reflectivity of the waveguide load, the guided wave has to be directed into the silicon carbide in a smooth and gentle way. This is, the electromagnetic properties within the waveguide must not change abruptly but rather transitional over several wavelength. Such a transition can be realized by tapering the silicon carbide within the waveguide and, thus, gradually changing the material properties seen by the guided wave.

For the waveguide load used in this thesis, a silicon carbide block with size 24.7 mm × 6.15 mm × 85 mm was sliced into plates with size 24 mm × 6.15 mm × 2 mm and 11 mm × 6.15 mm × 2 mm. To form a taper, the plates are inclined relative to the waveguide axis, see Fig. 4.27 for a sketch of the model. The height of the silicon carbide plate is 2 mm and, thus, smaller than the waveguide width (2.54 mm), while the plate is placed in the center of the waveguide width due to the split-block cutting plane. To clamp the silicon carbide and prevent any relocation, leave springs or screws are used. With this design, no special form of the silicon carbide (e.g., a cone) is necessary. The angle between the waveguide axis and the long edge of the silicon carbide slab is obtained by full-wave simulations as 13°. In general, a smaller angle realizes a smoother transition and consequently a lower reflection. A smaller angle, however, also requires a long and potentially very thin wall between the waveguide and the clearance for the silicon carbide slab. The latter is difficult to manufacture. The 13° are a compromise between performance and manufacturing effort.

#### 4.4.3 Evaluation of a Prototype Load

The prototype waveguide load is shown in Fig. 4.27. The silicon carbide slab is placed in the clearance. Two screws are used to fix the slab in the correct location. The thin nose (wall between the waveguide and the clearance for the slab) is the most difficult part to manufacture. After the manufacturing, a small sliver/burr remained. It could be removed with a toothpick.

Measured and simulated reflection are plotted in Fig. 4.27. The measured reflection is plotted for the prototype with the sliver (raw) and after removing the sliver/burr with a toothpick (cleand). In any case, the reflection is below –20 dB. By removing the sliver/burr, the reflection could be reduced by about 3 dB and is below –23 dB. The simulated reflection is below about –28 dB. The remaining reflection of the cleaned prototype, however, is considered sufficient.

### 4.5 WR10 Split-Block Transitions

When realizing a rectangular hollow waveguide in split-block technology, the rectangular cross-section is either cut in the E- or in the H-plane. Consequently, the waveguide

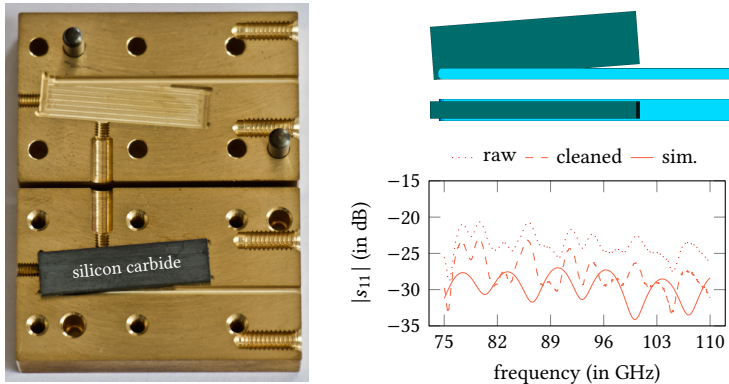


Fig. 4.27: Left: Image of the prototype WR10-absorber. Right: Simulated and measured reflection.

routing is only possible within this cutting plane. Due to space restrictions, it is beneficial to distribute the waveguide network over several displaced layers. In this section, consider a rectangular hollow waveguide that is cut in the middle of the *E*-plane. The proposed split-block transitions enable a connection of several split-block waveguide layers in *H*-plane direction.

The design of this component is driven by electrical and mechanical objectives. In terms of electrical properties, the reflection of the transition should be below  $-20$  dB. In terms of mechanical objectives, the transition should be machined by a 1 mm diameter milling tool aligned normal to the workpiece and, thus, parallel to the *E*-plane. This enables the manufacturing of the whole feed-network on a 3-axis milling machine with the same milling-tool as that for the waveguide. Hence, keeps the manufacturing process as simple as possible.

There are two possible alignments of the vertical transition: the forward and the backward alignment. The forward-aligned transition, see Fig. 4.28, keeps the direction in the cutting plane constant. This is, the wave follows the same in-plane direction in both layers. In contrast, the backward-aligned transition inverts this direction, see Fig. 4.29. In the following paragraphs, the individual models are described and a multilayer prototype network is evaluated.

#### 4.5.1 Fundamental Model of a Forward-Aligned Transition

The forward-aligned transition is sketched in Fig. 4.28. The dashed lines indicate the two cutting planes. To realize this transition, three metal pieces are required. The bottom and top layers are almost identical. Four step-like structures form a 90°-bend

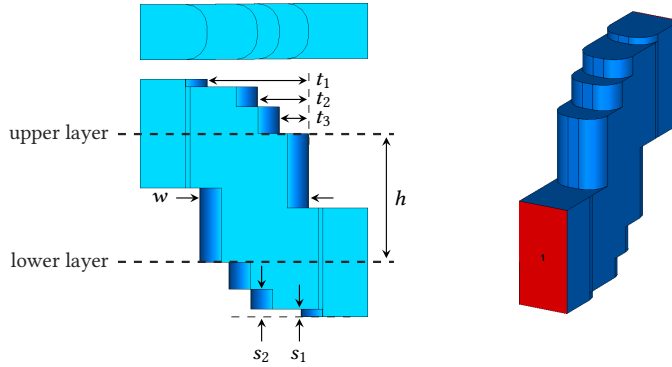


**Fig. 4.28:** Model of the forward-aligned transition. Cutting planes of both split-block layers are indicated by the bold dashed lines.

that direct the wave through an elongated hole (with width  $w$ ) in the central layer. The length of the steps ( $t_1$ ,  $t_2$  and  $t_3$ ) as well as their heights ( $s_1$  and  $s_2$ ) in the bottom and top layer are identical. The height of the third step is given by the cutting plane (i.e., half-width of the rectangular hollow waveguide). The height of the central layer  $h$  may be optimized. However, for the design of the phased array antenna it is chosen as  $h = 3$  mm and is constant for the complete feed network. This height is a compromise between space-consumption and stability/machinability of the individual split-block layers (milling tools with a diameter of 1 mm have a maximum milling depth of about 2 mm). The optimized values of the forward-aligned transition are obtained by full-wave simulation and are given in Tab. 4.6. The radii of the individual steps and the elongated hole are 0.5 mm corresponding to a 1 mm milling tool.

#### 4.5.2 Fundamental Model of a Backward-Aligned Transition

The backward-aligned transition is sketched in Fig. 4.29. Similar to the forward-aligned transition, it has two cutting-planes and, thus, consists of three metal layers. The bottom

**Table 4.6:** Dimensions of the forward-aligned transition for  $h = 3.0$  mm and edge-radius 0.5 mm.

$w$ (in mm)	$s_1$ (in mm)	$s_2$ (in mm)	$t_1$ (in mm)	$t_2$ (in mm)	$t_3$ (in mm)
2.531	0.177	0.644	2.356	1.189	0.679

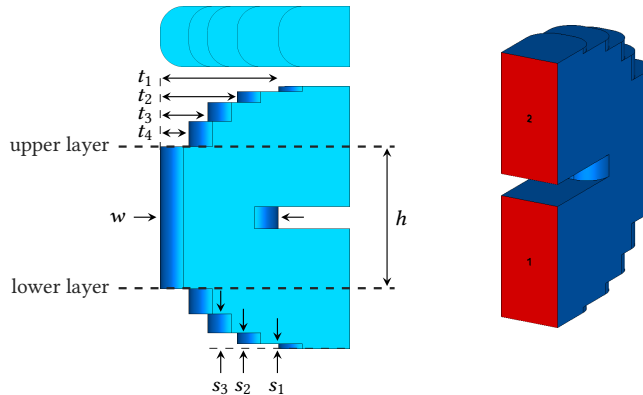


**Fig. 4.29:** Model of the backward-aligned transition. Cutting planes of both split-block layers are indicated by the bold dashed lines.

and the top layer are also almost identical. The wave is directed into an elongated hole by five steps. The step-heights ( $t_1 \dots t_4$ ) and step-widths ( $s_1 \dots s_3$ ) as well as the width  $w$  of the elongated hole are optimized by full-wave simulations. The height of the central layer is  $h = 3$  mm and the radii of the milled edges are 0.5 mm. The optimized values of the backward-aligned transition are given in Tab. 4.7.

### 4.5.3 Evaluation of a Prototype Multilayer WR10-Network

A prototype network to test the vertical transition has been manufactured and evaluated. It features two backward-aligned transitions and several wavelength of straight rectangular hollow waveguide. For the model and the prototype, see Fig. 4.30.

The prototype consists of four individual layers. For a good electrical contact, these layers have to be pressed together. This is either possible by placing screws in the near vicinity of the waveguide network or by an external mounting frame that realizes an areal force between the top and bottom layer. The former is used in prototype networks,

**Table 4.7:** Dimensions of the backward-aligned transition for  $h = 3.0$  mm and radius 0.5 mm.

$w$ (in mm)	$s_1$ (in mm)	$s_2$ (in mm)	$s_3$ (in mm)	$t_1$ (in mm)	$t_2$ (in mm)	$t_3$ (in mm)	$t_4$ (in mm)
2.495	0.112	0.339	0.740	2.502	1.626	1.007	0.608

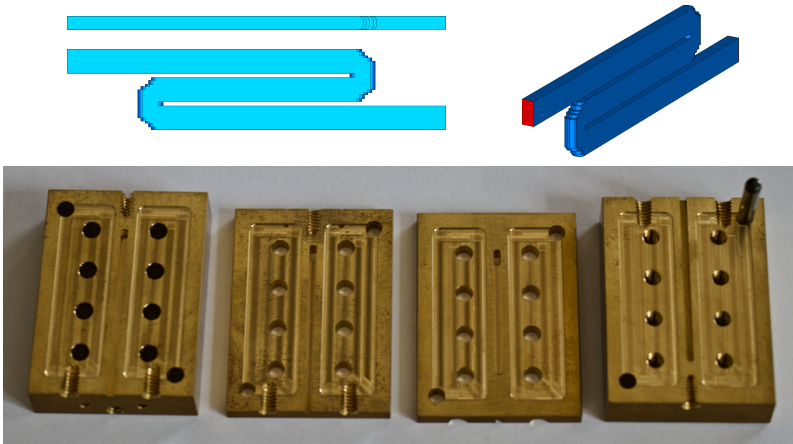


**Fig. 4.30:** Top: Model of the multilayer WR10-waveguide. The dimensions of the backward-aligned transition are given in Tab. 4.7. Bottom: Prototype of the multilayer WR10-waveguide. The material of the split-block layers is brass with a nominal conductivity of  $15.2 \times 10^6 \text{ Sm}^{-1}$ .

as it does not require an additional frame. For the multilayer prototype, eight screws are used, see Fig. 4.30. The external frame is employed in the phased array antenna, as the individual waveguides are placed too close together, not leaving any space for screws. The external frame surrounds the split-block network and eight screws enable an external force acting between the top and bottom split-block layer. The purpose of this prototype is consequently twofold: verify the vertical transition and analyze the crimping of the split-block layers by an external force.

The measurement and simulation results of the prototype network are given in Fig. 4.31. The reflection coefficient is shown in the left plot and the transmission coefficient in the right plot. The measured reflection is slightly worse as compared to the simulated reflection. It is smaller than  $-20 \text{ dB}$  in the major part of the operational bandwidth (75 GHz to 105 GHz). There is almost no difference in the reflection coefficient between the externally pressed (by means of an external frame) and the screwed prototype network. The simulated transmission is better than the measured transmission. The reason is that the nominal conductivity of the material was considered in the simulation. Hence, not considering surface roughness and a thereby virtually reduced conductivity. The pressed and screwed prototype configurations have almost similar transmission coefficients around  $-0.7 \text{ dB}$ . For frequencies above 90 GHz, the pressed prototype is even slightly better. The reflection and transmission of the measured and simulated model follow almost the same trend, indicating an overall good agreement

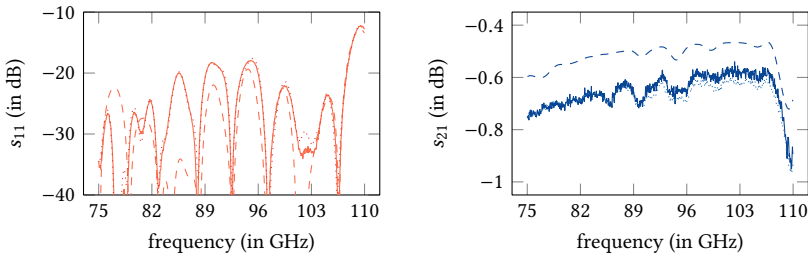


**Fig. 4.31:** Simulation (dashed) and measurement of two subsequent vertical transitions. Comparison between screwed (dotted) and pressed (solid) prototype.

between simulation and measurement.

In conclusion, the reflection of the prototype is below the envisaged  $-20$  dB and the crimping of the individual split-block layers by an external frame is possible. The insertion loss is at the expected level. There is almost no difference between using screws within the split-block network or an external force by means of a frame.

## 4.6 Parallel Plate Radiating Array Element

From the theoretical derivation of the Gaussian beam from the plane wave spectrum (2.76) it follows that a Gaussian beam may have two different beam parameters in both transverse axis. This property is utilized in this work. The Gaussian beam shape in the  $xz$ -plane (see Fig. 2.1) is steered and shaped by the array taper. This is, the individual array elements sample the Gaussian beam in the  $xz$ -plane as described in Section 3.3.1. The perpendicular Gaussian beam shape in the  $yz$ -plane is not affected by the array taper and may be different. In order to maximize the energy density in the measurement region and, thus, to improve the sensitivity of the system, the perpendicular beam shape ( $yz$ -plane) should be similar to the Gaussian beam in the steering plane. Thus, their focal regions overlap, concentrating the cross-sectional field to a small area. For all steering angles, the polarization of the electric field should be preserved and aligned with the  $x$ -axis or sampling direction.

The previous considerations and the whole design of the antenna as a phased array already direct the solution in a specific way. This is, the individual radiating elements have to provide an electric field in the aperture that enables the sampling of the Gaussian beam field, see Section 3.3. To ensure a steering-angle-independent polarization, a uniform field distribution in sampling direction is necessary. Thus, the aperture of the radiating element has to support only modes that have no variation in sampling direction and no cross-polarized components. The  $TE_{10}$ -mode in the rectangular hollow

waveguide provides such a field, if the short wall is aligned with the sampling direction of the beam field ( $x$ -axis), see Section 2.4.1. Additionally, the radial parallel plate waveguide supports modes that have a uniform electric field normal to the plates, if the plate-spacing is smaller than half-a-wavelength, see Section 2.4.2 for the  $\text{TM}_{m0}^z$ -modes. Perpendicular to the steering plane of the phased array antenna (i.e., in the  $yz$ -plane), the electromagnetic field has to be shaped by the individual radiating elements such that it assembles the desired Gaussian beam shape.

Shaping a Gaussian beam with a beam waist in front of the aperture requires the phase near the propagation axis to be retarded with respect to the off-axis phase. Achieving this is either possible by a lens or a reflector [Gol98]. The lens has two drawbacks. Firstly, it requires a low-loss dielectric material to prolongate the electrical length near the beam axis. Dielectric materials, however, should be avoided in-vessel of a nuclear fusion experiment. Secondly, reflections occur at the intersection between vacuum and dielectric, which lead to a degraded performance as compared to reflector elements [Boh89]. Reflectors, on the other hand, do not have any of these drawbacks. Consequently, the individual radiating element of the phased array antenna is realized in radial parallel plate technology to provide a uniform electric field in sampling direction ( $x$ -axis). The Gaussian beam perpendicular to the steering direction ( $y$ -axis) is shaped by a reflective contour. This contour has a two-dimensional shape in the  $yz$ -plane that is illuminated by an  $H$ -plane sectoral horn antenna. The reflective contour tries to transform the horn field into that of the desired perpendicular Gaussian beam shape. In summary, each radiating element has its own parallel plate reflector that is illuminated by an  $H$ -plane sectoral horn antenna.

An alternative approach is to use a single reflector that is illuminated by the phased array antenna. In the steering direction, the Gaussian beam is still shaped by sampling the transverse field. In the perpendicular direction, the beam is shaped by a single three-dimensional reflector contour. In this case, both orthogonal beam-shapes are interconnected at the reflector. As a result, the frequency-dependent array taper is more complex and it has to compensate for the moving reflection point on the reflector when steering the beam. Besides, the three-dimensional reflector contour will lead to a steering angle dependent cross-polarization, which degrades the performance of the measurement system [Cut47; Gol98]. Considering these aspects, it is more favorable to realize a single reflector for each radiating element.

In addition to the electrical properties, the antenna has to withstand plasma disruptions. Here, the area of the antenna perpendicular to the steering plane (i.e., the area in the  $yz$ -plane) is most critical, due the alignment of the static magnetic field of the nuclear fusion experiment to the parallel plate area. If a plasma disruption and, thus, a rapid change in the magnetic flux occurs, a strong force acts on the reflector, eventually leading to a damage of the antenna or, in the worst case, damage of the nuclear fusion experiment. Thus, the reflector design has to withstand these plasma disruptions. To reduce the impact of the disruption force, the parallel plate area has to

be as small as possible. Support concerning plasma disruption and an analysis of the disruption force for the final reflector contour was carried out by Irene Zammuto from the “Max-Planck-Institut für Plasmaphysik” in Garching, Germany.

Again, when radiating a Gaussian beam that is to be focused in a certain distance from the radiating element, the on-axis phase has to be altered. It has to be altered in such a way that the aperture field is virtually positioned behind the focal plane when looking towards the propagation direction. When using a horn antenna, this cannot be fulfilled. The curvature of the phase is always aligned in a way to model the Gaussian beam that has already passed the focal plane. A horn radiates a diverging field. To compensate for this effect, a reflector is shaped such that it transforms the horn field into that of the desired Gaussian beam. Finding a suitable reflector contour is the topic of the following sections. In many designs, “canonical” surfaces such as ellipsoidal or paraboloidal surfaces are employed to either transform rays radiating from one focal point to another focal point or to form parallel propagation paths, respectively [Gol98]. These methods, however, neglect the transversal phase dependency of the Gaussian beam and, thus, represent only an approximation. A method that considers the transverse dependency of the Gaussian beam, numerically computes a suitable reflector contour by matching the phase of the incident and reflected Gaussian beam [Boh89]. A similar method can be applied to find suitable reflector contours to transform the field of a horn antenna to that of the desired Gaussian beam. Besides, commercial software packages such as GRASP and POS from TICRA, Copenhagen, Denmark are available that claim to find an optimized reflector contour based on full-wave analysis of the individual components.

In the following, the fundamental reflector model is presented to clarify the alignment of the Gaussian beam with respect to the horn antenna. To evaluate the horn field in an efficient way, it is represented by a set of cylindrical waves. A method to obtain the cylindrical wave coefficients is presented followed by the procedure that iteratively determines the reflector contour. Finally, a prototype reflector is evaluated.

#### 4.6.1 Fundamental Reflector Model

The shape of the Gaussian beam in the steering plane ( $xz$ -plane) of the phased array antenna is sampled by the individual array elements. The shape of the Gaussian beam perpendicular to the steering plane ( $yz$ -plane) is shaped by a reflective contour. In Fig. 4.32, the  $yz$ -plane of the problem is sketched. A primary  $H$ -plane sectoral horn illuminates the reflector. From the incident field, the reflector shapes the desired Gaussian beam. This Gaussian beam propagates along the  $z$ -axis with the electric field being  $x$ -polarized. Hence, the electric field within the aperture has to support only modes that have a uniform electric field in  $x$ -direction and the reflector contour is uniform along the  $x$ -axis.

The radial parallel plate waveguide can support the desired field and provide the necessary restriction to the electric field if both plates have a spacing smaller than half-

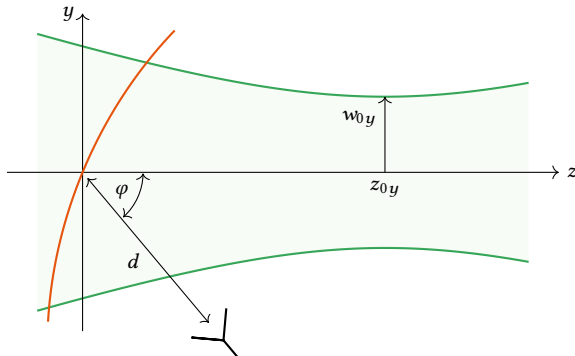


**Fig. 4.32:** Sketch of the reflector geometry with the desired Gaussian beam and the primary feed horn. The Gaussian beam is specified with the beam waist radius  $w_0y$  and the focal distance  $z_0y$ . The position of the primary feed is in a distance  $d$  from the origin and tilted by  $\varphi$  relative to the propagation axis of the Gaussian beam.

a-wavelength, see Section 2.4.2. For the geometry sketched in Fig. 4.32, the two plates are aligned parallel to the  $yz$ -plane. The field in the radial parallel plate waveguide is fed by an  $H$ -plane sectoral horn antenna and the WR10-waveguide connected to it. For a correct field alignment and to avoid any waveguide-height perturbations, the spacing between both plates equals the rectangular waveguide height  $b$  and, thus, is smaller than half-a-wavelength. As a consequence, only  $TM_{m0}^x$ -modes can propagate in the radial parallel plate waveguide. Their electric field is uniform in  $x$ -direction.

Excited by the beam-forming feed network, the field is first transformed from the  $TE_{10}$ -mode to a set of cylindrical waves by means of the  $H$ -plane sectoral horn antenna. The reflective contour modifies the radial parallel plate field such that it forms the desired Gaussian beam propagating in  $z$ -direction. This beam is simultaneously excited in each radiating element with the corresponding complex weight. At the aperture of the reflector, the individual radiating elements sample the Gaussian beam along the steering-axis ( $x$ -axis) and, thus, eventually form the desired Gaussian beam.

The shape of the reflector is dependent on the Gaussian beam, the primary feed horn, and its relative position to the Gaussian beam in terms of  $d$  and  $\varphi$  from the intersection of both main beams, see Fig. 4.32. Each variable has an influence on the quality and the shape of the Gaussian beam. They also alter the size of the reflector. As already stated, the reflector size is a critical requirement. If the reflector area is too large, the array antenna can not be installed in the ASDEX Upgrade tokamak. The quality of the beam is of secondary importance. The reflector should increase the energy density in the measurement region, the actual shape of the Gaussian beam perpendicular to the

steering direction is of minor importance for Doppler reflectometry.

#### 4.6.2 *H*-plane Sectoral Horn Antenna

The design of the *H*-plane sectoral horn antenna is kept as simple as possible. The goal is to make the required space of the reflector as small as possible while providing easy manufacturing. The flare of the horn follows the dependency

$$v(u) = \frac{1}{2} \sqrt{a^2 + (A^2 - a^2) u^2 / L^2}, \quad (4.12)$$

where the *u*-axis is directed along the propagation direction and *v* is the perpendicular axis, see Fig. 4.33. For *u* = 0 mm, the horn profile is equal to the waveguide width *a*. At the outermost position *u* = *L*, the length of the horn, the horn profile equals the aperture width *A*. There is no erratic transition from the rectangular hollow waveguide to the horn antenna.

The amplitude distribution in the horn aperture is cosine-shaped. The phase in the aperture plane is diverging and dependent on the frequency. This is, the phase center of the horn moves with frequency. This diverging phase front is transformed into that of the desired Gaussian beam by means of the reflector contour. However, on the reflector contour the amplitude of the horn field will not match the amplitude of the desired Gaussian beam. This leads to higher order Gaussian beam modes and eventually to side-lobes. The frequency dependent phase results in a frequency dependent focal length. If the overall dimension of the horn can be kept small in terms of wavelengths, the phase center moves only little with frequency, see the evaluation of the phase center for different horn dimensions in [Mue70]. It is also dependent on the flare of the horn. However, also the focal length of the Gaussian beam in the steering plane is frequency dependent. If the overall variation of the phase center is small, the influence on the focal plane shift of the Gaussian beam is expected to be small. Again, the main goal of the reflector is to focus energy and be compliant with the disruption forces. It is not a goal to excite a stigmatic beam. Consequently and to keep the optimization process simple, the design and optimization of the reflector is carried out at 90 GHz, the center of the operational frequency band. Deviations from the desired beam shape at other frequencies are expected and accepted.

The *H*-plane sectoral horn antenna was simulated in CST Microwave Studio® (version 2015.6). In the simulation, the horn is fed by a fundamental rectangular hollow waveguide. The horn is shaped in the *H*-plane according to (4.12). The flare can be controlled by the horn length *L* and the aperture width *A*. In the simulation, the top and bottom walls of the horn and the WR10-waveguide are perfectly electrically conducting. The thickness of the flare-walls is 1 mm.

For the computation of the reflector contour, the electric field of the horn at arbitrary positions in the *yz*-plane in Fig. 4.33 is necessary in order to match the phase with the

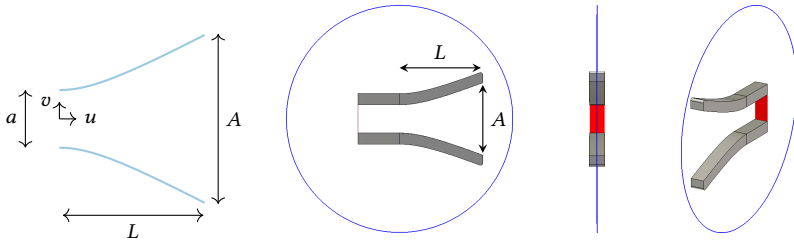


**Fig. 4.33:** Simulation model of the  $H$ -plane sectoral horn that is fed by a WR10-waveguide. The top and bottom wall (parallel to the paper-plane in the left image) are perfectly electrically conducting and spaced by the waveguide height  $b$ . The radiated field is evaluated on the surrounding circle and represented by cylindrical waves.

desired Gaussian beam. To accelerate the computation of the horn field, it is represented in terms of cylindrical waves. For this, a circle is placed around the geometry of the primary feed horn, see Fig. 4.33. On this circle, the electric field is evaluated and decomposed in terms of cylindrical modes that represent the horn field by an equivalent cylindrical wave source. From this equivalent source, the electrical field in the  $yz$ -plane of the primary feed horn can efficiently be computed.

#### 4.6.3 Equivalent Representation of the Horn Field

To accelerate the computation of the radiated field of the primary feed horn at any point away from the source, the radiated field is represented by a set of cylindrical waves propagating in radial direction. More precisely, the electric field component  $E_x$  around the horn antenna (in the parallel plate waveguide) is expanded in terms of propagating  $\text{TM}_{m0}^x$ -modes in the form of (2.159). This is only valid if the spacing between both plates is  $h < \lambda/2$ . Then, the expansion is

$$E_x(\rho_h, \phi_h) = \sum_{m=-\infty}^{\infty} H_m^{(2)}(k\rho_h) (b_m \cos(jm\phi_h) + c_m \sin(jm\phi_h)), \quad (4.13)$$

where  $\rho_h$  and  $\phi_h$  are the radial and angular dependencies in the  $uv$ -coordinate system of the horn, see Fig. 4.33. The trigonometric functions may be combined according to

$$a_m e^{jm\phi_h} = a_m/2 \cos(m\phi_h) + j a_m/2 \sin(m\phi_h), \quad (4.14)$$

with  $b_m = a_m/2$  and  $c_m = j a_m/2$ , yielding

$$E_x(\rho_h, \phi_h) = \sum_{m=-\infty}^{\infty} a_m H_m^{(2)}(k\rho_h) e^{jm\phi_h}. \quad (4.15)$$

Multiplying with  $e^{-jn\phi_h}$  and integrating over  $\phi_h = 0 \dots 2\pi$  for a fixed  $\rho_h = \rho_{h,0}$  yields [Jin15]

$$\int_0^{2\pi} E_x(\rho_{h,0}, \phi_h) e^{-jn\phi_h} d\phi_h = \int_0^{2\pi} a_m H_m^{(2)}(k\rho_{h,0}) e^{j(m-n)\phi_h} d\phi_h. \quad (4.16)$$

Due to the orthogonality of the modes ( $\int_0^{2\pi} e^{j(m-n)\phi_h} d\phi_h$  being an integral representation of the Dirac-delta function) [Jin15], the cylindrical wave coefficients follow as

$$a_n = 1/H_n^{(2)}(k\rho_{h,0}) \int_0^{2\pi} E_x(\rho_{h,0}, \phi_h) e^{-jn\phi_h} d\phi_h. \quad (4.17)$$

Once the cylindrical wave coefficients  $a_n$  have been computed, the electric field can be evaluated at any point outside the circle enclosing the  $H$ -plane horn antenna in the  $uv$  (or  $yz$ )-plane by means of (4.15). Note that the indices  $m$  and  $n$  have the same meaning. The  $uv$ - and  $yz$ -coordinates are connected by a coordinate transformation. This is, by a rotation and translation with  $\varphi$  and  $d$ , see Fig. 4.33).

For equally spaced  $E_x(\rho_h, \phi_h)$ -samples on the circle around the feed horn, the computation of the coefficients can be accelerated by the fast Fourier transform [Jin15]. The fast Fourier transform yields as many cylindrical wave coefficients as sampling points, while only those larger than a certain threshold may be kept for the evaluation of the electric field with (4.15).

To verify the previous method, an  $H$ -plane sectoral horn antenna according to (4.12) with an aperture width  $A = 9$  mm and a length  $L = 12$  mm was simulated in CST Microwave Studio® (version 2017.5). The electric field for the equivalent cylindrical wave coefficients is sampled equidistantly on a circle with diameter  $1.4L$  and an angular sample spacing of about  $\lambda/10$ . To compare the accuracy of the cylindrical wave representation against the full-wave simulation in CST Microwave Studio® (time-domain solver with a  $\lambda/40$  mesh), a comparison field was evaluated and exported on a straight line that extends from  $(u, v) = (30 \text{ mm}, -60 \text{ mm})$  to  $(u, v) = (90 \text{ mm}, 60 \text{ mm})$ . The results are plotted in Fig. 4.34. The maximum relative amplitude error is  $-50$  dB and the maximum phase deviation is  $4^\circ$ . The computation of 5000 field values by means of the cylindrical wave source took less than 0.3 s. In terms of accuracy, the cylindrical wave representation yields perfect results. Once the cylindrical wave coefficients are obtained, the field at a certain point can be computed in negligible time.

#### 4.6.4 Computation of the Reflector Contour

In order to radiate a Gaussian beam with a focal plane in front of the antenna, the amplitude and phase on the reflector contour have to match those of the Gaussian beam.

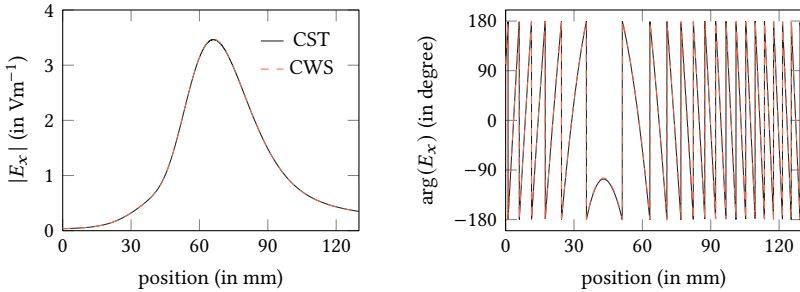


**Fig. 4.34:** Radiated field from an  $H$ -plane horn antenna with  $A = 9 \text{ mm}$  and  $L = 12 \text{ mm}$  in a parallel-plate waveguide. The field is evaluated on a straight line from  $(u, v) = (30 \text{ mm}, -60 \text{ mm})$  to  $(u, v) = (90 \text{ mm}, 60 \text{ mm})$ . Shown is a comparison between the full-wave simulation in CST Microwave Studio<sup>®</sup> (version 2017.5) and the cylindrical wave representation. The achieved agreement is better than  $-50 \text{ dB}$  relative amplitude deviation and better than  $4^\circ$  phase deviation with 71 cylindrical waves.

Matching amplitude and phase simultaneously is not possible [Boh89]. Depending on the position and tilt of the  $H$ -plane sectoral horn relative to the desired Gaussian beam, the reflector contour changes. In this work, the reflector contour is designed such that it matches the phase of the desired Gaussian beam with that of the horn field. The agreement of the individual field magnitudes is evaluated. The final reflector contour minimizes the area consumption and the amplitude mismatch.

Let the electric field of the desired Gaussian beam be denoted as  $E_x^g(y, z)$  and the horn field as  $E_x^h(y, z)$ . The horn field follows from the equivalent cylindrical wave source, which is evaluated at the appropriate coordinate in the coordinate system of Fig. 4.32. For the evaluation of the horn field by means of (4.15), the  $(y, z)$ -coordinates are rotated and translated according to the horn position relative to the Gaussian beam ( $\varphi$  and  $d$ ) to obtain the corresponding  $(\rho_h, \phi_h)$ -coordinates.

The first point of the contour is the intersection of the Gaussian beam axis and the main beam direction of the  $H$ -plane sectoral horn antenna at  $(y, z) = (0, 0)$ . Similar to [Boh89], the accumulated phase at this point is

$$\arg \{E_x^g(0, 0)\} + \arg \{E_x^h(0, 0)\} = \varphi_c, \quad (4.18)$$

where  $\varphi_c$  is a constant and arbitrary phase value. In order to have an equal “phase delay” from the horn field to the Gaussian beam field, the accumulated phase on valid reflector contour points has to equal the arbitrary constant  $\varphi_c$ . This is, for every valid

contour point  $(y_c, z_c)$  the equality

$$\arg \{E_x^g(y_c, z_c)\} + \arg \{E_x^h(y_c, z_c)\} = \varphi_c \quad (4.19)$$

must hold. In a similar manner, for also matching the amplitude of both fields, the additional condition of a valid contour point is [Boh89]

$$|E_x^g(y_c, z_c)| = u_c |E_x^h(y_c, z_c)|, \quad (4.20)$$

where  $u_c$  is a proportionality constant scaling one field to the other. This constant is determined at the intersection point as  $|E_x^g(0, 0)|/|E_x^h(0, 0)| = u_c$ . However, as only one of both conditions (phase and amplitude) can be fulfilled at the same time, the other has to be variable. In this work, the phase of both fields is matched at the reflector contour. Hence, the proportionality constant of the amplitude values may vary for all reflector contour points and, thus, can be denoted as

$$u_c(y_c, z_c) = \frac{|E_x^g(y_c, z_c)|}{|E_x^h(y_c, z_c)|}. \quad (4.21)$$

The ratio of the proportionality factor at a contour point to the proportionality factor at the intersection point is a measure of how well the amplitudes are matched. This is, for a perfect amplitude match the ratio  $u_c(y_c, z_c)/u_c(0, 0)$  tends to unity at every contour point. Any deviations from unity yield an amplitude mismatch and represent a measure of how good or bad the amplitudes of both fields are matched.

Starting from the intersection point at the origin of the  $yz$ -coordinate system, the contour points are obtained in an iterative manner. For this, the contour is split into two parts: an upper part for  $y > 0$  and a lower part for  $y < 0$ . To find the next valid contour point, the Gaussian beam field and the horn field are evaluated on a half-circle around the intersection point. To get a contour point in the upper part, the half-circle is open towards the lower part and, vice versa. The radius of the half-circle should be smaller than  $\lambda/50$  and the angular spacing of the evaluated points on the contour should be similarly small. If the radius or the spacing is too large, the final contour may have errors or a roughness on a similar scale that lead to non-negligible phase errors. The point on the half circle that is closest to  $\varphi_c$ , i.e.,

$$\min \left| \arg \{E_x^g(y_c, z_c)\} + \arg \{E_x^h(y_c, z_c)\} - \varphi_c \right|, \quad (4.22)$$

is taken as the next valid contour point. In the next step, the fields are evaluated on a half-circle around the lastly obtained contour point. The point that comes closest to the reference phase constant  $\varphi_c$  is the next contour point. This iterates until the amplitude of the Gaussian beam field has dropped below a certain level (e.g.,  $-25$  dB of the main beam amplitude). An equivalent loop runs for the lower part of the contour, just that the

half-circle is now open towards the upper part. The amplitude proportionality factor is stored for every valid contour point and serves as quality measure of the contour.

With this procedure, many valid contours for different  $H$ -plane sectoral horn configurations ( $L$  and  $A$ ) and their alignment with the Gaussian beam ( $d$  and  $\varphi$ ) may be computed. The computation of a contour is fast, as the horn field is represented by cylindrical waves and the Gaussian beam has an analytical representation. The computational time of a single contour with about 1000 points is on the order of a second.

To decide for a suitable reflector contour, two quality measures are employed: the amplitude match as the ratio of  $u_c(y_c, z_c) / u_c(0, 0)$  and the area consumption of the reflector. The latter can be computed by numerically integrating the reflector contour along the  $y$ -axis, see Fig. 4.32.

In this work, the final reflector contour for a targeted Gaussian beam with  $w_{0y} = 20$  mm and  $z_{0y} = 200$  mm was obtained in three steps. First, a database with cylindrical wave representations of 529  $H$ -plane sectoral horn configurations, covering the range  $A/\text{mm} = 4, 4.5, \dots, 15$  and  $L/\text{mm} = 4, 4.5, \dots, 15$ , was generated. The full-wave simulation of these geometries is relatively fast, as the simulation volume is small compared to the wavelength. Only those horn antennas with a  $s_{11} < -20$  dB were considered for further computations. In the next step, reflector contours were computed for horn alignments in the range  $\varphi/\text{degree} = 40, 45, \dots, 70$  and  $d/\text{mm} = 40, 45, \dots, 70$ . The contours were computed for relative amplitudes of the Gaussian beam above  $-25$  dB. The area consumption and amplitude mismatch was evaluated for each contour. In the last step, the sampling resolution of the  $\varphi$  and  $d$  was increased in a range around the best contour. The configuration that leads to the best compromise between space consumption and amplitude mismatch was chosen for the reflector. Overall, the whole process of finding a suitable reflector contour is brute-force. The final decision is subjective and supported by the two measures of area consumption and amplitude mismatch. However, this procedure is considered sufficient for this problem. Especially in view of the secondary importance of the beam quality that is influenced by the reflector contour.

The final configuration for the radiating element of the phased array antenna are an  $H$ -plane sectoral horn with  $A = 6.5$  mm and  $L = 7.5$  mm aligned to the desired Gaussian beam with  $\varphi = 58.5^\circ$  and  $d = 55$  mm. The final contour has 1388 points. The search radius was  $\lambda/50$  and the angular resolution was  $0.01^\circ$ . From the design procedure, the phase of both fields is perfectly matched on the reflector contour with a maximum deviation of  $2 \times 10^{-5}$  degree. For an evaluation of the amplitude mismatch, see Fig. 4.35. The amplitudes on the lower part of the reflector are matched well: the relative amplitude proportionality factor varies between 0.8 and 1.2 for Gaussian beam amplitudes above  $-20$  dB. The amplitude of the horn field follows that of the Gaussian beam, see right plot in Fig. 4.35. In contrast, the upper part of the reflector is not matched equally well. The amplitude proportionality factor drops below 0.4. The horn field replicates the Gaussian beam field well for amplitudes above roughly  $-5$  dB.

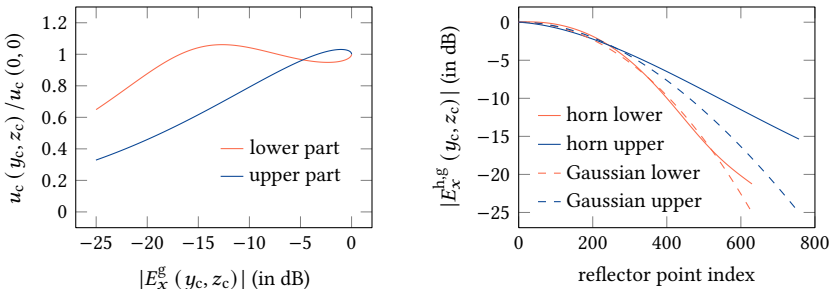


**Fig. 4.35:** Left: Relative amplitude proportionality factor on the reflector contour. Right: Amplitude of the horn field and Gaussian beam field on the reflector contour normalized to the corresponding amplitude at the intersection point.

For weaker amplitudes, the error increases. The horn field not even decays below  $-20$  dB. This is due to the geometrical alignment of the horn to the reflector contour, see Fig. 4.32. The field on the upper half of the contour reflects the horn field from a smaller angular region of the horn aperture as compared to the reflection of the lower half of the contour.

This amplitude mismatch will excite higher-order Gaussian beams or side-lobes. A further iteration that tries to modify/tune the amplitude distribution of the horn field, by modifying the horn flare in a non-symmetric way, may account for this deviation. This, however, has not been investigated in this work as the realized beam was already considered good enough.

#### 4.6.5 Evaluation of a Prototype Reflector

A prototype of the reflector contour, the  $H$ -plane sectoral horn antenna and a WR10-waveguide were realized in aluminum AL99.5, see Fig. 4.36. The prototype is split into two parts: a block with the milled reflector contour, the horn, and the WR10-waveguide, and a second block that serves as a cap that closes the contours. In the reflector area, tracks of the milling tool remain. These tracks, however, have a small depth and do only affect the realized conductivity of this surface.

Measurements were carried out with the volumetric near-field scanner as described in [HKN+18; KHSE16]. As only a small angular range of the probe antenna was scanned, where its pattern changes only little, no probe correction was performed. A full-wave simulation of the reflector prototype was carried out in CST Microwave Studio<sup>®</sup> (version 2017.5).

For a two-dimensional representation of the radiated beam at the frequencies 75 GHz,

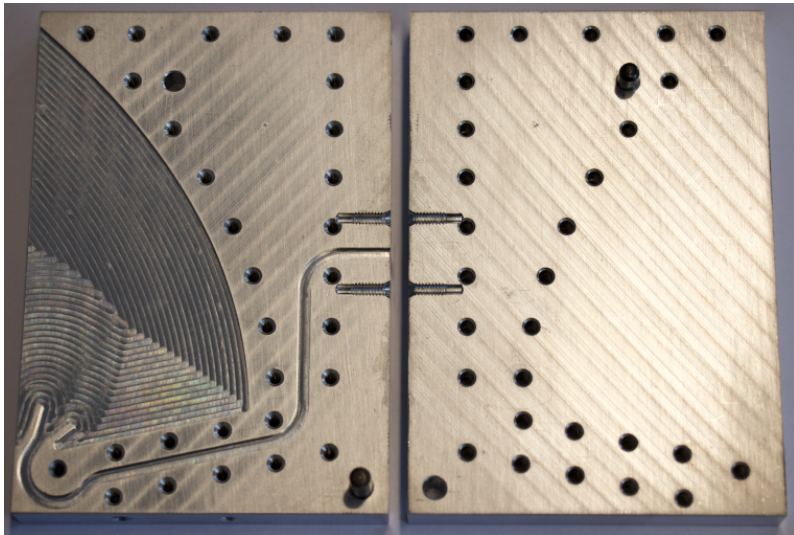


**Fig. 4.36:** Image of the prototype reflector milled in aluminum AL99.5. The reflector contour is milled in one block with a depth of 1.27 mm corresponding to the full height of the WR10 and parallel-plate waveguide. A flat cap closes the contours.

90 GHz, and 105 GHz, see Fig. 4.37. There, the left plot shows the beam radius ( $-8.69$  dB contour) and the right plot shows the  $-15$  dB contour. At 90 GHz, the beam waist radius is slightly larger as the desired 20 mm. The beam waist radius gets larger for lower frequencies and smaller for higher frequencies.

The transverse field amplitude and phase at the desired beam waist location ( $z = 200$  mm) is plotted in Fig. 4.38. The measured field is represented by solid lines, whereas the simulated field is represented by dashed lines. The left plot shows the relative amplitude dependency along the  $y$ -axis. The amplitudes are normalized to the maximum amplitude of the corresponding  $y$ -axis cut. It can be seen that the amplitudes are not symmetric with respect to  $y = 0$  mm. This is due to the unequally illuminated reflector contour through the horn antenna, see Fig. 4.35. The phase, depicted in the right plot of Fig. 4.38, varies in a range of less than  $\pm 15^\circ$  for the measurement and by less than  $\pm 5^\circ$  for the simulation within the desired beam waist radius  $w_{0y} = 20$  mm. The difference between simulated and measured phase can be explained by manufacturing tolerances and a possible small misalignment of the prototype reflector towards the linear stage of the near-field scanner [HKN+18; KHSE16].

In summary, the radiated beam is not perfect. It is non-symmetric and has several

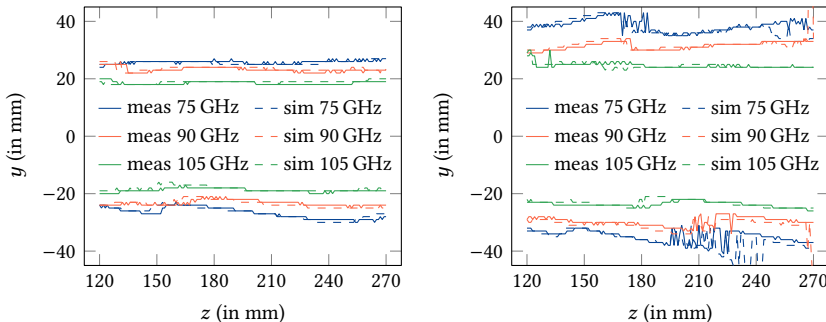


**Fig. 4.37:** Simulated and measured Gaussian beam contours for the frequencies 75 GHz, 90 GHz, and 105 GHz. Left:  $-8.69$  dB to amplitude at  $x = 0$  mm. Right:  $-15$  dB to amplitude at  $x = 0$  mm. Measurement without probe correction due to the small angular range.

side-lobes or a certain roughness of the transverse amplitude. However, it concentrates the energy towards the beam axis which is the most important part. Besides, the simulation of the plasma disruption force on a stack of 39 of these reflectors (by Irene Zammuto) yielded forces on an acceptable level. Hence, these reflectors have clearance for in-vessel installation at the ASDEX Upgrade tokamak.

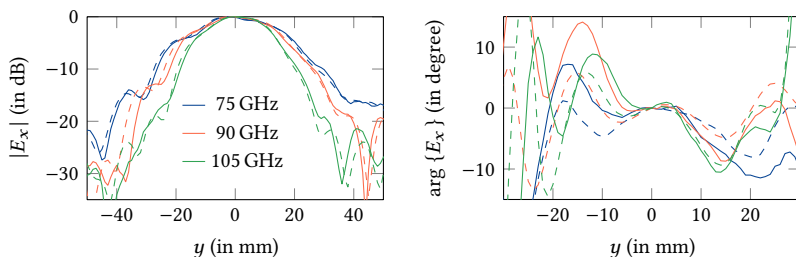


**Fig. 4.38:** Simulated and measured radiated Gaussian beam at  $z = 200$  mm. Solid lines represent the measured field, dashed lines represent the simulated field.



# 5 The Phased Array Antenna

In this part of the thesis, the techniques and components that were presented in the previous sections are employed to assemble a phased array antenna for Doppler reflectometry in the ASDEX Upgrade tokamak. Firstly, the system design with the environmental requirements, the desired radiated beam, and a schematic of the phased array antenna are repeated and discussed. This is followed by the arrangement of the individual elements to form the feed network and eventually the phased array antenna. Full-wave simulation results of the whole phased array antenna wrap up this chapter.

## 5.1 System Design

### 5.1.1 Environment, Materials, and Installation Space

The phased array antenna is dedicated for installation in sector 11 of the ASDEX Upgrade tokamak. The installation location is in-vessel and close to the plasma. There, the phased array antenna has to sustain the environmental conditions and must not affect the nuclear fusion experiment in any unwanted way.

During a plasma discharge, the antenna is prone to the static magnetic field with the potential of a plasma disruption as well as all the radiation emitted by the plasma. The static magnetic field has field strengths of up to 2.8 T. The antenna should not be affected by this, and, even more important, not affect this field. The hot plasma emits nuclear radiation as well as electromagnetic radiation ranging from infrared to hard X-ray. Here, aging and activation of the materials in use must be considered. In case of a plasma disruption, that is an abrupt break off of the plasma current, the antenna must not damage any other components in the fusion experiment and should not be damaged itself.

Apart from the regular operation, the phased array antenna must withstand semi-regular vessel baking up to 150 °C and support the ultra-high vacuum with pressures within the vessel down to  $10^{-9}$  mbar.

Materials that may be used in-vessel are approved by the ASDEX Upgrade team. Most dielectrics do not comply with the ultra-high vacuum requirements and may be used in very small amounts, only. The materials at choice are the following four non-magnetic metals:

- stainless steel 1.4301 [nominal conductivity  $1.37 \times 10^6 \text{ Sm}^{-1}$ ]

- pure copper [nominal conductivity  $59.6 \times 10^6 \text{ Sm}^{-1}$ ]
- almost pure aluminum AL99.5 [nominal conductivity  $35 \times 10^6 \text{ Sm}^{-1}$ ]
- Albromet-W 200 [nominal conductivity  $22 \times 10^6 \text{ Sm}^{-1}$ ]

In terms of electrical properties, the favorable material for the antenna would be pure copper. However, its good conductivity is disadvantageous in case of a plasma disruption as the induced currents are very strong. The currents and, thus, the disruption force can be handled by reducing the conductivity or the area of the metal. For a component (such as the reflector) that has a fixed size, the only possibility for keeping the disruption force within the allowed limits, is to trade Ohmic losses with sustainability to plasma disruptions. Hence, by taking a material with a slightly lower electrical conductivity. We did decide against a coating of the surface, as it also has to be approved by the AUG team and the overall manufacturing process is already very complex.

Equally important is the machine-ability of the material. Stainless steel is hard and maybe too hard for small milling tools. In contrast, pure aluminum is soft and small slots (as they are required in the hybrid-junction of the variable phase shifter) might be smeared. Albromet-W 200 is somewhere in-between both extremes.

In summary, Albromet-W 200 seems to be the best compromise. It has an acceptable (and not too good) electrical conductivity and a reasonable good machine-ability. On these grounds, it is the dedicated material of the feed-network and the radiating elements. For all non-electrically important parts such as fixtures, stainless steel 1.4301 is employed.

Apart from these metals, the following materials may be installed inside the vessel

- Piezo ceramic
- silicon carbide
- PEEK (in small portions as a dry-lubricant)
- fused silica

Clearly, this list is not complete. It covers only those materials that were considered for this thesis.

The phased array antenna is mounted in ASDEX Upgrade tokamak on a massive stainless steel console, see Fig. 5.10 for the final model. This console provides the 0-degree steering angle alignment. The phased array antenna is tight to the console by a clamp. The whole fixture is strong enough to support and hold the antenna in place, even if a plasma disruption occurs.

In the coordinate system of the Gaussian beam Fig. 2.1, the  $x$ -axis is normal to the mounting surface of the console, and the  $y$ -axis is parallel to the surface of the console,

compare Fig. 5.10. The  $y$ -axis is aligned parallel to the static magnetic field, whereas the  $x$ -axis is aligned perpendicular to the static magnetic field.

The installation space is limited by the port size and the spatial extension of other diagnostic instruments. The latter also includes that a diagnostic must not cover the view of another diagnostic into the plasma. For the phased array antenna, the available space can be specified by a rectangular box with dimensions  $(D_x, D_y, D_z) = (90 \text{ mm}, 120 \text{ mm}, 300 \text{ mm})$ . The individual dimensions are in the coordinate system of the desired beam. This is, the  $D_x$  is parallel with the steering-axis, the  $D_y$  is perpendicular to the steering plane, and the  $D_z$  is parallel to the propagation axis. The  $D_x$ -dimension limits the number of elements. The  $D_y$  dimension limits the size of the reflector. The  $D_z$  limits the maximum length of the phased array antenna.

### 5.1.2 Schematic of the Phased Array Antenna

The schematic of the phased array antenna is sketched in Fig. 5.1. The underlying topology is a centrally fed serial array. The serial topology is preferred over a parallel topology as only one (two in case of a centrally fed topology) actuator to control the phase shifters is required. For in-vessel use and for reliability of the phased array antenna, keeping actuating elements at a minimum is more important than to have the better efficiency of the parallel feed. The centrally fed topology is preferred over a single ended topology because of a better efficiency. This is, the major part of the energy is already tapped-off at the first elements in a branch due to the array taper that has its maximum at the center of the array. In the single ended feed, the energy has to pass half of the phase shifters first, to arrive at the center of the array. Thus, the centrally fed serial array absorbs less energy as compared to the single ended serial array.

With reference to the schematic Fig. 5.1, the wave enters the feed network at the lower central node. From there, it travels through a three-way power divider that directs the required amount of energy to the central radiating element and into both arms of the serial feed.

The branch towards the central radiating element consists of an equalizing waveguide section that matches the electrical length from the input to each radiating element in order to omit any frequency scanning behavior and, thus, a splitting of the beam. After the equalizing waveguide follows a focusing section that models the required frequency-dependent phase at each element. The wave finally leaves the array antenna through the radiating element.

The left and right branch that leave the three-way power divider at the center of the serial chain, feed the remaining radiating elements. The branches are built up equally and symmetrically, only the phase shifters realize the phase shift in the opposite direction. Down the line of each branch, a phase shifter is followed by a coupling structure that taps-off the correct amount of energy towards the connected

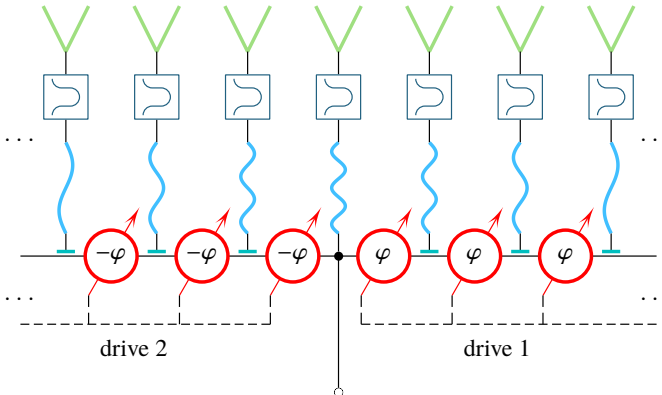


**Fig. 5.1:** Schematic of the phased array antenna [KSE17c], which is a centrally fed array with 39 radiating elements. Individual elements are phase shifters (red), coupling structures (dark green), equalizing waveguide sections (light blue), focusing elements (dark blue), and radiating elements (light green). The phase shifters are controlled by two drives, one for each arm.

radiating element, which is followed by another phase shifter. The phase shifters in each branch share the same reference plane and are controlled by a single actuator. After the last coupling structure in each branch, the remaining energy is absorbed in a load. The tapered-off waves at each coupling structure travel subsequently through the equalizing waveguide sections, the focusing section, and finally emit through the individual radiating elements.

To realize the phased array antenna as outlined by the schematic in Fig. 5.1, the individual elements from Chapter 4 are employed. Their detailed design and arrangement are presented and discussed in Section 5.2.

### 5.1.3 Desired Gaussian Beam and Steering Properties

As discussed in Section 3.1.2, the optimum beam properties are dependent on the plasma configuration. For the dedicated position of the phased array antenna in AUG and its view into the plasma, the beam should probe the plasma in the *W*-band with X-mode polarization, see Section 2.5.2. The optimum beam properties were communicated by Garrard Conway and Tim Happel in the framework of the Helmholtz Virtual Institute to be a fundamental mode Gaussian beam with a beam waist radius of  $w_{\text{opt}} = 7\lambda_0$  in a focal distance from the array aperture in the range from 200 mm to 400 mm. The Gaussian beam should be synthesized in *W*-band for the frequency range from 75 GHz to 105 GHz. The upper limit is due to a notch filter at the reflectometer input that

protects the hardware from the high-power electron cyclotron heating.

The required steering angle follows from the desired turbulence wavenumber spectrum range to be probed, which follows from the Bragg condition discussed in (3.2). According to Garrard Conway and Tim Happel, this is about  $\pm 20^\circ$  from the 0-degree alignment of the mounting surface or broadside radiation from the phased array antenna. Larger steering angles sample turbulence sizes that result in a weak refraction.

As the plasma turbulence is to be probed in X-mode, the polarization of the radiated beam has to be normal to the magnetic field. From the alignment of the mounting console to the static magnetic field  $B_0$ , the Gaussian beam is synthesized by the array taper along the  $x$ -axis (normal to the console surface in AUG). The perpendicular beam shape along the  $y$ -axis is synthesized by the radiating element. The beam is steered in the  $xz$ -plane.

### 5.1.4 Synthesis of the Array Taper

Following the procedure from Section 3.3, the Gaussian beam is synthesized by sampling its transverse field with the individual radiating elements. This is, in the steering plane of the phased array antenna ( $xz$ -plane), the Gaussian beam is synthesized by the array taper. In normal direction to the steering plane ( $yz$ -plane), the Gaussian beam is synthesized by the individual radiating reflector element. The polarization of the electric field has to be parallel to the steering plane (X-mode alignment). Thus, the radiating element is a parallel plate waveguide that supports only  $TM_{m0}^z$ -modes that yield a uniform electric field in array direction.

The element spacing is restricted by the maximum desired steering angle. This is, it has to be small enough to guarantee that no grating-lobe occurs at the maximum steering angle. From (3.21) follows the maximum element spacing. With the smallest wavelength at 105 GHz and the maximum steering angle  $\Theta_{p,max} = 20^\circ$ , the element spacing is limited to  $d_x \leq 2.1$  mm. To have a safety margin and due to raw material considerations, the element spacing is  $d_x = 2$  mm.

The number of elements would normally follow from the desired side-lobe level, see the considerations in Section 3.3.2. The side-lobe level, however, should be “as good as possible”. Consequently, the available installation space is the limiting factor. In the steering direction, the installation space is limited by  $D_x = 90$  mm. To have some space for fixtures, the number of elements is 39 leading to an array length of about 80 mm (+2 mm for the cap of the last element).

The weights of the individual elements follow directly from (3.27). To keep the antenna design simple, the amplitude distribution is defined to be frequency-invariant at the array aperture. This leads to frequency-invariant coupling values (from the trunk line to the radiating element), but inevitably leads to a frequency-dependent focal distance which increases for higher frequencies, see Fig. 3.14.

The synthesis procedure of the array taper is described in Section 3.3.7. Following

this recipe for the desired beam, the amplitude distribution of the array aperture is defined at 75 GHz for a fundamental Gaussian beam with beam waist radius  $w_0 = 7\lambda$  and a focal length of 200 mm. At this frequency, the Gaussian beam has the smallest focal length, which now corresponds to the minimal measurement distance from the array aperture as described in Section 5.1.3. The amplitude at each element follows from (3.27). Again, the amplitude distribution is the same for all frequencies. The beam waist is controlled by the phase taper. For this, the focal length follows from (3.33) and the frequency dependent radius of curvature at the array aperture follows from (3.35). The final array taper is summarized in (3.36) with a frequency dependent phase distribution at the array aperture that models the desired  $w_0 = 7\lambda$ . The beam shape for different frequencies is plotted in Fig. 3.14.

The frequency-independent amplitude distribution can be realized by the coupling structure as presented in Section 4.1. The frequency dependent phase distribution can be realized by the focusing section as presented in Section 4.3.1. In the following sections, these individual elements are combined with the variable phase shifters, the compensation lines, and the radiating elements to build up the phased array antenna as outlined in Fig. 5.1.

## 5.2 Design of the Phased Array Antenna

The phased array antenna is composed of the individual components presented in Chapter 4, which are arranged such that all phase shifters can be controlled by two Piezo actuators and that an element spacing of  $d_x = 2$  mm is achieved. The former basically requires that the sliding shorts of all phase shifters in a branch, see Fig. 5.1, share the same reference plane. The latter restricts the spacing and positioning of the individual components in the array direction.

In the following subsections, the arrangement of the individual components to fulfill both criteria is described. For this, the individual elements are combined to five sub-assemblies. The whole phased array antenna is built from these sub-assemblies. Subsequently, the dimensions of the individual elements are synthesized based on the desired amplitude taper and the material properties.

### 5.2.1 Periodic Element in the Serial Feed Chain

The phase shifter and the coupling structure, as presented and prototyped in Section 4.2.4, built up a periodic element in the serial feed chain of the phased array antenna, see Fig. 5.1. This is, they make up a repeating pattern. The spacing between the input and output port of the phase shifter is 2.0604 mm and, thus, slightly larger than the element spacing of  $d_x = 2$  mm. In addition, a coupling structure has to be placed in-between two phase shifters in order to tap-off the required amount of power to the radiating element, see also in the antenna schematic in Fig. 5.1. Hence, the

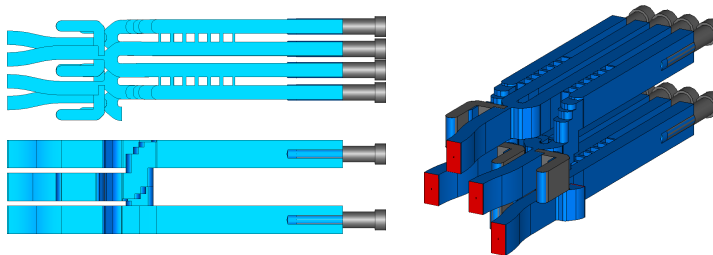


**Fig. 5.2:** Serial periodic section comprising coupling structures, straight waveguide sections, vertical transitions, and phase shifters. Several sections may be combined to form a longer chain.

spacing between two neighboring elements largely exceeds the desired element spacing of 2 mm. There is not enough space on a single split-block layer to place these elements in a serial fashion, while realizing a common reference plane for all sliding shorts. Thus, the design of the serial chain is extended onto three waveguide layers. The connection between the individual layers is realized with the vertical transitions as described in Section 4.5.

A model of the periodic structure is given in Fig. 5.2. Starting at the lower right of the perspective view in Fig. 5.2, a coupling structure is the first element. A straight waveguide section connects this coupling structure to a phase shifter. Both elements are on the same split-block layer. At the output port of the phase shifter, a forward-aligned vertical transition follows. The waveguide is now on the central split-block layer, see lower left view in Fig. 5.2. A coupling structure follows after the vertical transition. The coupling structure is mirrored in array direction with respect to the first coupling structure (compare the orientation of the inserts). The rotation is required to provide enough space for the insert and its fixture. Another forward-aligned vertical transition follows after the second coupling structure. The waveguide is now on the upper layer, where a second phase shifter follows subsequently. On the output of this phase shifter, a straight waveguide section and the third coupling structure are connected. The insert is now aligned in the same direction as that of the first coupling structure. After the last coupling structure, a straight waveguide section, the third phase shifter, another forward-aligned vertical transition, and the fourth coupling structure follow. The fourth coupling structure is located on the central split-block layer. A forward-aligned vertical transition, the fourth phase shifter, and a straight waveguide section close the loop to the lower split-block layer — where the whole sequence may start again. Several of these serial periodic sections build up the whole phased array antenna.

The individual building blocks in-between two coupling structures are always the same. Only their sequence changes. As a consequence, the electrical length between two coupling structures is equal for all elements. The coupling structure is alternatingly

mirrored in array direction, which is necessary to provide enough space for the insert and has the benefit that the propagation direction through the coupling structure does not change. However, the electric field lines in the coupled port are also mirrored with the geometry. Hence, there is a fixed and frequency-invariant 180° phase shift between both orientations. Mirroring the coupling structure must not change the element spacing and, thus, the output port of the coupling structure needs to be (and actually is) symmetric with respect to the mirroring plane Section 4.1.3.

The element spacing is controlled by the short sections that connect the coupling structure with the phase shifter. Namely the straight waveguide section and the forward-aligned vertical transition. They may be expanded or compressed in array direction like an accordion by routing them slightly obliquely.

The short-circuited ports of the phase shifters share a single reference plane for their axial positioning. Consequently, all sliding shorts in a branch can be controlled by a single Piezo actuator.

As the geometry might not be clear from the model in Fig. 5.2 and the description above, the important aspects are repeated in a few statements:

- The serial arrangement of the individual elements follows one of two schemes:
  - either: coupling structure – straight waveguide section – phase shifter – vertical transition – next coupling structure,
  - or: coupling structure – vertical transition – phase shifter – straight waveguide section – next coupling structure.
- The electrical length of both schemes is equal.
- The element spacing is controlled by expanding or compressing the vertical transition and the straight waveguide section in array direction.
- The coupling structures alternate their alignment (mirrored in array-direction).
- The propagation direction through a coupling structure is always the same.
- The coupled port of the coupling structure includes a translation in array direction such that the coupled waveguide is symmetric to the mirroring plane.
- The mirroring also affects the electrical field lines. Hence, there is a frequency-invariant 180° phase shift between both alignments.
- All sliding shorts share the same reference plane.

As already stated, several of these periodic sub-assemblies in Fig. 5.2 may be connected in a serial fashion to form a long feed-chain. As the phased array antenna is centrally-fed, the central sub-assembly of the serial chain differs from the others to also incorporate the input waveguide and the central element feed line.

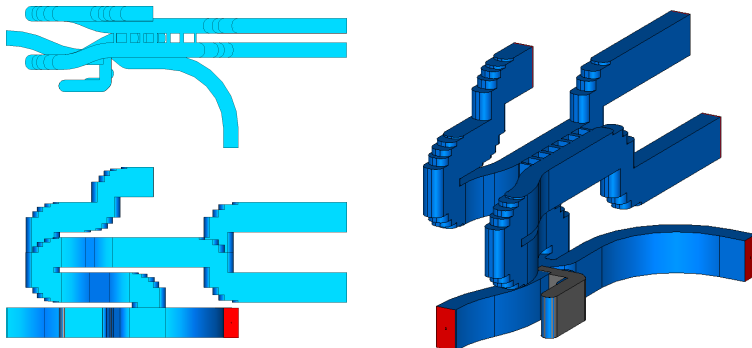


**Fig. 5.3:** Central element in the serial feed chain. The wave enters at the lower right of the perspective view. It first propagates through a coupling structure, where the required amount of power is tapped off for the central element. The remaining part is split by a hybrid-junction for both arms of the central-fed series feed.

### 5.2.2 Central Element in the Serial Feed Chain

The central element splits the incoming wave into three directions; towards the central radiating element, and the two opposing array directions, compare Fig. 5.1. For the model of the central element, see Fig. 5.3. In the perspective view, the wave is incident at the lower right waveguide with the  $90^\circ$ -bend. The wave first approaches a coupling structure, where the desired amount of power is tapped off towards the central radiating element. Two backward-aligned transitions follow subsequently. The connecting waveguide between coupling structure and backward-aligned transition is slightly bent to provide a space in-between both transitions for a waveguide to fit in (central compensation line). After the vertical transition follows a branch-guide coupler that splits the wave into two parts. One for each direction of the array. At the through and coupled port of the hybrid-junction follows a forward-aligned transition. They are aligned in opposite direction — one upward and one downward — to enable the connection to the periodic sections of Section 5.2.1. In the perspective view in Fig. 5.3, the coupled port of the hybrid-junction has an upward aligned forward-transition and feeds the periodic sections towards the right (perspective view). The through port of the hybrid-junction has a downward aligned forward-transition and feeds the periodic sections towards the left. The isolated port of the hybrid-junction is connected to a load as of Section 4.4 (not visible in Fig. 5.3), such that the power does not remain in the feed network.

The coupling factor of the hybrid-junction has to be constant throughout the operational frequency range. Otherwise, the aperture taper would be asymmetric and

erroneous with respect to the central axis. Thus, the design of the hybrid-junction in the variable phase-shifter is also employed in the central section, see Section 4.2.3. This component has the broadest operational frequency range that can be manufactured by milling at the workshop of the Technical University of Munich, Chair of High-Frequency Engineering.

### 5.2.3 Phase-Equalizing Waveguide Sections

The phase-equalizing waveguide sections connect the outputs of the coupling structures to the focusing sections, see Fig. 5.1. There are two reasons for adding such a long waveguide section in-between the serial feed-chain and the radiating elements. The first is to have a Gaussian beam that does not steer with frequency. To suppress this behavior, the electrical length from the input to the output port has to be equal (neglecting the phase taper). The second reason originates from the centrally fed serial feed design. A frequency scanning of both individual branches would lead to a splinting beam. Thus, if one wants to relinquish the long waveguide sections for easier manufacturing and lower losses, the overall feed design has to be modified to a single branch series feed. For the proposed antenna, a major design goal was to have a frequency-invariant beam steering. Hence, equalizing waveguides are required. In this case, the centrally fed array is a better solution as compared to the single branch series feed, as the overall length of the compensation line is smaller. Only the electrical length from the center of the feed to the outermost elements has to be compensated.

The length of the individual compensation lines is determined by the electrical length from the input to the output port of the serial feed chain (combination of coupling structures, forward-aligned transitions, and phase shifters). In order to suppress any frequency steering, the electrical length from the input to each radiating element has to be adjusted. To enable this, the dispersion characteristic of the compensation waveguides has to match the dispersion characteristic of the periodic section in the serial feed chain.

As the geometry of the serial feed chain is rather complex, the electrical length in-between two elements is determined by full-wave simulations in CST Microwave Studio<sup>®</sup> (version 2017.5). The phase of the periodic feed chain can be decomposed in a phase with approximately WR10-dispersion and a frequency-invariant phase. The WR10-dispersion contribution is due to the connecting waveguides. The frequency-invariant phase offset is due to the 180° from mirroring the coupling structure and an additional 90° from the hybrid-junction of the phase shifter.

Thus, for this feed-network, the electrical length in-between two ports is compensated by a linear combination of a WR10-waveguide section and a frequency-invariant phase offset. The former is compensated by WR10-waveguides with an appropriate length. The latter is compensated by the frequency-invariant phase shifter as presented in Section 4.3.2. This frequency-invariant phase shifter is incorporated in the focusing



**Fig. 5.4:** Compensation line of the outermost element, which represents the shortest compensation line. It has six vertical transitions and spreads over two split-block layers.

section, see Fig. 5.1, as it is described in Section 5.2.4. Hence, the compensation lines only need to equate the phase offset due to the WR10-dispersion.

For an image of a short and a long compensation line see Fig. 5.4 and Fig. 5.5, respectively. To minimize space consumption, especially in case of the long compensation line, they are spread over several split-block layers. To mitigate any effect of the vertical transition on the electric length of the overall compensation-length, each compensation line is composed of the same number (for this design: 6) of vertical transitions.

The length of the compensation line is determined as follows: The two different periodic sections of the serial feed chain from Section 5.2.1 in the form of

- coupling structure – straight waveguide section – phase shifter – vertical transition – next coupling structure,
- coupling structure – vertical transition – phase shifter – straight waveguide section – next coupling structure,

are simulated in CST Microwave Studio® (version 2017.5). Their electrical length is deduced from the phase lag and split in terms of an equivalent WR10-waveguide length and a frequency-invariant portion. This is, the realized phase lag is decomposed into a phase lag due to a WR10-waveguide with a certain length and a frequency-invariant phase lag.

As already stated, the frequency-invariant phase lag is influenced by the hybrid-junction, the alternating electric field alignment in the coupling structure and, in parts due to a non-perfect WR10-dispersion in the vertical transition and in the coupling structure. For the proposed design of the periodic element, see Section 5.2.1, the frequency-invariant portion in the phase lag is  $180^\circ$  and the compensation line length is about 30 mm. The phase in-between two elements is compensated by the WR10-waveguide with appropriate length (the compensation line) and a fixed  $180^\circ$  phase



**Fig. 5.5:** Compensation line of the central element, which represents the longest compensation line. It has six vertical transitions and spreads over five split-block layers.

lag. Within one branch of the centrally fed array, the frequency-invariant phase compensation realizes an alternating  $0^\circ$  and  $180^\circ$  phase lag along the array direction.

The central element introduces a different compensation line length as well as a different frequency-invariant phase lag. The frequency-invariant phase lag is compensated by a  $297^\circ$  constant phase sections. The compensation line length is about 60 mm. Due to the hybrid-junction in the central element, see Fig. 5.3, the left branch (serial feed chain) of the centrally fed array has a  $90^\circ$  frequency-invariant phase lag with respect to the right branch. Consequently, the frequency-invariant phase compensating part alternates between  $90^\circ$  and  $270^\circ$  in the right branch and between  $0^\circ$  and  $180^\circ$  in the left branch of the centrally fed array.

The frequency-invariant phase compensation is realized by the model described in Section 4.3.2 and incorporated into the focusing section, see Fig. 5.1 and Section 5.2.4. The remaining phase lag is compensated by the WR10-waveguide sections. The outermost element yields the shortest compensation line which connects the serial feed chain with the focusing section, see Fig. 5.4. For each element that comes closer to the central element, the compensation line is elongated by 30 mm, representing the additional WR10-line length in-between two coupling structures. The central compensation line has an additional 60 mm, due to the slightly longer waveguide section in-between the central coupling structure and the first element in each branch of the serial feed chain. Thus, the central compensation line is the longest of all, see Fig. 5.5.

Although the overall phase compensation mechanism is very promising, the phase in-between neighboring elements cannot be compensated perfectly throughout the desired frequency range. The remaining phase error is about  $\pm 10^\circ$ . This error, however, is equal to all individual periodic sections for a certain frequency. Thus, it reassembles a progressive phase on the aperture and can be corrected for by adapting the  $0^\circ$ -degree position of the phase shifters. This procedure for a correction of the remaining phase error in-between two elements is covered in Section 5.3, as it requires the full-wave simulation or measurement of the whole feed network.

In summary, equalizing the line-lengths from the input port to the individual elements of the array, requires full-wave simulations. Here, the phase lag in-between two elements needs to be compensated. The dispersion in-between two elements does in general not match that of the compensating waveguide (WR10 for this design). As a consequence, the overall compensation line needs to be decomposed into several dispersion characteristics. For this design, the WR10-dispersion and a frequency-invariant phase yielded acceptable results. The remaining phase error in-between two elements from 75 GHz to 105 GHz is in the range of  $\pm 10^\circ$ . For a fixed frequency, the phase error assembles a progressive phase on the array aperture. This progressive phase error can be corrected by calibrating the  $0^\circ$ -degree steering angle position of the phase shifters for each frequency.

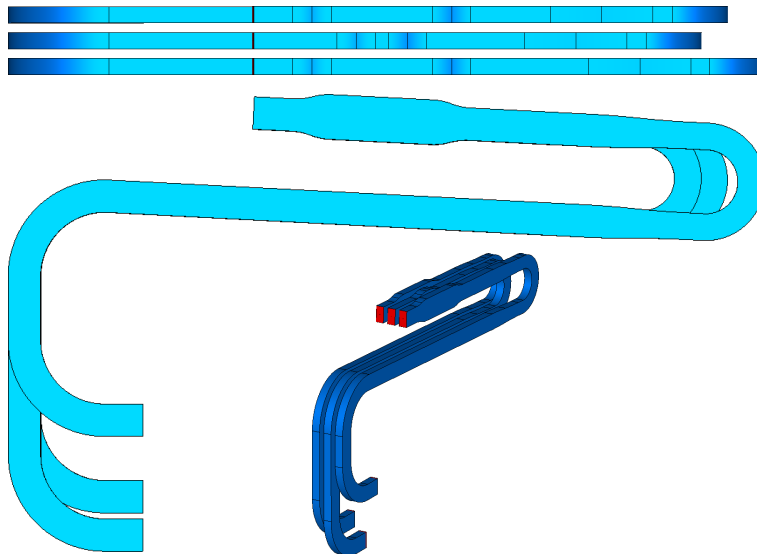


**Fig. 5.6:** Focus structure that incorporates the frequency-dependent phase taper and the constant phase compensation line places all radiating elements on a line along the array direction. The input is on the lower-left and the output on the upper-left.

#### 5.2.4 Focusing and Frequency-Invariant Phase Compensation

The last component that contributes to the array taper is the focusing section, see Fig. 5.1. In the design of the phased array antenna, the focusing section has three functions. It assembles the connection to the radiating elements such that the radiating elements are all placed on a line along the array direction, it realizes the required frequency-dependent phase taper for shaping the desired Gaussian beam and it realizes the required frequency-invariant phase compensation. The geometrical model of the focusing section is depicted in Fig. 5.6.

Due to the geometry of the periodic section and the compensation lines, the waveguides coming from the serial feed network are not located on the same split-block layer. Ensuring this would introduce an unequal number of vertical transitions in the compensating lines and, thus, introduce an erroneous dispersion. In the proposed design, all compensation lines have six vertical transitions and consequently do not suffer from this error. However, their output ports are located on different split-block layers. The focusing section compensates this displacement by a trombone-like geometry. The input-ports, see lower-left in Fig. 5.6, have a different vertical position. The output ports

of each focusing section are all placed on a line along the array direction. The electrical line length of the focusing sections are equalized for all elements by the trombone-like structure (apart from the frequency-dependent phase taper and the frequency-invariant phase compensation).

The frequency-dependent phase taper for shaping the desired Gaussian beam is realized by the component described in Section 4.3.1. Here, a rectangular hollow waveguide with a slightly reduced width and, thus, modified dispersion characteristics reassembles the desired frequency-dependent phase taper. The reduced-width waveguide section is also modeled in the trombone – right before the  $180^\circ$ -bend, see Fig. 5.6. A taper reduces the waveguide width to the desired  $a_f = 2.1$  mm. On each side of the bend, half of the required length  $\ell_f = \ell_0 + \ell$  with an offset length  $\ell_0 = 2$  mm and the negative length  $\ell$  for Gaussian beam focusing (4.5) is added.

The frequency-invariant phase shift, as it is required by the compensation lines in Section 5.2.3, is realized by the constant-phase waveguide section described in Section 4.3.2. Here, a linear combination of the lengths of a slightly over-sized waveguide section and the WR10-waveguide realize the desired phase lag. The over-sized waveguide section is located near the output of the focus section, see upper-left in Fig. 5.6. The required WR10 section is incorporated in the trombone-like structure.

The three functions of the focusing sections lead to different geometries for every element. There is none like another. Thus, the focusing section has to be realized individually for each radiating element. Note that the focusing section cannot be realized anymore by cutting the WR10-waveguide in the  $E$ -plane. To precisely realize the radii and waveguide width, the rectangular hollow waveguide is cut at an edge parallel to the broad side. The radiating reflector is realized in the same cut, hence, both components are manufactured in a single piece. The milled waveguide and reflector structure is closed by a cap. Thus, at the output of the feed network and at the input to the radiating elements, a change in the manufacturing alignment occurs. The individual sections are connected by a flange.

### 5.2.5 Waveguide-Model of the Phased Array Antenna

The phased array antenna is composed of the previously described assemblies and the components presented in Chapter 4. See Fig. 5.7 for a waveguide model of the whole phased array antenna and its analogy to the schematic of the phased array antenna in Fig. 5.1. For clarity, the radiating reflectors are not displayed in the model.

The centrally fed series feed chain is composed of the central element, see Section 5.2.2, and the periodic element, see Section 5.2.1. Together, these elements form the serial feed chain of the phased array antenna. They incorporate the phase shifters and coupling structures and, thus, provide beam steering capabilities and the amplitude taper to shape the desired Gaussian beam. Attached to the serial feed chain follow the compensation lines of Section 5.2.3, which equalize the electrical length from the input

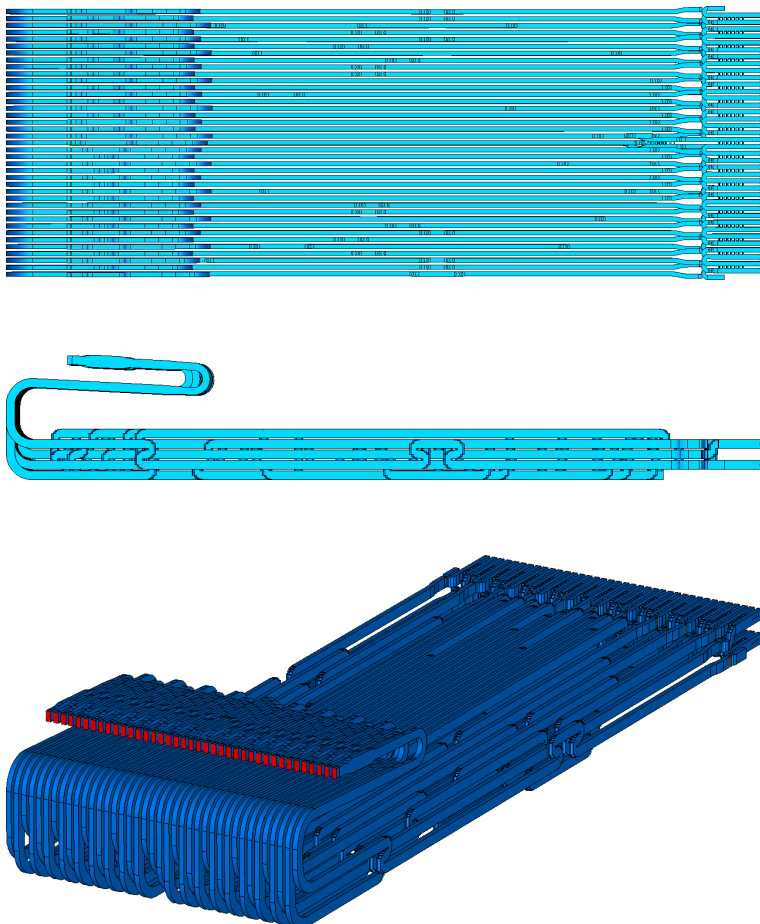


**Fig. 5.7:** Waveguide model of the feed network of the AUG phased array antenna. From top to bottom: top-view, side-view, and perspective view. The radiating elements are not displayed. Starting at the right: serial feed chain with the central element (Section 5.2.2) and the periodic element (Section 5.2.1), compensation lines (Section 5.2.3), and focusing sections (Section 5.2.4).

to each radiating element and, thus, suppress any frequency scanning behavior. In Fig. 5.7, the compensation lines take up most space. Finally, the focusing section of Section 5.2.4 for the frequency-dependent phase taper to realize the frequency-dependent beam waist radius, connects the compensation lines to the radiating elements. The radiating elements are not displayed in the geometry in Fig. 5.7 due to the size of the image. They shape the Gaussian beam perpendicular to the array direction and ensure the correct polarization of the electric field.

### 5.2.6 Synthesis of the Coupling Structures

The synthesis of the coupling structure starts with the required power at the radiating elements. From the amplitude taper (3.30) and the desired beam configuration, see Section 5.1.3, follows the discretized amplitude taper according to

$$|m(n)| = |m(x - nd_x)|, \quad (5.1)$$

with the element index  $n = -19, -18, \dots, 19$  and the element spacing  $d_x = 2$  mm. The normalized radiated power at each element follows as

$$P_{\text{rad}}(n) = \frac{|m(n)|^2}{\sum_{i \in n} |m(i)|^2}. \quad (5.2)$$

The compensation lines have a different length for each element, see Section 5.2.3. Thus, they realize a different insertion-loss which has to be considered when synthesizing the coupling structures. For this, the compensation line of each element is simulated in CST Microwave Studio® with the expected (machined) conductivity of Albromet-W 200 (about  $12 \times 10^6$  Sm $^{-1}$ ). The corresponding transmission coefficient  $s_{21}(n)$  is denoted as  $t_{\text{comp}}(n)$ . From this, the required power level at the coupled port of each coupling structure can be deduced according to

$$P_c(n) = P_{\text{rad}}(n) 10^{-t_{\text{comp}}(n)/10}. \quad (5.3)$$

For the compensation lines of the AUG phased array antenna, the transmission coefficients  $t_{\text{comp}}(n)$  are in a range from  $-3.84$  dB of the central element to  $-0.72$  dB of the outermost element.

In the synthesis of the coupling structure, the coupling structure itself is considered as a node. The power entering the coupling structure has to leave it at the other two ports. If starting the synthesis process at the central element, the remaining power in the feed is unknown. Hence, the synthesis has to start at the outermost elements. Here, either the remaining power towards the absorber or the coupling factor of the last element may be defined to disambiguate the synthesis. It is a variable that allows to synthesize the coupling inserts in a machinable range. This is, if the coupling factor is larger, the remaining power in the feed is lower and vice versa. Thus, the other coupling

factors shift accordingly to larger or smaller values. For this thesis, the coupling factor of the outermost element  $n = 19$  is chosen to be  $c_{\text{coup}}(19) = -16 \text{ dB}$ . The remaining power at the end of the serial feed chain thus follows as

$$P_{\text{rem}}(19) = P_c(19) 10^{-c_{\text{coup}}(19)/10}. \quad (5.4)$$

The input power at the last coupling structure is accordingly

$$P_{\text{in}}(19) = P_{\text{rem}}(19) + P_c(19). \quad (5.5)$$

Note that an equal relation holds for the other branch of the serial fed structure. That is, for the element  $n = -19$ . In the following, only the branch with positive element indices is considered. The other branch follows equally as the array taper is symmetric.

The input power at the  $n = 18$  coupling structure is given by the sum of the coupled power of the  $n = 18$  coupling structure and required input power of the  $n = 19$  coupling structure plus the lost power in-between two coupling structures (predominantly due to attenuation in the phase shifter). For the design of the periodic section, see Section 5.2.1, the transmission from one coupling structure to the next is  $t_{\text{cc}} = -0.42 \text{ dB}$ . Consequently, the required input power at the  $n = 18$  coupling structure is

$$P_{\text{in}}(18) = P_c(18) + P_{\text{in}}(19) 10^{-t_{\text{cc}}/10}. \quad (5.6)$$

This represents a recursive process, which can be denoted as

$$P_{\text{in}}(n-1) = P_c(n-1) + P_{\text{in}}(n) 10^{-t_{\text{cc}}/10}. \quad (5.7)$$

for all elements  $n = 1, 2, \dots, 19$  in a branch. This recursive process loops until the central element.

At the central element  $n = 0$ , the required input power of both branches (positive and negative element indices) are combined by the hybrid-coupler. Together with the transmission coefficient through the coupler to the subsequent element  $t_{\text{central}}$  and the required coupled power at the central element  $P_c(0)$  follows the required input power at the central element  $P_{\text{in}}(0)$  as

$$P_{\text{in}}(0) = P_c(0) + P_{\text{in}}(1) 10^{-t_{\text{central}}/10}. \quad (5.8)$$

Once the input power  $P_{\text{in}}(n)$  at each element and the required coupled power  $P_c(n)$  are known, the coupling factor of the corresponding coupling structure follows as

$$c_{\text{coup}}(n) = 10 \log_{10} (P_c(n) / P_{\text{in}}(n)). \quad (5.9)$$

The previous synthesis procedure does not cover the frequency axis. This is, it is a synthesis for a fixed frequency or, alternatively, for the mean in the operational frequency range. However, the insertion loss of the compensation lines and the insertion

loss in-between two coupling structures has a certain frequency dependency. This can be accounted for by treating the power levels and insertion losses as a function of the frequency and applying a recursive scheme. Again, once these values have been obtained by the iterative scheme, the required frequency-dependent coupling factor in each coupling structure can be synthesized.

For the final design of the AUG phased array antenna, the frequency axis was sampled by 11 equally spaced frequency points in the range 75 GHz to 105 GHz. The previously described procedure yields frequency-dependent coupling factors at each coupling structure. These values were the target goal of an optimization by full-wave simulations of each coupling structure in CST Microwave Studio® (version 2017.5). Each coupling structure was individually optimized to the desired frequency-dependent coupling factor, yielding the final dimensions of the inserts.

### 5.2.7 Control of the Variable Phase Shifters

Within the periodic section of the serial feed chain are the phase shifters. They follow the design described in Section 4.2. Each phase shifter is composed of a hybrid-junction and two synchronously moved and positioned sliding shorts. In this design, both sliding shorts share the same reference plane. Moreover, the periodic section of the series feed chain, see Section 5.2.1, is designed such that all the sliding shorts within a branch can share the same reference plane. Thus, the phase shifters in each branch can be controlled by a single actuator. The sliding shorts in the other branch need to move in opposite direction in order to realize the negative phase shift, compare Fig. 5.1.

For the AUG phased array antenna, a mounting frame positions all sliding shorts of a branch in the corresponding open-ended waveguide, see Fig. 5.8. It ensures that the sliding shorts are all located at the correct axial position within the rectangular hollow waveguide. The radial positioning of the sliding shorts is guaranteed by the design of the phase shifter, see Section 4.2. The mounting frame slides on a linear stage that guarantees frictionless movement in vacuum and correct alignment. The linear stage is driven by a Piezo actuator.

The Piezo actuator has a range of motion of 1.5 mm or  $\pm 0.75$  mm. For the corresponding phase shift, see Fig. 4.17. From 75 GHz to 105 GHz, the possible phase shifts are roughly within the range  $\pm 90^\circ$  to  $\pm 150^\circ$ . Given the  $d_x = 2$  mm spacing of the elements, this yields a steering range of  $\pm 30^\circ$  to  $\pm 36^\circ$ . For Doppler reflectometry, only  $\pm 20^\circ$  steering angle is required. Thus, each branch has a certain range of motion left for calibration.

The broadside radiation represents the  $0^\circ$  phase shift. Within the mounting frame of the sliding shorts, there are reference pins ranging into the feed network to a reference plane. These pins provide the  $0^\circ$ -steering angle position of the mounting frame. When assembling the phased array antenna, the Piezo actuators are set to their  $0^\circ$ -steering angle position before the screws in the elongated hole (see upper right view in Fig. 5.8)

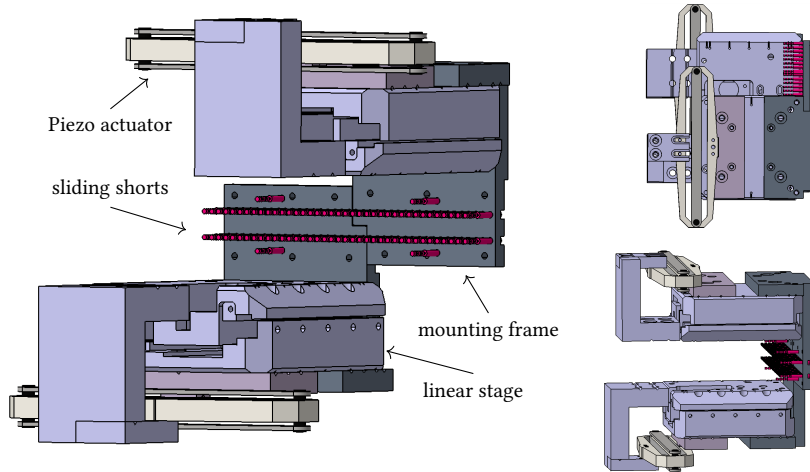


**Fig. 5.8:** Model of the phase shifter control unit. It is composed of two identical subunits. The sliding shorts for the phase shifters in one branch are fixed and axially positioned by a mounting frame. The mounting frame is connected to a linear stage for frictionless movement with the correct alignment. The linear stage is driven by a Piezo actuator. Reference pins in each mounting frame provide the reference position for broadside radiation of the beam, i.e.,  $0^\circ$  phase shift.

are tightened. By tightening the screws, the Piezo actuators zero-position is linked to the  $0^\circ$ -phase shift in-between the elements.

### 5.2.8 Model of the Phased Array Antenna

For the model of the phased array antenna, see Fig. 5.9. The 39 radiating reflectors are stacked on top of each other. The reflector stack is tightened by long screws to a single unit. The serial feed chain is composed of 6 individual split-block layers. Due to the dense waveguide routing within the split-block layers, screws are not applicable to realize enough contact pressure between the individual layers. Thus, two band springs and a U-shape fixture apply an external force. The reflector unit is connected to the serial feed chain. Two forceps pull the flange together.

In AUG, the beam is to be radiated in X-mode polarization. A console, see Fig. 5.10, correctly aligns the phased array antenna towards the plasma. The reflector unit as well as the U-shaped fixture are firmly connected to the console. The console is designed as to hold the antenna in place in case of a plasma disruption.

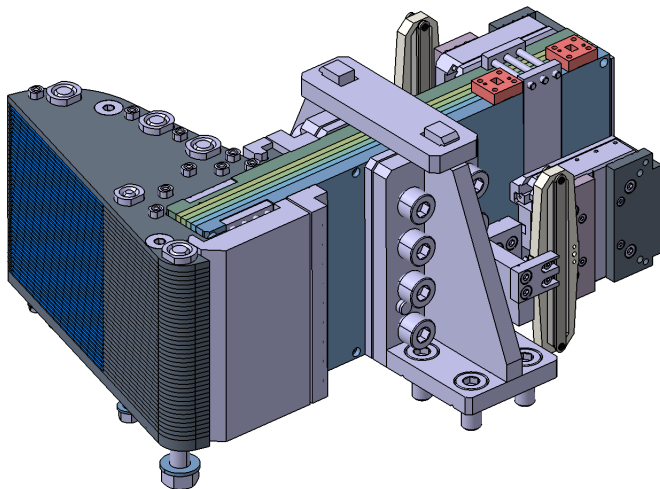


**Fig. 5.9:** Model of the phased array antenna for ASDEX Upgrade tokamak. It is composed of the reflector unit and the feed network with the serial feed chains and compensation lines. Two anchors clamp both units together. The layer of the feed network are pressed together by two spring plates and the U-shape fixture.

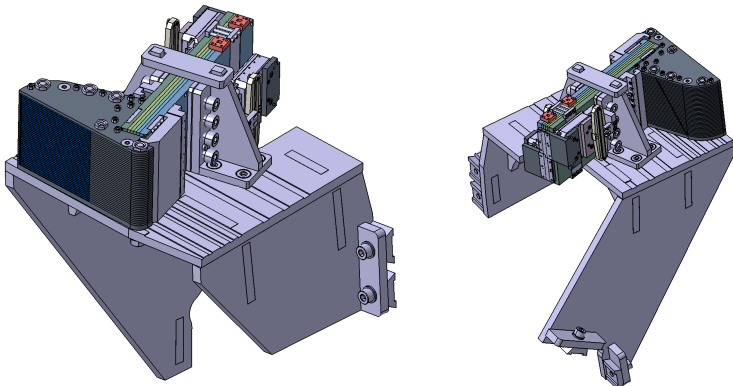


**Fig. 5.10:** Model of the phased array antenna for ASDEX Upgrade tokamak mounted on a console. The console realizes the correct alignment of the radiated beam into the plasma and holds the antenna in position — even in case of a plasma disruption.

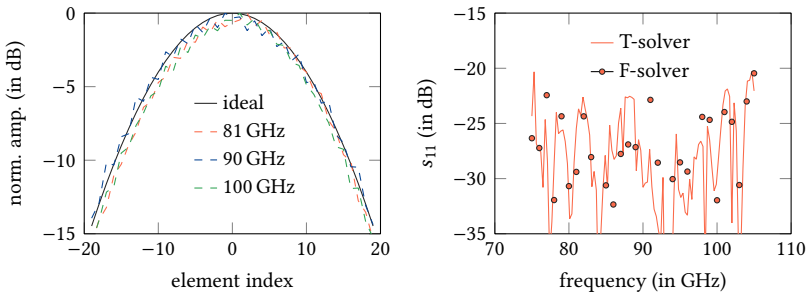


**Fig. 5.11:** Simulation results of the AUG phased array antenna. Left: Amplitude distribution at the radiating elements with reference to the desired taper. Right: Reflection coefficient from simulation in the frequency- and in the time-domain.

### 5.3 Simulation Results

The feed-network as of Fig. 5.7 was simulated in CST Microwave Studio<sup>®</sup> (version 2017). The geometry was solved in the time- and frequency-domain, for comparison. In the time-domain simulation, the whole feed-network was simulated in one-piece. In contrast, for the frequency-domain simulation, the compensation lines were separated from the serial feed chain to reduce the overall memory consumption of the simulation.

#### 5.3.1 Amplitude and Phase at the Array Aperture

The realized array taper and the input reflection are evaluated in this section. For the normalized amplitude at the radiating elements, see the left plot in Fig. 5.11, and for the input reflection, see the right plot in Fig. 5.11.

The amplitude distribution is evaluated at three frequency points (81 GHz, 90 GHz, and 100 GHz) distributed over the desired bandwidth. The amplitude distribution at 90 GHz follows the ideal distribution with a relative variation smaller than 1 dB. It is symmetric about the central element. At 81 GHz and 100 GHz, the amplitude distribution is slightly unsymmetrical with smaller amplitudes at the negative element indices. This is due to the branch-guide coupler that divides the incoming wave slightly unsymmetrical into both branches. Nevertheless, the overall amplitude distribution is roughly within an error bar of  $\pm 1$  dB from the ideal amplitude distribution.

The input reflection is below  $-20$  dB throughout the desired band and, thus, very low. The reason is again the hybrid-junction that divides the incoming wave into both branches. The reflection coefficient within each branch of the serial feed-chain appears to have the same amplitude and phase due to the symmetry. Equally to the variable phase shifter, the reflected waves add up coherently at the absorbing port, while they

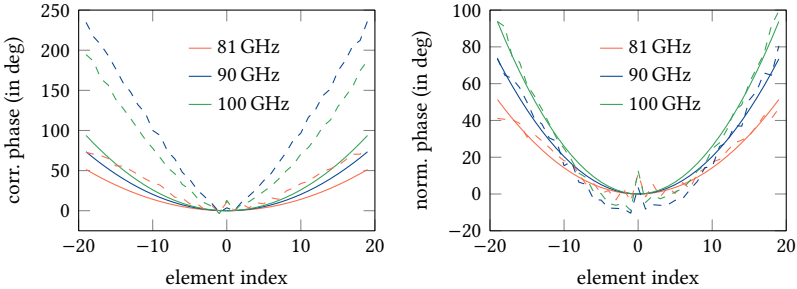


**Fig. 5.12:** Desired (solid) and simulated (dashed) phase taper. Left: Simulation results without phase correction. Right: Simulation results with phase correction according to Tab. 5.1.

add up destructively at the input port. All reflections that occur after the  $90^\circ$ -phase compensation in the focusing section of the radiating elements add up coherently at the input port and destructively at the absorbing port of the hybrid-junction. The phase compensation is the last element before the radiating element. Thus, the overall reflection at the input port is low. This low self-reflection of the phased array antenna is beneficial in the monostatic arrangement of the Doppler reflectometer, as the reflected signal would overlay the measured signal and, thus, reduce the sensitivity of the system.

For the phase distribution along the individual elements of the array aperture, see Fig. 5.12. The left plot shows the uncorrected phase distribution from the frequency domain simulation and the desired phase taper for reference. The simulated phase distribution without any correction does not agree well with the desired phase taper. The phase error is about  $200^\circ$  in the worst case. The origin of this error is in part due to the non-perfect constant-phase compensation, see Fig. 4.25 where the phase error is in the range of  $+5^\circ$  to  $-7^\circ$ . Clearly, other imperfections also add up to the overall phase error in Fig. 5.12. The major part of this phase error, however, models a progressive phase along the individual branches. This is, a constant phase error is present between the individual elements. The variable phase shifter can correct for that by slightly adapting the phase shifter position.

In Tab. 5.1, a correcting progressive phase shift for the positive and the negative array direction are given. These minimize the error between the realized and the desired phase shift. Both simulations in the frequency- and time-domain yielded similar results. For the corrected phase taper, see the right plot in Fig. 5.12 that shows the phase taper from the frequency-domain simulation with an applied linear phase correction and the desired phase taper for reference. With the compensation of the progressive phase error, the phase taper equals the desired phase taper to about  $\pm 10^\circ$ . A small outlier remains at the central element, which cannot be corrected by the phase shifters.

**Table 5.1:** Phase correction (linear phase per element) in positive and negative array direction. The correction values are listed for the frequency-domains (F) as well as the time-domain (T).

Frequency	Solver	positive array direction	negative array direction
81 GHz	F	-1.64°	-1.67°
81 GHz	T	-0.81°	-0.74°
90 GHz	F	-8.20°	-8.47°
90 GHz	T	-8.89°	-9.11°
100 GHz	F	-4.61°	-5.30°
100 GHz	T	-6.47°	-7.04°

At other simulated frequencies, the aperture taper either has similar error bounds or is completely useless. For example, the frequencies 82 GHz, 84 GHz, ..., 98 GHz have a maximum amplitude error from the ideal taper of +1.5 dB and -2.5 dB for all frequencies and all elements. The maximum phase error is in the range of  $\pm 13^\circ$ . On the other hand, at, e.g., 80 GHz, the reflections in each branch of the serial feed chain add up coherently at the central-elements hybrid-junction, see Section 5.2.2. As a consequence, only a small portion of the input power is radiated while a larger part is reflected from the branches and eventually absorbed in the load. Normally, this effect results in an increased input reflection and this frequency would not be used for radiation. For the particular design of the AUG phased array antenna, the power in the branches drops by about 3 dB while the radiated power at the central element stays the same. This distorts the aperture taper and, thus, the radiated beam.

The efficiency of the feed network, in terms of available power transmitted from the input to the radiating elements, reaches from about 12% at 75 GHz to above 22% at 105 GHz. This is basically due to the stronger attenuation of the rectangular hollow waveguide at lower frequencies. At the representative frequencies that are used to evaluate the radiated beam, the efficiencies are 17.5% at 81 GHz, 19.3% at 90 GHz, and 21.9% at 100 GHz. These values are deduced from the frequency-domain simulation.

### 5.3.2 Radiated Beam in the Steering Plane

Based on the simulated aperture field distribution and the plane wave spectrum representation of the radiated field from the radiating element, see Section 2.2.3, the synthesized and radiated Gaussian beam can be computed. In this section, the beam is radiated in broadside direction and evaluated in the steering plane, only. The cross-sectional beam profile is evaluated in the subsequent section.

For the Gaussian beam shape within the steering plane, see Fig. 5.13. The field

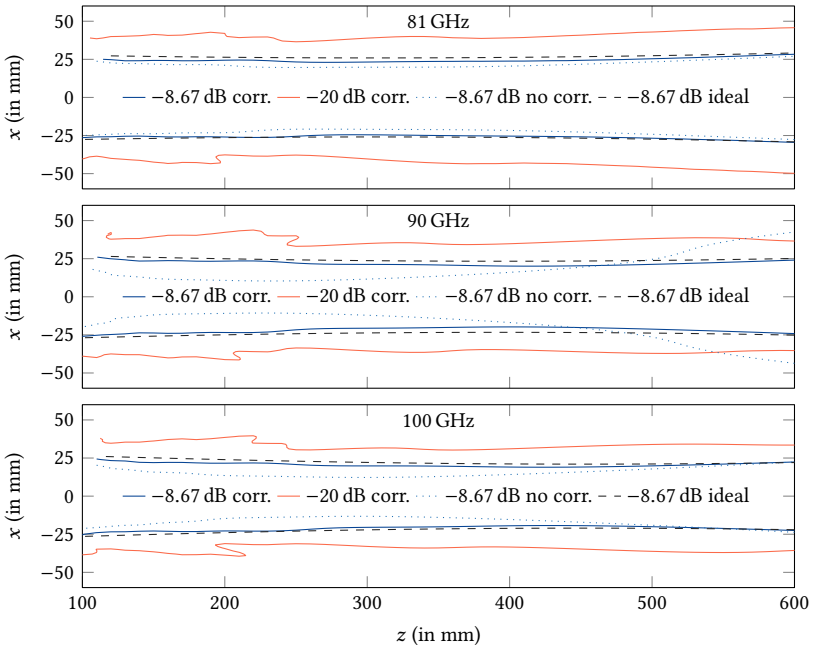


**Fig. 5.13:** Realized Gaussian beam shape from the plane wave spectrum evaluation of the simulated (frequency-domain) and corrected aperture field distribution in the steering plane. Propagation of the aperture field in broadside direction with  $z$  as the distance from the array aperture and  $x$  as the transverse coordinate. Amplitude of the field is normalized to the maximum amplitude in a distance column  $z$ . The desired beam shape is denoted as ideal.

is evaluated at the frequencies 81 GHz, 90 GHz, and 100 GHz with the corrected and uncorrected aperture field distribution of Fig. 5.12. The desired beam shape, which would follow from a continuous source field distribution, is denoted as the ideal beam contour.

The beam waist radius is represented by the  $-8.67$  dB contour in Fig. 5.13. At 81 GHz, the corrected and non-corrected aperture field distribution lead to a beam shape that is very close to the desired one, while the corrected phase taper is slightly better. At 90 GHz and 100 GHz, the uncorrected aperture taper leads to beams that are far from the desired beam shape. With the appropriate phase correction, however, the radiated beam assembles the desired beam shape very well. This is, the beam waist radius and focal distance are as expected.

The ratio of the realized beam waist radius from the correct aperture taper to the

**Table 5.2:** Ratio of sampled and synthesized beam waist radii with respect to the desired beam waist radius of the continuous aperture distribution.

Frequency	Ratio sampled/desired	Ratio synthesized/desired
81 GHz	0.947	0.923
90 GHz	0.965	0.857
100 GHz	0.958	0.917

desired beam waist radius is listed in Tab. 5.2. As described in Section 3.3.1, the sampling process leads to a smaller beam waist due to the single element pattern of the radiating or sampling element. The beam waist ratio of the sampled aperture distribution to that of the continuous aperture distribution is about 0.95. The simulated and correct aperture taper leads to a beam waist ratio of about 0.92 at 81 GHz and 100 GHz and 0.86 at 90 GHz.

For the transverse field distribution in the focal plane, see Figs. 5.14 to 5.16. In these plots, the normalized amplitude distribution and the normalized phase within the steering plane ( $xz$ -plane) for broadside radiation is evaluated in the focal distance from the array aperture. The left plot in each figure shows the normalized amplitude due to the (ideal) continuous and sampled aperture field distributions compared to those realized by the simulated and corrected aperture tapers from the time- and frequency domain. The right plot in each figure shows the normalized phase. The evaluated frequencies are again 81 GHz, 90 GHz, and 100 GHz.

The side-lobe level of the ideal sampled and the simulated and corrected aperture fields is below  $-25$  dB for the evaluated frequencies. Moreover, the beam-contour of the simulated aperture field follows that of the sampled field relatively accurate. This is, the zeros and maxima occur at the same transversal positions. The uncorrected simulated aperture field (no phase correction) has non-negligible glitches for the 90 GHz and 100 GHz field, see Fig. 5.15 and Fig. 5.16 respectively. The beam waist radius is smaller and the side-lobe level higher.

In the focal distance, the ideal transverse phase equals that of a plane wave. This is, the normalized phase is  $0^\circ$ . Within the beam waist, the ideally sampled and the simulated and corrected phase distribution is very close to that of the zero-phase. The variation is in the range of  $\pm 10^\circ$  for the evaluated frequencies. Again, the uncorrected simulated aperture field 90 GHz and 100 GHz leads to strong discrepancies and the phase is far from that of a plane wave.

Note that the simulated and correct aperture field from the time-domain and that from the frequency-domain lead to almost equal beam shapes. Clearly, this is expected, but it provides additional confidence for simulation models of the electrical size of the

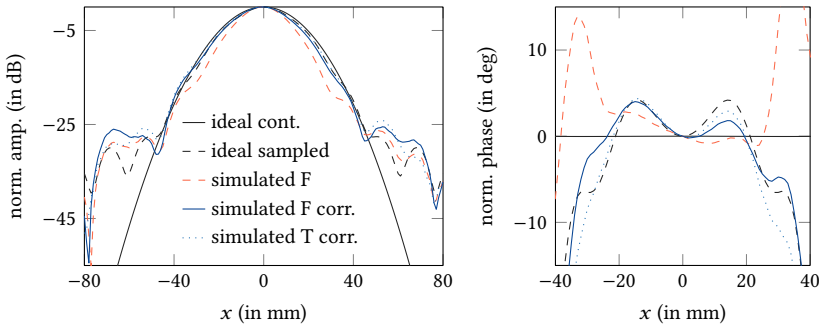


**Fig. 5.14:** Transverse field distribution of the radiated beam at 81 GHz in a distance of  $z = 307$  mm (broadside). Left: normalized amplitude distribution. Right: normalized phase distribution.

phase array antenna.

Overall, the transverse field distribution within the steering plane is in the expected range from the investigation in Section 3.3.3. In particular, the amplitude error of  $\pm 1$  dB and phase error of  $\pm 10^\circ$  on the aperture taper led to a phase deviation below  $\pm 10^\circ$  in the focal plane and a side-lobe level below  $-20$  dB, see Fig. 3.9. This agrees well with the simulated transverse fields in Figs. 5.14 to 5.16.

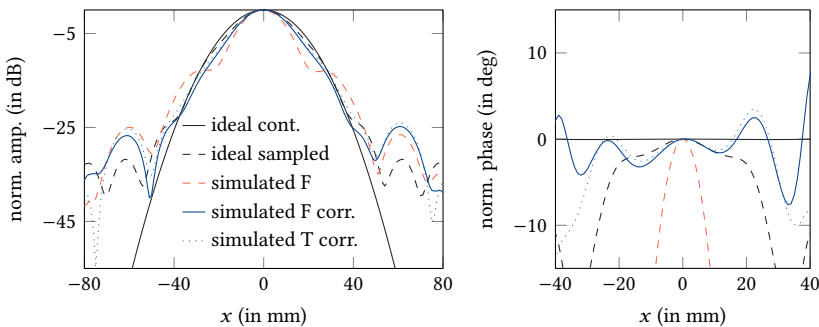


**Fig. 5.15:** Transverse field distribution of the radiated beam at 90 GHz in a distance of  $z = 394$  mm (broadside). Left: normalized amplitude distribution. Right: normalized phase distribution.

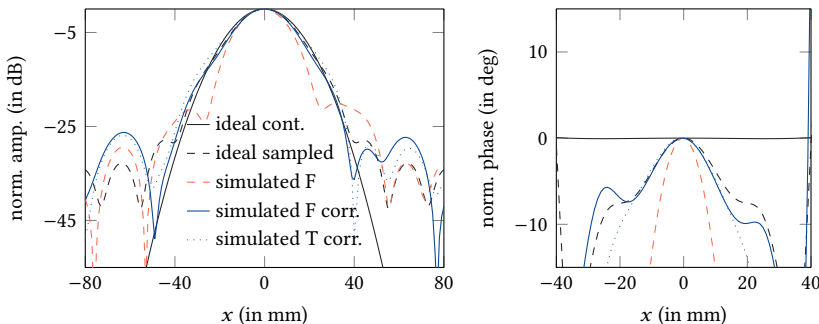


**Fig. 5.16:** Transverse field distribution of the radiated beam at 100 GHz in a distance of  $z = 453$  mm (broadside). Left: normalized amplitude distribution. Right: normalized phase distribution.

### 5.3.3 Cross-Sectional Beam with Beam Steering

The field distribution in the transverse plane at the focal distance is evaluated in this section. For this, the radiated field of the reflector elements is decomposed into a two-dimensional plane wave spectrum as described in Section 2.2.3. For this, the radiated field is evaluated on a transverse plane in a distance of  $10\lambda$  from the array aperture, similar to the procedure in Section 3.3.6. Two different source fields are investigated. The first source field follows from a full-wave simulation of the reflector stack (all 39 elements) with the ideal array taper for the desired beam. This source field includes all mutual coupling effects, but the beam cannot be steered (changing the weights in CST Microwave Studio<sup>®</sup>, version 2017, requires a new full-wave simulation). The second source field distribution is synthesized from the radiated field of an active reflector element with three passive neighboring elements on each side. This models the mutual coupling effects of the direct neighbors, while allowing to modify the element weights, see Section 3.3.6. The weights of the individual radiating elements follow from the full-wave simulation of the feed network with the subsequent phase correction, see previous section. This is, the corrected array taper is employed for the second source field. All fields are evaluated at the frequencies 81 GHz, 90 GHz, and 100 GHz.

The left plot of Figs. 5.17 to 5.19 shows the beam waist in broadside direction of the full-wave source field, the beam waist from the synthesized source field, and for comparison the desired beam waist (note that  $w_{0x} = 7\lambda = w_{0y}$  for these plots). The beam shape in  $y$ -direction is controlled by the reflector contour. The beam shape in  $x$ -direction is shaped by the array taper.

Similar to the results in Tab. 5.2, the synthesized beam waists in  $x$ -direction are smaller than the desired beam waist for all three frequencies. The realized Gaussian

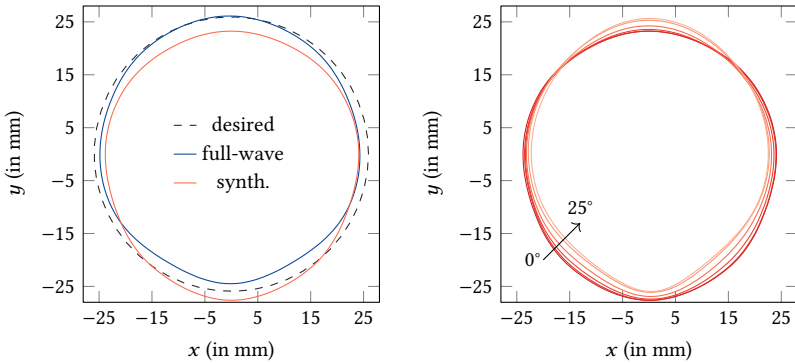


**Fig. 5.17:** Cross-sectional beam waist at 81 GHz and a focal plane distance  $z = 307$  mm. Left: comparison of the full-wave radiated field (ideal array taper) and the sampled/synthesized radiated field (simulated array taper) with the desired beam waist ( $w_{0x} = 7\lambda = w_{0y}$ ). Right: beam waist from the sampled/synthesized source field for steering angles from  $0^\circ, 5^\circ, \dots, 25^\circ$ .

beam always has a smaller beam waist as compared to the desired beam waist. This is due to the radiating element pattern and, thus, can be considered when defining the array taper, see the discussion in Section 3.3.1. At 90 GHz, where the aperture phase error is worst, the deviation is largest. In  $y$ -direction, no special beam shape is required for Doppler reflectometry. The goal is to maximize the energy density in the measurement region. The focal distance of the Gaussian beam in the  $yz$ -plane is closer to the antenna than the focal distance of the Gaussian beam in the steering plane. For higher frequencies and, thus, larger focal distances, the beam waist in  $y$ -direction is larger. Hence, the cross-sectional beam shape is more the form of an ellipse.

The right plot in Figs. 5.17 to 5.19 shows the progression of the synthesized cross-sectional beam waist for steering angles in the range  $0^\circ, 5^\circ, \dots, 25^\circ$ . There is only a small dependency of the beam waist on the steering angle. Up to  $10^\circ$ , the beam waist does not vary much and may be assumed constant. For larger steering angles, from  $15^\circ$  to  $25^\circ$ , the beam waist shrinks more and more. This is due to the influence of the single element pattern for larger steering angles. The effect also correlates with the investigation in the right plot of Fig. 3.11.

Overall, steering the radiated beam has a small influence on the beam shape. The beam quality mainly depends on the realized array taper. At 81 GHz and 100 GHz, the realized beam waist comes closer to the desired beam waist as compared to 90 GHz. The realized beam waist is always smaller than the desired one by about 5% to 10%, which is due to the element pattern of the radiating element. This effect should be considered in the array taper, by synthesizing it for a slightly larger beam waist radius.

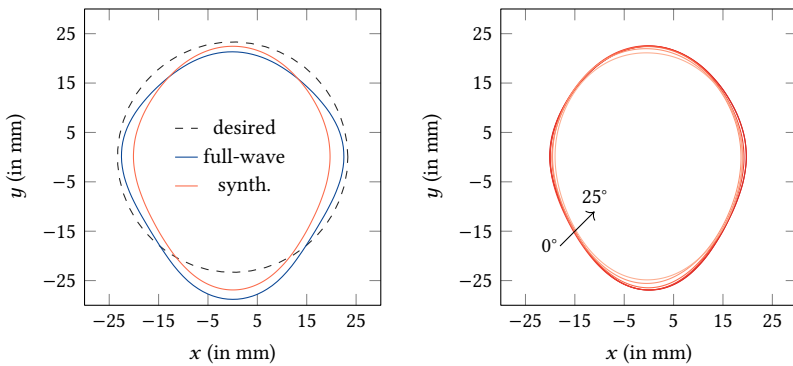


**Fig. 5.18:** Cross-sectional beam waist at 90 GHz and a focal plane distance  $z = 394$  mm. Left: comparison of the full-wave radiated field (ideal array taper) and the sampled/synthesized radiated field (simulated array taper) with the desired beam waist ( $w_{0x} = 7\lambda = w_{0y}$ ). Right: beam waist from the sampled/synthesized source field for steering angles from  $0^\circ, 5^\circ, \dots, 25^\circ$ .

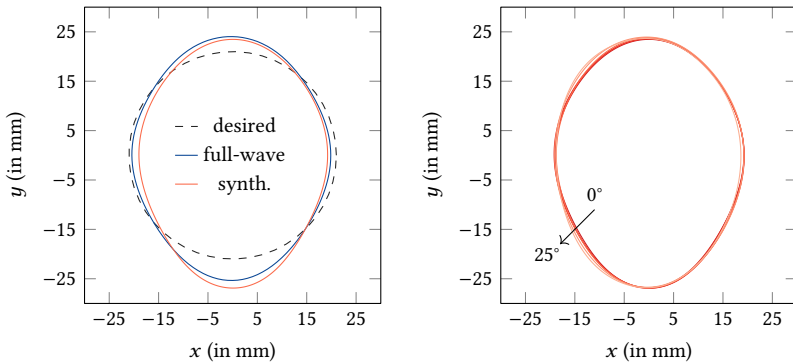


**Fig. 5.19:** Cross-sectional beam waist at 100 GHz and a focal plane distance  $z = 453$  mm. Left: comparison of the full-wave radiated field (ideal array taper) and the sampled/synthesized radiated field (simulated array taper) with the desired beam waist ( $w_{0x} = 7\lambda = w_{0y}$ ). Right: beam waist from the sampled/synthesized source field for steering angles from  $0^\circ, 5^\circ, \dots, 25^\circ$ .



## 6 Conclusions

The goal of this thesis was to realize a front-end antenna for Doppler reflectometry in the ASDEX Upgrade tokamak. Due to the limited installation space inside the nuclear fusion vessel and the harsh environmental conditions near the plasma, the only feasible front-end is a phased array antenna build predominantly from metal.

The radiated field had to be a Gaussian beam with a frequency-dependent beam waist in the *W*-band (particularly from 75 GHz to 105 GHz). Shaping such a beam is possible by sampling its transverse field distribution in the plane of the array aperture, where the radiating elements represent the sampling elements. Moreover, the Gaussian beam can be synthesized by an array in one principle plane and by a continuous source field distribution in the other principle plane.

Steering the beam is necessary to measure plasma turbulence for different turbulence sizes (wavenumber) and, thus, finally obtain a turbulence spectrum. Beam steering should be fast and precise, enabling a high spatial and spectral resolution of the plasma turbulence spectrum. The desired steering angle was in the range of  $\pm 20^\circ$  from broadside radiation. For this thesis, the steering angle had to be controlled independently from the frequency of the radiated field. Thus, realizing the same steering angle for the incident beam into the plasma as well as for the returning Doppler shifted beam that is back-scattered from the turbulent cut-off layer. Enabling this measurement requires actively controlled phase shifters. Due to the limited installation space and lifetime expectations of the actuators, only a few moving parts had to realize the beam steering capability.

The final phased array antenna was designed in WR10-rectangular hollow waveguide technology with a centrally fed series feed. It is composed of 39 individual radiating reflector elements and a feed-network that provides the desired frequency-dependent complex element weights. Two Piezo actuators are employed to steer the beam. The individual components that realize the required aperture field distribution were specifically designed and their functionality was verified by prototypes. Among the realized components are two that have an outstanding performance that should be summarized here. Namely, a broadband power divider (or coupling structure) that can tap-off a portion of power from the main feed line of a serial feed network and a reflection-type phase shifter.

The power divider was realized in two pieces: a WR10-*E*-plane T-junction and a wire-eroded insert that controls the coupling. Nearly constant coupling values were realized in the range from  $-10\text{ dB}$  to  $-25\text{ dB}$  with a variation of about  $\pm 0.5\text{ dB}$  throughout the

entire *W*-band. The mean coupling agreed to about  $\pm 0.1$  dB with the desired values.

The reflection-type phase shifter is composed of a branch-guide coupler as hybrid-junction and two synchronously moved sliding shorts. Misalignment of the sliding short in the waveguide is avoided by design. The insertion loss of the prototype phase shifter is at about 0.2 dB to 0.4 dB from 80 GHz to 105 GHz, while the input reflection is below  $-25$  dB. The realized phase shift agrees to  $+8^\circ$  and  $-6^\circ$  with the desired phase shift. Influence of manufacturing tolerance of the sliding shorts results in a phase error smaller than  $\pm 1^\circ$ .

A model of the phased array antenna was simulated in the time- and in the frequency-domain. Both simulations yielded similar results. At frequencies that are not affected by the stop-band effect of the series feed, the realized aperture taper agrees at least to  $+1$  dB and  $-2.5$  dB in amplitude and at least to  $\pm 13^\circ$  in phase with the desired aperture taper. However, a calibration of the phase of the radiating elements by adjusting the zero-degree phase shifter position is necessary. The input reflection of the phased array antenna is below  $-20$  dB throughout the entire *W*-band, which is beneficial in a mono-static measurement setup where the self-reflection of the front-end may degrade the sensitivity of the whole system. The reason is the hybrid-junction that splits the incoming wave into both serial branches and directs all coherent reflections to an internal load. Just before the radiating elements are phase shifters rectifying the  $90^\circ$  phase offset between both individual branches. Subsequent reflections (also from the plasma) are directed to the input port of the phased array antenna. The mechanism may be considered similar to that in a balanced amplifier.

The radiated beam has been evaluated by propagating the plane wave spectrum of the synthesized aperture field. Mutual coupling of the neighboring elements was considered by full-wave simulations of the embedded element. The beam waist in the steering plane reassembles the desired frequency dependency, while the realized beam waist is smaller by about 5% to 10% with reference to the desired beam waist. This is due to the single element pattern of the radiating reflector elements and should be considered in the definition of the array taper by choosing the design beam waist larger by a factor of about 1.1. The beam shape in the orthogonal plane is shaped by the reflector elements. This increases the energy density in the measurement region and eventually the sensitivity. Steering the beam is possible and has only a small effect on the cross-sectional beam shape. The overall efficiency of the phased array antenna is between 17.5% and 21.9% from 81 GHz to 100 GHz. A large contributor to the overall loss are certainly the compensation lines.

There are two points that definitely should be considered when designing a phased array antenna similar to that presented in this thesis. First, the array taper has to consider the radiation pattern of the individual elements. An estimate of the realized beam follows from the plane wave spectrum propagation of the sampled aperture field distribution. The array taper should be tuned such that it realizes the desired beam waist when sampled and propagated by the plane wave spectrum method. The second point

relates to the compensation lines. Allowing a certain frequency-dependent steering angle would shorten the compensation lines and increase the overall efficiency.

Further work may focus on extending the operational frequency range over the full *V*-band and *W*-band. Both bands may have their own feed-network and a common radiating reflector, where the individual elements are combined before the horn antenna. If desired, the beam shape perpendicular to the steering plane may be further optimized by shaping also the horn flare and, thus, modifying the amplitude distribution.

Manufacturing of the phased array antenna is challenging and still ongoing. The complexity is in part due to the non-magnetic nature of the base material that makes it difficult to clamp and in part due to the desired accuracy and surface quality. Measurement results are, thus, not available at the time of writing this thesis.



## Bibliography

- [AAP+87] F. Arndt, I. Ahrens, U. Papziner, U. Wiechmann, and R. Wilkeit, “Optimized E-plane T-junction series power dividers”, *IEEE Trans. Microw. Theory Techn.*, vol. 35, no. 11, pp. 1052–1059, Nov. 1987.
- [Bal05] C. A. Balanis, *Antenna Theory: Analysis and Design*. Hoboken, NJ: John Wiley and Sons, 2005.
- [Bal12] ——, *Advanced Engineering Electromagnetics*. Hoboken, NJ: John Wiley and Sons, 2012.
- [BR98] S. Barker and G. M. Rebeiz, “Distributed MEMS true-time delay phase shifters and wide-band switches”, *IEEE Trans. Microw. Theory Techn.*, vol. 46, no. 11, pp. 1881–1890, Nov. 1998.
- [Bet39] H. A. Bethe, “Energy production in stars”, *Phys. Rev.*, vol. 55, no. 5, pp. 434–456, 1939.
- [Boh89] M. Boheim, “Focusing mirrors for Gaussian beams”, in *IEEE MTT-S International Microwave Symposium Digest*, vol. 3, Long Beach, CA, USA, Jun. 1989, pp. 1255–1258.
- [BR82] M. K. Brewer and A. V. Räisänen, “Dual-harmonic noncontacting millimeter waveguide backshorts: Theory, design, and test”, *IEEE Trans. Microw. Theory Techn.*, vol. 30, no. 5, pp. 708–714, May 1982.
- [CP71] L. M. V. Camargo and I. Palócz, “A new Fraunhofer zone and some of its applications”, *Proceedings of the IEEE*, vol. 60, no. 1, pp. 149–150, 1971.
- [Con08] G. D. Conway, “Turbulence measurements in fusion plasmas”, *Plasma Physics and Controlled Fusion*, vol. 50, no. 12, p. 124 026, 2008.
- [CPHt10] G. D. Conway, E. Poli, T. Happel, and the ASDEX Upgrade team, “Interaction of mean and oscillating plasma flows across confinement mode transitions”, *Plasma and Fusion Research*, vol. 5, S2005, 2010.
- [CSK+04] G. D. Conway, J. Schirmer, S. Klenge, W. Suttrop, E. Holzhauer, *et al.*, “Plasma rotation profile measurements using Doppler reflectometry”, *Plasma Physics and Controlled Fusion*, vol. 46, no. 6, pp. 951–970, 2004.
- [Cut47] C. C. Cutler, “Parabolic-antenna design for microwaves”, *Proceedings of the IRE*, vol. 35, no. 11, pp. 1284–1294, Nov. 1947.

- [Dur87] J. Durnin, “Exact solutions for nondiffracting beams. I. The scalar theory”, *J. Opt. Soc. Am. A*, vol. 4, no. 4, pp. 651–654, 1987.
- [DME87] J. Durnin, J. J. Miceli, and J. H. Eberly, “Diffraction-free beams”, *Phys. Rev. Lett.*, vol. 58, no. 15, pp. 1499–1501, 1987.
- [FT61] A. G. Fox and L. Tingye, “Resonant modes in a maser interferometer”, *The Bell System Technical Journal*, vol. 40, no. 2, pp. 453–488, 1961.
- [FKR+13] A.-L. Franc, O. H. Karabey, G. Rehder, E. Pistono, R. Jakoby, and P. Ferrari, “Compact and broadband millimeter-wave electrically tunable phase shifter combining slow-wave effect with liquid crystal technology”, *IEEE Trans. Microw. Theory Techn.*, vol. 61, no. 11, pp. 3905–3915, Nov. 2013.
- [Gar72] R. V. Garver, “Broad-band diode phase shifters”, *IEEE Trans. Microw. Theory Techn.*, vol. 20, no. 5, pp. 314–323, May 1972.
- [Gol98] P. F. Goldsmith, *Quasioptical Systems: Gaussian Beam Quasioptical Propagation and Applications*. New York: IEEE Press, 1998.
- [GSB11] S. Gong, H. Shen, and N. S. Barker, “A 60-GHz 2-bit switched-line phase shifter using SP4T RF-MEMS switches”, *IEEE Trans. Microw. Theory Techn.*, vol. 59, no. 4, pp. 894–900, Apr. 2011.
- [Hap10] T. Happel, *Doppler Reflectometry in TJ-II Stellarator: Design of an Optimized Doppler Reflectometer and its Application to Turbulence and Radial Electrical Field Studies*. Universidad Carlos III de Madrid, 2010.
- [Har01] R. F. Harrington, *Time-Harmonic Electromagnetic Fields*. New York: IEEE Press, 2001.
- [HG13] H.-J. Hartfuß and T. Geist, *Fusion Plasma Diagnostics with mm-Waves: An Introduction*. Weinheim, Germany: Wiley-VCH, 2013.
- [HHT+04] P. Hennequin *et al.*, “Doppler backscattering system for measuring fluctuations and their perpendicular velocity on Tore Supra”, *Review of Scientific Instruments*, vol. 75, no. 10, pp. 3881–3883, 2004.
- [HH04] M. Hirsch and E. Holzhauer, “Doppler reflectometry with optimized temporal resolution for the measurement of turbulence and its propagation velocity”, *Plasma Physics and Controlled Fusion*, vol. 46, no. 4, pp. 593–609, 2004.
- [HHB+01] M. Hirsch, E. Holzhauer, J. Baldzuhn, B. Kurzan, and B. Scott, “Doppler reflectometry for the investigation of propagating density perturbations”, *Plasma Physics Controlled Fusion*, vol. 43, no. 12, pp. 1641–1660, 2001.
- [HM78] E. Holzhauer and J. H. Massig, “An analysis of optical mixing in plasma scattering experiments”, *Plasma Physics*, vol. 20, no. 9, pp. 867–877, 1978.

- [Jac99] J. D. Jackson, *Classical Electrodynamics*. Hoboken, NJ: John Wiley and Sons, 1999.
- [Jin15] J.-M. Jin, *Theory and Computation of Electromagnetic Fields*. Hoboken, NJ: John Wiley and Sons, 2015.
- [Kar05] K. W. Kark, *Antennen und Strahlungsfelder*. Wiesbaden: Vieweg+Teubner Verlag, 2005.
- [Ker76] D. M. Kerns, “Plane-wave scattering-matrix theory of antennas and antenna-antenna interactions: Formulation and applications”, *Journal of Research of the National Bureau of Standards – B. Mathematical Sciences*, vol. 80B, no. 1, pp. 5–51, 1976.
- [Ker88] A. R. Kerr, “An adjustable short-circuit for millimeter waveguides”, National Radio Astronomy Observatory, USA, Electronics Division Internal Report 280, Jul. 1988.
- [KPY+02] H.-T. Kim, J.-H. Park, J. Yim, Y.-K. Kim, and Y. Kwon, “A compact V-band 2-bit reflection-type MEMS phase shifter”, *IEEE Microw. Wireless Compon. Lett.*, vol. 12, no. 9, pp. 324–326, Sep. 2002.
- [Kit68] C. Kittel, *Einführung in die Festkörperphysik*. München: Oldenbourg Verlag, 1968.
- [LCG+17] C. Lechte, G. D. Conway, T. Görler, C. Tröster-Schmid, and the ASDEX Upgrade team, “X-mode Doppler reflectometry k-spectral measurements in ASDEX Upgrade: Experiments and simulations”, *Plasma Physics and Controlled Fusion*, vol. 59, no. 7, p. 075 006, 2017.
- [Lev73] R. Levy, “Zolotarev branch-line couplers”, *IEEE Trans. Microw. Theory Techn.*, vol. 21, no. 2, pp. 95–99, Feb. 1973.
- [LCCS07] C.-S. Lin, S.-F. Chang, C.-C. Chang, and Y.-H. Shu, “Design of a reflection-type phase shifter with wide relative phase shift and constant insertion loss”, *IEEE Trans. Microw. Theory Techn.*, vol. 55, no. 9, pp. 1862–1868, Sep. 2007.
- [LNIM01] Y. Lin, R. Nazikian, J. H. Irby, and E. S. Marmar, “Plasma curvature effects on microwave reflectometry fluctuation measurements”, *Plasma Physics and Controlled Fusion*, vol. 43, no. 1, pp. L1–L8, 2001.
- [LC57] P. D. Lomer and J. W. Crompton, “A new form of hybrid junction for microwave frequencies”, *Proceedings of the IEE - Part B: Radio and Electronic Engineering*, vol. 104, no. 15, pp. 261–264, May 1957.
- [Mai05] R. J. Mailloux, *Phased Array Antenna Handbook*. Norwood, MA: Artech House, 2005.

- [Mai07] ——, “Electronically scanned arrays”, *Synthesis Lectures on Antennas*, vol. 2, no. 1, pp. 1–82, 2007.
- [Mar51] N. Marcuvitz, *Waveguide Handbook*, ser. Radiation Laboratory Series. New York: McGraw-Hill Book Company, Inc., 1951, vol. 10.
- [MB93] D. H. Martin and J. W. Bowen, “Long-wave optics”, *IEEE Trans. Microw. Theory Techn.*, vol. 41, no. 10, pp. 1676–1690, 1993.
- [MWK95] W. R. McGrath, T. M. Weller, and L. P. B. Katehi, “A novel noncontacting waveguide backshort for submillimeter wave frequencies”, *Int. J. Infrared Millimeter Waves*, vol. 16, no. 1, pp. 237–256, 1995.
- [MDP48] C. G. Montgomery, R. H. Dicke, and E. M. Purcell, *Principles of Microwave Circuits*, ser. Radiation Laboratory Series. New York: McGraw-Hill Book Company, Inc., 1948, vol. 8.
- [MPR01] V. S. Möttönen, P. Piironen, and A. V. Räisänen, “Novel tunable waveguide backshort for millimeter and submillimeter wavelengths”, *IEEE Microw. Wireless Compon. Lett.*, vol. 11, no. 9, pp. 370–372, Sep. 2001.
- [Mue70] E. Muehldorf, “The phase center of horn antennas”, *IEEE Trans. Antennas Propag.*, vol. 18, no. 6, pp. 753–760, 1970.
- [NK92] T. Newman and T. N. Kwong, “Planar noncontacting short circuits for millimeter-wave and submillimeter-wave applications”, *IEEE Microw. Guided Wave Lett.*, vol. 2, no. 10, pp. 412–414, Oct. 1992.
- [Orf16] S. J. Orfanidis, *Electromagnetic Waves and Antennas*. Piscataway, NJ: S. J. Orfanidis, 2016.
- [PZ02] D. Parker and D. C. Zimmermann, “Phased arrays-part II: Implementations, applications, and future trends”, *IEEE Trans. Microw. Theory Techn.*, vol. 50, no. 3, pp. 688–698, Mar. 2002.
- [PPP01] E. Poli, A. G. Peeters, and G. V. Pereverzev, “TORBEAM, a beam tracing code for electron-cyclotron waves in tokamak plasmas”, *Computer Physics Communications*, vol. 136, pp. 90–104, 2001.
- [Poz11] D. M. Pozar, *Microwave Engineering*. Hoboken, NJ: John Wiley and Sons, 2011.
- [RTH02] G. M. Rebeiz, G.-L. Tan, and J. S. Hayden, “RF MEMS phase shifters: Design and applications”, *IEEE Microw. Mag.*, vol. 3, no. 2, pp. 72–81, Jun. 2002.
- [Ree58] J. Reed, “The multiple branch waveguide coupler”, *IRE Trans. Microw. Theory Techn.*, vol. 6, no. 4, pp. 398–403, Apr. 1958.

- [Rib52] H. Riblet, “Short-slot hybrid junction”, in *Proceedings of the I.R.E.*, Washington, D.C., USA, Feb. 1952, pp. 180–184.
- [Riz88] P. A. Rizzi, *Microwave Engineering: Passive Circuits*. Englewood Cliffs, NJ: Prentice Hall, 1988.
- [RWK+13] P. Rohmann, S. Wolf, W. Kasperek, B. Plaum, and J. Hesselbarth, “A 32-element frequency-steered array antenna for reflectometry in W-band”, in *IEEE Int. Symp. Phased Array Systems and Technology*, Waltham, MA, USA, Oct. 2013, pp. 559–563.
- [Sch62] F. Schwering, “On the range of validity of Fresnel-Kirchhoff’s approximation formula”, *IRE Transactions on Antennas and Propagation*, vol. 10, no. 1, pp. 99–100, 1962.
- [Sie86] A. E. Siegman, *Lasers*. Mill Valley, CA: University Science Books, 1986.
- [SB13] J. R. Stanec and N. S. Barker, “A rectangular-waveguide contacting sliding short for terahertz frequency applications”, *IEEE Trans. Microw. Theory Techn.*, vol. 61, no. 4, pp. 1488–1495, Apr. 2013.
- [Ste48] A. F. Stevenson, “Theory of slots in rectangular wave-guides”, *Journal of Applied Physics*, vol. 19, no. 1, p. 24, 1948.
- [Str11] U. Stroth, *Plasmaphysik, Phänomene, Grundlagen, Anwendungen*. Wiesbaden: Vieweg+Teubner Verlag, 2011.
- [Trö08] C. H. Tröster, *Development of a Flexible Doppler Reflectometry System and its Application to Turbulence Characterization in the ASDEX Upgrade Tokamak*. Ludwig-Maximilians-Universität München, 2008.
- [WBB+82] F. Wagner *et al.*, “Regime of improved confinement and high beta in neutral-beam-heated divertor discharges of the ASDEX Tokamak”, *Phys. Rev. Lett.*, vol. 49, no. 19, pp. 1408–1412, Nov. 1982.
- [Wat46] W. H. Watson, “Resonant slots”, *Journal of the Institution of Electrical Engineers - Part IIIA: Radiolocation*, vol. 93, no. 4, pp. 747–777, 1946.
- [WKM95] T. M. Weller, L. P. B. Katehi, and W. R. McGrath, “Analysis and design of a novel noncontacting waveguide backshort”, *IEEE Trans. Microw. Theory Techn.*, vol. 43, no. 5, pp. 1023–1030, May 1995.
- [WC74] R. B. White and F. F. Chen, “Amplification and absorption of electromagnetic waves in overdense plasmas”, *Plasma Physics*, vol. 16, no. 7, pp. 565–587, 1974.
- [You62] L. Young, “Synchronous branch guide directional couplers for low and high power applications”, *IRE Transactions on Microwave Theory and Techniques*, vol. 10, no. 6, pp. 459–475, Nov. 1962.

- [ZB90] O. Zinke and H. Brunswig, *Hochfrequenztechnik 1: Hochfrequenzfilter, Leitungen, Antennen*. Springer-Verlag, 1990.

## Own Publications

- [KGE13] C. Koenen, M. E. Gruber, and T. F. Eibert, “Computation of the rectangular cavity Green’s function using the inverse fast Fourier transform and a Lagrange polynomial interpolation”, in *Kleinheubacher Tagung*, Miltenberg, Germany, Sep. 2013.
- [GKE14] M. E. Gruber, C. Koenen, and T. F. Eibert, “Rectangular cavity Green’s functions with Ewald summation technique and fast Fourier transform acceleration”, in *International Conference on Scientific Computing in Electrical Engineering (SCEE)*, Wuppertal, Germany, Jul. 2014.
- [KSE+14] C. Koenen, U. Siart, T. F. Eibert, G. D. Conway, and U. Stroth, “Broadband Gaussian beam-shaping in a 32-element linear W-band horn array”, in *Kleinheubacher Tagung*, Miltenberg, Germany, Sep. 2014.
- [LKBD14] G. A. Lukasz, C. Koenen, N. Basta, and A. Dreher, “SEQAR: An efficient MATLAB tool for design and analysis of conformal antenna arrays [EM Programmer’s Notebook]”, *IEEE Antennas and Propagation Magazine*, vol. 56, no. 4, pp. 178–187, 2014.
- [SNC+14] U. Stroth *et al.*, “Experimental turbulence studies for gyro-kinetic code validation using advanced microwave diagnostics”, in *25th IAEA Fusion Energy Conference*, Saint Petersburg, Russia, Oct. 2014.
- [GKE15] M. E. Gruber, C. Koenen, and T. F. Eibert, “An inverse fast Fourier transform accelerated Ewald summation technique for the computation of rectangular cavity Green’s functions”, *Journal of Computational Physics*, vol. 280, pp. 570–578, Jan. 2015.
- [KSE+15a] C. Koenen, U. Siart, T. F. Eibert, G. D. Conway, and U. Stroth, “A configurable coupling structure for broadband millimeter-wave split-block networks”, *IEEE Trans. Microw. Theory Techn.*, vol. 63, no. 12, pp. 3954–3961, Dec. 2015.
- [KSE+15b] ——, “Broadband amplitude tapering for a linear W-band array antenna for Gaussian beam-shaping”, in *German Microwave Conf.*, Nuremberg, Germany, Mar. 2015, pp. 202–204.
- [KSE+15c] ——, “Methods for optimum aperture tapering in a near-field focusing linear W-band horn array”, in *Fachtagung des ITG Fachausschusses 7.5 (WFMN 2015)*, Chemnitz, Germany, Feb. 2015.

- [KSE+15d] C. Koenen, U. Siart, T. F. Eibert, T. Happel, G. D. Conway, and U. Stroth, “Development of an actively steered phased array antenna for Doppler reflectometry”, in *12th International Reflectometry Workshop (IRW12)*, Jülich, Germany, May 2015.
- [SNC+15] U. Stroth *et al.*, “Experimental turbulence studies for gyro-kinetic code validation using advanced microwave diagnostics”, *Nuclear Fusion*, vol. 55, no. 8, p. 083 027, 2015.
- [AKSE16] H. Azodi, C. Koenen, U. Siart, and T. F. Eibert, “Empirical discretization errors in sparse representations for motion state estimation with multi-sensor radar systems”, in *10th European Conference on Antennas and Propagation (EUCAP)*, Davos, Switzerland, Apr. 2016.
- [KHSE16] C. Koenen, G. Hamberger, U. Siart, and T. F. Eibert, “A volumetric near-field scanner for millimeter-wave antenna measurements”, in *10th European Conference on Antennas and Propagation (EUCAP)*, Davos, Switzerland, Apr. 2016.
- [KSE+16a] C. Koenen, U. Siart, T. F. Eibert, G. D. Conway, and U. Stroth, “A millimeter-wave phased array antenna for small-scale plasma turbulence studies on ASDEX Upgrade Tokamak”, in *Kleinheubacher Tagung*, Miltenberg, Germany, Sep. 2016.
- [KSE+16b] ——, “Design of a millimeter-wave phased array antenna for Gaussian beam shaping and steering”, in *IEEE Int. Symp. Phased Array Systems and Technology*, Waltham, MA, USA, Oct. 2016.
- [FCC+17] S. Freethy *et al.*, “Validation of ion-scale GENE simulations in L-mode plasmas at ASDEX Upgrade using CECE measurements of electron temperature fluctuations”, in *22nd EU-US Transport Task Force Meeting*, Williamsburg, VA, USA, Apr. 2017.
- [KSE17a] C. Koenen, U. Siart, and T. F. Eibert, “A low-reflectivity vacuum window”, in *Kleinheubacher Tagung*, Miltenberg, Germany, Sep. 2017.
- [KSE17b] ——, “Computation of reflector contours for Gaussian beam shaping phased array antenna elements”, in *IEEE Int. Symp. Antennas and Propagation*, San Diego, CA, USA, Jul. 2017.
- [KSE17c] ——, “Millimeter-wave Gaussian beam shaping and steering phased array antenna”, in *14th European Radar Conference (EuRAD 2017)*, Nürnberg, Germany, Oct. 2017.
- [KSEC17] C. Koenen, U. Siart, T. F. Eibert, and G. D. Conway, “A self-aligning cylindrical sliding short plunger for millimeter-wave rectangular waveguides and its application in a reflection-type phase shifter”, *IEEE Trans. Microw. Theory Techn.*, vol. 65, no. 2, pp. 449–458, Feb. 2017.

- [KSE+17] C. Koenen, U. Siart, T. F. Eibert, G. D. Conway, and U. Stroth, “A broadband millimeter-wave hollow waveguide coupling structure configured by a wire-eroded metal plug-in”, *IEEE Microw. Wireless Compon. Lett.*, vol. 27, no. 5, pp. 434–436, May 2017.
- [FGC+18] S. J. Freethy *et al.*, “Validation of gyrokinetic simulations with measurements of electron temperature fluctuations and density-temperature phase angles on ASDEX Upgrade”, *Physics of Plasmas*, vol. 25, no. 5, p. 055 903, Feb. 2018.
- [HKN+18] G. F. Hamberger *et al.*, “Setup and characterization of a volumetric-band near-field antenna measurement system”, *IEEE Trans. Antennas Propag.*, vol. 66, no. 10, pp. 5498–5510, Oct. 2018.
- [KHS+18] C. Koenen *et al.*, “A low-reflectivity vacuum window for rectangular hollow waveguides”, *IEEE Trans. Microw. Theory Techn.*, vol. 66, no. 1, pp. 128–135, Jan. 2018.



## **Supervised Theses**

- [Mor14] C. Moroder, “Phasenschieber für eine strahlschwenkende Millimeterwellenantenne zur Plasmadiagnostik bei Fusionsexperimenten”, Master’s Thesis, Technical University of Munich, Munich, Germany, Mar. 2014.
- [Kol15] P. Kolesa, “A W-band H-plane Horn Reflector Array Element for Gaussian Beam Shaping in a Doppler Reflectometry System”, Master’s Thesis, Technical University of Munich, Munich, Germany, Jul. 2015.
- [Sch16] D. Schroll, “Fehleranalyse eines planaren W-Band Nahfeld-Messplatzes”, Master’s Thesis, Technical University of Munich, Munich, Germany, Feb. 2016.